INSTITUT OBERFLÄCHENTECHNIK

Lehrstuhl für Oberflächentechnik im Maschinenbau
Rheinisch-Westfälische Technische Hochschule Aachen
Prof. Dr.-Ing. K. Bobzin

Deformation and Fracture Mechanics of Compounds with Nitride Hard Coatings for Tooling Applications

Muhammad Tayyab

März 2026

Schriftenreihe Oberflächentechnik, Band 85

Hrsg.: Prof. Dr.-Ing. K. Bobzin

Partner im
LABORATORIUM
FÜGETECHNIK
OBERFLÄCHENTECHNIK

RWTH AACHEN UNIVERSITY

Deformation and Fracture Mechanics of Compounds with Nitride Hard Coatings for Tooling Applications

Verformungs- und Bruchmechanik von Werkstoffverbunden mit nitridischen Hartstoffschichten für Werkzeuganwendungen

Von der Fakultät für Maschinenwesen der Rheinisch-Westfälischen Technischen Hochschule Aachen zur Erlangung des akademischen Grades eines Doktors der Ingenieurwissenschaften genehmigte Dissertation

vorgelegt von

Muhammad Tayyab

Berichter/in: Univ.-Prof. Dr.-Ing. Kirsten Bobzin
Univ.-Prof. Dr.-Ing. Christoph Broeckmann

Tag der mündlichen Prüfung: 17. Dezember 2025

Diese Dissertation ist auf den Internetseiten der Universitätsbibliothek online verfügbar.

Schriftenreihe Oberflächentechnik

Band 85

Muhammad Tayyab

Deformation and Fracture Mechanics of Compounds with Nitride Hard Coatings for Tooling Applications

Shaker Verlag
Düren 2026

Bibliographic information published by the Deutsche Nationalbibliothek
The Deutsche Nationalbibliothek lists this publication in the Deutsche Nationalbibliografie; detailed bibliographic data are available in the Internet at http://dnb.d-nb.de.

Zugl.: D 82 (Diss. RWTH Aachen University, 2025)

Printed in Germany.

Print-ISBN	978-3-8191-0547-0
PDF-ISBN	978-3-8191-0498-5
ISSN	1864-0796
eISSN	2944-5736

Shaker Verlag GmbH • Am Langen Graben 15a • 52353 Düren
Phone: 0049/2421/99011-0 • Telefax: 0049/2421/99011-9
Internet: www.shaker.de • e-mail: info@shaker.de

Acknowledgement

I would like to express my sincere gratitude to Prof. Dr.-Ing. Kirsten Bobzin for providing me with the opportunity to work at Surface Technology Institute (IOT) of RWTH Aachen University and for her constant supervision and invaluable guidance over the last five years. I am also grateful to Prof. Dr.-Ing. Christoph Broeckmann for accepting the role of second examiner and Prof. Dr.-Ing. Thomas Bergs for chairing the examination committee.

The results presented in this work stem from two research projects, "Experimental and simulative investigations on the fatigue behavior of compounds, consisting of Cr-based nitride hard coatings on steel substrate under cyclic impact loads and bending stresses" project number 422784687, and subproject D1 "Development of a greybox model for wear prognosis of PVD coated carbide tools during high performance turning of steels" project number 521280523, from priority research program SPP 2402 “Greybox models for the qualification of coated tools for high-performance cutting”. I am grateful to the German Research Foundation (DFG) for the generous financial support of these projects.

My sincere thanks go to all current and former colleagues at the IOT for their technical support, valuable insights and helpful scientific discussions, particularly Dr.-Ing. Nina Stachowski, Dr.-Ing. Christoph Schulz, Dr.-Ing. Matthias Thiex, Dr.-Ing. Lidong Zhao, Jessica Borowy, Dr.-Ing. Parisa Aghdam Tönnißen, Marta Miranda Marti, Lore Stalpers, Thomas Offermann, Xiaoyang Liu, Max Philip Möbius, Dirk Grünhagen, Julia Janowitz, Dennis Hoffmann, Wenting Xu and Azadeh Taheri Mofassal. For their mentorship, I would like to express my appreciation to my former group leader Dr.-Ing. Marco Carlet and my chief engineer Dr.-Ing. Christian Kalscheuer. Furthermore, I am thankful to all my students, especially Arda Kiyildi and Shahin Athar Nouri, for their dedicated assistance. To all current and former colleagues from administrative team at the IOT, I am grateful for your support during my academic journey.

Parts of the experimental investigations presented in this work were carried out at the Central Facility for Electron Microscopy (GFE) of RWTH Aachen University. In this context, I appreciate the professional support from Prof. Dr. rer. nat. Thomas Weirich, Martina Schiffers, Cleopatra Herwartz, Kevin Kistermann, Claudia Pütz, Ruth Harscheidt, Fabian Mariano and Dr. rer. nat. Silvia Richter.

I am eternally grateful to my beloved parents, Zahida Munir and Muhammad Munir, as well as to my lovely wife, Rida Fatima Ahmed, for their unwavering support, sacrifices and encouragement throughout my professional and personal endeavors. Last but not the least, I extend my heartfelt gratitude to my siblings Sana Munir, Abdul Mannan Munir and Abdul Hannan Munir for their constant assistance in my life.

Abstract

The functional performance of tools plays an important role for productivity improvement of forming and cutting processes. With the development of high strength workpiece materials, the stress collectives on the tools are increasing. Nitride hard coatings, deposited with physical vapor deposition (PVD), can increase the damage resistance of tools against abrasion, adhesion, oxidation and diffusion. However, to avoid tool failure by plastic deformation and crack growth, the compound of coating and tool substrate material needs to withstand the mechanical or thermomechanical loads in challenging forming and cutting operations. For this purpose, knowledge-based coating designs to increase the functional capability of PVD coated tools are required. Hence, this dissertation focuses on fundamental investigation of deformation and fracture mechanics of compounds in correlation with the coating thickness, residual stress state or coating architecture under indentation loadings.

The investigated compounds include CrAlN coated high-speed steel HS6-5-2C and TiAlCrSiN coated cemented carbide (WC-Co). Instrumented indentation testing is used to understand the deformation behavior of coatings as well as the compounds. Moreover, coating deformation and crack growth mechanisms under indentation loadings are studied with high resolution electron microscopy. For CrAlN/HS6-5-2C compounds, increasing the coating thickness from $s \approx 1.7$ µm to $s \approx 3.5$ µm reduces plastic deformation of compounds under indentation loading. Moreover, coupling of $s \approx 1.7$ µm and moderate compressive residual stresses $\sigma_r \approx (2 - 3)$ GPa increases impact fatigue resistance of compounds. For monotonic indentation loading of the TiAlCrSiN/WC-Co compounds, higher coating thickness of $s \approx 3.6$ µm compared to $s \approx 2.0$ µm simultaneously increases the plastic deformation and crack resistance of compounds at room as well as at higher temperatures until $T = 600$ °C. Despite the lower crack resistance of oxynitride top layer, the additional interface in the bilayer TiAlCrSiN/TiAlCrSiON architecture leads to comparable temperature dependent compound deformation and surface crack resistance with the monolayer TiAlCrSiN architecture. The utilization of indentation test data is extended to understand the correlations between temperature dependent compound deformation behavior, mechanisms of coating deformation and the fracture mechanics. Moreover, a data driven modeling approach is developed to predict the temperature dependent compound deformation and surface cracking behavior by combining indentation test data with the coating characteristics using machine learning algorithms.

Zusammenfassung

Die Funktionsfähigkeit der Werkzeuge ist für die Produktivitätssteigerung der Umform- und Zerspanungsprozesse entscheidend. Die Entwicklung hochfester Werkstückwerkstoffe führt zu einer Zunahme der Beanspruchungskollektive an den Werkzeugen. Um die Werkzeugschädigung durch Abrasion, Adhäsion, Oxidation und Diffusion zu vermindern, werden nitridische PVD-Hartstoffschichten eingesetzt. Zur Vermeidung von Werkzeugversagen infolge plastischer Verformung und Rissbildung muss der Verbund aus Beschichtung und Substratwerkstoff den mechanischen oder thermomechanischen Beanspruchungen standhalten. Hierzu sind wissensbasierte Schichtkonzepte zur Erhöhung der Funktionsfähigkeit PVD-beschichteter Werkzeuge erforderlich. Diese Dissertation fokussiert sich daher auf grundlegende Untersuchungen der Verformungs- und Bruchmechanik von Werkstoffverbunden unter Indentationsbeanspruchungen in Korrelation mit der Schichtdicke, dem Eigenspannungszustand oder der Schichtarchitektur.

Die untersuchten Werkstoffverbunde sind CrAlN-beschichteter Schnellarbeitsstahl HS6-5-2C und TiAlCrSiN-beschichtetes Hartmetall (WC-Co). Das Verformungsverhalten der Beschichtungen sowie der Werkstoffverbunde wurde mittels instrumentierter Eindringprüfungen charakterisiert. Die Deformationsmechanismen und das Risswachstum wurden mittels hochauflösender Elektronenmikroskopie untersucht. Für CrAlN/HS6-5-2C reduziert eine Erhöhung der Schichtdicke von $s \approx 1{,}7$ µm auf $s \approx 3{,}5$ µm die plastische Verformung der Verbunde. Darüber hinaus erhöht eine Kombination von $s \approx 1{,}7$ µm und moderaten Druckeigenspannungen $\sigma_r \approx (2 – 3)$ GPa die Ermüdungsfestigkeit der Verbunde unter zyklischer Stoßbelastung. Für TiAlCrSiN/WC-Co steigert eine Schichtdicke von $s \approx 3{,}6$ µm im Vergleich zu $s \approx 2{,}0$ µm den Widerstand gegen plastische Verformung und Rissbildung sowohl bei Raumtemperatur als auch bis $T = 600$ °C. Trotz der niedrigeren Rissbeständigkeit von TiAlCrSiON führt das zusätzliche Interface in der Bilayer TiAlCrSiN/TiAlCrSiON-Architektur zu einer vergleichbaren temperaturabhängigen Verformungsmechanik des Werkstoffverbundes analog zum Monolayer TiAlCrSiN. Die Zusammenhänge zwischen dem temperaturabhängigen Verformungsverhalten, den Deformationsmechanismen und dem Risswachstum werden unter anderem mittels Messdaten aus Eindringprüfungen erklärt. Weiterhin wird ein datengetriebener Ansatz zur Vorhersage des temperaturabhängigen Verformungsverhaltens und der Rissbildung an der Oberfläche mittels Algorithmen des maschinellen Lernens entwickelt.

Table of Contents

List of Figures

List of Tables

List of Abbreviations

ANN	Artificial neural network
BF	Bright field
CLSM	Confocal laser scanning microscopy
dcMS	direct current magnetron sputtering
DF	Dark field
DIC	Digital image correlation
DIN	German Institute for Norm
	de. Deutsches Institut für Normung e.V.
EDX	Energy dispersive X-ray spectroscopy
EPMA	Electron probe microanalysis
fcc	face-centered cubic
FIB	Focused ion beam
GFE	Central Facility for Electron Microscopy
	de. Gemeinschaftslabor für Elektronenmikroskopie
GfT	Society for Tribology
	de. Gesellschaft für Tribologie
H1	Hypothesis 1
H2	Hypothesis 2
HP	Hyperplane
HPPMS	High power pulse magnetron sputtering
IOT	Surface Engineering Institute
	de. Institut für Oberflächentechnik
ISO	International Organization for Standardization
JCPDS	Joint Committee on Powder Diffraction Standards
ML	Machine learning
MLP	Multilayer perceptron

nc	nanocrystal
PR	Polynomial regression
PVD	Physical vapor deposition
RF	Random forest
RQ	Research question
SAED	Selected area electron diffraction
SEM	Scanning electron microscopy
STEM	Scanning transmission electron microscopy
SVM	Support vector machine
TEM	Transmission electron microscopy
XRD	X-ray diffraction

List of Symbols

ACC	Model accuracy
A_{proj}	Projected area
CTE	Coefficient of thermal expansion
d	Thickness
D	Diameter
E	Young's modulus
E_{IT}	Indentation modulus
F	Force
f	Frequency
F_{max}	Maximum force
f_{pulse}	Pulse frequency
h	Indentation depth
H	Hardness
h_e	Recovered indentation depth
HF	Adhesion strength class
H_{IT}	Indentation hardness
h_{max}	Maximum indentation depth
h_p	Permanent indentation depth
$h_{p,s}$	Permanent scratch depth
I	Current
k	Thermal conductivity
K_{IC}	Stress intensity factor
K_{IF}	Indentation fracture toughness
L_c	Critical normal force
MAE	Mean absolute error
$MAPE$	Mean absolute percentage error

$MaxAE$	Maximum absolute error
N	Number of cycles
n_{Table}	Table rotation speed
p	Pressure
P_{dcMS}	Power of dcMS cathode
P_H	Heating power
p_H	Hertzian contact pressure
P_{HPPMS}	Average power of HPPMS cathode
PPV	Model precision
$Q(Ar)$	Argon flow
$Q(N_2)$	Nitrogen flow
$Q(O_2)$	Oxygen flow
r	Radius
R^2	R-squared
s	Coating thickness
Sa	Average area roughness
SD	Standard deviation
t	Time
T	Temperature
t_{off}	Pulse off-time
t_{on}	Pulse duration
TRS	Transverse rupture strength
U	Voltage
U_B	Substrate bias
v	Poisson's ratio
VB	Flank wear land width
v_s	Sliding velocity

W_{elast}	Elastic reverse deformation work
W_{plast}	Plastic deformation work
W_t	Total mechanical work
x(Element)	Contribution of an element to the metallic content of the coating
Y	Yield stress
2θ	Diffraction angle of XRD
α	Cone angle
Δ	Difference
λ	Wavelength
ρ	Density
ε	Strain
ε_1, ε_2	Principal strain
η_{elast}	Elastic work percentage
η_{he}	Recovered indentation depth percentage
η_{hp}	Permanent indentation depth percentage
η_{plast}	Plastic work percentage
θ	Angle
σ_1, σ_2	Principal stress
σ_r	Residual stress
ω	Incidence angle

1 Introduction

The economic viability of component production for industrial applications is dependent on productivity of the manufacturing processes such as forming and cutting operations. Here, the functional performance of the tool plays an important role. For instance, the productivity of cutting operations can be improved by increasing the cutting speed at the expense of higher thermomechanical tool loading. Additionally, the development of new difficult to process high strength workpiece materials is increasing the stress collectives on the tools. Main degradation mechanisms of forming and cutting tools include abrasion, adhesion and oxidation as well as diffusion, plastic deformation and crack growth in certain operations. The contribution of individual degradation mechanisms to tool functionality and service life varies with process dynamics, workpiece and tool material. To increase the tool wear resistance, physical vapor deposition (PVD) nitride hard coatings are widely used in the industry. The mix of covalent, metallic and ionic bonds between constituent elements contributes to the high hardness as well as chemical and thermal stability of these coatings. This increases the coated tool resistance against abrasion, adhesion, oxidation and diffusion. To avoid tool failure due to the plastic deformation, crack growth and fracture, the compound of coating and tool substrate material needs to withstand the mechanical or thermomechanical loads in challenging forming and cutting operations. For this purpose, fundamental investigations on deformation and cracking behavior of the coated tool materials are required.

Instrumented indentation testing is a method to study the deformation behavior of thin PVD coatings or the compound of coating and substrate. During the indentation test, the sample is subjected to the indentation load with in situ-measurement of force and indentation depth. Depending on the indentation force, the measurement data can be analyzed either to characterize the deformation behavior of the coating or the compound. Such investigations are carried out at room as well as at higher temperatures with monotonic, cyclic or sliding indentation loads. Moreover, in situ- or ex situ-analysis of the indentation imprints with high resolution electron microscopy provides detailed information on mechanisms of deformation and crack growth in nitride hard coatings. Hence, the mechanical or thermomechanical loadings can be simulated with instrumented indentation tests for in-depth analysis of the compound deformation and fracture mechanics. Current fundamental investigations with such tests are largely focused on the coating rather than the compound. The measurement data from the tests at low loads of $F \leq 10$ mN, i.e. nanoindentations, is used to calculate the coating

indentation hardness H_{IT} and indentation modulus E_{IT} of the coatings. These parameters, together with empirically transferred analytical models from the bulk materials, are used to characterize and compare the plastic deformation and crack resistance of the coatings. The deformation mechanism of columnar nitride coatings is explained based on the grain boundary sliding [JLL+16] and column inclination accompanied with the crack initiation along the column boundaries [BBK+16]. However, such studies are carried out at room temperature for shallow deformation zones largely concentrated in the coating. The influence of coating residual stresses and multilayering for improving the crack resistance of the nitride hard coatings is well understood. In this regard, further research requirement is to understand the effect of coating thickness in combination with the residual stress state or coating architecture. Moreover, the focus should be extended to the characterization of combined deformation response of coating and substrate rather than just the coating.

The **main goal** of this dissertation is to advance the fundamental understanding on deformation behavior and fracture mechanics of compounds. This can enable coating designs to increase functional capability and service life of the tools for challenging forming or cutting operations. In this context, a further objective is to maximize the utilization of measurement data from the instrumented indentation tests for characterization of compound deformation behavior. The investigated compounds for challenging tooling applications include CrAlN coated high-speed steel HS6-5-2C and TiAlCrSiN coated cemented carbide (WC-Co). In addition to the deformation behavior characterization with instrumented indentation tests, the coating deformation and crack growth mechanisms under different indentation loading conditions are studied with high resolution electron microscopy. At first, the cumulative effect of coating chemical composition, thickness and residual stress state on CrAlN/HS6-5-2C deformation under monotonic indentation, coating fracture under sliding indentation and fatigue behavior under cyclic impact loads are investigated. Afterwards, the influences of coating thickness and architecture on the temperature dependent deformation behavior and fracture mechanics of TiAlCrSiN/WC-Co compounds under the indentation loadings are studied. For this purpose, instrumented indentation tests at higher temperatures until T = 600 °C and microscratch tests at room temperature are carried out. In the end, a data driven modeling approach is presented to predict the temperature dependent deformation mechanics and surface cracking behavior of compounds. For this purpose, the measurement data from instrumented indentation tests is combined with the coating characteristics using machine learning algorithms.

2 Theory and state of the art

The chapter starts with a brief introduction on degradation mechanisms of forming and cutting tools. The PVD process and coating systems relevant to this dissertation are presented. Afterwards, the motivation for studying the deformation and fracture mechanics of compounds and the potential of instrumented indentation tests in this context are discussed. Subsequently, state of the art on correlations between the deformation behavior, coating properties and fracture mechanics as well as the mechanisms of plastic deformation and crack initiation in nitride hard coatings are presented. The chapter concludes by summarizing the literature review and identifying research requirement for extending the understanding of deformation and fracture mechanics of compounds with nitride hard coatings for tooling applications.

2.1 Degradation mechanisms of forming tools

As per DIN 8580, the forming operations belong to the second main group of manufacturing processes. During forming, the workpiece form is changed through the plastic deformation without any material removal. The desired geometry and size of the workpiece is achieved by application of tensile, compressive, shear or combination of these stress types through forming tools. Depending on the interplay of material properties, deformability as well as the desired grain structure and strength characteristics of the workpiece, the forming processes are carried out at varying temperatures. Cold forming takes place at room temperature without prior heating of the workpiece material. In case of steel workpieces, warm forming is usually carried out between 600 °C < T < 950 °C, while the hot forming requires workpiece temperatures between 1,100 °C < T < 1,300 °C [Her13]. Forming tools are subjected to multiple degradation mechanisms, stemming from high tribological contact pressures and repetitive mechanical or thermomechanical loading in operation. Understanding these degradation mechanisms is crucial for selection of tool substrate material and protective coatings to increase the tool functionality and prolong the tool life. Depending on the process temperatures, the main degradation mechanisms of forming tools include abrasion, adhesion, oxidation, mechanical or thermomechanical fatigue and plastic deformation. The fundamentals of the forming tool degradation mechanisms are summarized from [LCG+92, Ges02, PL15].

Abrasive wear refers to material removal by hard surface asperities or abrasive particles in contact areas during relative motion between two surfaces. For forming tools, the abrasive wear is a dominant tool degradation mechanism when processing multiphase materials with hard

particles. The degradation of forming tools due to **adhesion** starts with plastic deformation of surface asperities under contact pressure leading to local micro welds between tool surface and workpiece. This results in gradual transfer and adhesion of the workpiece material on the tool surface, also known as galling in extreme cases [Sch94]. The removal of these adhered particles during tool operation is accompanied by material loss from the tool surface. **Oxidation** is a result of chemical reaction between the workpiece or tool and the oxygen in the atmosphere. Depending on the tool material, workpiece material and process temperature, the oxide phases can positively or negatively influence the tool wear. Friction reducing oxide phases can have a positive effect on tool performance [BME+14]. On the other hand, the hard oxide scales increase the tool abrasive wear [GKH+14]. The material **fatigue** refers to continuous localized material damage in form of cracks under cyclic loading. In extreme cases, material fatigue results in tool fracture below the ultimate tensile strength of the material. Due to cyclic operations, the forming tools may exhibit **surface fatigue** visible as surface crack networks and material chipping. For forming operations at higher temperatures, the cyclic heating and cooling of the tool surfaces combined with mechanical loading can lead to extensive crack networks of **thermomechanical fatigue**, see Figure 2.1(a).

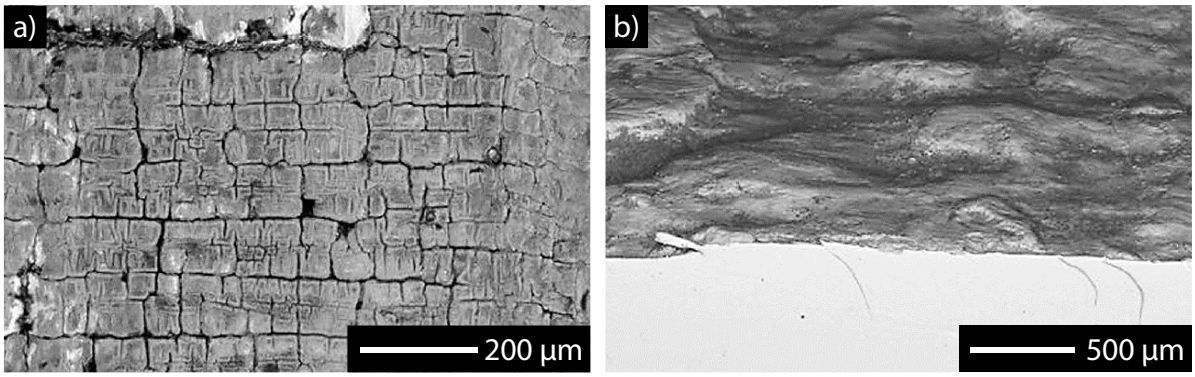

Figure 2.1: Examples of (a) thermomechanical surface fatigue crack networks after N = 8,700 cycles and (b) plastic deformation combined with abrasive wear and cross-sectional cracks after N = 6,900 cycles in hot forming tools, [GKH+14]

The localized or overall **plastic deformation** of the tool is caused by the mechanical stresses exceeding the yield strength of tool material at given process temperature. This degradation mechanism is more common for forming operations involving high mechanical or thermo-mechanical tool loads, such as forming of advanced high-strength steels for automotive

applications [MKŞ+20]. The distortion of the tool geometry due to plastic deformation may manifest as gradual change in contour or a swollen region accompanied with cracks on the tool surface, see Figure 2.1(b). This means loss of dimensional accuracy and incorrect shape for the formed part. Therefore, studying the deformation mechanics of tool materials at room as well as at higher temperatures is crucial to understand the forming tool degradation from plastic deformation and thermomechanical fatigue mechanisms.

2.2 Degradation mechanisms of cutting tools

As per DIN 8580, the cutting operations with geometrically defined cutting edges are categorized under the third main group of manufacturing processes. During cutting, material is removed from the workpiece in form of chips using the cutting edge of tool. The goal is to adapt the shape and surface quality of the workpiece as per the requirements of technical application. Two widely used cutting processes are milling and turning. Milling involves machining of a stationary or moving workpiece with rotating tool, whereas in turning stationary tools machine a rotating workpiece. As cutting processes involve tribological contact between the tool and workpiece, the mechanisms of abrasion, adhesion, oxidation and diffusion can contribute to the degradation of cutting tools. **Diffusion** is a temperature and time-dependent process involving simultaneous solubility of the materials in each other. Due to the high pressures and temperatures in the contact zones, the cutting processes offer favorable conditions for diffusion processes between the workpiece and the uncoated tool substrate material [Klo17]. Depending on the workpiece and tool material as well as cutting parameters, the tool degradation takes different forms. Figure 2.2 shows the most common forms of damage around the cutting edge of cutting tools.

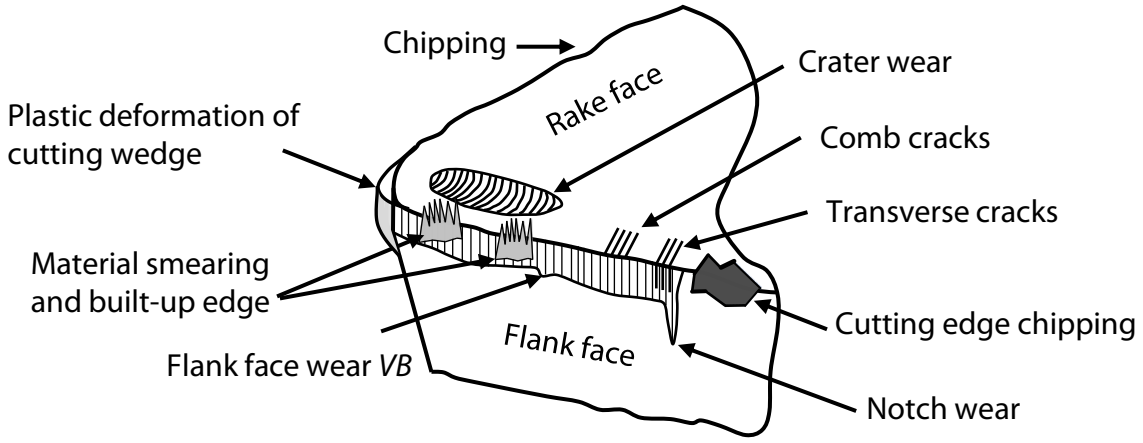

Figure 2.2: Schematic of common damage forms around cutting edge of cutting tools, [Klo17]

The presented fundamental knowledge on the damage forms of cutting tools is derived from [TTW00, KK08, Klo17]. **Crater wear** is trough-shaped material removal on the tool rake face within the tool/chip interaction zone. For coated cemented carbide tools, crater wear starts after coating removal from the rake face by abrasion. The tungsten carbide grains in the exposed tool substrate decompose at higher temperatures. This results in carbon diffusion into the steel chip and iron diffusion into the exposed substrate. The **flank face wear** is mainly a consequence of abrasive wear driven by the frictional contact between the tool and workpiece. This damage form is visible as wear marks with vertical groves below the cutting edges on main and secondary flank faces of the tool. **Material smearing and built-up edges** are hardened layers of the workpiece material, which accumulate on the cutting edge because of adhesion. The **notch wear**, at the end of the tool/workpiece contact zone along the cutting edge, is caused by abrupt transition of thermomechanical loads as well as the abrasive character of the sharp-edged chip. The cutting operations involving cyclic thermomechanical tool loading, such as milling, may result in **fatigue cracks** on the tool cutting edge. Moreover, **comb cracks** mainly initiate on the tool rake face due to thermal cycling. The thermomechanical overloading of the cutting tool, particularly for difficult to machine workpiece materials like titanium alloys and high-speed steels, can lead to the **plastic deformation, chipping and fracture of the cutting edge,** see Figure 2.2. The influencing factors for the tool damage driven by the thermomechanical loadings are workpiece material, cutting conditions, cutting parameters, tool geometry and the high temperature characteristics of tool material such as hot hardness, deformation behavior, compressive strength and creep behavior [US17]. In practice, mostly the cutting process parameters and conditions are adjusted to avoid the plastic deformation and fracture of the cutting edge [Kul92]. However, the fundamental investigations on temperature dependent deformation and cracking behavior of tool materials can contribute to the enhancement of functional capability and higher service life of tools for challenging cutting processes.

2.3 Physical vapor deposition coatings for tooling applications

Physical vapor deposition (PVD) has been used in the industry since ~1980 to deposit wear-resistant protective coatings on forming and cutting tools. Over the years, several PVD nitride hard coatings such as CrN, CrAlN, TiN, TiAlN and TiAlSiN shown promising results to improve the service life of cutting tools [Bob17]. In the following section, the fundamentals of PVD process along with the coating architectures and coating systems relevant for this dissertation are presented.

2.3.1 Process description

PVD is a vacuum-based technology to deposit thin coatings from a gaseous phase or plasma using physical processes. The solid coating material is vaporized using thermal energy from electric arc or electron beam or through bombardment of high energetic ions. The PVD coating process can be divided into three characteristic phases, see Figure 2.3. Depending on the process variant, the process dynamics within these phases can vary. Considering the focus of current work on PVD coatings deposited with magnetron sputtering, the following description is limited to the same. The basic knowledge of PVD goes back to the 19th century. However, the process description in this dissertation is derived from [KD95, Mat10, Bob13].

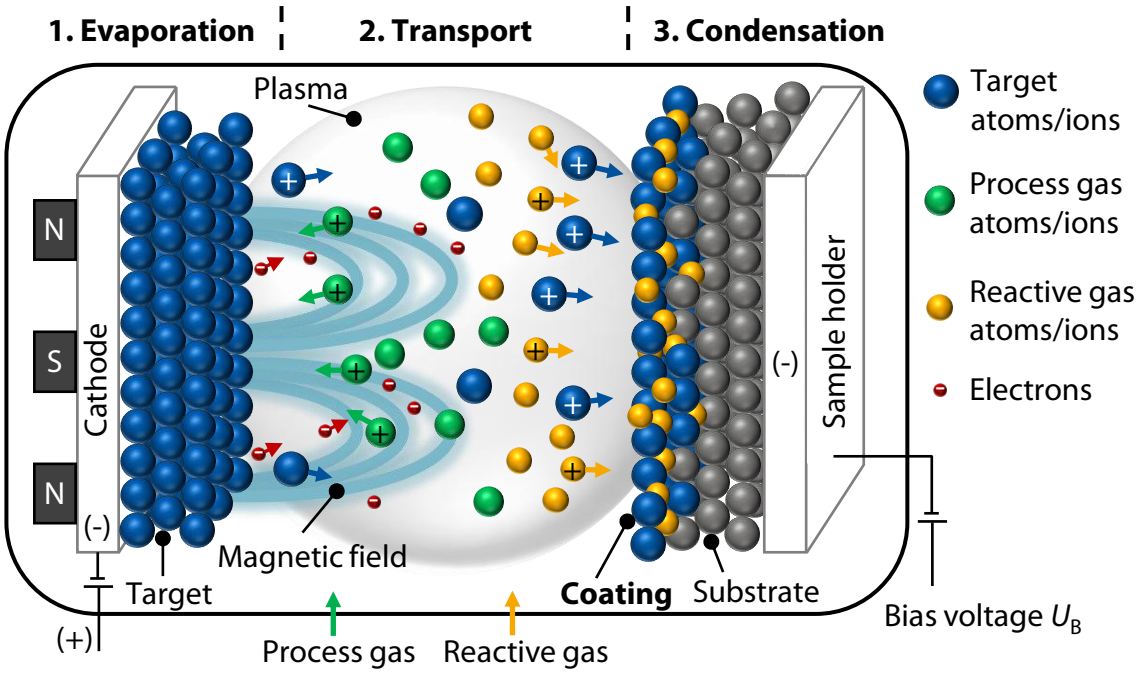

Figure 2.3: Schematic of PVD coating process with magnetron sputtering as per [Bob13]

During the evaporation phase, the atoms, molecules and ions required for layer formation are converted from the starting solid state into the gaseous phase or plasma. For this purpose, all or some of the coating elements are installed on cathodes as solid targets. For sputtering the targets, inert process gas, such as argon, is introduced into the evacuated coating chamber. A glow discharge plasma is generated by applying negative voltage to the targets. The released electrons collide with gas particles to ionize the inert gas. The positively charged process gas ions are accelerated towards the cathodes and atomize the targets by knocking out atoms and ions through momentum transfer. The electrons in front of the cathodes can be directed on to

circular paths by application of magnetic field, hence the name magnetron sputtering. This leads to higher impact rates and increased ionization of plasma in front of the targets. During the transport phase, the atomized particles travel in the direction of substrate, i.e. the workpiece to be coated. The particles can collide with each other or with the chamber walls and partially lose the energy required for layer formation and adhesion. However, applying a negative voltage to the substrate, i.e. bias voltage U_B, accelerates the positively charged layer forming ions to increase their kinetic energy on impact with the substrate surface. Moreover, reactive gases such as N_2 and O_2 can be introduced into the coating chamber to deposit nitride, oxide or oxynitride coating systems. The coating growth takes place during the condensation phase. Depending on the angle of incidence and energy of the layer forming particles upon reaching the substrate surface, they are either reflected or loosely bound on the surface as so-called adatoms. The adatoms can accumulate and form clusters with other impinging layer forming particles. Upon reaching a critical nucleus size, the clusters grow together to form a continuous coating structure.

Magnetron sputtering can be carried out with different power modes of the cathode. The two variants relevant to this dissertation are **direct current magnetron sputtering (dcMS)** and **high power pulse magnetron sputtering (HPPMS)**. The dcMS mode is characterized by a constant cathode power input. The maximum possible cathode power is limited by the heating of target material during sputtering [CTD+13]. In HPPMS mode, the cathodes are operated with high energy pulses at a low pulse frequency [CTS+04]. The pulse on-time t_{on} is typically in the range of 40 µs ≤ t_{on} ≤ 200 µs and the pulse frequency f_{pulse} in the range of 500 Hz ≤ f_{pulse} ≤ 4,000 Hz. This allows significantly higher peak powers at cathodes and an increase in the plasma density with metal ions as compared to the dcMS [BAC+05]. Moreover, the target materials can cool down between the pulses to avoid overheating. The higher degree of plasma ionization with HPPMS reduces the line-of-sight characteristics, typical limitation of PVD processes. This increases the homogeneity of coating thickness distribution, e.g. on the rake and flank face of the cutting tools [BBI+09]. Moreover, lower surface roughness and denser morphology is reported for HPPMS coatings as compared to dcMS [FSO+14]. However, the HPPMS is known for lower coating deposition rate in comparison to the dcMS. This is based on higher pulse off-time t_{off} [ABS09] and self-sputtering of high energy metal ions on substrate surface [Chr05]. Hybrid processes with both dcMS and HPPMS operated cathodes can combine the individual advantages of both process variants.

2.3.2 Coating architectures and coating systems

The protective role of PVD nitride hard coatings for tooling applications, among other factors, is dependent on the coating architecture as well as the microstructure. In the following section, the coating architectures and coating systems relevant for this dissertation are explained.

Coating architectures

Nitride hard coatings are deposited in various architectures shown schematically in Figure 2.4. The monolayer represents the coatings with a consistent chemical composition across the thickness. The monolayer nitride hard coatings deposited with PVD typically show a columnar morphology. The coating columns can consist of several grains. The increase in column length and width with higher coating thickness is accompanied by the increase in compressive residual stresses. This can lead to abrupt fracture and delamination of the coating under mechanical load. The multilayer architecture consists of individual layers, with varying chemical composition, arranged across the coating thickness. This can alter the residual stress gradient over the coating thickness to achieve relatively higher coating thicknesses as compared to monolayer architecture. For nanolaminate or superlattice, the alternate variation in chemical composition of layers over the coating thickness is in nanometer range. The nanocomposite architecture consists of hard nanoparticles embedded in an amorphous matrix.

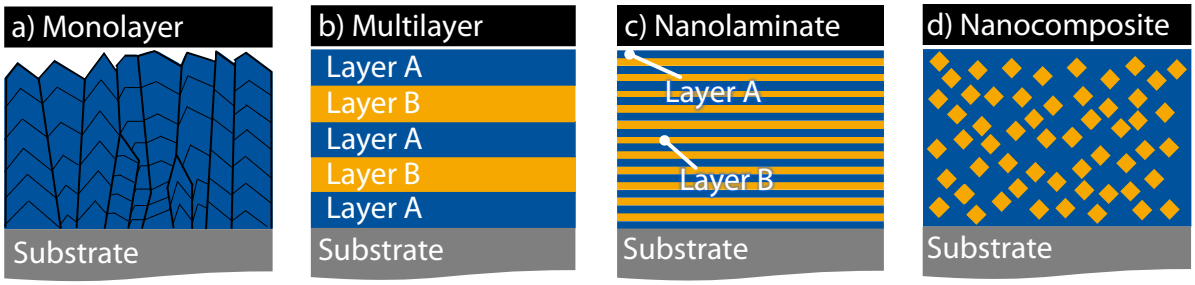

Figure 2.4: Coating architectures of PVD nitride hard coatings, [Bob13]

CrAlN

CrAlN is an extension of the binary CrN coating system. CrN is characterized as an interstitial solid solution with a face-centered cubic (fcc) NaCl structure. The smaller nitrogen atoms occupy interstitial sites in the metallic crystal lattice of Cr atoms [Hol84], see Figure 2.5. With addition of Al to the CrN, a substitutional solid solution is formed. The difference in atomic radius of Cr and Al atoms increases the lattice distortion and hardness of the resulting CrAlN coating [KAB+90]. However, the hardness increase is dependent on Al content and resulting

lattice structure of the coating, see Figure 2.5. For Al contents up to $x(Al) \leq 60$ at. %, a fcc-NaCl structure is formed. Further increase in the Al content leads to formation of hexagonal AlN phases and reduce the hardness of the CrAlN [SKM97]. As compared to CrN, the formation of Cr containing Al_2O_3 passivation layer increases the oxidation resistance of CrAlN until $T = 800$ °C in ambient atmosphere [HJ90]. Hence, the CrAlN coatings with $x(Al) \leq 60$ at. %, are widely used in the industry to increase the resistance of forming and cutting tools against abrasion and oxidation driven degradation.

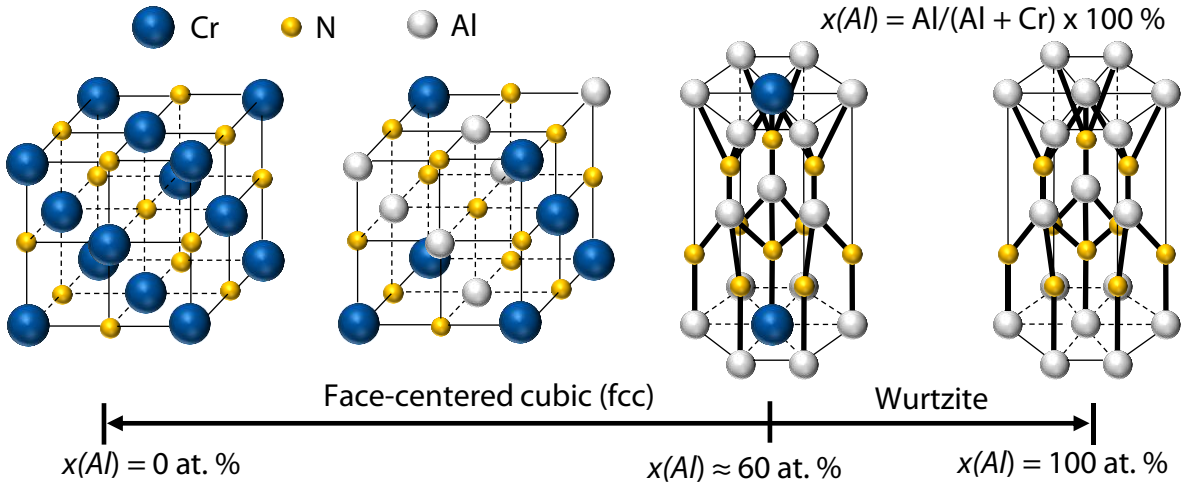

Figure 2.5: Schematic of lattice structure changes from CrN to CrAlN and AlN

TiAlCrSiN

TiAlCrSiN represents an advanced nanocomposite coating system to potentially combine the individual advantages of Al, Cr and Si incorporation to TiN matrix in a single coating. Al and Cr additions increase the lattice distortion and hardness compared to binary TiN. Moreover, Al, Cr and Si are known to build protective oxide layers to increase the oxidation resistance of coating. Si can form amorphous Si_3N_4 matrix and restrict the grain size of (Ti, Al, Cr)N crystals in nm-range, resulting in a nanocomposite structure [VRS95], see Figure 2.6(a). The reduced grain size as well as high cohesive strength between nanocrystals (nc) and the amorphous matrix result in higher hardness and crack resistance as compared to the polycrystalline TiN [VRS95] and TiAlN coatings [MPM+01]. The Si_3N_4 matrix inhibits the diffusion processes at the grain boundaries and increases the thermal stability [MPM+01] of the Si-based nanocomposite coatings. However, for Si contents higher than $x(Si) = (4 - 6)$ at. %, the coating hardness decreases due to the increase in amorphous content of the coating [JSM+04]. For milling operations involving difficult to machine high-speed steel HS6-5-3C workpieces, the TiAlCrSiN

nanocomposite coatings have shown promising potential to improve the abrasive wear resistance of the coated tool [BBK+20, BBM+21]. Moreover, the addition of oxygen in TiAlCrSiN reduces adhesion tendency of steel workpiece material to the coated tool [BKT24b]. However, the oxygen incorporation increases the amorphous content to reduce the hardness and the abrasive wear resistance of TiAlCrSiON coated tools [BBK+21]. As reported in [BKT+25a], the advantages of TiAlCrSiON can be combined with that of TiAlCrSiN in a bilayer coating architecture with nitride interlayer and an oxynitride top layer, see Figure 2.6(b).

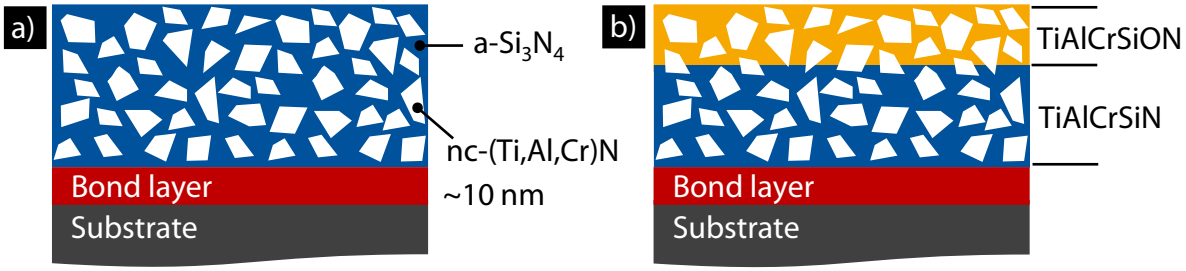

Figure 2.6: (a) Schematic of monolayer TiAlCrSiN and (b) bilayer TiAlCrSiN/TiAlCrSiON

2.4 Interim summary and research motivation

The forming and cutting tools are subjected to multiple degradation mechanisms such as abrasion, adhesion, oxidation as well as plastic deformation and crack growth in application. Depending on the interplay of workpiece material, process conditions, process parameters as well as the tool geometry and material, the contribution of individual degradation mechanisms and corresponding damage forms on the service life of tool varies. PVD nitride hard coatings are one of the most widely used solutions in the industry for service life improvement of the tools. The favorable dynamics of PVD processes allows to combine elements like Cr, Ti, Al and Si with N to deposit thin coatings with high hardness, oxidation resistance and thermal stability. This increases the coated tool resistance against abrasion, adhesion and oxidation. However, for forming and cutting operations involving high strength materials as workpieces, the plastic deformation and crack growth in tools induced by the challenging mechanical, thermal or thermomechanical loading conditions gains significance. Moreover, in order to increase the productivity of such forming and cutting operations for component production, tool designs with higher functional capability are required. The compound of coating and tool substrate material should withstand the challenging stress collectives in application. Hence, fundamental investigations on deformation and cracking behavior of PVD coated tool materials are essential to enable knowledge-based coating designs for challenging forming and cutting operations.

2.5 Deformation and fracture mechanics of PVD coated substrates

In this section, a literature review on deformation behavior and crack growth in compounds with nitride hard coatings along with relevant investigation approaches are presented. The focus is placed on coating-substrate combinations for tooling applications.

2.5.1 Edge zone of compounds for tooling applications

High-speed steels and cemented carbides are widely used to make dies and molds for cold and warm forming, while hot working tool steels are preferred for hot forming. For cutting tools, cemented carbides and high-speed steels are among the widely used tool materials. To ensure good adhesion between the coating and tool substrate material, the edge zone design varies with substrate material. Figure 2.7 illustrates the edge zone of compounds with steel and cemented carbide substrates. The steel substrates are generally case-hardened by plasma nitriding before coating. This improves substrate support for the PVD hard coating to avoid abrupt coating fracture by the eggshell effect. Because of the higher hardness and stiffness as compared to steels, the cemented carbide substrates do not require such pre-treatment. Hence, edge zone design should be considered while studying the deformation behavior of compounds.

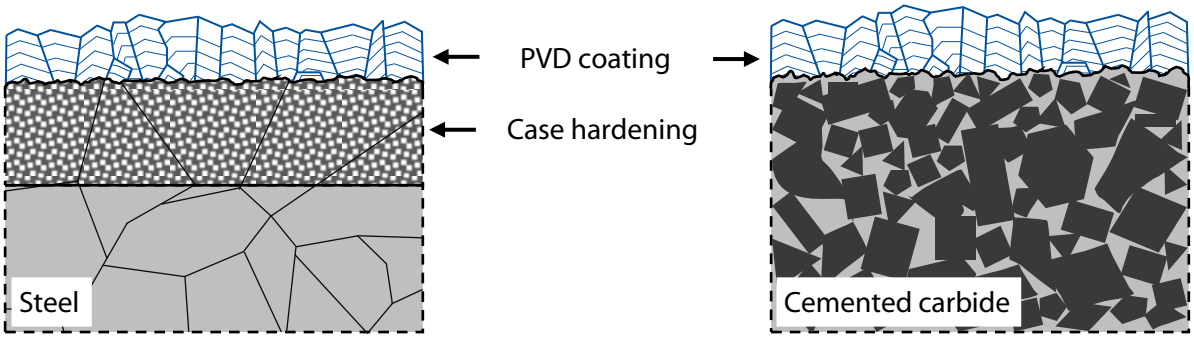

Figure 2.7: Schematic of compound edge zone with steel and cemented carbide substrates

2.5.2 Investigation scales

Fundamental investigations on deformation and damage mechanisms of materials are carried out at micro-, meso- and macroscale. Table 2.1 explains the difference between these scales and focus of the corresponding investigations. The possibilities for in-depth damage analysis decrease from micro- to macroscale. Considering the usual thickness range 1 µm ≤ s ≤ 10 µm of PVD coatings for tooling applications, the mesoscale investigations provide structure-dependent understanding of the deformation behavior and crack formation in the edge zone of

compounds. This is particularly helpful to identify the effect of coating or substrate dependent variables and their interactions on the compound deformation and fracture mechanics.

Table 2.1: Investigation scope of the micro-, meso- and macroscale

Scale	Description
Micro	Focuses on individual components of the material from atoms and molecules up to the lattice structure of the grains
Meso	Emphases on microstructural aspects e.g. arrangement, morphology and orientation of grains
Macro	Consideration of the overall material response through homogenization of the micro- and mesoscopic aspects over representative volume of the material

2.5.3 Instrumented indentation tests

On the experimental side, instrumented indentation test is a promising method for multiscale investigations on deformation and cracking behavior of compounds. The mechanical or thermomechanical loadings can be simulated in reduced form for in-depth analysis of the compound deformation and fracture mechanics during coating development phase. During the instrumented indentation test, the sample is subjected to force- or displacement-controlled load using an indenter tip with the geometry of choice such as Berkovich, Vickers, Conical, etc., see Figure 2.8(a). The indentation force F and indentation depth h are measured in situ during the indentation.

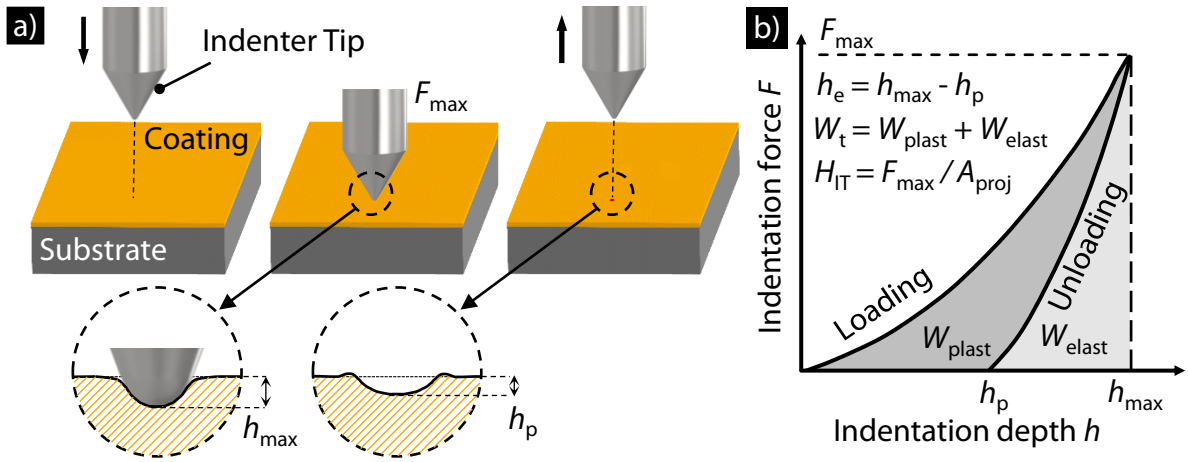

Figure 2.8: (a) Schematic of instrumented indentation test and (b) the measurement data in form of force-indentation depth curve

The measurement data as force-indentation depth curves can be analyzed to characterize the elastic-plastic deformation behavior of the sample, see Figure 2.8(b). The force-indentation depth curve consists of loading and unloading segments. During the loading segment, the applied force is continuously increased until the predefined maximum indentation force or indentation depth is reached. The indentation depth at the end of loading segment, corresponding to the maximum indentation force F_{max}, is defined as maximum indentation depth h_{max}. During the unloading segment, the indentation force is reduced to zero and the remaining indentation depth is called permanent indentation depth h_p. The difference between h_{max} and h_p, resulting from elastic recovery of the material, can be characterized as recovered indentation depth h_e. The total mechanical work W_t during the indentation is calculated as area under the loading segment of the curve. W_t represents the sum of elastic reverse deformation work W_{elast} and the plastic deformation work W_{plast}. W_{elast} is calculated as the area under the unloading segment of the curve, whereas W_{plast} represents the area between the loading and unloading segments, i.e. the difference between W_t and W_{elast}. For intuitive understanding of elastic-plastic deformation response of the sample the percentual work contributions η_{elast} and η_{plast} from W_{elast} and W_{plast} to W_t, respectively can be calculated as per Equation 2.1.

$$\eta_{plast} = (W_{plast} / W_t) \times 100\ \% \quad , \quad \eta_{elast} = (W_{elast} / W_t) \times 100\ \% \qquad \text{Equation 2.1}$$

Moreover, the force-indentation depth curves are used to calculate the indentation hardness H_{IT} and the indentation modulus E_{IT} of the material. For this purpose, one of the most widely used methods is described in [OP92]. The H_{IT} is calculated by dividing the maximum indentation force F_{max} to the corresponding projected area A_{proj} of the indentation, see Figure 2.8(b). The E_{IT} is dependent on the slope of unloading segment. As per DIN EN ISO 14577, depending on the indentation force F and depth h, the instrumented indentation tests can be carried out in nano- ($h \leq 0.2$ µm), micro- ($F < 2$ N; $h > 0.2$ µm) or macro-range ($2\ \text{N} \leq F \leq 30$ kN). This allows for multiscale investigations on deformation mechanics of compounds with nitride hard coatings. Moreover, with the choice of indenter tip geometries, a controlled deformation zone can be induced in the compound as per the focus of the investigation. For instance, sharp Berkovich tips are used for shallow deformation zones largely concentrated in the coating. The conical tips, on the other hand, allow for deeper spherical shaped deformation zones, more suited to study the combined deformation response of coating and substrate [SFA+09].

2.5.4 Review of analytical and experimental approaches to combine indentation test data with fracture mechanics of compounds

It is often mentioned in the literature that the resistance of nitride coatings to wear and plastic deformation can be improved by increasing the H/E or H^3/E^2 ratios, respectively. The H/E ratio originates from the analytical model by [GW66], based on Hertzian contact theory, for calculating the limit of elastic contact between two solid flat bodies. In [Hal86], the model was extended to the thin ceramic like coatings for elastic contact conditions. The H^3/E^2 ratio is based on the analytical models from [Tab51, Joh85] to calculate the yield pressure P_y or resistance to plastic deformation in the elastic-plastic contacts between metals. These models assume that the material hardness H is three times its yield strength Y. In a substantial number of subsequent studies, for instance in [TPO+95, LM00, PRB+22], these ratios were empirically correlated with the wear and plastic deformation resistance of PVD coated compounds, irrespective of the tribological contact conditions. Here, the indentation hardness H_{IT} and indentation modulus E_{IT} of the coatings, measured with nanoindentation, were used for H/E ratio calculations of the compound. However, as mentioned in [SSB08, LPS15, BBK+17b], these correlations do not always hold, especially when investigating the application behavior of coated tools. In practice, the coated tools are subjected to degradation mechanisms like adhesion and oxidation, which are not directly dependent on elastic-plastic properties of the coating. Moreover, most of the studies advocating H/E ratios ignore the effect of coating thickness and substrate material on overall elastic-plastic compound deformation. It is important to consider that the hardness H is not a fundamental material property. Hardness value of a material varies depending on the measurement method as well as the test parameters. Hence, H_{IT} and E_{IT} values of coating and corresponding ratios cannot characterize the combined deformation response of the coating and substrate, as argued in [PH93] as well.

For bulk ceramic materials, an approach to determine fracture toughness is based on the measurement of crack lengths of the indent imprints carried out by pyramid shaped tips. The analytical model is derived from elastic-plastic fracture mechanics of ceramics by [LEM80] and later extended by [ACL+81, Lau87]. Equation 2.2 correlates indentation fracture toughness K_{IF} to the applied load, elastic-plastic material parameters and crack lengths. The exact form of the equation varies with the indenter tip geometry and the corresponding material dependent morphology of the observed cracks, namely median, radial, half-penny, etc.

$K_{IF} = (P_{max} / c^{3/2}) \,.\, \Pi\, (E/H, \alpha, a/l)$ Equation 2.2

P_{max}: Applied load, E: Young's modulus, H: Hardness, α: Dimensionless tip geometry factor, a: Distance between center and corner of the indent imprint, l: Crack length, c: $a + l$

Hence, the short comings for this model based fracture toughness measurement include adjustment of general equation as per the ceramic material, the crack morphology and tip geometry as well as the transferability of tip geometry factors to different materials [GSM+20]. Nonetheless, the model is empirically transferred to determine or compare the fracture toughness of PVD coatings, as in [KWC+02, SSK+22]. However, in doing so, the substrate influence on deformation response of the compound is ignored. Moreover, the substrate material, the coating residual stress and the applied load can substantially alter the crack morphologies [SJH+15a]. Furthermore, the use of H_{IT} and E_{IT} values for characterization of compound deformation response is an oversimplification.

Another method to determine the fracture toughness of thin nitride hard coatings is based on micro-compression tests with in situ-nanoindentation. For this purpose, microscale cantilever beam [RDS+12] or pillar shaped specimens [SJH+15b] from the coating are prepared using focused ion beam (FIB). These samples are subjected to nanoindentation inside an electron microscope. The indentation load at the sample fracture is determined through in situ-analysis of sample deformation during nanoindentation. Subsequently, the sample geometry specific analytical equations are used to calculate the fracture toughness of the coating [SJH+15a]. However, the FIB preparation of specimens with the size of few micrometers significantly alters their residual stress state compared to the actual compound. Accordingly, the deformation behavior of the coating specimen deviates from the as-deposited coating on the substrate. Hence, such micro-compression tests are not suitable for application relevant investigation of the deformation and cracking behavior of PVD coatings or compounds.

In instrumented indentation testing, pop-in phenomenon is defined as sudden displacement bursts during sample loading. For metals, these pop-ins are associated with onset of plasticity through defect nucleation or formation of dislocation networks and their movement [GvS01]. Similarly, for bulk ceramics, pop-in events during the indentation are associated to deformation or crack formation [POM92]. Analogous to that, the onset of cracking in nitride hard coatings is compared with the help of pop-in events during the instrumented indentation tests, as shown

in [MCH+06, WZY16]. However, the number and intensity of the pop-in events are dependent on the indenter geometry and applied load. Moreover, in case of compounds, the pop-in events at high indentation loads can occur due to the substrate-related deformation effects [PMD+24]. Hence, the distinction of pop-in events based on the onset of plasticity and cracking as well as the coating and substrate dependent effects require extensive experimental and simulative investigations.

The experimental test data can be used to develop numerical simulations of the indentation tests. Depending on the material model used for the coating and substrate, the unknown variables, such as coating yield stress Y, are set as free parameters. Starting from random values, the free parameters can be iteratively adjusted to achieve a good match between simulative and experimental force-indentation depth curves [BKC+23]. Accordingly, the force-indentation depth curves can be converted into stress-strain curves [BBB+15]. Although promising, the simulation models struggle to determine unique set of coating material parameters which accurately simulate the experimental deformation of the compound over wide range of loading conditions. Realistic modeling of coating, coating-substrate interface as well as the deformation and crack initiation mechanisms remain a challenge. Considering the focus of this dissertation on experimental work, the simulative approaches are not reviewed.

In short, the analytical and experimental approaches utilizing the indentation test data for characterization of compound deformation are based on empirical transfer from bulk materials to the coating-substrate combinations. Moreover, the ambiguous coating variables, such as indentation hardness H_{IT} and modulus E_{IT}, are insufficient to characterize the combined deformation response of the coating and substrate. Hereby, the influence of coating thickness and substrate effect on the compound deformation are largely ignored. For this purpose, data driven approaches using machine learning (ML) methods can help to understand and predict intricate correlations between coating characteristics and compound deformation mechanics, which are otherwise overlooked in analytical and numerical models due to simplification assumptions. Machine learning (ML) is a subset of artificial intelligence dealing with algorithms and statistical models to identify patterns as well as correlations in the dataset. ML models allow computers to interpret, learn and adapt from available data as well as make predictions and decisions like humans. Hence, the potential of ML models to combine indentation test data and deformation mechanics of compounds with PVD nitride hard coatings should be studied.

2.5.5 High temperature investigations

With growing interest in instrumented indentation tests for mechanical characterization of materials, the instruments have significantly advanced. As summarized in [Bea21], intensive work has been done in the last two decades to enable stable measurements at temperatures until T = 800 °C. Challenges such as instrument drift, oxidation of the sample and indenter tip as well as accelerated tip wear at elevated temperatures [WAH+15] have been addressed through specially designed modules featuring precise control of heating, cooling and atmospheric conditions during measurements. This is particularly suitable to study deformation behavior of coatings and compounds close to the application relevant tool temperatures during application. For instance, effect of Al content on temperature dependent indentation hardness H_{IT} of TiAlN coating was investigated in [GCB+19]. The nanoindentation measurements until T = 300 °C showed lower temperature dependent drop in H_{IT} with addition of Al up to $x(Al) < 60$ at.%. The effect of vacuum annealing after deposition on high temperature H_{IT} and cutting performance of TiAlN coated cemented carbide tools were investigated in [FEB+08]. The drop in H_{IT} at measurement temperature of T = 500 °C was significantly reduced for the coating annealed at T = 700 °C as compared to the as-deposited variant. This correlated to the higher service life of coated and annealed cutting tools during end milling of X40CrMoV5-1 tool steel workpiece. Recent study from Surface Engineering Institute (IOT) investigated the temperature dependent indentation hardness H_{IT} and indentation modulus E_{IT} of TiAlCrSiN coatings until T = 600 °C for cemented carbide cutting tools [BKT+25a]. In correlation to application behavior, the higher temperature dependent H_{IT} of the monolayer TiAlCrSiN as compared to the bilayer TiAlCrSiN/TiAlCrSiON resulted in increased abrasive wear resistance of the coated cemented carbide inserts during dry turning of C45+N steel. The investigations combining temperature dependent deformation behavior and fracture mechanics of compounds using high temperature indentation testing are limited. Micro-compression tests for nitride hard coatings were carried at elevated temperatures in [LWM+16]. However, their suitability to application relevant investigations remains limited due to the change in the residual stress state of the samples. In [BSG+07], the instrumented indentation testing at T = 500 °C was used to study the fracture resistance of TiAlN coated cemented carbides under cyclic impact loading. The pop-in phenomenon in measurement data was used as fracture probability criteria for the TiAlN coatings with varying Al content. An increase in coating Al content was correlated with higher fracture resistance of the coating. Similar methods were used in [BBI+19] to exhibit the superior high temperature fracture resistance of multilayer TiAlN/TiSiN as compared to monolayer

TiAlSiN deposited on cemented carbide substrates. However, due to the overreliance on H_{IT} and E_{IT} values of the coating, the investigations provide limited understanding of interplay between the compound deformation behavior and coating fracture.

2.6 Plastic deformation and crack initiation mechanisms of nitride hard coatings

The fundamental investigations on plastic deformation mechanisms in nitride hard coatings offer different opinions. In [WRC+14], the deformation behavior is explained based on micro-scale mechanism of dislocation motion and dislocation pile-ups in the nitride hard coatings. The motivation is derived from the well-known plastic deformation mechanism of metals. The dislocations or line defects are present inside the crystal lattice of constituent atoms with metallic bonding. These dislocations can move under stress, facilitating atomic planes to slip or slide past each other, allowing the metals to deform without fracturing. However, the nitride hard coatings have a mix of different chemical bonding types, namely metallic, covalent and in some cases ionic bonds [Hol90]. Depending on the constituent elements, the nitride coatings can have higher content of metallic or covalent bonding. As shown in [And07, BBK+17a], the nitride hard coatings do contain defects. However, describing the coating plastic deformation based on microscale mechanism of dislocation motion is an oversimplification of the complicated lattice structure of crystalline nitride hard coatings.

For Si-based nanocomposite nitride coatings, a theoretical microscale model of deformation mechanism and crack growth is proposed in [Vep97, VNM+00]. Under external load, nano-cracks initiate within the amorphous matrix of coating. These cracks are deflected or restricted upon reaching the nearby nanocrystals. The coating deformation mechanism is based on energy absorption by partial opening of nanocracks during loading and energy release by partial crack closing upon unloading. Moreover, the strong cohesive bonds between the nanocrystals and the matrix inhibit grain boundary sliding and increase the plastic deformation resistance of nanocomposite coatings compared to polycrystalline coatings. Although the model provides sound theoretical basis, the experimental validation is still an open research question.

Another opinion in literature is based on mesoscale description of deformation mechanism in columnar nitride hard coatings. In [BXH+04, MCH+05], combination of instrumented indention testing and ex situ-high resolution electron microscopy was used to study the deformation of TiN coatings on steel substrates. It was assumed that the substrate rather than

the columnar coating undergoes plastic deformation during indentation with a spherical tip. The coating was considered brittle like ceramics. During the compound deformation, the coating follows the substrate through intercolumnar sliding and shear fracture along column boundaries, see Figure 2.9. However, in subsequent study with a sharp Berkovich tip [BJB05], elastic-plastic deformation of the columnar TiN coating was suggested at low indentation loads.

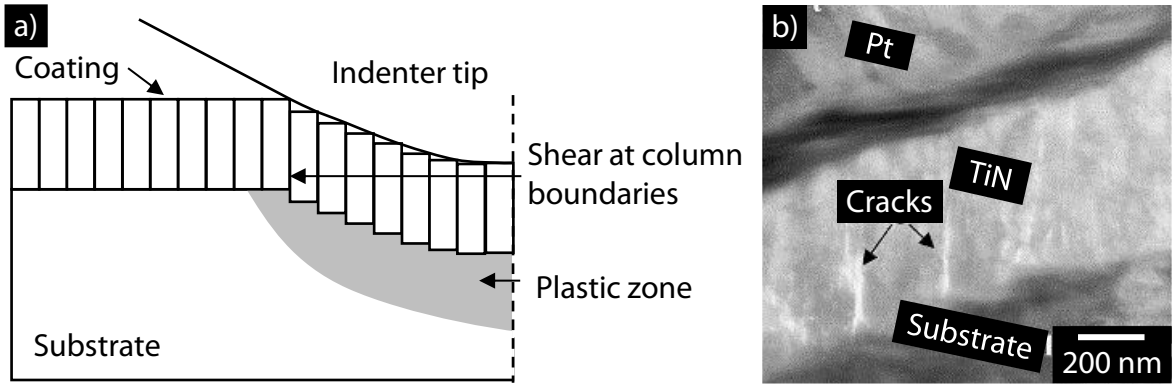

Figure 2.9: (a) Deformation mechanism suggested by [BXH+04]on the basis of (b) observed cross-sectional cracks at column boundaries of TiN from [MCH+05]

In [JLL+16] the elastic-plastic deformation mechanism of TiN coatings was studied with in situ-deformation analysis during nanoindentation using transmission electron microscopy (TEM). For this purpose, TiN coatings were deposited with pulsed laser deposition (PLD) on Si substrates. Special thin samples were prepared for in situ-TEM analysis of the coating cross-section and surface during indentation. The TiN coatings exhibited columnar morphology and cubic crystal lattice structure. The nanoindentations were carried out with a wedge-shaped diamond indenter. To avoid substrate effect, the indentation depth was limited to h_{max} = 50 nm for in situ-cross-sectional analysis and h_{max} = 100 nm for in situ-surface analysis of the coatings. Figure 2.10 shows the exemplary cross-sectional TEM bright field (BF) images from the investigation at different intervals during nanoindentation. The rectangle marks the two columnar grains with diameter D = 40 nm and interaxial angle of θ = 26° before loading, see Figure 2.10(a). The interaxial angle changes to θ = 9° as result of clockwise tilt of the top grain at the maximum load, see Figure 2.10(b). Upon unloading, the top grain tilts counterclockwise and the interaxial angle changes to θ = 22°, see Figure 2.10(c). The difference of $\Delta\theta$ = 4° before and after unloading confirms the plastic deformation of the coating due to grain activity.

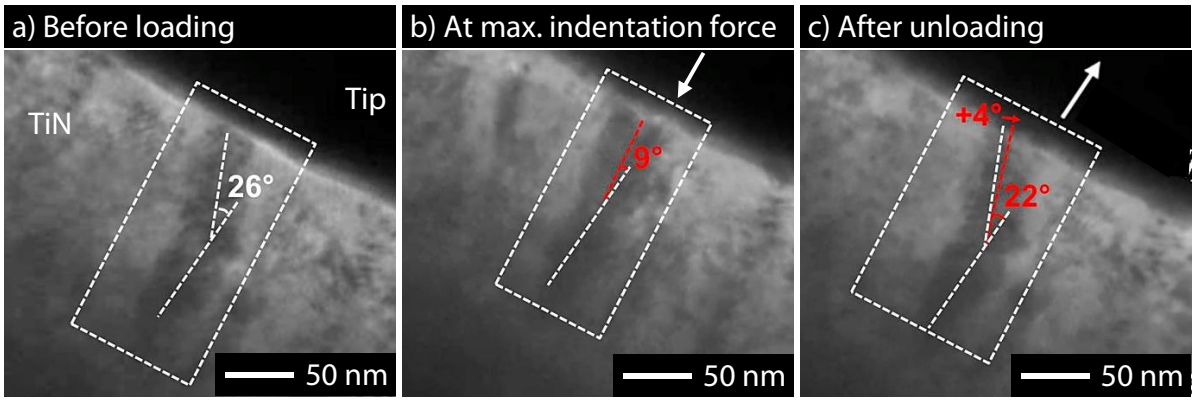

Figure 2.10: TEM BF images of TiN coating grains (a) before loading, (b) at maximum indentation force and (c) after unloading, [JLL+16]

The exemplary TEM dark field (DF) images from the coating surface are shown in Figure 2.11. The contrast patterns represent different grains. The contrast patterns of the three marked grains changed during and after loading. Moreover, two neighboring grains become visible after unloading as a result of rearrangement of grain boundaries by grain activity, see Figure 2.11(c). Hence, these observations confirm the grain rotation and grain boundary sliding as plastic deformation mechanism of crystalline nitride coatings.

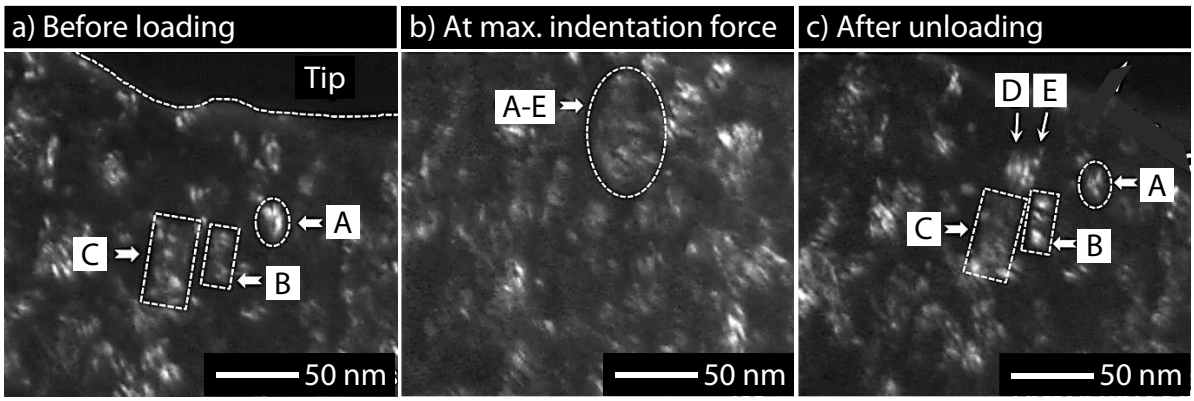

Figure 2.11: TEM DF of TiN coating grains at the surface (a) before loading, (b) at maximum indentation force and (c) after unloading, [JLL+16]

The plastic deformation mechanism and crack propagation in CrAlN coatings deposited on X20Cr13 steel has been investigated at IOT using microscratch tests and TEM [BBK+16]. Regarding the plastic deformation mechanism, no classical dislocation movements were observed in the deformation zone. As compared to relatively vertical grain orientations in undeformed areas, grain inclinations of $\theta = 10°$ and $\theta = 30°$ in deformation zone of the coating

under scratch track were observed, see Figure 2.12(a-c). Moreover, the coating exhibited cross-sectional cracks along the boundaries of coating columns. Based on these observations, the schematic of the plastic deformation and crack initiation mechanisms in the coating is shown in Figure 2.12 (d,e). In absence of dislocation motion, the columnar coating deforms through column inclination and grain boundary sliding. The extensive column inclination outside the compression zone is accompanied with shear stress and leads to crack growth along the column boundaries. A similar approach was used to confirm grain boundary sliding and nanograin rotation as deformation mechanisms in CrN/AlN nanolaminates [BBK+17a]. However, these investigations were carried out with the sharp Berkovich indenter tip to induce shallow deformation zones largely concentrated in the coating. Hence, the effect of coating thickness or substrate deformation on crack growth in coating was not explicitly investigated.

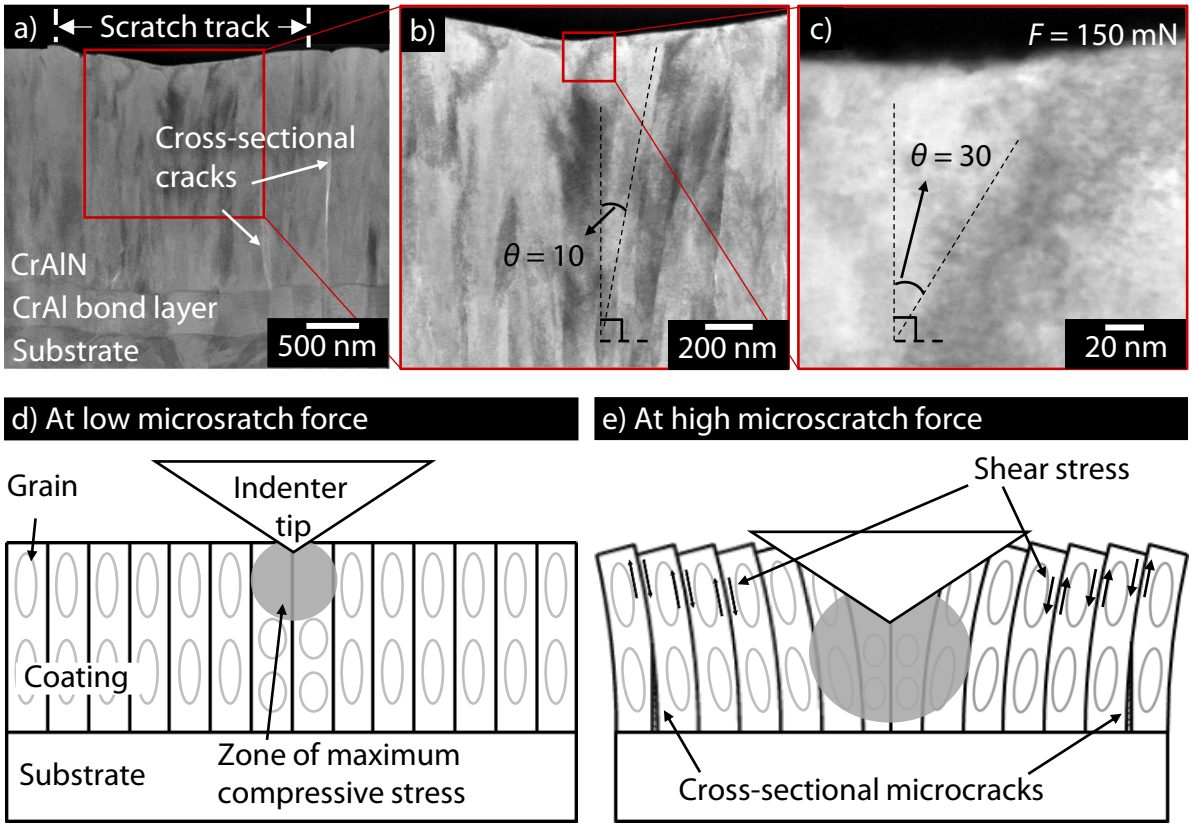

Figure 2.12: (a) TEM BF images of cross-sectional cracks along the boundaries of coating columns, grain inclination of (b) $\theta = 10°$ and (c) $\theta = 30°$ in scratch deformation zone along with (d,e) the schematics of deformation mechanism and crack initiation, [BBK+16]

2.7 Influence of residual stresses

Residual stresses play a significant role in ensuring mechanical integrity of the PVD coatings. The origins of residual stresses in PVD coatings are thermal, intrinsic and extrinsic [HT77]. Thermal mismatch between the coating and substrate material gives rise to thermally induced residual stresses during deposition. Lower coefficient of thermal expansion for nitride hard coatings as compared to metallic substrates can induce compressive and tensile stresses in the coating and substrate, respectively. Intrinsic residual stresses originate during the coating growth phase due to the underlying physical as well as chemical processes such as ion-bombardment, defects and phase transformations. The post-treatment processes after coating deposition or the thermomechanical loading during application extrinsically induce additional stresses in the coating.

Depending on the loading condition, the coating can fracture due to transverse, cross-sectional or a combination of both cracks. The compressive residual stresses σ_r in the coating increase the resistance against crack growth. However, high extrinsically induced stresses due to the applied load can lead to the coating spalling or debonding at the interface between the coating and substrate. Hence, the crack resistance and fracture mode of the compound depends on the loading condition as well as on the magnitude of compressive residual stress σ_r in the coatings. In [OW95], the fracture behavior of TiN coatings with $|\sigma_r| \approx 0.5$ GPa and $|\sigma_r| \approx 2.5$ GPa on steel substrates was investigated using four-point bending and scratch tests. The coating with lower compressive residual stress σ_r showed an earlier initiation of cracks under external tensile bending stresses. However, under sliding indentation load during scratch test, the higher compressive residual stress promoted adhesive failure of the coating. The damage in TiN variant with lower compressive residual stresses σ_r was limited to the cohesive failure for comparable scratch force. For cyclic bending loads, the nitride hard coatings have been associated with improved resistance of coated steel compounds against fatigue damage [BV14, BGG+21]. This is attributed to the compressive residual stresses of coating, which delay the growth of fatigue cracks in the steel substrate. However, the positive effect of coating on fatigue behavior of the coated steels is also dependent on the bending stress amplitudes [BKT24a] as well as the deformation behavior of coating and substrate. In [SBK+17], the deformation and cracking behavior of TiAlN coated cemented carbides under cyclic impact loading was investigated. The compounds with higher compressive residual stresses of the coating exhibited lower plastic deformation, measured as indentation depth of the impact imprint. Moreover, the

coating with $|\sigma_r|$ ~ 2.0 GPa – 3.0 GPa exhibited higher resistance against fracture under cyclic impact and improved tool life during dry turning of C45 steel. For TiAlCrSiN coated cemented carbide milling tools, similar range of coating σ_r is suggested in [BBM+21] for higher crack resistance and tool service life during milling of high-speed steels. Depending on the stress collective, very high $|\sigma_r| > 3$ GPa can accelerate the coating fracture and decrease the cutting tool life [KGS+10]. In addition to the coating, the residual stress state of the substrate before and after coating can significantly influence the damage behavior of the compounds or the coated tools [BD13]. The substrate heating during coating deposition as well as the compressive residual stress gradient of PVD nitride hard coatings can shift the residual stress levels in edge zone of cemented carbide [BD13] or steel substrates [STG+14] in direction of tensile stresses.

2.8 Influence of multilayering

The tailored adjustment of coating architecture with multiple layers of differing chemical composition can improve the crack resistance and fracture toughness of the nitride hard coatings. The interfaces between individual layers act as energy dissipation sites as well as barrier to crack propagation through crack deflection and splitting [HS95]. Moreover, for columnar coatings, the resistance against crack initiation through shear sliding of columns can be increased through multilayering. The interfaces can suppress the intercolumn sliding and increase the intergranular shear area to increase the energy consumption during deformation [XHM+08]. Furthermore, the coating deformation and crack initiation mechanisms inside the multilayer coating can be varied through combination of metallic and nitride layers. A metallic bond layer is commonly used to improve the adhesion between the nitride coating and the substrate material. In [WSG+14], the cracking behavior of multilayer Cr/CrN coatings was investigated with instrumented indentation testing. Increasing the volume fraction of Cr layers reduced the H_{IT} and E_{IT} of the coating but increased the crack resistance. The cross-sectional cracks in the coating with higher volume fraction of Cr layers were largely limited to CrN layers with interfaces acting as crack growth barriers. The grain boundary sliding and deformation by twining in Cr layers increased the coating ability to accommodate large plastic strains without cracking. The advantageous range of interface volume inside a multilayer coating varies depending on chemical composition and resulting properties of the individual layers. For tooling applications, multilayering is used to combine individual strengths of different coating systems in a single coating to suppress specific tool degradation mechanisms. For instance, better adhesion tendency of TiAlN coating to cemented carbide substrate was combined with

higher toughness and thermal stability of TiAlSiN coating for suppressing notch wear during turning of the high temperature alloys like Inconel 718 [IS14]. The thickness of individual layers can be reduced even to few nanometers to achieve superlattice or nanolaminate coating architecture for improving the tribological contact conditions and wear resistance in tooling applications [HE19].

2.9 Summary and research requirement

The forming and cutting tools coated with PVD nitride hard coatings are subjected to challenging mechanical or thermomechanical loading conditions during the production of workpieces from high strength materials. This can lead to coated tool degradation due to plastic deformation and crack growth. The instrumented indentation tests provide promising basis for fundamental investigations of the elastic-plastic deformation behavior of the coatings and the compounds of coating-substrate combinations. Current investigations mainly focus on the coating and rely on the empirically implemented analytical models developed for the bulk materials. The overreliance on the coating H_{IT} and E_{IT} values undermines the potential of indentation test data as well as ignores the effects of coating thickness and substrate on the compound deformation. The influence of coating residual stresses and multilayering on cracking behavior of the nitride hard coatings is well investigated. However, the effect of coating thickness in combination with the residual stresses or coating architecture on cracking behavior is not understood. Moreover, the temperature dependent deformation behavior of compounds in correlation with the coating thickness and multilayering is not well investigated for tooling applications. The mesoscale deformation mechanisms of grain boundary sliding and column inclination as well as crack growth in cross-section of columnar coatings are studied for shallow deformation zones concentrated in the coatings. These mechanisms should be understood for loading conditions involving combined coating-substrate deformation at room as well as at higher temperatures. Moreover, the focus should be extended from cross-sectional cracks to large surface cracks in the coating. In application, the surface crack networks are an indication of tool degradation due to the thermomechanical fatigue or the plastic deformation. Hence, fundamental investigations are required to further understand the deformation behavior of compounds with nitride hard coatings and substrate materials for tooling applications. Moreover, the potential of instrumented indentation tests to provide reasonable measurement data-based parameters for the characterization and prediction of the temperature-dependent deformation as well as the surface cracking behavior of compounds needs to be evaluated.

3 Research objectives and solution approach

The **main goal** of this dissertation is to advance the fundamental understanding of compound deformation and fracture mechanics. This can enable coating designs to extend functional capability and increase service life of tools for challenging forming or cutting operations. In this context, a subgoal is to maximize the utilization of measurement data from the instrumented indentation tests for characterizing and understanding compound deformation behavior. The investigations are based on two hypotheses (H) and corresponding research questions (RQ) related to compounds with nitride hard coatings for forming and cutting tool applications.

H1: Crack resistance of compounds can be increased through knowledge-based adjustment of coating properties resulting from advanced understandings on coating and compound deformation behavior as well as coating deformation mechanism.

RQ1: How do the coating thickness, chemical composition and resulting residual stress state influence the compound deformation behavior and surface crack resistance of CrAlN coated high-speed steel substrates under cyclic impact loading?

RQ2: How do the coating thickness and coating architecture influence the deformation behavior and surface crack growth in compounds with TiAlCrSiN coatings and cemented carbide substrates under monotonic indentation loading?

RQ3: To what extent is the fracture behavior of TiAlCrSiN coated cemented carbide compounds under sliding indentation load affected by the coating thickness, architecture and deformation mechanism?

RQ4: How does the temperature in correlation with the coating thickness and architecture influence the deformation behavior and crack growth in TiAlCrSiN coated cemented carbide compounds under monotonic indentation loading?

H2: Measurement data from instrumented indentation tests combined with coating characteristics provide reasonable parameters to characterize and predict the temperature dependent surface crack resistance of compounds.

RQ5: Which data-based parameters from instrumented indentation tests are helpful for understanding the correlations between temperature dependent deformation behavior and resistance of compounds against surface cracks?

RQ6: Which data-based modeling methods can be used to predict the deformation behavior and surface cracking of compounds?

The research questions are answered in chapters 4 to 7 of the dissertation. The breakdown of research questions by results chapters is shown in Table 3.1. The investigations in chapter 4 are driven by application scenarios related to cold forming and milling tools with high-speed steels as tool substrate materials and widely used CrAlN coatings. Investigations in chapters 5 and 6 are motivated by application scenarios, such as cold forming, warm forming and cutting operations, with cemented carbides as tool substate material. Considering higher stress collectives on tools in such applications, the deformation and fracture behavior of compounds with advanced nanocomposite TiAlCrSiN coatings is studied.

Table 3.1: Breakdown of research questions and results chapters

Research question	Chapter
RQ1	4 Deformation and impact fatigue behavior of CrAlN coated high-speed steel
RQ2, RQ3 & RQ5	5 Fracture mechanics of TiAlCrSiN coatings on cemented carbide substrates
RQ4 & RQ5	6 High temperature deformation behavior of TiAlCrSiN coated cemented carbides
RQ6	7 Data driven models for prediction of deformation mechanics

In chapter 4 the compounds of CrAlN coatings on high-speed steel HS6-5-2C substrates are studied. The residual stresses in CrAlN coating properties are varied by changing the Al content and thickness of the coating. The deformation and fracture behavior of the coated compounds is examined through instrumented indentation tests and scratch tests, respectively. Cyclic impact tests are carried out to investigate the effect of coating properties and compound deformation behavior on impact fatigue of compounds. Finally, the fatigue damage propagation on mesoscale and underlying deformation mechanism of the coatings is studied using high resolution electron microscopy.

Chapter 5 includes fundamental investigations on compound deformation behavior and fracture mechanics of TiAlCrSiN coated cemented carbide substrates under indentation loadings in correlation with coating architecture and thickness variation. For this purpose, monolayer TiAlCrSiN and bilayer TiAlCrSiN/TiAlCrSiON architectures are considered. Other than coating characterization, instrumented indentation tests and microscratch tests with

varying indentation forces are carried out at room temperature. The deformation behavior of the compounds is characterized and correlated with coating fracture behavior using the measurement data from the instrumented indentation tests. The mesoscale mechanisms of coating deformation and crack growth under sliding indentation load are understood using high resolution electron microscopy.

Chapter 6 focuses on high temperature deformation and fracture mechanics of the compound variants investigated in chapter 5. For this purpose, instrumented indentation tests in nano- as well as in micro-range are carried out with varying combinations of indentation force F and measurement temperatures until $T = 600$ °C. The influence of the temperature on deformation and fracture mechanics of the sample variants is studied with the help of measurement data from the indentation tests. Moreover, the influence of coating architecture and thickness on initiation and propagation of cracks at higher temperatures is understood using high resolution electron microscopy.

Chapter 7 explores the potential of data driven modeling approaches for predicting the temperature dependent deformation mechanics of compounds. This chapter also includes basic knowledge on machine learning methods for understanding the modeling approach. Three machine learning algorithms for prediction of the temperature dependent compound deformation and surface cracking behavior are trained, tested and evaluated. The exemplary dataset for the model development includes the instrumented indentation test data and the coating characteristics from chapter 5 and chapter 6.

4 Deformation and impact fatigue behavior of CrAlN coated high-speed steel

This chapter focuses on RQ1 of the dissertation by investigating four CrAlN coatings with varying Al content or thickness deposited on high-speed steel substrates. Firstly, experimental methods including coating deposition processes, coating characterization and system tests are presented. Afterwards, the results related to the effect of coating properties on deformation behavior and impact fatigue of compounds are discussed. Some of the results have already been published in [BKC+21, BKT23].

4.1 Substrate material and coating deposition

As substrate material, high-speed steel HS6-5-2C was procured in form of round bar with radius r = 25 mm and length l = 500 mm from Abrams Industries GmbH & Co. KG, Osnabrück, Germany. HS6-5-2C is commonly used in industry for manufacturing cold forming and cutting tools. Table 4.1 shows the chemical composition of the substrate material, determined by the supplier with spectrometer analysis. Other than C, the major alloying elements of high-speed steel HS6-5-2C are the Cr, Mo, V and W. These elements form stable carbides to increase the hot hardness and abrasion resistance of the steel. Moreover, Cr increases the hardenability of steel by reducing the required cooling rate for martensite formation during quenching.

Table 4.1: Chemical composition of the high-speed steel HS6-5-2C used as substrate

Element/-	C	Co	Cr	Cu	Mn	Mo
Weight percentage / wt. %	0.94	0.67	4.15	0.14	0.29	4.70
Element/-	Ni	Si	V	W	Others	Fe
Weight percentage / wt. %	0.20	0.26	1.84	6.14	< 0.1 %	Balance

Samples with cylindrical geometry, radius r = 25 mm and thickness d = 8 mm, were prepared from the round bar. To avoid the eggshell effect, the substrate samples were quenched and tempered to achieve the surface hardness of H = (61 ± 1) HRC. This substrate pre-treatment step was carried out as per the common industrial practice at Härtha – Aldenhoven GmbH, Aldenhoven, Germany. At the start, the samples were pre-heated in a controlled atmosphere in two steps to T = 470 °C and T = 870 °C, respectively, with holding time of t_{hold} = 10 min at each step. Afterwards, the austenitizing of high-speed steel samples was carried out by heating to T = 1,180 °C with t_{hold} = 5 min. This step was followed by quenching to the room temperature. At the end, three tempering cycles were carried out with heating to T = 550 °C, t_{hold} = 60 min

and cooling to room temperature in between. Finally, the sample surfaces were ground, lapped and polished, respectively, to achieve an average area roughness $Sa = 0.005$ µm. Scanning electron microscopy (SEM) image of substrate grain structure is shown in Appendix I.

CrAlN coatings with low and relatively high Al content, each with thickness $s \approx 1.7$ µm and $s \approx 3.5$ µm, were deposited using hybrid dcMS/HPPMS processes. In total, four coating variants are investigated. Coatings were deposited using CC800/9 HPPMS industrial coating unit from CemeCon AG, Wuerselen, Germany. The coating unit consists of four dcMS and two HPPMS cathodes, see Figure 4.1(a).

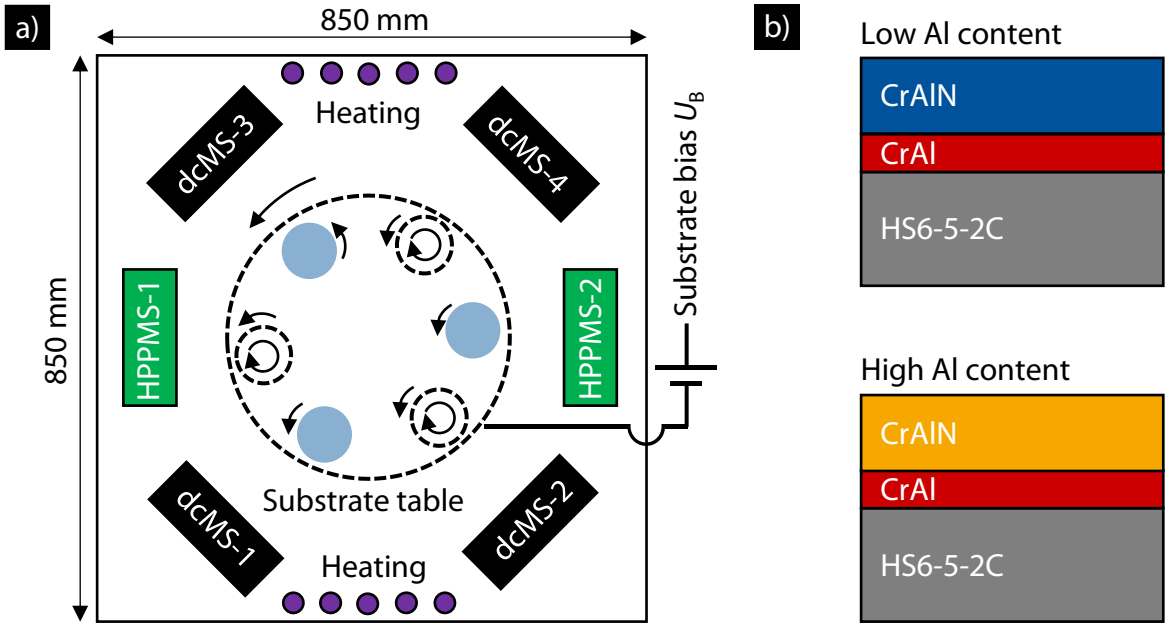

Figure 4.1: (a) Schematic of CC 800/9 HPPMS coating chamber along with (b) architecture of investigated CrAlN coatings

The coating Al content and thickness were varied through target configuration and coating time, respectively. The target configuration for Al content variation is shown in Table 4.2. The CrAl20 target consists of Cr base with 20 Al plugs of diameter $D = 15$ mm. Similarly, AlCr30 and AlCr20 targets have Al base with 30 and 20 Cr plugs, respectively. The coating architecture consists of a CrAl metallic bond layer, followed by the CrAlN functional layer, see Figure 4.1(b). For all investigated coatings, the bond layer was deposited using CrAl20 target installed at HPPMS-2 cathode. In order to exclude any effect of the bond layer thickness on subsequent investigations, the CrAl coating time $t_{CrAl} = 25$ min was kept constant for all four variants.

Table 4.2: Target configuration for deposition of CrAlN coatings with varying Al content

Process	dcMS-1	dcMS-1	dcMS-1	dcMS-1	HPPMS-1	HPPMS-2
Low Al content	CrAl20	CrAl20	CrAl20	CrAl20	CrAl20	CrAl20
High Al content	AlCr20	AlCr30	CrAl20	AlCr30	AlCr30	CrAl20

During the deposition process, the substrate table was rotated at a speed of $n_{Table} = 1\ min^{-1}$ and the samples were subjected to a three-fold rotation. The process parameters, which were constant during the deposition of the CrAlN functional layers, are shown in Table 4.3. To avoid HS6-5-2C tempering during the coating deposition, the coating chamber temperature was limited to $T \approx 500$ °C. Moreover, no change in substrate hardness of $H = (61 \pm 1)$ HRC before and after coating deposition was guaranteed with Rockwell C hardness test.

Table 4.3: Process parameters for the deposition of CrAlN functional layer

Parameter	Unit	Value
Pressure p	mPa	620
Argon flow $Q(Ar)$	sccm	200
Nitrogen flow $Q(N_2)$	sccm	Pressure controlled
Heating power P_H	kW	4
Substrate temperature T_s	°C	420
Substrate bias U_B	V	-100
Average power of HPPMS cathodes P_{HPPMS}	kW	5
Pulse frequency f_{pulse}	Hz	1,000
Pulse duration t_{on}	µs	40
Power of dcMS cathodes P_{dcMS}	kW	3

4.2 Coating characterization methods

To analyze coating morphology and coating thickness, fracture cross-sections of coated samples were examined by SEM. For this purpose, Zeiss DSM 982 Gemini, Carl Zeiss AG, Oberkochen, Germany, was used. Chemical composition of coatings was determined by electron probe microanalysis (EPMA) using a Schottky emitter electron microprobe, JEOL JXA-8530F, Tokyo, Japan. These investigations were carried out at Central Facility for Electron Microscopy (GFE), RWTH Aachen University, Germany. Confocal laser scanning microscopy (CLSM), Keyence VKX-210, Tokyo, Japan, was used to measure the average area roughness *Sa* of the coated

samples. The phase composition of the coatings was analyzed by X-ray diffraction (XRD) method. The working principle of XRD is based on Bragg's law, which states that the constructive interference of X-rays occurs when scattered by the atomic planes in a crystal at specific angles. The crystalline phases in a polycrystalline material are identified by their characteristic set of peaks on exposure to X-rays. For this purpose, X-ray beam of known wavelength λ is directed onto the sample surface at a constant or varying angle of incidence ω, while a detector records the intensities over the diffraction angle 2θ. During the phase analysis, the measured intensity peaks are associated to the individual phases using the comparison spectra of the Joint Committee on Powder Diffraction Standards (JCPDS). In present study, the XRD measurements were carried out by X-ray diffractometer 3003, GE Energy Germany GmbH, Ratingen, Germany. As X-ray beam, Cu-Ka radiation at U = 40 kV and I = 40 mA having wavelength λ = 0.1540598 nm was used. Other measurement parameters, commonly used for XRD measurements of thin PVD coatings, were incidence angle ω = 2°, diffraction angle 2θ = 20° - 80°, step size $\Delta 2\theta$ = 0.01° and step time t = 10 s.

4.3 Compound characterization methods

The adhesion between the coating and substrate was analyzed through Rockwell C indentation test according to DIN 4856 using HP100 Rockwell tester, KNUTH Machine Tools GmbH, Wasbek, Germany. A diamond tip with Rockwell geometry and cone angle of θ = 120° was used to indent the surface with normal force $F \approx$ 1,471 N. The edge areas of the imprints were analyzed for crack networks and coating delamination by CLSM. The adhesion strength class *HF* was determined based on the observed damage extent, as shown schematically in Figure 4.2(a). The adhesion strength $HF \leq 4$ is recommended for industrial applications.

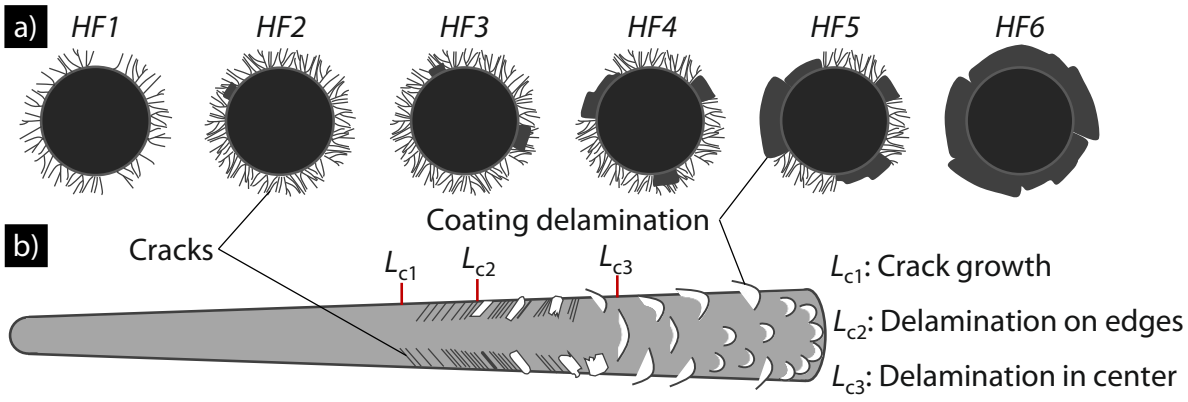

Figure 4.2: Selection criteria for (a) adhesion strength class *HF* and (b) critical normal force L_c

Fracture behavior of the compounds under sliding indentation load was studied using constant force scratch tests according to DIN EN ISO 20502. The coated surfaces were scratched with normal force from F = 10 N till F = 70 N with ΔF = 5 N and the sliding velocity v_s = 10 mm/min. Rockwell diamond tip was installed on Scratch Tester HPG 200/2, Gesellschaft für Fertigungstechnik und Entwicklung Schmalkalden e.V., Schmalkalden, Germany, for this purpose. The scratch imprints were analyzed for cracks and coating delamination using CLSM to determine the critical normal forces L_{c1} – L_{c3}, see Figure 4.2(b).

4.4 Residual stress measurement method

Residual stress state of the CrAlN coatings was analyzed with focused ion beam/digital image correlation (FIB/DIC) - ring core method. The method involves three main experimental steps as shown schematically in Figure 4.3. The preliminary steps involve the SEM analysis of surface to determine the suitability of topographic characteristics for the DIC analysis. If required, an artificial pattern can be applied to the surface, as explained in [BBK+22].

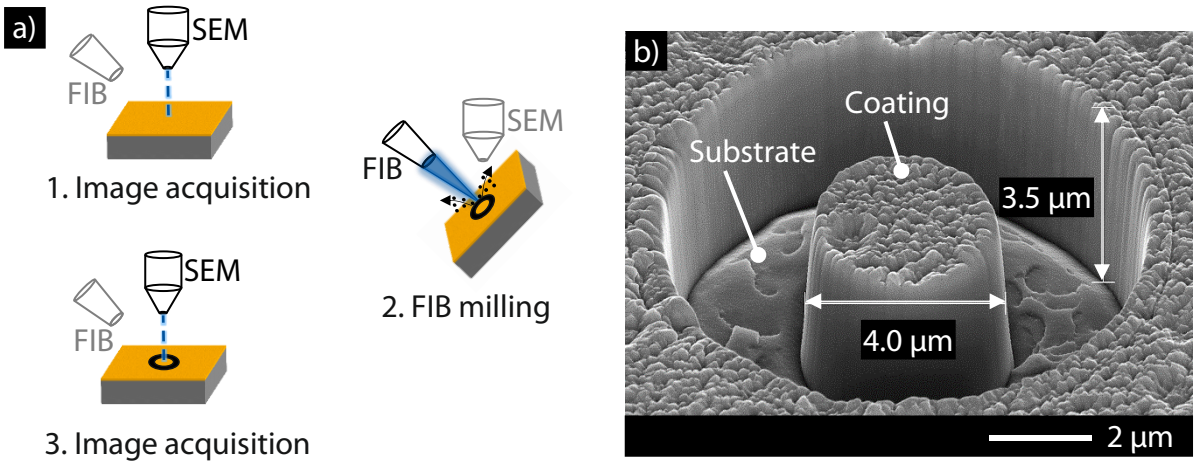

Figure 4.3: (a) Schematic of experimental steps for residual stress measurement with FIB/DIC ring core method along with (b) exemplary SEM image of a ring core

In first step, a SEM reference image of the chosen measurement location before FIB milling is acquired. Afterwards, a ring core with pre-defined diameter and height is milled into the surface with FIB. In order to release the residual stresses inside the ring core, the diameter and height should at least correspond to the coating thickness [KSB09]. After ring core milling, the second SEM image of the measurement location is captured. In order to calculate the strains ε_{xx}, ε_{yy} and ε_{xy}, resulting from release of residual stresses in the ring core, the SEM images of measurement location before and after milling of the ring core are compared using DIC analysis. The mean

strain values are used, as mentioned in [Läp16], to calculate the principal strains ε_1 and ε_2, see Equation 4.1.

$$\varepsilon_1 = \frac{\varepsilon_{xx}+\varepsilon_{yy}}{2} + \sqrt{\left(\frac{\varepsilon_{xx}-\varepsilon_{yy}}{2}\right)^2 + \left(\frac{\varepsilon_{xy}}{2}\right)^2}\ ,\ \varepsilon_2 = \frac{\varepsilon_{xx}+\varepsilon_{yy}}{2} - \sqrt{\left(\frac{\varepsilon_{xx}-\varepsilon_{yy}}{2}\right)^2 + \left(\frac{\varepsilon_{xy}}{2}\right)^2} \quad \text{Equation 4.1}$$

As per [KSB10], the principal stresses σ_1 and σ_2 for a non-equibiaxial stress state can be calculated using the principal strains ε_1 and ε_2, the E-modulus and the Poisson's ratio ν, see Equation 4.2. For present study, the E-modulus was replaced by indentation modulus E_{IT} of the coating. Poisson's ratio $\nu = 0.25$, as commonly for ceramic coatings, was assumed.

$$\sigma_1 = -\frac{E}{1-\nu^2}(\varepsilon_1 + \nu\varepsilon_2) \quad , \quad \sigma_2 = -\frac{E}{1-\nu^2}(\varepsilon_2 + \nu\varepsilon_1) \qquad \text{Equation 4.2}$$

The residual stress measurements were carried out at Institute for Materials Science, Leibniz University Hannover, Germany. For FIB milling, Zeiss Auriga Dual-beam SEM, Carl Zeiss AG, Oberkochen, Germany, was used. The DIC analysis was carried out using commercial software ViC-2D 2009, Correlated Solutions, Irmo, South Carolina, USA.

4.5 Elastic-plastic deformation behavior of coatings and compounds

In order to study the elastic-plastic deformation behavior of coatings, nanoindentation tests were carried out using TriboIndenter TI 950, Bruker Corporation, Billerica, Massachusetts, USA. The influence of surface roughness on measurements was minimized by polishing the selected measurement area for $t \approx 3$ s using a rotating steel ball and diamond suspension. The measurements were carried out inside the resulting circular imprint on the surface with an average area roughness $Sa < 0.02$ µm. To minimize the influence of substrate on deformation response of the CrAlN coatings, the indentation force was limited to $F = 8$ mN. For each coating variant, 50 measurements using a diamond indenter tip with Berkovich geometry and nominal radius $r \approx 150$ nm were carried out. Poisson's ratio $\nu = 0.25$, as commonly known for the ceramic coatings, was assumed to calculate the indentation modulus E_{IT} and indentation hardness H_{IT} as per [OP92]. The deformation behavior of the compounds as well as the uncoated HS6-5-2C was investigated by carrying out indentation tests in micro-range. For this purpose, a conical shaped diamond tip with nominal cone angle $\alpha = 60°$ and nominal

radius r = 10 µm was installed on the TriboIndenter TI 950. The indentations with conical tip lead to a deeper and more spherical deformation zone, particularly suitable to study the combined deformation response of coating and substrate [SFA+09]. For each sample variant, 10 indentations with maximum normal force F = 250 mN, F = 500 mN and F = 750 mN and loading time $t_{loading}$ = 10 s, hold time t_{hold} = 3 s and unloading time $t_{unloading}$ = 10 s were carried out. The force-indentation depth curves from nano- and microindentation tests were analyzed to characterize the elastic-plastic deformation behavior of the coatings and compounds, respectively, as described in section 2.5.3.

4.6 Cyclic impact tests

In order to investigate the fatigue behavior of coated compounds under cyclic impact loading, Apollo NXG impact tester from Impact-BZ, London, UK, was used. The cyclic impact tests were carried out with an impact load of F = 1,000 N, frequency f = 50 Hz and cemented carbide ball of diameter D = 5 mm as counterbody. This resulted in an initial hertzian contact pressure of p_H = ~ 9.7 GPa. For each sample variant, two impact imprints were analyzed for surface cracks and coating delamination after N = 0.1, 0.5 and 1 million impacts using SEM. The plastic deformation of the compounds as well as uncoated substrate was characterized by measuring the permanent indentation depth h_p of the impact imprints using CLSM.

4.7 Damage analysis using FIB and TEM

In order to understand the initiation and propagation of cross-sectional cracks in correlation with deformation mechanism of coated compounds, selected impact imprints were analyzed in cross-section using a combination of FIB and transmission electron microscopy (TEM). For this purpose, the FIB lamellae were prepared using FEI FIB Strata 400, FEI Electron Optics B.V., now Thermo Fischer Scientific, Eindhoven, Netherlands. The lamella represents, in this case, a thin cross-sectional slice cut from the area of interest using the FIB. The method offers precise targeting of small damage areas for high resolution analysis, while preserving the true damage features during the preparation. This can give detailed information about crack initiation and growth in the material. For TEM investigations of the prepared FIB lamellae FEI Tecnai G^2 F20 S-TWIN, FEI Electron Optics B.V., Eindhoven, Netherlands, was used. The FIB preparations and the TEM investigations were carried out at Central Facility for Electron Microscopy (GFE), RWTH Aachen University, Germany.

4.8 Coating properties and adhesion strength

The coating properties such as chemical composition, surface roughness, thickness as well as adhesion strength class are summarized in Table 4.4. The coating type categorizes the variants with thickness $s \approx 1.7$ µm as thin and with $s \approx 3.5$ µm as thick. The coating designation is based on percentual atomic contribution from Al to the total metallic content of the coating. The $(Cr_{66}Al_{34})N$ coatings require relatively higher coating times to reach comparable thickness to the $(Cr_{90}Al_{10})N$ variants. This is attributed to the lower sputter rate of the Al compared to the Cr [KD95]. The average area roughness *Sa* increases with Al content and coating thickness. The nitrogen incorporation in the coatings slightly increases with the Al content. This is attributed to the higher reactivity of Al to N as compared to Cr.

Table 4.4: Properties and adhesion strength class *HF* of investigated CrAlN coatings

Coating type	Thin coatings		Thick coatings	
Sample ID	4036	4052	4183	4185
CrAlN layer coating time t_{CrAlN} / min	58	80	102	138
Coating thickness *s* / µm	1.6	1.7	3.5	3.4
Average area roughness *Sa* / µm	0.02	0.03	0.04	0.04
Cr content / at. %	43	31	44	31
Al content / at. %	5	16	5	16
N content / at. %	52	53	51	53
x(Al) = Al/(Al+Cr) / %	10	34	10	34
Adhesion strength class *HF* / -	1	2	2	2
Coating designation / -	$(Cr_{90}Al_{10})N$	$(Cr_{66}Al_{34})N$	$(Cr_{90}Al_{10})N$	$(Cr_{66}Al_{34})N$

The adhesion between the coating and substrate reduces from *HF1* to *HF2* with the increase in coating Al content or thickness. This indicates a change in coating as well as compound deformation behavior, which will be discussed in subsequent investigations. However, the adhesion strength class *HF* remains within the acceptable range of $HF \leq 4$ for the compounds. SEM images from the fracture cross-sections of the coatings are shown in Figure 4.4. All investigated coatings exhibit columnar morphology. The $(Cr_{90}Al_{10})N$ variants show slightly higher column thickness as compared to the finer columns of $(Cr_{66}Al_{34})N$. This change to finer columnar morphology increases the unevenness of surface and explains the higher average area roughness *Sa* of $(Cr_{66}Al_{34})N$ coatings. Other than the increase in column length, the thick coatings exhibit comparable columnar morphology to the corresponding thin variants.

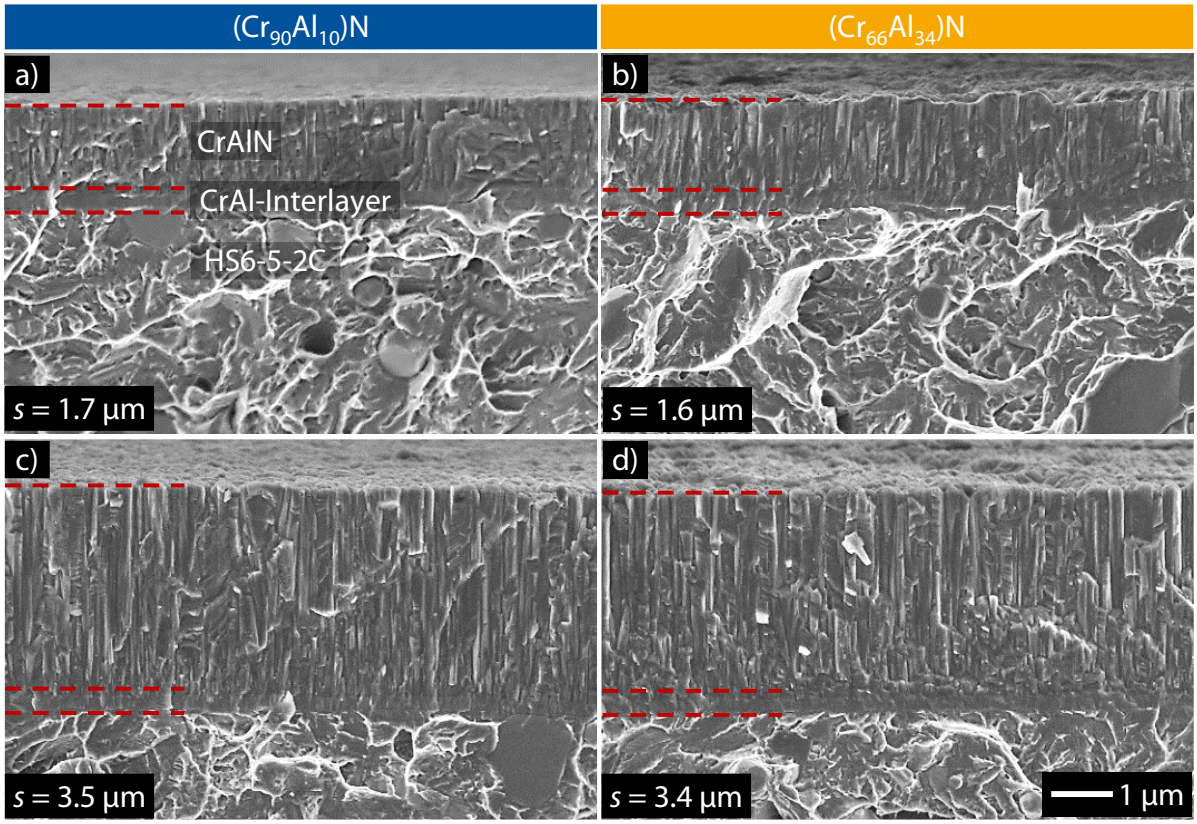

Figure 4.4: Morphology of (a,b) thin and (c,d) thick CrAlN coatings, [BKT23, BKC+21]

The phase composition of the coatings, analyzed by the XRD method, is shown in Figure 4.5. The diffraction peaks are associated to the cubic CrN and cubic AlN phases. The highest peak occurs at $2\theta \approx 38°$ with the preferred (111) orientation for all four coatings.

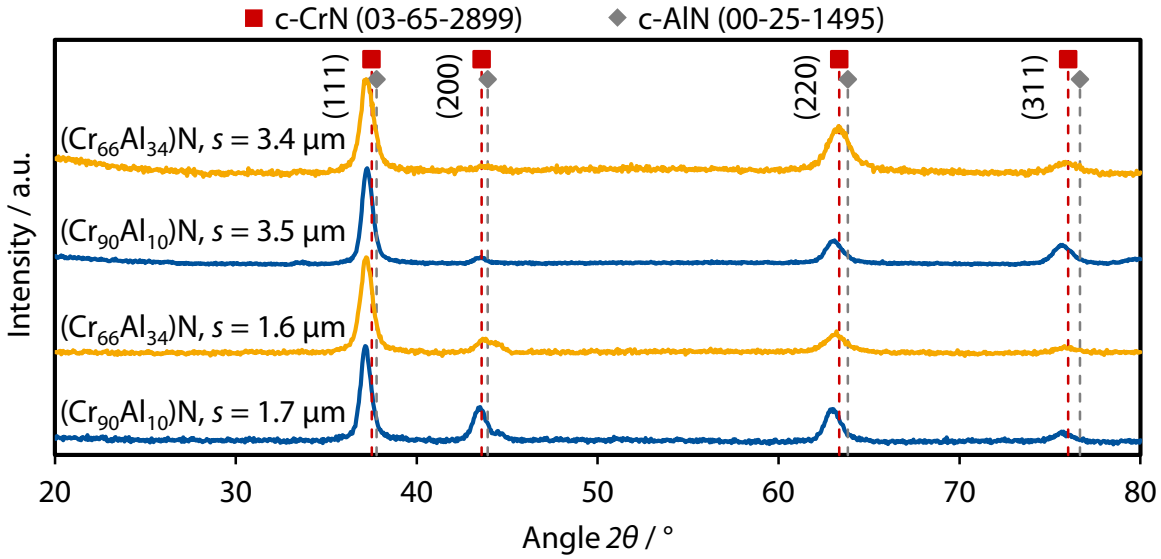

Figure 4.5: Diffractogram of thin and thick CrAlN coatings from XRD measurements

The (111) preferred orientation for nitride coatings with fcc-NaCl structure is associated with high resistance against plastic deformation [CYH02]. In case of the thin coatings, minor reductions in intensity of (200), (220) and (311) peaks are observed with higher Al content. This is associated with the increase in shift to c-AlN, which slightly flattens the peaks. The increase in coating thickness for $(Cr_{90}Al_{10})N$ results in higher peak intensity for (311) at the cost of (200). For $(Cr_{66}Al_{34})N$, the (220) and (311) peak intensities increase while the (200) diminishes with higher coating thickness. This is presumably related to thickness dependent change in residual stresses of the coatings, promoting growth of (220) and (311) orientations.

4.9 Residual stress state of CrAlN coatings

The strain distribution maps inside the ring core after FIB milling, determined by DIC analysis, are shown exemplarily for thick $(Cr_{66}Al_{34})N$ coating in Figure 4.6. The purple to aqua blue areas, which dominate the distribution maps for ε_{xx} and ε_{yy}, represent expansion of the surface resulting from the release of compressive residual stresses in the ring core after FIB milling. The distribution maps for shear strains ε_{xy} are mainly aqua blue to green in color, representing a mean strain distribution close to zero.

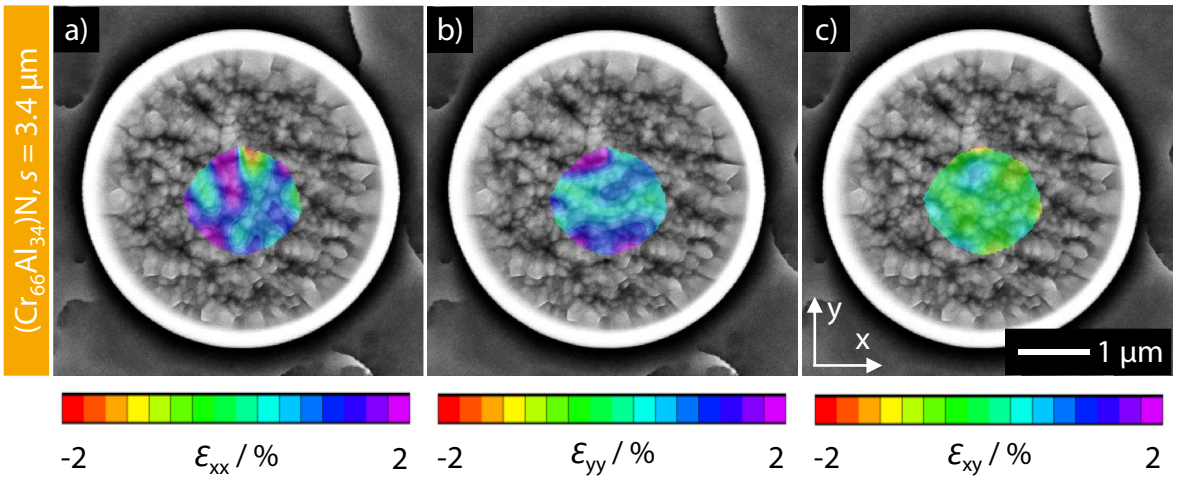

Figure 4.6: Strain distributions maps from DIC analysis inside the ring-core of $(Cr_{66}Al_{34})N$ thick coating in (a) ε_{xx}, (b) ε_{yy} and (c) ε_{xy} direction, [BKT23]

The mean strain distributions from DIC analysis and the calculated principal stresses for all coating variants are shown in Table 4.5. An increase in coating Al content leads to higher compressive residual stresses. Due to the difference in atomic radius, the increased substitution of Cr with Al in the CrAlN lattice results in higher lattice distortion and consequentially higher

compressive residual stresses. Moreover, the compressive residual stresses increase with coating thickness, a known phenomenon in columnar PVD coatings. As columns grow lengthier at higher coating thicknesses, they tend to expand sideways. However, this expansion is resisted by the neighboring columns striving to expand themselves. This leads to higher compressive residual stresses with the increase in thickness of columnar coating.

Table 4.5: Mean strain distributions ε_{xx}, ε_{yy} and ε_{xy} as well as principal stresses σ_1 and σ_2 of CrAlN coatings with varying Al content and thickness

Coating	$(Cr_{90}Al_{10})N$	$(Cr_{66}Al_{34})N$	$(Cr_{90}Al_{10})N$	$(Cr_{66}Al_{34})N$
s / µm	1.6	1.7	3.5	3.4
ε_{xx} / %	0.57	0.79	1.13	0.95
ε_{yy} / %	0.47	0.54	0.59	0.89
ε_{xy} / %	0.06	0.03	0.04	-0.13
σ_1 / GPa	-2.1	-3.0	-4.1	-3.8
σ_2 / GPa	-1.9	-2.4	-2.8	-3.4

4.10 Deformation behavior under monotonic indentation load

The elastic-plastic deformation behavior of the coatings characterized by nanoindentations at F = 8 mN is shown in Table 4.6. The maximum indentation depth at F = 8 mN and remaining depth of the indent after unloading are denoted as h_{max} and h_p, respectively. Percentual contribution from plastic work W_{plast} to the total mechanical work W_t during indentation is represented as η_{plast}. The indentation hardness H_{IT} increases with coating Al content. This is consistent with the compressive residual stress magnitudes of thin coatings but inconsistent for thick coatings. The indentation modulus E_{IT} remains almost comparable for all coatings.

Table 4.6: Deformation behavior of CrAlN coatings with varying Al content and thickness

Coating	$(Cr_{90}Al_{10})N$	$(Cr_{66}Al_{34})N$	$(Cr_{90}Al_{10})N$	$(Cr_{66}Al_{34})N$
s / µm	1.6	1.7	3.5	3.4
H_{IT} / GPa	22.7 ± 2.1	27.2 ± 2.0	22.0 ± 2.3	26.1 ± 2.4
E_{IT} / GPa	290 ± 25	301 ± 18	303 ± 25	293 ± 22
h_{max} / nm	131 ± 5	123 ± 4	131 ± 6	126 ± 5
h_p / nm	56 ± 5	47 ± 6	60 ± 6	49 ± 4
η_{plast} / %	38 ± 3	33 ± 2	40 ± 3	34 ± 2

The $(Cr_{66}Al_{34})N$ coatings exhibit lower h_{max}, h_p and η_{plast} as compared to $(Cr_{90}Al_{10})N$ variants, see Table 4.6. This confirms higher resistance of $(Cr_{66}Al_{34})N$ coatings against plastic deformation due to the Al content. The increase in coating thickness does not exhibit any significant effect on elastic-plastic deformation behavior of the coatings during nanoindentation. Despite the higher compressive residual stresses, the thick coatings show comparable H_{IT}, E_{IT}, h_{max}, h_p and η_{plast} to the corresponding thin variants with differences $|\Delta| < 10$ %. These counterintuitive results related to the residual stress magnitude and deformation response of the coatings can be understood by considering the limitations of the residual stress measurement method and nanoindentation of thin PVD coatings. Firstly, the FIB/DIC - ring core method measures the homogenized effect of the residual stress gradient in the coating cross-section on the surface of the ring core. The residual stress gradient varies with the coating thickness and accordingly the measured stress values from the method. Secondly, for columnar coatings with column sizes in submicron range, the ring core contains large number of grains, as evident in Figure 4.6. This means that the FIB/DIC - ring core method measures type I or average macroscopic residual stresses in the columnar coating. However, during indentations in nano-range with indentation depths $h < 0.2$ µm, the deformed coating volume and the resulting projected area A_{proj} of the indent imprint is much smaller than the size of ring core. In the present case, the diameter of ring core corresponds to the coating thickness. On the other hand, the projected area of the indents, calculated as per [OP92], is $A_{proj} \leq 0.4$ µm^2 for the investigated coatings. This means that only a small number of coating columns deform during nanoindentation. In this case, the localized type II intergranular residual stresses and intragranular type III residual stresses dominate the deformation response of the coating rather than the average macroscopic residual stresses measured by the FIB/DIC - ring core method. Hence, no effect of coating thickness and corresponding macroscopic residual stress increment is observed on the localized coating deformation response during the nanoindentation. On the other hand, the change in lattice distortion with higher Al content changes the localized type II and type III compressive residual stresses in the coating. This effect is captured by nanoindentation, as $(Cr_{66}Al_{34})N$ coatings show higher resistance against plastic deformation compared to the $(Cr_{90}Al_{10})N$ coatings, irrespective of the coating thickness. Accordingly, the thin variants exhibit correlation between the macroscopic residual stress magnitudes and the localized deformation response of the coating during nanoindentation. However, for the thick coatings, the macroscopic residual stresses include combined influence of coating thickness as well as the Al content and therefore do not correlate with coating deformation behavior during nanoindentation.

The elastic-plastic deformation behavior of the uncoated HS6-5-2C and coated compounds was characterized by indentation tests in micro-range. Figure 4.7(a) shows the average maximum indentation depth h_{max} as sum of h_p and recovered indentation depth h_e. Figure 4.7(b) displays the average percentual contributions η_{plast} and η_{elast} from plastic work W_{plast} and elastic reverse deformation work W_{elast}, respectively, to the total mechanical work W_t during indentation. W_{elast} is calculated as the area under the unloading segment of the force-indentation depth curve whereas W_{plast} represents the area between the loading and unloading segments, i.e. the difference between W_t and W_{elast}, see section 2.5.3. Any contributions from the crack growth in the sample to the total energy consumption during indentation is not considered in W_t. As all average values in Figure 4.7 have a standard deviation $SD \leq 5$ %, the error bars are not shown in the plots. The coated variants exhibit a significant reduction in h_{max}, h_p, W_t and η_{plast} as well as higher η_{elast} in comparison to uncoated HS6-5-2C. Hence, the CrAlN coatings increase the resistance of coated compounds against plastic deformation for the considered indentation load range. Among the coated variants, the deformation behavior varies with coating Al content, thickness and indentation force. The thin coating variants show a slight difference in h_p, η_{plast} and η_{elast} but comparable h_{max} and W_t at F = 250 mN. As the substrate effect increases with indentation force, the effect of coating Al content on deformation response diminishes. Higher coating thickness increases the plastic deformation resistance in terms of lower h_{max}, h_p, W_t and η_{plast} as well as higher η_{elast} of thick coating compounds as compared to the thin variants. Moreover, the coupling of higher coating thickness with Al content decreases the h_p, η_{plast}, increases η_{elast} and shows no effect on h_{max} and W_t for thick coating compounds. This means that for the same coating thickness, higher coating Al content increases elastic recovery of the compound. The effect of coating Al content on compound deformation correlates well with the corresponding trends observed for compressive residual stresses and elastic-plastic deformation response of the investigated CrAlN coatings. Higher Al content increases the compressive residual stresses and resistance of the coating against plastic deformation during nano-indentation tests, see Table 4.5 and Table 4.6, respectively. The cumulative effect of coating thickness, Al content and residual stresses on compound deformation response becomes apparent at higher indentation forces with deeper deformation zones extending beyond the coatings. Hence, the compound with thick $(Cr_{66}Al_{34})N$ coating consistently shows higher resistance against plastic deformation in terms of lower h_p and η_{plast} as well as higher η_{elast} among the investigated variants, see Figure 4.7. This means that thick coatings, with higher compressive residual stress magnitudes, can distribute the applied indentation load more

effectively to reduce the stress concentration in the substrate and decrease overall compound deformation as compared to thin coatings. As the substrate effect increases with higher indentation force, the cumulative effect of coating thickness, Al content and residual stresses on the deformation response of the compounds decreases.

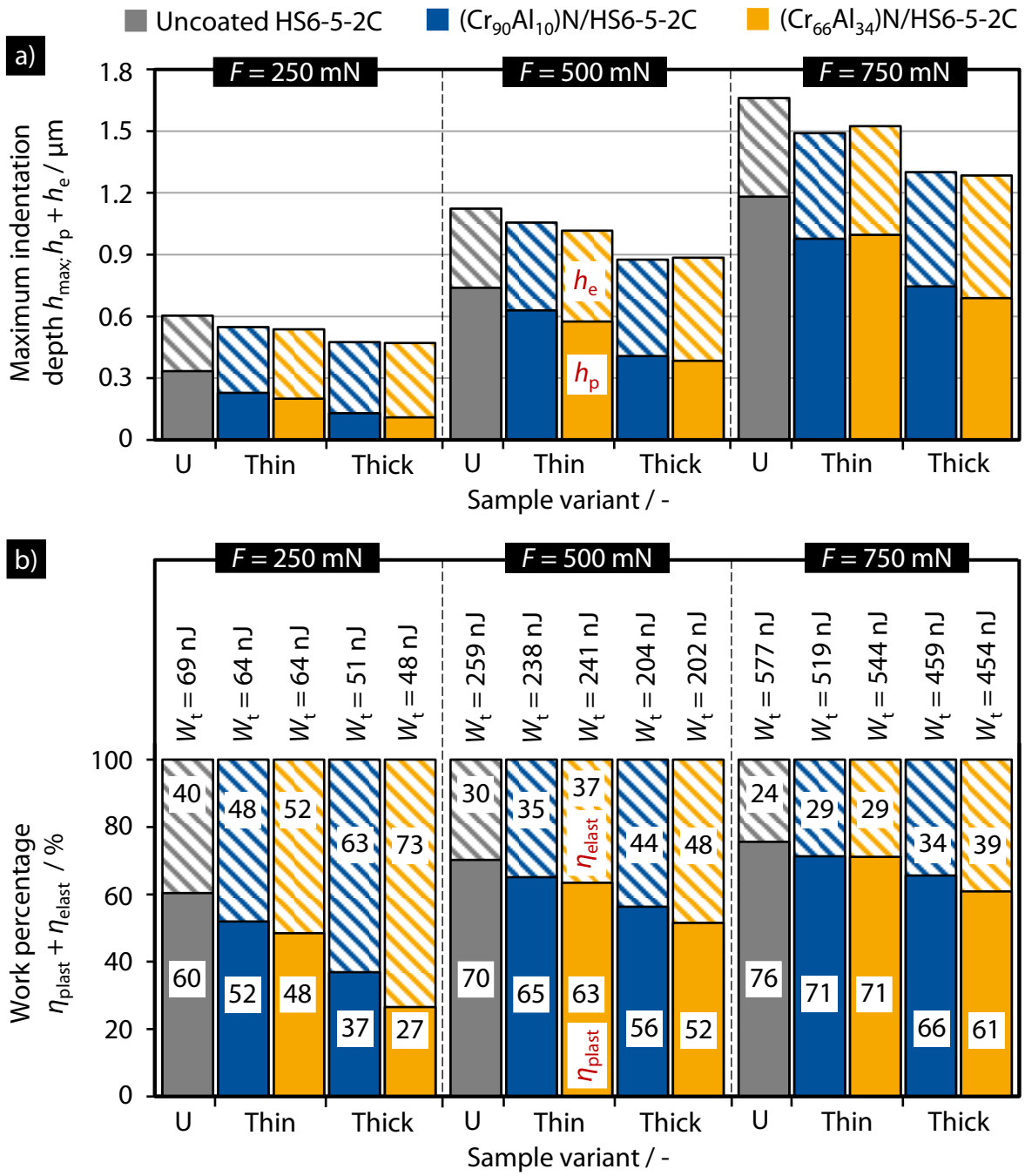

Figure 4.7: (a) Maximum indentation depth h_{max} (b) total indentation work W_t, plastic work percentage η_{plast} and elastic work percentage η_{elast} of uncoated HS6-5-2C and coated compounds at indentation force F = 250 mN, F = 500 mN and F = 750 mN

4.11 Fracture behavior under sliding indentation load

To characterize the fracture behavior of coated compounds under sliding load, the scratch test results are shown in Table 4.7. Critical normal force L_{c1} represents the onset of cracking, whereas L_{c2} is the normal force for initiation coating delamination at scratch track boundaries. The onset of coating delamination in center of the scratch track defines critical normal force L_{c3}.

Table 4.7: Critical normal force L_{c1}, L_{c2} and L_{c3} of CrAlN coatings deposited on HS6-5-2C

Coating	$(Cr_{90}Al_{10})N$	$(Cr_{66}Al_{34})N$	$(Cr_{90}Al_{10})N$	$(Cr_{66}Al_{34})N$
s / µm	1.6	1.7	3.5	3.4
L_{c1} / N	30	30	20	20
L_{c2} / N	45	40	35	25
L_{c3} / N	60	60	65	50

As apparent from the difference in critical normal forces L_{c1} and L_{c2}, thick coating compounds exhibit crack initiation and coating delamination at lower normal forces as compared to the thin variants. Furthermore, the coatings with higher thickness display large areas of abrupt delamination at the corresponding critical normal loads L_{c2}, see Figure 4.8.

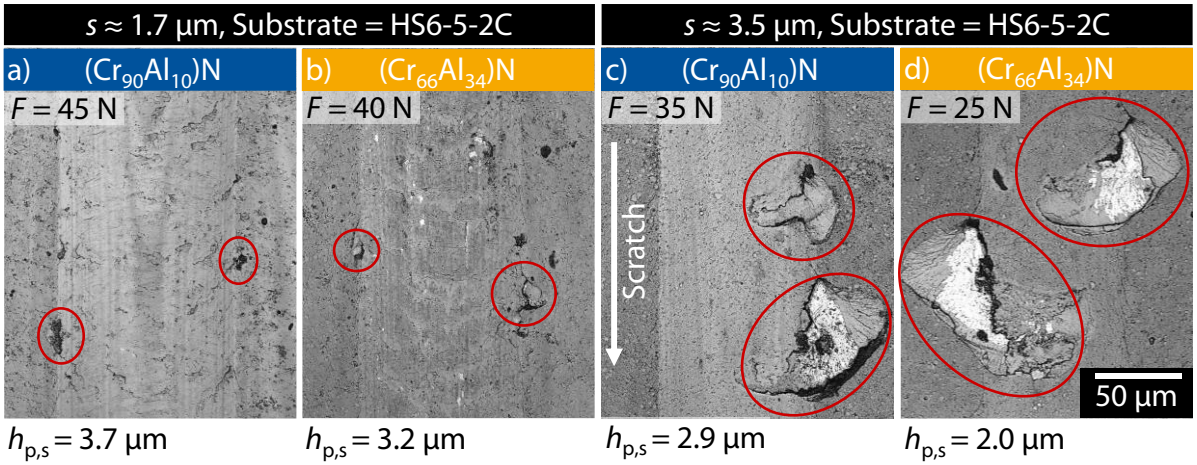

Figure 4.8: Scratch tracks of the CrAlN coatings with varying Al content and thickness at critical normal force L_{c2}, [BKT23]

Despite the higher L_{c2} and the corresponding higher permanent scratch depth $h_{p,s}$, such large coating delamination areas around the scratch boundary are absent for the thin coatings. This points to lower resistance against cohesive and adhesive damage of the thick coatings compared to the thin variants under sliding indentation load. This is understood by considering the

deformation and stress profile around the boundary region of scratch. Figure 4.9(a) shows residual depth profile of the scratch on compound with thick $(Cr_{90}Al_{10})N$ at critical normal force L_{c2}, measured using CLSM. A similar trend in terms of the shape of residual depth profile was observed for other variants. The high contact pressure from indenter tip in the central region of scratch track combined with the sliding movement of indentation load results in material flow and pile-up in the boundary region of scratch track. Figure 4.9(b) schematically shows the extrinsic stress profile in x-direction, along the sample cross-section i.e. z-axis, at material pile-up location of scratch track. The location of neutral axis depends on the height of material pile-up resulting from material dependent permanent scratch depth $h_{p,s}$ at given scratch force F. In the present case, the height of material pile-up $h \approx 1$ µm is less than the coating thickness $s = 3.5$ µm, see Figure 4.9(a). Hence, the extrinsic stresses in material pile-up region change from tensile to compressive inside the coating cross-section from surface towards the substrate. The deformation profile and accompanying extrinsic stress conditions in material pile-up region combined with the higher compressive residual stresses of thick coatings contribute to brittle transverse coating fracture i.e. along the x-y plane in Figure 4.9(b). Accordingly, the thick coatings with $|\sigma_r| > 3$ GPa show abrupt delamination around the shoulder region of scratch as well as reduced resistance against cohesive and adhesive damage characterized with critical normal force L_{c2}, see Figure 4.8. Therefore, coupling of higher coating thickness and compressive residual stresses $|\sigma_r| > 3$ GPa amplifies the brittle fracture of coatings on high-speed steel HS6-5-2C substrates under sliding indentation load.

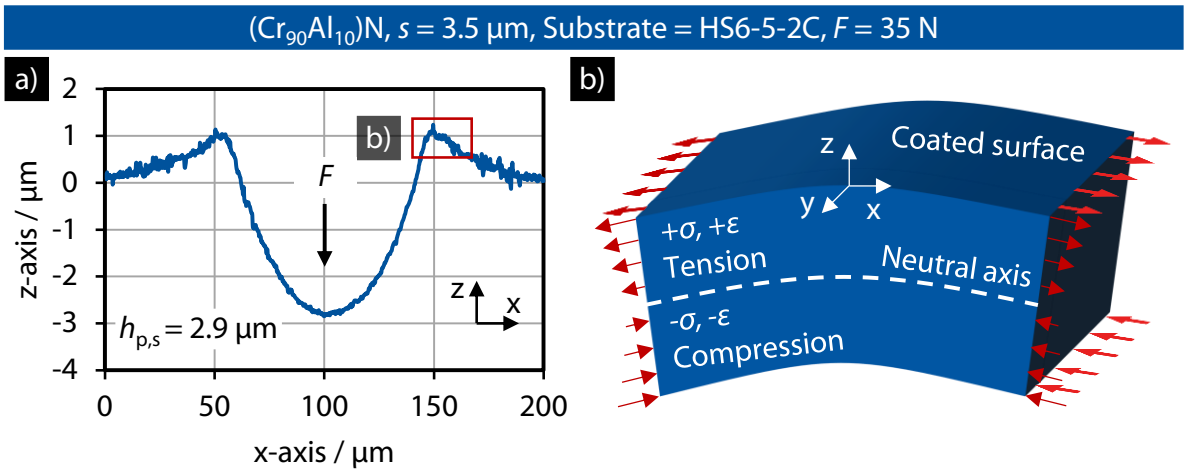

Figure 4.9: (a) Residual depth profile of the scratch on compound with thick $(Cr_{90}Al_{10})N$ at $F = 35$ N along with (b) schematic representation of the extrinsic stress profile at material pile-up location in scratch boundary region

4.12 Fatigue behavior under cyclic impact load

The impact test results for coated compounds as well as uncoated substrate reference, are shown in Figure 4.10. The plastic deformation of the samples was characterized by measuring the permanent indentation depth h_p of impact imprints after specified number of impact cycles. The thin coating compounds show almost similar h_p to the uncoated substrate for the considered impact force and cycles. However, higher coating thickness reduces the h_p of thick coating compounds by Δh_p = (0.5 – 1.0) µm compared to the thin variants. A similar trend is observed for the instrumented indentation tests with monotonic indentation loading in section 4.10. Hence, the thick coating compounds maintain their superior plastic deformation resistance to the thin coating compounds during the cyclic impact tests. The effect of coating Al content on h_p of the compounds is noticeable for thick coatings at N = 0.1 million cycles. However, as the impact cycles increase, no significant difference in h_p between $(Cr_{90}Al_{10})N$ and $(Cr_{66}Al_{34})N$ thick coating compounds is apparent. For thin coating compounds, the coating Al content shows no significant effect as the h_p remains comparable to the uncoated substrate. Moreover, all coated samples as well as uncoated substrate variants exhibit an overall increase of Δh_p = ~ 0.8 µm from N = 0.1 million to N = 1 million impacts. This confirms that the coating thickness influences the plastic deformation of the compounds at the start of impact tests. However, as the impact cycles increase, the permanent indentation depth h_p of impact imprints is largely governed by the work hardening and plastic deformation of the HS6-5-2C substrate.

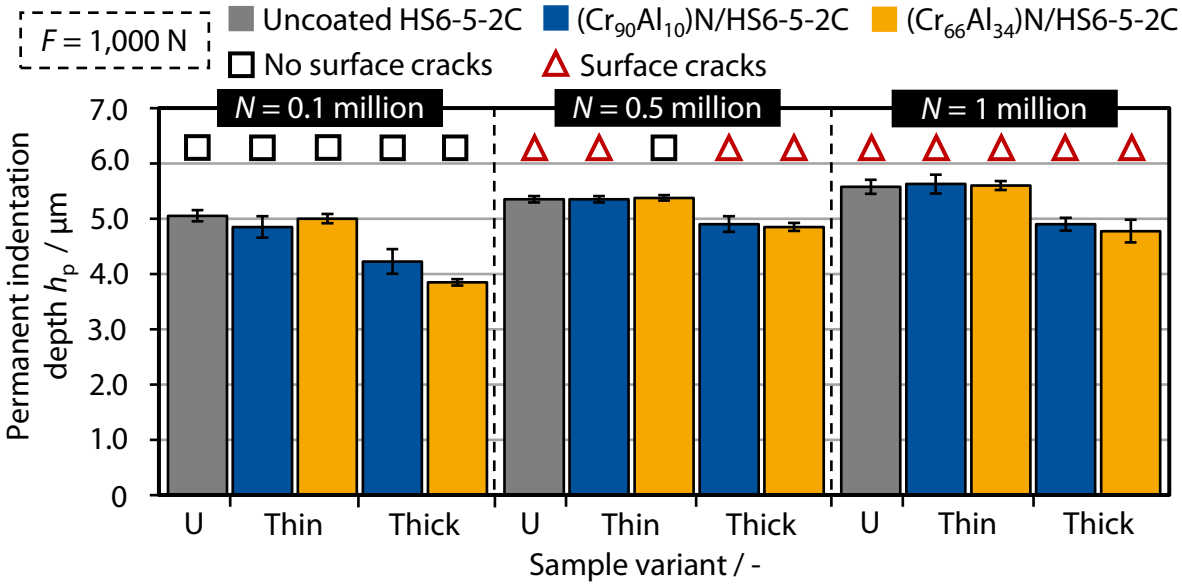

Figure 4.10: Permanent indentation depth h_p of impact imprints on uncoated substrate and coated compounds after varying number of impact cycles with F = 1,000 N

Regarding the fatigue behavior, all investigated variants, except the $(Cr_{66}Al_{34})N$ thin coating compound, show surface cracks at $N = 0.5$ million impacts. For $(Cr_{66}Al_{34})N$ thin coating compound, surface cracks are noticed at $N > 0.5$ million impacts, see Figure 4.10. Among the investigated variants, the $(Cr_{66}Al_{34})N$ thin coating compound exhibits improvement in fatigue behavior by withstanding the highest number of impact cycles before appearance of surface cracks. Figure 4.11 exemplarily shows the SEM images of circumferential surface cracks around boundary region of the impact imprints on coated compounds after $N = 1$ million impacts. The white areas inside the impact imprint represent the adhesions from the cemented carbide ball counterbody, as confirmed by the energy dispersive X-ray spectroscopy (EDX) analysis. It is worth mentioning that the compounds do not exhibit coating delamination or substrate exposure until $N = 1$ million impacts. The fatigue damage, observed from the surface, consists of circumferential cracks. The uncoated HS6-5-2C exhibited surface chipping and cracks inside the impact imprint. Considering the focus of investigation on coated compounds, the impact imprint for uncoated substrate after $N = 1$ million impacts is exemplarily shown in Appendix I.

Despite the lower indentation depth h_p at higher coating thickness, no significant improvement in resistance against initiation of surface cracks is apparent for thick coating compounds. This is attributed to the coupling of higher coating thickness and compressive residual stresses $|\sigma_r| > 3$ GPa which amplifies the brittle fracture of coatings on high-speed steel substrates. As observed in section 4.11, the thick coatings show lower resistance to cohesive damage initiation under sliding indentation load due to the superposition of deformation induced extrinsic stresses and the compressive residual stresses of the thick coating. The same is true under cyclic impact loading around boundary region of the impact imprint. The role of coating thickness in crack initiation and propagation around boundary region of the impact imprint is further discussed in subsequent FIB/TEM investigations. The $(Cr_{66}Al_{34})N$ thin coating compound has higher impact fatigue resistance due to the optimal combination of coating chemical composition, thickness and resulting compressive residual stress magnitude as well as elastic-plastic deformation behavior. These results show promising potential to simultaneously improve the plastic deformation resistance and fatigue behavior of the PVD coated cold forming tools. For instance, the overall coating thickness can be increased while maintaining the compressive residual stress magnitude of the coating in moderate range of $|\sigma_r| = (2 – 3)$ GPa. This can be achieved through targeted adjustment of coating chemical composition, coating architecture and process parameters like bias voltage U_B.

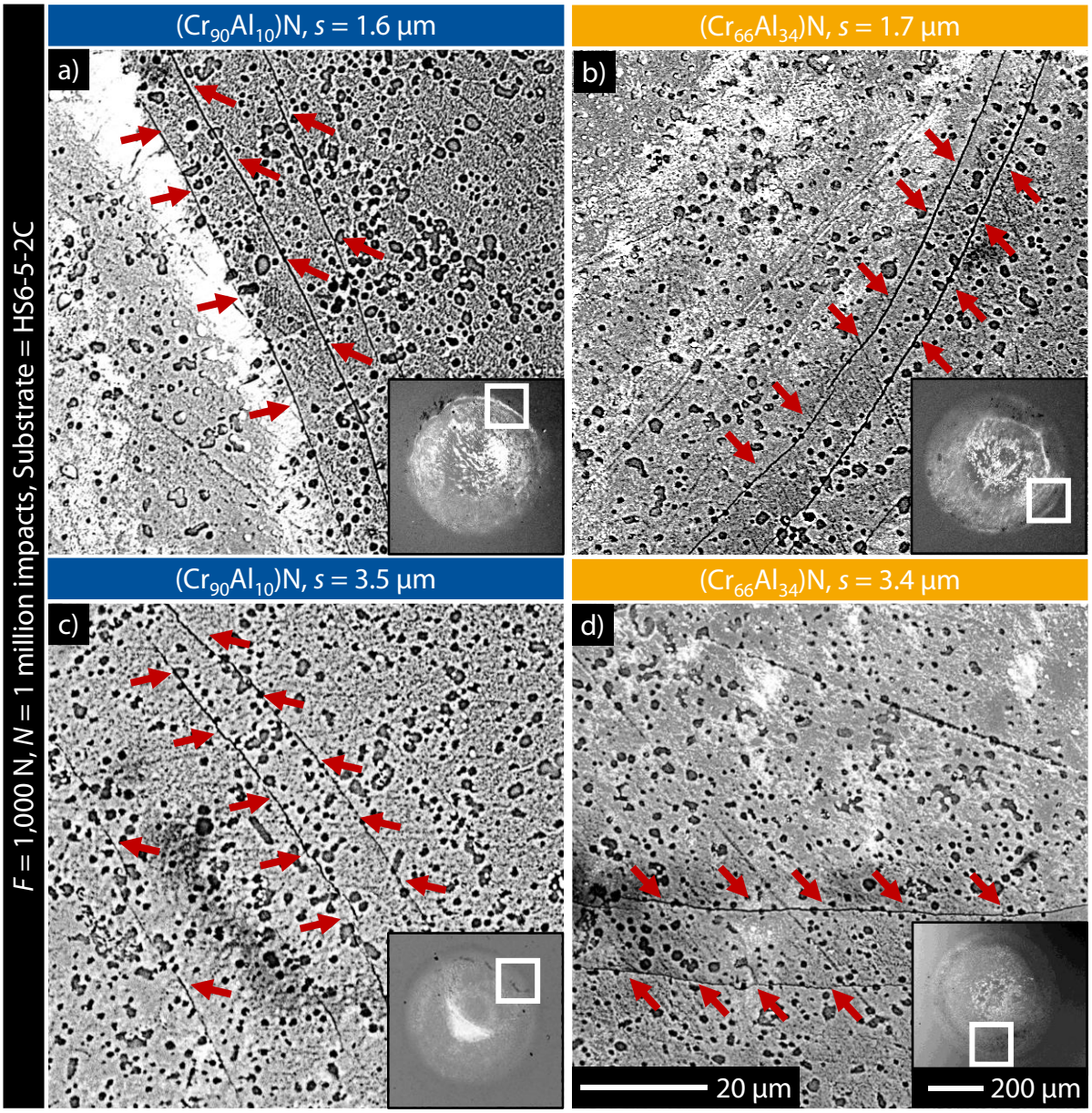

Figure 4.11: Impact imprints with enlarged crack areas for (a,b) thin and (c,d) thick coating compounds after $N = 1$ million impacts with $F = 1{,}000$ N, [BKT23, BKC+21]

4.13 Deformation mechanism and fatigue damage propagation

The compounds with thin and thick $(Cr_{66}Al_{34})N$, subjected to $N = 1$ million impacts, were selected for FIB/TEM analysis in cross-section. As the focus of the FIB/TEM investigations is to understand the mesoscale mechanisms of deformation and crack growth in columnar coatings, the variants with low Al content coating are not explicitly studied. For each selected variant, one FIB lamella from the center of the impact imprint, approximately representing the area with maximum indentation depth h_p, was prepared. The second lamella was cut from the

boundary region, where the circumferential surface cracks were observed. For variant with thin coating, one additional FIB lamella between the center and boundary of the impact imprint was prepared for coating deformation and crack growth analysis in the transition zone. Moreover, a reference lamella outside the impact imprint was prepared for comparison between undeformed and deformed coating. The bright field as well as dark field images were taken in scanning transmission electron microscopy (STEM) mode.

Figure 4.12 shows the locations and the exemplary STEM bright field (BF) images of the cross-sectionally cut FIB lamellae from thin $(Cr_{66}Al_{34})N$ variant. The nanolaminate architecture, evident in the STEM BF images, represents Cr-rich and Al-rich alternate nanolayers. Such architecture is an expected outcome when the targets with different chemical compositions are used during the deposition process with substrate rotation. For instance, in the present case, when the sample came across the AlCr20 or AlCr30 target, an Al-rich nanolayer was deposited. Similarly, the CrAl20 targets were responsible for Cr-rich nanolayers. From left to right small bumps and waviness of these nanolayers roughly represent the boundaries between the coating columns, see red and yellow lines in Figure 4.12(b). The FIB lamellae from locations c) and d) in Figure 4.12(a) show no evidence of cross-sectional cracks in the coating, interface or substrate, see Figure 4.12(c) and (d). Moreover, the coating thickness and morphology inside the deformation zone is comparable to the reference location b). This means that the coating in the central region of the impact imprint follows the substrate to deform plastically. The surface of the FIB lamellae inside the impact imprint is flatter as compared to the reference location, see Figure 4.12(b-d). This indicates that the coating columns are largely pressed down by the counterbody as the compound deforms. Figure 4.12 (e-h) shows the STEM BF cross-sectional images from the location e) in Figure 4.12(a), where the fatigue damage in form of circumferential surface cracks is observed. The circumferential cracks observed on the surface clearly run through the coating up to the substrate. Here, the interface between CrAlN and CrAl bond layer acts as a barrier to the crack propagation. The large crack branches into two smaller thin cracks upon reaching the CrAl bond layer, see Figure 4.12(f). The crack growth stops upon reaching the substrate, see Figure 4.12(g). This is associated with the higher fracture toughness of high-speed steel as compared to the CrAlN coating. Hence, higher crack energies are required for crack growth from the coating into the substrate. The crack path inside the CrAlN is concentrated mainly along the column boundaries, see Figure 4.12(h).

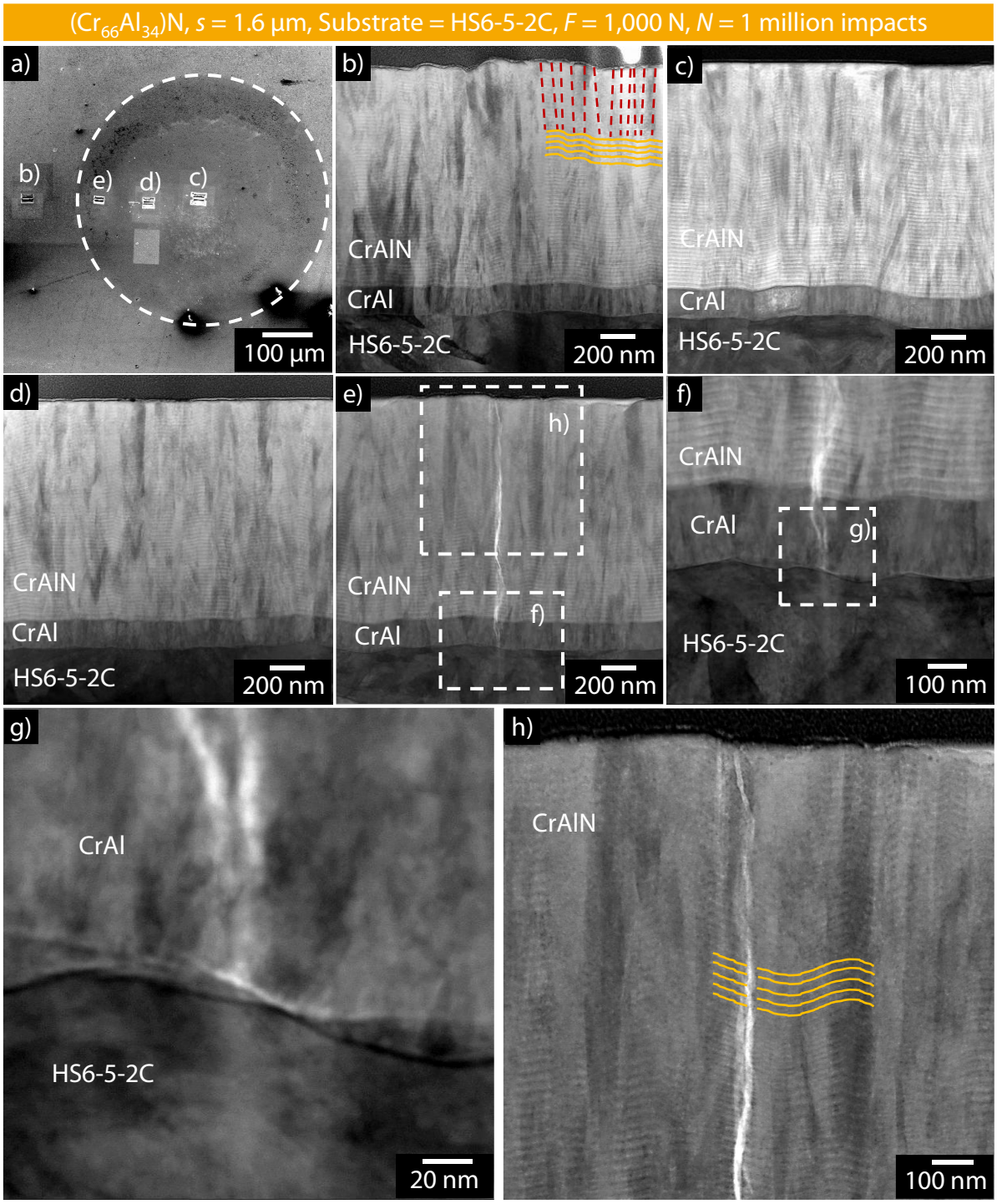

Figure 4.12: (a) SEM image of impact imprint with FIB lamellae locations and (b-h) STEM BF images of the cross-sectionally cut lamellae from compound with the thin $(Cr_{66}Al_{34})N$ coating, [BKT23]

To study the coating thickness effect on crack growth corresponding thick coating variant is analyzed. The STEM BF images for compound with thick $(Cr_{66}Al_{34})N$ are shown in Figure 4.13.

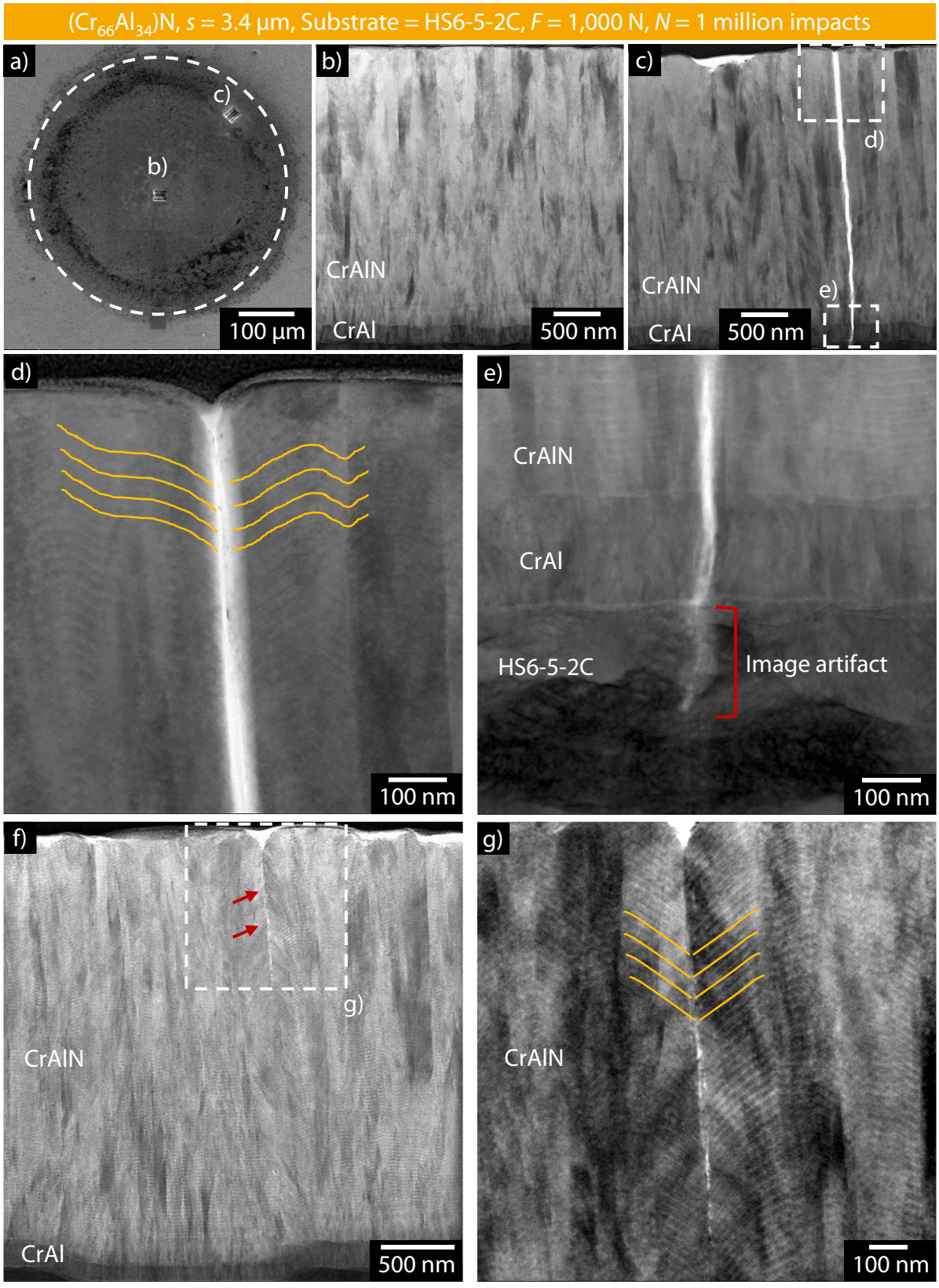

Figure 4.13: (a) Impact imprint with FIB lamellae locations and (b-g) STEM BF images of cross-sectionally cut lamellae from compound with thick $(Cr_{66}Al_{34})N$, [BKT23]

No cracks are evident in central region of the impact imprint on compound with thick $(Cr_{66}Al_{34})N$, see Figure 4.13(b). The central region of the impact imprint includes the area with maximum deformation in terms of indentation depth h_p. The thin coating variant also exhibits no cracks in this region, see Figure 4.12(c). However, at the location c) of the impact imprint in Figure 4.13(a), one large crack and an additional smaller thin crack are evident at different locations inside the analyzed FIB lamella, see Figure 4.13(c-g). The larger thick crack runs through the coating up to the substrate and does not propagate further, see Figure 4.13(c-e). The smaller thin crack propagates almost till half of the coating, see Figure 4.13(f) and (g). It is interesting to note that the waviness of nanolayers due to the column boundaries increase around the crack area near the surface, see Figure 4.13(d) and (g). However, in the interface area below, the waviness of nanolayers at column boundaries is unaffected, see Figure 4.13(e). In contrast to the thin coating, thick coating exhibits higher waviness of the nanolayers at column boundaries around the crack areas near the coating surface, see Figure 4.12(h) and Figure 4.13(d, g). Firstly, it confirms that the lengthier columnar grains of the thick coating undergo extensive inclination. This column inclination combined with shear sliding between the columnar grains lead to crack initiation and growth in the coating. Secondly, the cracks initiate near the surface, in the region with extensive columnar inclination and propagate along the columnar boundaries up to the substrate.

4.14 Discussion

Based on the observation from the FIB/TEM analysis, the deformation mechanism in correlation with damage initiation in the columnar coatings under cyclic impact loading is shown schematically in Figure 4.14. The columnar CrAlN coating follows the substrate and deforms plastically during the initial phase of cyclic impact loading. Here, the coating deformation mechanism in boundary region of the impact imprint is primarily governed by the column inclination and grain boundary shear sliding, as reported in [JLL+16] and [BBK+16] for monotonic indentation load. After the initial phase of cyclic impacts, the compound plastic deformation in terms of permanent indentation depth h_p increments slows down due to the work hardening of the steel substrate. Nonetheless, as the compound iteratively undergoes elastic-plastic deformation during the loading and elastic recovery during the unloading, the column inclination and shear sliding in the boundary region of the impact area increase. This ultimately leads to fatigue damage initiation in form of circumferential surface cracks. These cracks grow in coating cross-section over successive impact cycles and propagate mainly along

the column boundaries up to the substrate. Here, the interface between two coating layers or between the coating and the substrate acts as barrier to crack propagation. Therefore, no crack propagation into the substrate is observed in the present case.

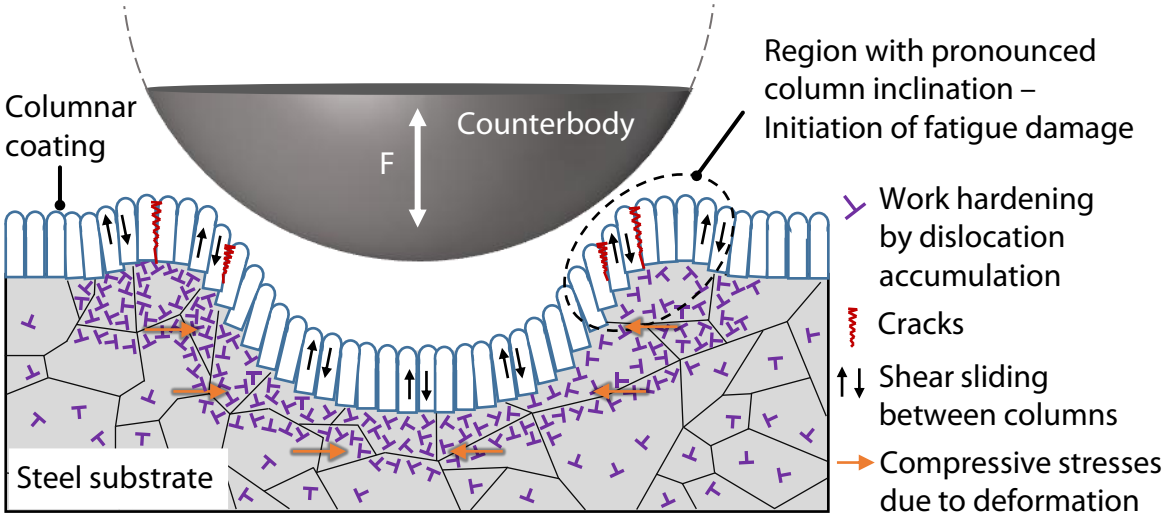

Figure 4.14: Schematic illustration of deformation mechanism in correlation with fatigue damage initiation in columnar coatings under cyclic impact loading, [BKT23]

The compressive stresses introduced by the compound deformation along with the work hardening of steel substrate increase the resistance to inclination of coating columns in the central region of the impact imprint. Here the coating columns are largely pressed down by the counterbody to deform along with the substrate. Furthermore, as per [Kre10], additional compressive stresses in the coating accumulate in central region of the imprint due to elastic recovery mismatch between coating and substrate during unloading. This superposition of compressive stresses from elastic mismatch and the plastic deformation of the compound is beneficial in preventing crack initiation in the coating. Therefore, no large cracks or smaller thin cracks in the central region of the impact imprint are observed in the present study. However, for larger indentation depths at higher impact forces or number of impacts, these compressive stresses can lead to coating spalling or delamination in central region of the impact imprint. Moreover, a too brittle deformation response of the coating, coating defects or an extensive deformation of the substrate can result in earlier initiation of cracks in the coating. Considering the present study, all investigated compounds show no surface cracks for at least $N = 0.1$ million impacts. However, as the impact cycles increase, the CrAlN coatings exhibit circumferential surface cracks at varying number of cycles. For instance, the surface cracks are

evident at N = 0.5 million impacts for thick coating compound with higher Al content coating, whereas the corresponding thin coating variant shows no cracks at same number of impacts. Here, the coating properties such as chemical composition, thickness, residual stress state as well as the elastic-plastic deformation behavior of the compound play a significant role. As the permanent indentation depth h_p of the impact imprint increases over the impact cycles, the augmented brittle fracture behavior of the thick coatings combined with extensive inclination and shear sliding of lengthier columnar grains result in reduction of the resistance of thick coatings against the fatigue damage.

4.15 Conclusions on deformation and impact fatigue behavior

As per RQ1, the cumulative effect of coating chemical composition, thickness and resulting residual stress on deformation mechanics and impact fatigue of CrAlN coated high-speed steel was investigated. Following conclusions answer RQ1 of the dissertation:

- Under monotonic indentation load, the plastic deformation of CrAlN coated high-speed steel HS6-5-2C decreases by coupling higher coating thickness and compressive residual stresses. Al addition until $x(Al) \approx 34$ at. % without change in thickness of CrAlN coating does not significantly affect the overall compound deformation but increases the elastic recovery to reduce the plastic deformation of compound.
- Under sliding indentation load, simultaneous increase in coating thickness to $s \approx 3.5$ µm and compressive residual stresses to $|\sigma_r| > 3$ GPa amplifies the brittle fracture by reducing the cohesive and adhesive damage resistance of the CrAlN coating on HS6-5-2C substrate.
- During cyclic impact loading, the plastic deformation mechanism of the CrAlN columnar coating is based on irreversible inclination of the columns in combination with shear sliding along the column boundaries. Depending on the impact force, impact cycles and the resulting compound deformation, the cracks initiate in the boundary region of the impact imprint and propagate along the column boundaries up to the substrate.
- An optimal combination of coating chemical composition, thickness and resulting compressive residual stresses increases the impact fatigue resistance of CrAlN coated high-speed steel HS6-5-2C. In the present case, the coupling of coating thickness $s \approx 1.7$ µm with $x(Al) \approx 34$ at. % leads to moderate compressive residual stresses $|\sigma_r| = (2 - 3)$ GPa in the coating. Consequentially, the compound resistance against fatigue damage under cyclic impact loading increases.

5 Fracture behavior of TiAlCrSiN coatings on cemented carbide substrates

In order to address RQ2, RQ3 and RQ5 of the dissertation, this chapter presents fundamental investigations on the deformation behavior and crack mechanics of compounds with monolayer TiAlCrSiN and bilayer TiAlCrSiN/TiAlCrSiON coatings for cemented carbide-based tooling applications. The deformation and cracking behavior of compounds with varying coating architecture and coating thickness are studied at room temperature with instrumented indentation tests. Moreover, microscratch tests are carried out to simulate the sliding indentation loading condition. The mesoscale mechanisms of coating deformation and crack growth under the indentation loading are understood using SEM and FIB/TEM analysis of scratches. A part of the presented results and findings is published in [BKT25b].

5.1 Coating deposition and characterization methods

Cemented carbide inserts SNUN 120412, with submicron grain size ISO code K20-K40, from CERATIZIT Luxembourg S.à.r.l, Mamer, Luxembourg, were used as substrate material. SEM image of grain structure of the cemented carbide substrate is shown in Appendix II. Chemical composition, physical properties and Vickers hardness of the cemented carbide substrate from the material data sheet are shown in Table 5.1.

Table 5.1: Chemical composition, physical properties and Vickers hardness of the cemented carbide (WC-Co) substrate material

Substrate material	WC-Co
Co / wt. %	9.0
Additives / wt. %	1.0
WC / -	Rest
Density ρ / g/cm^3	14.55
Transverse rupture strength *TRS* / GPa	3.65
Stress intensity factor (Shetty / Palmqvist) K_{IC} / MPa.m$^{0.5}$	10.7
Young's modulus *E* / GPa	586
Poisson's ratio *v* / -	0.21
Thermal conductivity *k* / W/m.K	74
Coefficient of thermal expansion *CTE* / 10^{-6}.K^{-1}	5.10
Vickers hardness *H* / HV30	1,590
Vickers hardness *H* / HV10	1,610

Monolayer TiAlCrSiN and bilayer TiAlCrSiN/TiAlCrSiON, each with thickness $s \approx 2.0$ µm and $s \approx 3.6$ µm, were deposited cemented carbide substrates. The designation of coating architecture is based on the number of functional layers in addition to the bond layer, see Figure 5.1. To improve the adhesion between the coating and substrate, all investigated coatings have a TiAlCrN bond layer. The monolayer variants consist of a single TiAlCrSiN top layer, whereas the bilayer coating architecture comprises of TiAlCrSiN interlayer and an oxynitride TiAlCrSiON top layer. The variants for each coating architecture with $s \approx 2.0$ µm are categorized as thin and with $s \approx 3.6$ µm as thick coatings. In total, four coating variants are investigated.

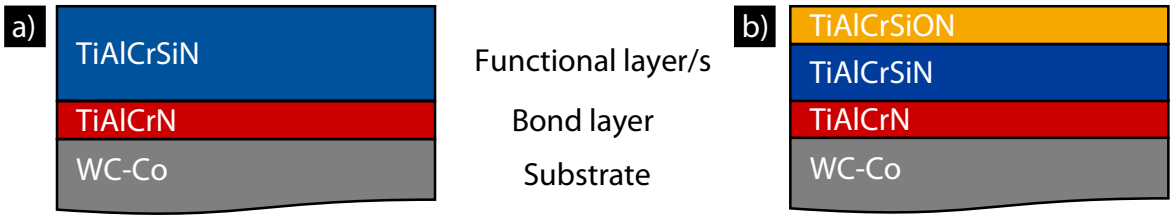

Figure 5.1: Schematic of (a) monolayer and (b) bilayer coating architectures

The process parameters and target configuration for coating deposition are shown in Table 5.2. The coatings were deposited using the same coating unit mentioned in section 4.1. The cathodes dcMS-3 and dcMS-4 were not used during the deposition process. An additional heating element was installed in the center of coating chamber to increase the process temperature. The temperature inside the coating chamber was measured by placing a K-Type thermocouple between the substrate holders and additional heating element. The coating process of monolayer TiAlCrSiN was used as the basis for bilayer architecture, which means the process parameters until the deposition of TiAlCrSiON were same for the two coating architectures, see Table 5.2. In case of the bilayer architecture, oxygen with a flowrate of $Q(O_2) = 18$ sccm was introduced after deposition of TiAlCrSiN interlayer. During the preliminary studies of the investigated coatings, it was observed that the oxygen introduction leads to poisoning of dcMS operated Si and Cr targets and reduce Si and Cr incorporation in oxynitride top layer [BKT24b]. To minimize the influence of target poisoning on Si and Cr contents of the oxynitride layer, the power of dcMS-1 and dcMS-2 cathodes was increased for deposition of TiAlCrSiON top layer. The coating times for TiAlCrSiN interlayer and TiAlCrSiON top layer were adjusted to achieve comparable overall coating thickness to monolayer TiAlCrSiN. Moreover, for variation of overall coating thickness of each coating architecture, the coating times for TiAlCrSiN and TiAlCrSiON deposition were almost doubled for thick variants as compared to corresponding

thin variants. The influence of TiAlCrN bond layer thickness on subsequent investigations was excluded by keeping a constant bond layer coating time for all investigated coatings. During the coating deposition, the substrate samples were subjected to a three-fold rotation with the table speed n_{Table} = 2.5 min^{-1}.

Table 5.2: Process parameters for monolayer TiAlCrSiN and bilayer TiAlCrSiN/TiAlCrSiON deposition with the industrial coating unit CC 800/9 HPPMS

Coating process	Monolayer	Bilayer
Sample ID /-	5067* | 5071**	5072* | 5068**
Pressure p / mPa	520	520
Argon flow $Q(Ar)$ / sccm	200	200
Nitrogen flow $Q(N_2)$ / sccm	Pressure controlled	Pressure controlled
Oxygen flow $Q(O_2)$ / sccm	-	18***
Heating power on sides P_H / kW	8	8
Heating power in centre P_H / kW	4	4
Maximum coating temperature T_{max} / °C	590	590
Substrate bias U_B / V	-80	-80
HPPMS-1 Target | Power $P_{HPPMS-1}$ / kW	TiAl48 | 7	TiAl48 | 7
HPPMS-2 Target | Power $P_{HPPMS-2}$ / kW	TiAl20 | 7	TiAl20 | 7
dcMS-1 Target | Power P_{dcMS-1} / kW	Si | 0.6	Si | 0.6 / 1.0***
dcMS-2 Target | Power P_{dcMS-2} / kW	Cr | 0.3	Cr | 0.3 / 0.7***
Pulse frequency f_{pulse} / Hz	2,000	2,000
Pulse duration t_{on} / µs	60	60
Coating time TiAlCrN bond layer $t_{TiAlCrN}$ / min	90	90
Coating time TiAlCrSiN $t_{TiAlCrSiN}$ / min	138* & 266**	90* & 180**
Coating time TiAlCrSiON $t_{TiAlCrSiON}$ / min	-	45* & 75**

*Thin coating | **Thick coating | ***For deposition of TiAlCrSiON

For determination of coating thickness, morphology, average area roughness *Sa*, chemical composition and phase composition, same experimental methods and instruments mentioned in section 0 were used. In addition to XRD measurements, the phase composition of coatings was analyzed with selected area electron diffraction (SAED) patterns recorded by TEM using FEI Tecnai G^2 F20 S-TWIN, Thermo Fischer Scientific, Eindhoven, Netherlands. An aperture

with a diameter of $D \approx 100$ nm was used for this purpose. For SAED analysis, cross-sectional lamellae were prepared from selected samples with focused ion beam (FIB) using PFIB Helios 5, Thermo Fischer Scientific, Eindhoven, Netherlands. FIB preparations and SAED analysis were carried out at GFE, RWTH Aachen University. The adhesion strength class *HF* of the coatings with the substrate was determined with Rockwell C indentation test according to DIN 4856 using HP100 Rockwell tester, KNUTH Machine Tools GmbH, Wasbek, Germany. For this purpose, a Rockwell shaped diamond tip with a cone angle of $\alpha = 120°$ was used to indent the surface with normal force $F \approx 588.4$ N.

5.2 Instrumented indentation testing of coatings and compounds

For monotonic indentation loading condition, instrumented indentation tests were carried out in nano- and micro-range using TriboIndenter TI 950, Bruker Corporation, Billerica, Massachusetts, USA. The elastic-plastic deformation behavior of the coatings was studied with nanoindentation. To minimize the influence of surface roughness on measurements, the samples were polished for $t \approx 3$ s using a rotating steel ball and diamond suspension resulting in a circular imprint on the surface with an average area roughness $Sa < 0.02$ µm. For each coating variant, 50 measurements with indentation force $F = 8$ mN were carried out inside the circular imprint. For this purpose, a diamond indenter tip with Berkovich geometry and nominal radius $r \approx 150$ nm was used. The sharp Berkovich tips with indentation forces in nano-range induce shallow deformation zones largely concentrated in the coating. This allows for characterization of elastic-plastic deformation behavior of thin coatings with minimum substrate influence. The indentation hardness H_{IT} and indentation modulus E_{IT} were calculated from the measurement data as per the method by Oliver and Pharr [OP92]. As commonly known for ceramic coatings, Poisson's ratio $\nu = 0.25$ was used for calculations.

For investigation of compound deformation and cracking behavior, instrumented indentation tests in micro-range with $F = 750$ mN, $F = 1{,}000$ mN, $F = 1{,}250$ mN and $F = 1{,}500$ mN were carried out. The indentation force range was selected on two criteria. Firstly, to characterize the deformation behavior of all investigated samples from relatively low to high indentation loading conditions. Secondly, to have an extended measurement dataset for identifying differences in surface cracking behavior of the samples. To exclusively study the deformation response of cemented carbide, indentations tests on uncoated substrate were carried out as reference. For each indentation force and sample variant combination, 5 measurements with conical diamond

indenter tip, nominal cone angle $\alpha = 60°$ and nominal radius $r = 10$ µm, were performed. The micro-range indentations with conical tips induce deeper spherical shaped deformation zones suitable to study the combined deformation response of coating and substrate. The force function consisted of loading segment with $t_{loading} = 10$ s, hold period with $t_{hold} = 3$ s and unloading segment with $t_{unloading} = 10$ s. The measurement data in form of force-indentation depth curves at varying F and sample variant combinations was analyzed to characterize the elastic-plastic compound deformation behavior. The characterization of deformation behavior with instrumented indentation tests is discussed in section 2.5.3. To investigate the surface cracking behavior, the indent imprints were analyzed with SEM, Zeiss DSM 982 Gemini, Carl Zeiss AG, Oberkochen, Germany, at GFE, RWTH Aachen University.

5.3 Microscratch tests

In order to study the cracking behavior under sliding indentation load, microscratch tests on uncoated cemented carbide and coated compounds were carried out, see Figure 5.2. For this purpose, a conical shaped diamond indenter with nominal cone angle $\alpha = 60°$ and nominal radius $r = 10$ µm was installed on Nanoindenter UNAT, ASMEC GmbH, Dresden, Germany. Microscratch tests were performed with normal force $F = 300$ mN, $F = 500$ mN and $F = 1{,}000$ mN and sliding velocity $v_s = 10$ µm/s. For each sample variant and normal force, three microscratches were carried out. The deformation behavior of the samples was characterized by measuring permanent scratch depth $h_{p,s}$ and scratch depth profiles with CLSM as well as by analyzing fracture cross-sections of scratch tracks with SEM. Moreover, the scratch tracks were examined for surface cracks using SEM.

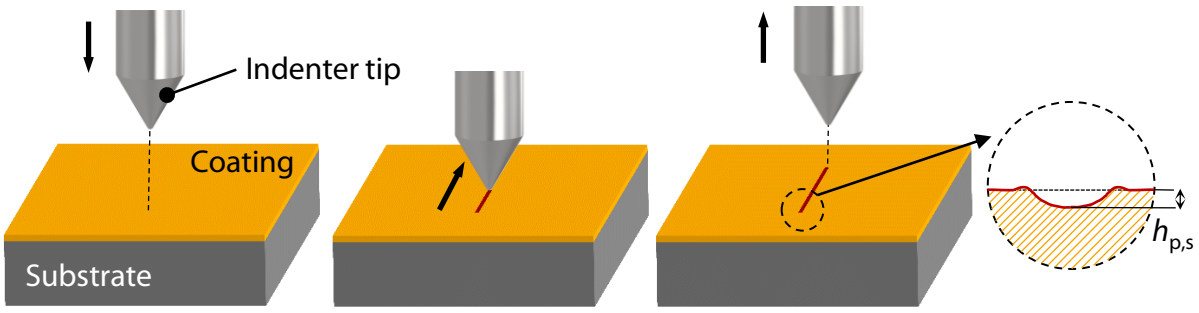

Figure 5.2: Schematic of microscratch test along with depth profile of the scratch

For studying coating deformation mechanism in correlation with crack growth in compounds, selected microscratches were analyzed in cross-section using a combination of FIB and TEM.

PFIB Helios 5, Thermo Fischer Scientific, Eindhoven, Netherlands, was used for FIB lamellae preparation, whereas FEI Tecnai G² F20 S-TWIN, Thermo Fischer Scientific, Eindhoven, Netherlands, was used for TEM analysis. The FIB preparations, SEM and TEM investigations were carried out at GFE, RWTH Aachen University.

5.4 Characterization of monolayer TiAlCrSiN and bilayer TiAlCrSiN/TiAlCrSiON

Coating thickness, chemical composition of the top layer, average area roughness *Sa* and adhesion strength class *HF* of the thin as well as thick coating variants are shown in Table 5.3. The chemical composition of the coatings was measured by the EPMA method.

Table 5.3: Coating thickness *s*, average area roughness *Sa*, chemical composition and adhesion strength class *HF* of investigated monolayer TiAlCrSiN and bilayer TiAlCrSiN/TiAlCrSiON thin as well as thick variants

Coating designation	Monolayer-Thin	Bilayer-Thin	Monolayer-Thick	Bilayer-Thick
s / µm	1.9	2.0	3.4	3.6
Sa / µm	0.05	0.05	0.1	0.08
Ti / at.%	17	15	17	15
Al / at.%	26	21	26	21
Cr / at. %	2	3	2	3
Si / at. %	2	3	2	3
O / at. %	< 0.5	22	< 0.5	22
N / at. %	53	36	53	36
HF / -	1	1	1	1

For bilayer architecture, the chemical composition of the TiAlCrSiN interlayer is similar to the monolayer TiAlCrSiN. For TiAlCrSiON top layer, incorporation of oxygen mainly comes at the expense of nitrogen along with minor contributions from Ti and Al. As compared to the TiAlCrSiN, non-metallic content in terms of atomic percentage contributions of N and O increases for the oxynitride TiAlCrSiON top layer. This change in chemical composition has two underlying reasons. Firstly, the pressure $p = 520$ mPa during the deposition was held constant by controlling the nitrogen flow, see Table 5.2. With the introduction of oxygen, the nitrogen flow was reduced by the pressure controller to maintain the predefined pressure in the chamber. Hence, the nitrogen availability for the coating deposition decreased. Secondly, as previously observed in [BKC+22] for CrAlON and TiAlON, oxygen as reactive gas increases

the non-metal/metal ratios in the hybrid dcMS/HPPMS plasma during the deposition. This can reduce the incorporation of elements such as Ti and Al and increase the non-metallic content of the coating.

Fracture cross-sections of the coatings are shown in Figure 5.3. All coatings exhibit similar cauliflower like morphology resulting from large clusters of fine vertical columns. The thick coatings comprise of lengthier columns as compared to their thin variants. The thickness of TiAlCrN bond layer for all variants is $s_{TiAlCrN} \approx 0.5$ µm. The thickness of TiAlCrSiON top layer, calculated based on coating time, is $s_{TiAlCrSiON} \approx 0.5$ µm for the thin bilayer variant and $s_{TiAlCrSiON} \approx 1.0$ µm for the thick bilayer variant. These calculated thicknesses of individual layers are also confirmed by FIB/TEM analysis in later investigations.

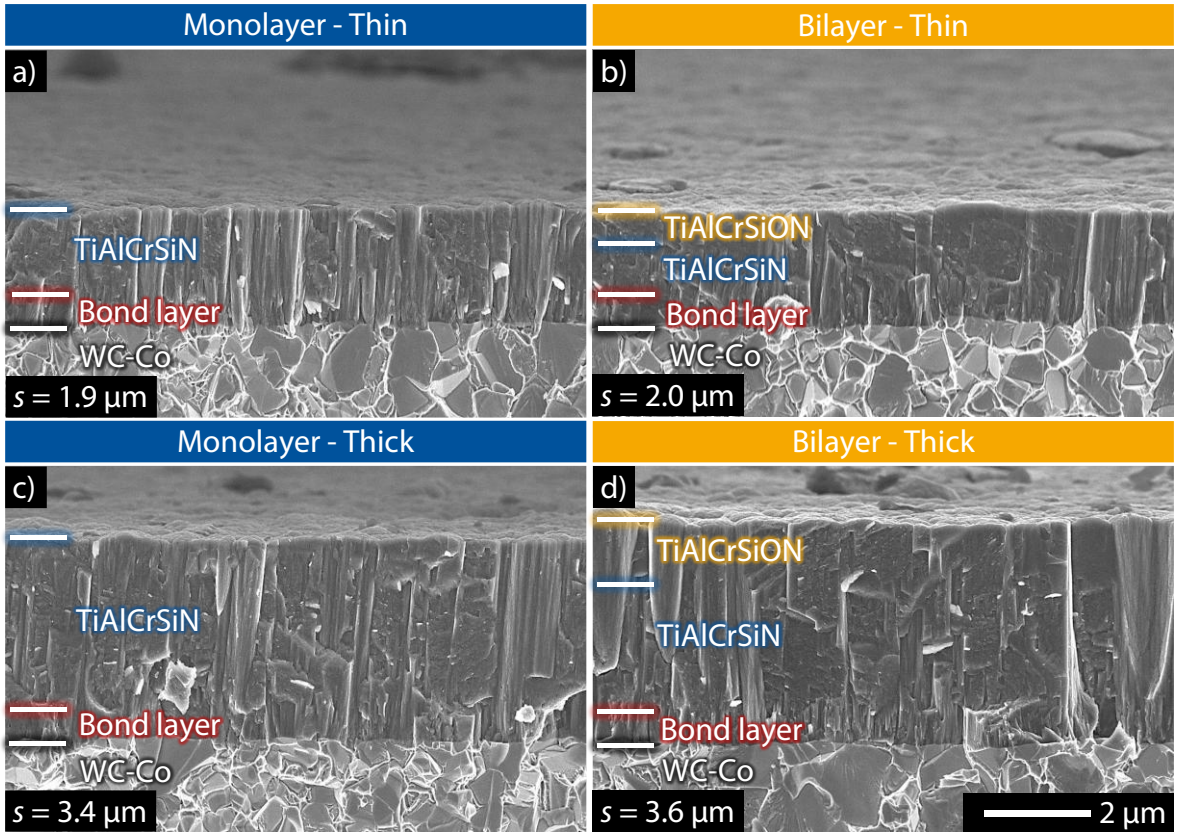

Figure 5.3: Morphology of the (a,c) monolayer and (b,d) bilayer variants, [BKT25b]

5.5 Phase composition

The phase composition of the coatings determined with XRD is shown in Figure 5.4. The (111), (200) and (220) diffraction peaks are assigned to the cubic TiN, CrN and AlN phases. Additionally, diffraction peaks belonging to cemented carbide substrate are observed. The

diffraction peaks for (311) and (222) orientations overlap with the substrate peaks and are too weak to be distinguished. For all four coatings, the highest peak intensity, without any substrate overlap, is observed for the (200) orientation. Minor differences in the diffraction patterns are observed between the investigated variants. For instance, the peak intensities for the (111) orientation slightly reduce for bilayer coatings as compared to the monolayer variants. A similar trend is reported in [BKG+21] for TiAlON, in [BKM+25] for CrAlON and in [BBK+21] for TiAlCrSiON coatings. With the increase in coating thickness, the peak intensities for the (111) and the (220) orientations slightly increase. This is presumably related to change in residual stress state of the coatings with higher thickness. Moreover, no peaks belonging to silicon containing cubic phases are observed. This indicates that silicon preferably forms amorphous phases with nitrogen and oxygen for the considered coatings.

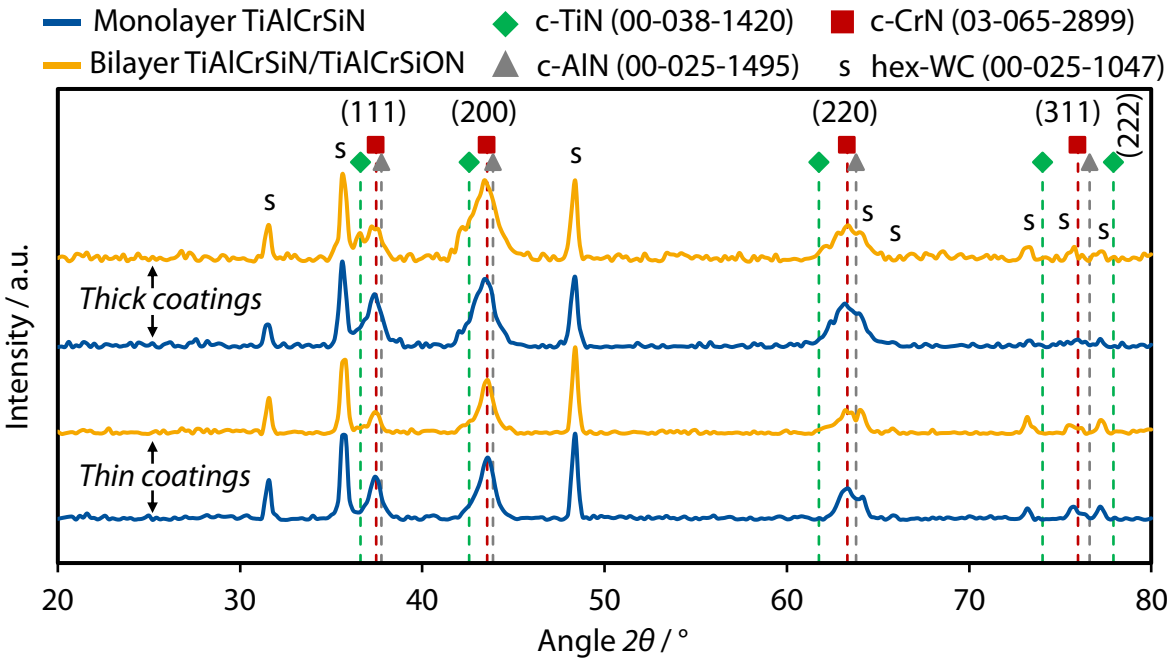

Figure 5.4: Phase composition and orientation of monolayer and bilayer coatings

Additionally, the phase composition of individual TiAlCrN, TiAlCrSiN and TiAlCrSiON layers is studied with the SAED analysis on cross-sectionally cut FIB lamellae from the coated variants, see Figure 5.5. For SAED analysis, an electron beam with TEM is directed onto the sample to produce diffraction patterns reflecting the atomic arrangement within the analyzed area. The SAED patterns contain array of bright spots for single crystals, resulting from constructive interference of diffracted electrons. Due to multiple overlapping diffractions from randomly

oriented grains, the SAED patterns for polycrystalline materials display a mix of concentric rings and spots, whereas, broad, diffusion rings or halos characterize the amorphous materials.

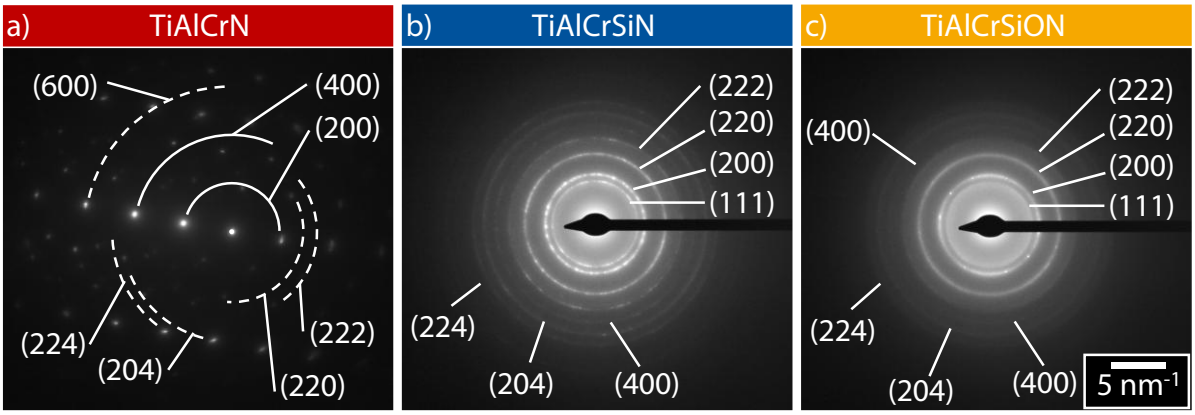

Figure 5.5: SAED patterns of (a) TiAlCrN, (b) TiAlCrSiN and (c) TiAlCrSiON

In present case, the TiAlCrN bond layer shows a polycrystalline structure with strong indications for the (200) and (400) orientations, see Figure 5.5(a). The SAED patterns for the TiAlCrSiN and the TiAlCrSiON display a mix of polycrystalline and amorphous phases, which confirm the nanocomposite structure consisting of (Ti,Al,Cr)N cubic crystals embedded in amorphous Si-matrix, see Figure 5.5(b,c). Since the used aperture has a diameter of $D \approx 100$ nm, a grain size of a few nanometers is inferred for the (Ti,Al,Cr)N crystals. Moreover, compared to TiAlCrSiN, the sharpness of rings reduces and the halo pattern increases for the TiAlCrSiON. This indicates an increase in amorphous content with oxygen addition. As discussed in [Car23], the oxygen incorporation in TiAlCrSiN promotes formation of amorphous oxides around the grain and column boundaries. The additional orientations for cubic (Ti,Al,Cr)N crystals in SAED patterns are not noticed in XRD analysis because of the diffraction angle limitation to $2\theta \leq 80°$. The influence of the discussed changes in the phase composition from the poly-crystalline TiAlCrN bond layer to the nanocomposite TiAlCrSiN as well as higher amorphous content of TiAlCrSiON on the deformation behavior or crack growth in the coatings is studied in subsequent investigations.

5.6 Deformation behavior of coatings

The indentation hardness H_{IT} and indentation modulus E_{IT} of the coatings measured by nanoindentation is shown in Figure 5.6. In terms of coating thickness, the thin coatings exhibit similar H_{IT} to their corresponding thick variants. The monolayer variants show higher

average H_{IT} compared to the bilayer variants, see Figure 5.6(a). As discussed in section 5.5, the incorporation of oxygen increases the amorphous content in the coating and thereby decreases the indentation hardness H_{IT}.

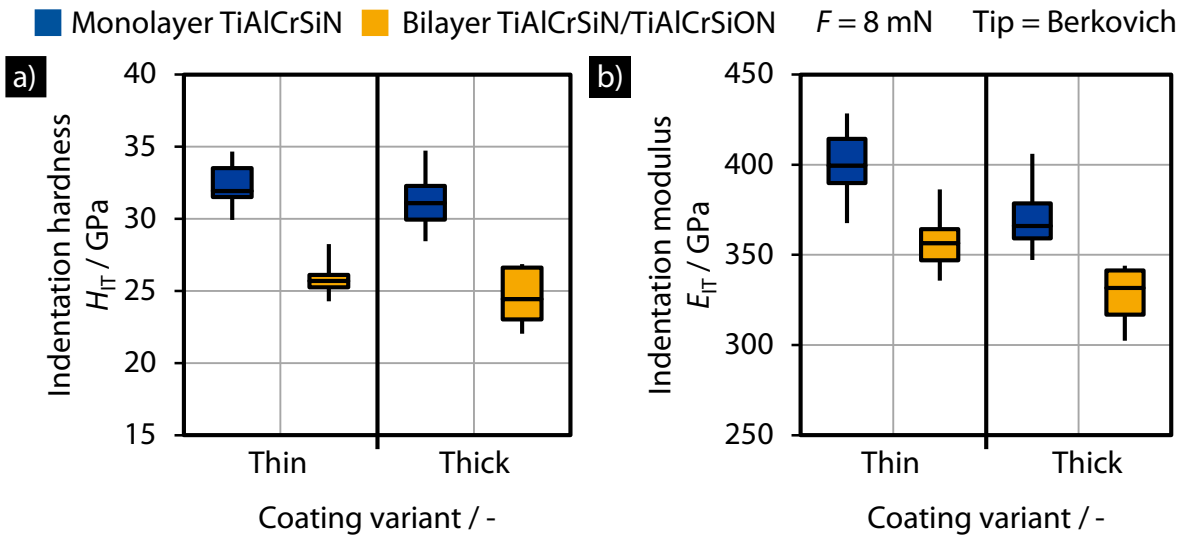

Figure 5.6: (a) Indentation hardness H_{IT} and (b) indentation modulus E_{IT} of the monolayer and bilayer variants measured by nanoindentation

Analogous to H_{IT}, the monolayer variants exhibit higher indentation modulus E_{IT} compared to the bilayer variants. In terms of coating thickness, the thin coatings exhibit slightly higher E_{IT} compared to their corresponding thick variants, see Figure 5.6(b). Increasing the coating thickness changes the macroscopic compressive residual stresses in the coating. However, this does not translate to the deformation behavior of the coating under nanoindentation due to the small deformation zone, as discussed in section 4.10. However, the effect of microstructural changes with the oxygen addition in bilayer variants are captured by nanoindentation in the present case. To characterize the elastic-plastic deformation behavior of the coatings, Figure 5.7 shows average force-indentation depth curves and plastic work percentage η_{plast}. The monolayer variants exhibit reduced plastic deformation as compared to the corresponding bilayer variants, as evident from the lower h_{max}, h_p and η_{plast}. The increase in coating thickness does not significantly affect the h_{max}, h_p and η_{plast}. However, the minor differences accumulate during the calculation of indentation modulus E_{IT}. The E_{IT} depends on the slope of the unloading segment of force-indentation depth curve. Nonetheless, the coating thickness related differences in E_{IT} remain for monolayer as well as bilayer variants $\Delta E_{IT} < 10$ %. These observations show that the nanoindentation measurements can track the effect of microstructural changes but are not

sufficient to characterize the coating thickness effect on elastic-plastic deformation behavior of the coatings or compounds. Hence, indentations in micro-range are required to study the coating thickness effect on compound deformation mechanics.

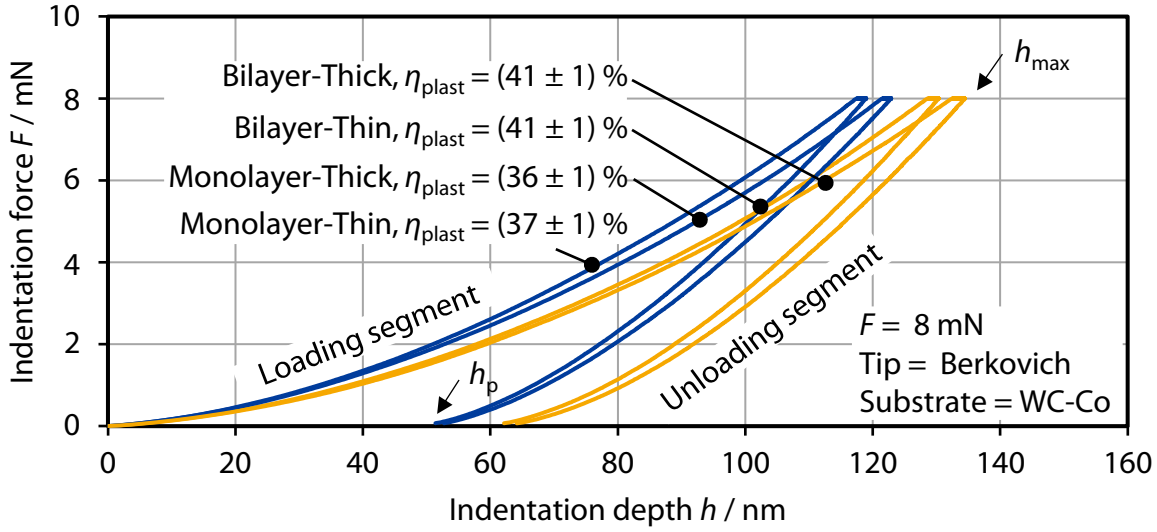

Figure 5.7: Average force-indentation depth curves of monolayer and bilayer variants from nanoindentation measurements with F = 8 mN

5.7 Deformation behavior and surface cracks under monotonic indentation load

Deformation behavior and surface crack analysis of the uncoated cemented carbide as well as coated compounds under monotonic indentation load are summarized in Figure 5.8. The average maximum indentation depth h_{max} corresponding to the maximum indentation force F before unloading is represented as sum of h_p and h_e, see Figure 5.8(a). Permanent indentation depth h_p denotes the remaining depth of the indent after unloading, whereas h_e characterizes the recovered indentation depth as difference in h_{max} and h_p. Figure 5.8(b) displays the average total mechanical work W_t during indentation as well as percentual contributions η_{plast} and η_{elast} from the plastic work W_{plast} and elastic reverse deformation work W_{elast} to the W_t. It is pertinent to mention that the work percentages η_{plast} and η_{elast} as well as W_t are calculated from the measured force-indentation depth curves during indentation. Any contributions from crack initiation and propagation in material to the total energy dissipation during indentation is not considered. Moreover, all the average values in Figure 5.8 have a standard deviation $SD \leq 5$ %. No significant pop-in events were observed in the individual force-indentation depth curves of all sample variants for the considered combination of indenter tip geometry and indentation force range.

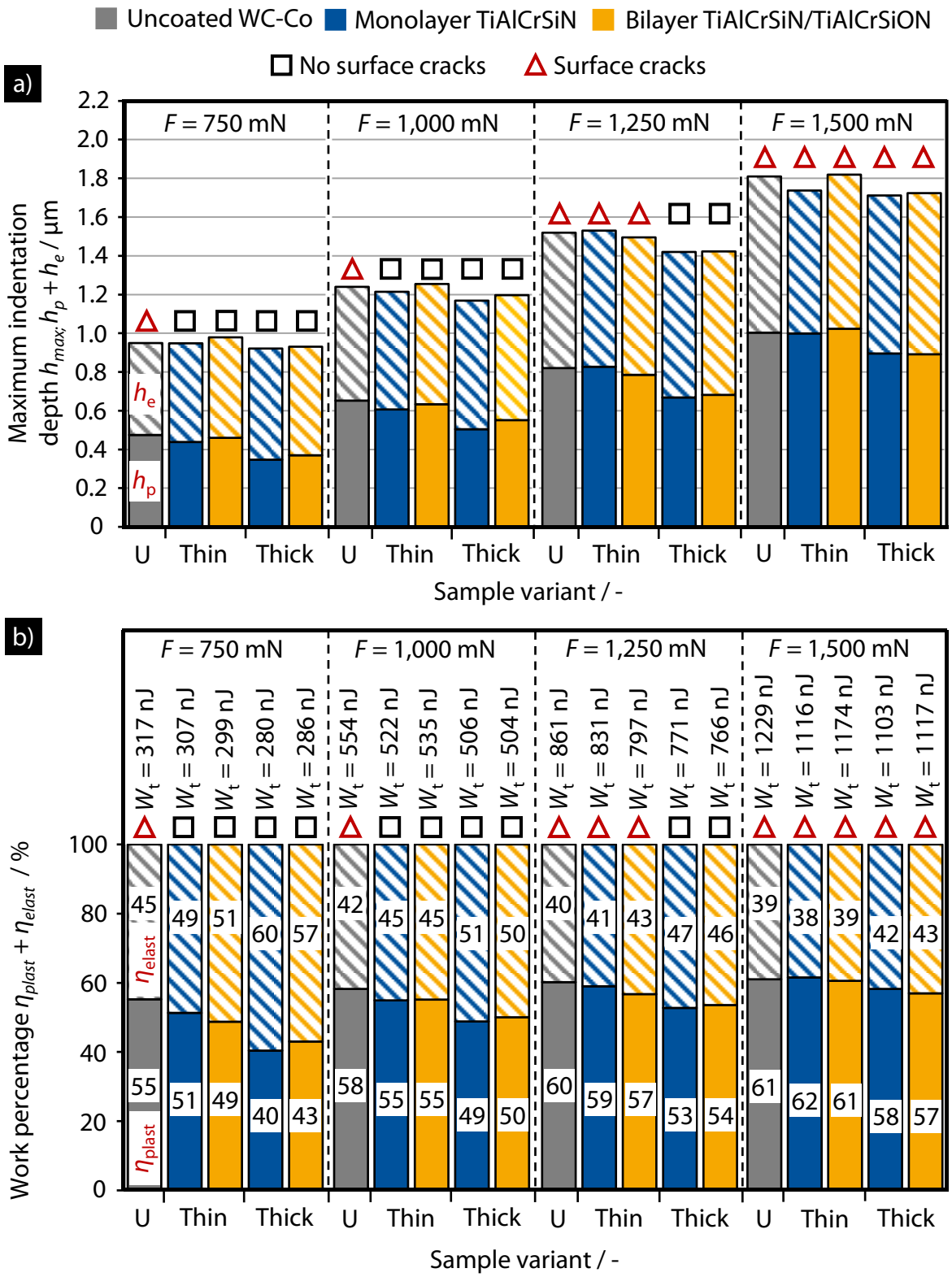

Figure 5.8: (a) Maximum indentation depth h_{max}, (b) total indentation work W_t, plastic work percentage η_{plast} and elastic work percentage η_{elast} of uncoated cemented carbides and coated compounds at varying indentation forces

As apparent from the results, the coated compounds exhibit higher resistance against surface cracks as compared to the uncoated cemented carbide. This is because of the higher load bearing capacity of compounds due to the nitride hard coatings having compressive residual stresses, as indirectly characterized by h_p, h_e, W_t, η_{plast}, η_{elast} and surface crack analysis. As compared to the uncoated cemented carbide, the thin coating compounds show lower total mechanical work W_t, plastic work percentage η_{plast} and higher elastic recovery in terms of η_{elast} for $F < 1{,}000$ mN. The thick coating compounds exhibit significant reduction in h_p, W_t, η_{plast} and higher η_{elast} compared to the uncoated cemented carbide for $F < 1{,}500$ mN. Moreover, the higher load bearing capacity of compounds can be understood in terms of total energy consumption by elastic-plastic deformation, characterized as W_t, before appearance of surface cracks. In present case, the uncoated cemented carbide display surface cracks from $W_t \approx 317$ nJ, while the coated compounds display much higher energy consumption in terms of W_t before initiation of surface cracks, see Figure 5.8(b). As the indentation force increases from $F = 750$ mN to $F = 1{,}500$ mN, the differences in h_p, h_e, η_{plast} and η_{elast} between the uncoated substrate and coated variants decrease. This is because of the substrate influence on the overall deformation response of the coated compound. Here, the coating thickness is a significant factor in reducing the substrate influence on the compound deformation response. Starting at $F = 750$ mN, the compounds with thin coatings show an absolute difference of $|\Delta\eta| = (4 - 6)$ % in η_{plast} and η_{elast} compared to the uncoated substrate. This difference more than doubles to $|\Delta\eta| = (12 - 15)$ % as the coating thickness increases. A similar trend in terms of permanent indentation depth h_p is apparent, see Figure 5.8(a). At $F = 750$ mN, the difference of $|\Delta h_p| = (15 - 40)$ nm for compounds with thin coatings and $|\Delta h_p| = (100 - 130)$ nm for compounds with thick coatings as compared to the uncoated substrate is observed.

For considered indentation force range, the compounds with thick coatings consistently exhibit lower h_{max}, h_p, W_t, η_{plast} and η_{elast} as compared to the corresponding thin coating compounds and uncoated substrate, see Figure 5.8. Hence, increasing the coating thickness decreases the plastic deformation of coated compounds. This translates into surface cracking behavior as the thick coating variants exhibit higher resistance against surface cracks and consequently higher load bearing capacity compared to thin coating compounds. This change in compound deformation behavior is attributed to the expected higher macroscopic compressive residual stresses of the thick coatings. Accordingly, thick coatings can distribute the applied load more effectively to reduce the stress concentration in the cemented carbide substrate as well as reduce overall

compound deformation as compared to thin coatings. In terms of coating architecture, the monolayer and bilayer variants show almost negligible differences in deformation behavior and similar surface crack resistance for the considered indentation loads, see Figure 5.8. This is attributed to the additional interface in bilayer variants, which allow for comparable plastic deformation and surface crack resistance to the monolayer variants during indentation. Considering the difference in the indentation hardness H_{IT} of the monolayer and bilayer variants, these results show the promising potential of the bilayer TiAlCrSiN/TiAlCrSiON in terms of compound deformation and cracking behavior. A combination of nitride interlayer with oxynitride top layer reduces the adhesion tendency of the steel workpiece to the tool in tribological contacts [BKT+25a]. At the same time, plastic deformation and surface crack resistance can be maintained comparable to the monolayer nitride hard coating despite the addition of relatively lower hardness oxynitride layer.

In the present study, the plastic work percentage η_{plast} correlates with the resistance of coated compounds against surface cracks under the monotonic indentation load. Irrespective of the coating thickness and indentation force, no surface cracks are observed for coated variants with $\eta_{plast} \leq$ ~55 %, see Figure 5.8(b). Hence, the plastic work percentage η_{plast}, calculated from the indentation test data, can be helpful in studying the surface crack resistance of the compounds under indentation loadings. In terms of energy absorption, a W_t range for initiation of surface cracks is identified. For present case, the thin coating compounds first exhibit surface cracks within $W_t \approx$ (550 – 800) nJ, whereas for compounds with the thick coatings the range is $W_t \approx$ (800 – 1,100) nJ, see Figure 5.8(b).

Another indentation test data-based parameter which correlates with the surface crack resistance of compounds is the percentual contribution of permanent indentation depth h_p to the maximum indentation depth h_{max}, represented as η_{hp} in Equation 5.1.

$$\eta_{hp} = (h_{plast} / h_{max}) \text{ x } 100\ \% \quad , \quad \eta_{he} = (h_{elast} / h_{max}) \text{ x } 100\ \% \qquad \text{Equation 5.1}$$

Figure 5.9 displays average percentual contributions η_{hp} and η_{he} from permanent indentation depth h_p and recovered indentation depth h_e, respectively, to the h_{max}. Here, $\eta_{hp} \leq$ ~51 % is the plastic deformation limit of the compounds, expressed in terms of indentation depth, for resistance against surface cracks. Alternatively, the surface crack resistance can be correlated

with elastic recovery of the coated compounds, characterized by η_{elast} and η_{he}. Irrespective of the coating thickness and indentation force, no surface cracks are observed for indents on coated variants with $\eta_{elast} \geq$ ~45 % or $\eta_{he} \geq$ ~49 %, see Figure 5.8(b) and Figure 5.9, respectively. As higher coating thickness increases the load bearing capacity of the compounds, the η_{plast}, η_{hp} and η_{elast}, η_{he} limits for surface crack resistance are reached at $F = 1{,}500$ mN for thick coating compounds as compared to $F = 1{,}250$ mN for the thin coating variants. Hence, the indentation data-based parameters η_{plast}, η_{elast}, η_{hp} and η_{he} are helpful in comparing the crack resistance of compounds with different coating systems. The limits of these parameters for surface crack resistance from current study will vary for other coating and substrate material combinations or indenter geometries.

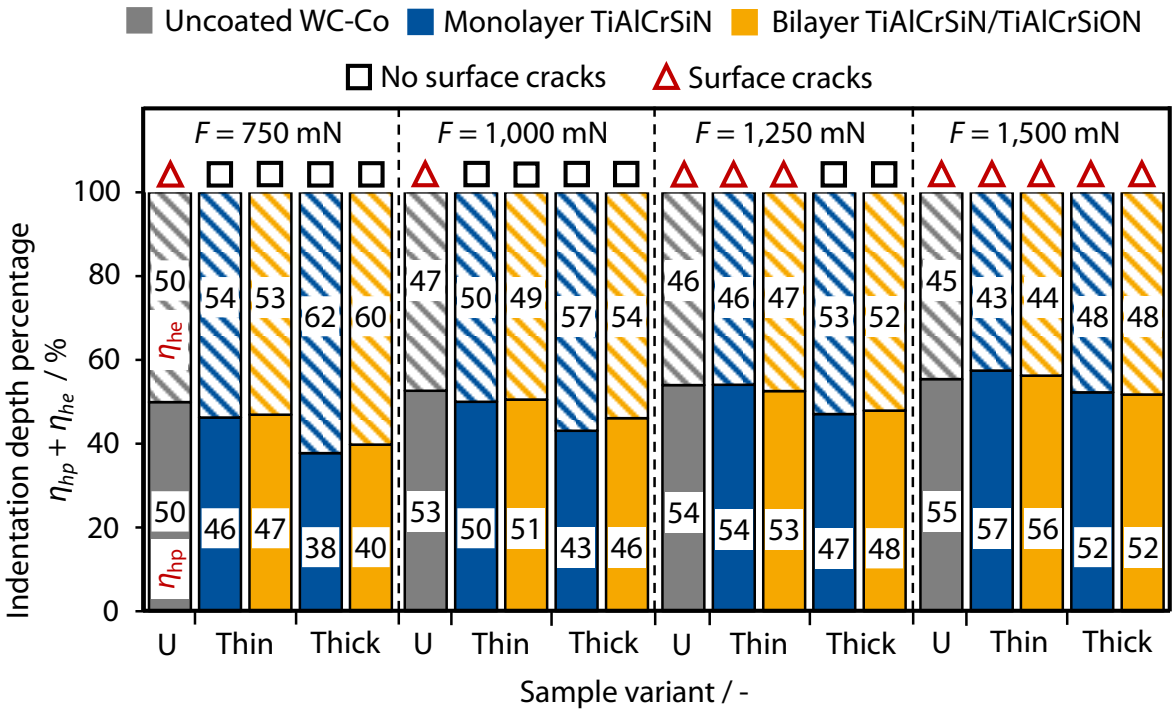

Figure 5.9: Percentual contributions η_{hp} and η_{he} from h_p and h_e to h_{max}, respectively, for uncoated cemented carbide and coated compounds at varying indentation forces

The exemplary indent imprints along with the surface crack areas for uncoated substrate as well as the compounds with thin and thick monolayer TiAlCrSiN at $F = 1{,}500$ mN are shown in Figure 5.10. A comparable trend in terms of surface cracks, when present, was observed for other combinations of indentation forces and sample variants.

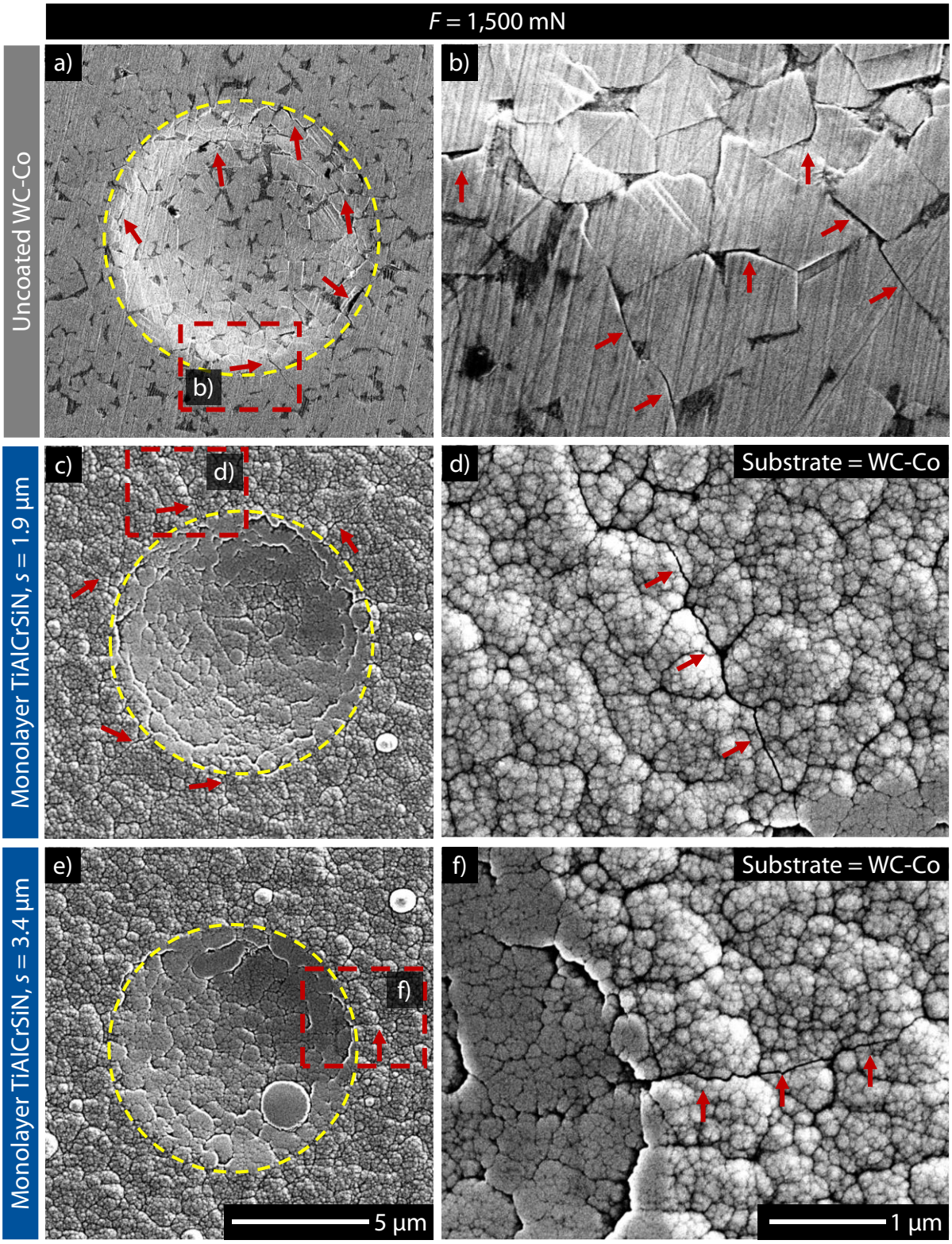

Figure 5.10: Indent imprints with enlarged surface crack areas for (a,b) uncoated cemented carbide, (c,d) compound with thin monolayer TiAlCrSiN and (e,f) compound with thick monolayer TiAlCrSiN at F = 1,500 mN

In Figure 5.10(a), (c) and (e), the yellow circles mark the indent imprint area, whereas red arrows point out the surface crack locations. The scratches on the surface of uncoated substrate are from sample preparation as the substrates were polished before coating. The indentation tests on uncoated cemented carbide were carried out in initial substrate condition before coating. For uncoated substrate, the surface cracks are present inside and in the boundary region of the indent imprint. The boundary region of the indent contains circumferential as well as radial surface cracks, see Figure 5.10(b). For coated compounds, the large surface cracks are limited to boundary region of the indents. Moreover, only radial surface cracks, proceeding outward from the boundary region, are observed, see Figure 5.10(d) and (f). The crack paths are mostly limited along the boundaries of large column clusters or through the clusters along the boundaries of individual fine columns, see Figure 5.10(d) and (f). The increase in coating thickness reduces the indent imprint area, number and length of radial surface cracks in coated compounds, see Figure 5.10(c-f). This further reiterates the increase in surface crack resistance with higher coating thickness, as explained during the characterization of compound deformation behavior with indentation data. The compounds exhibit higher radial crack lengths as compared to the uncoated substrate. Moreover, no large surface cracks are present inside the indent imprints on coated variants. The coating column clusters are pushed down and pressed against each other inside the indent area. The circumferential patterns inside the indent area arise from the height differences and rearrangement of pressed column boundaries on the semicircular depth profile of the indent. The additional compressive stresses due to the deformation under indentation loading prevent initiation of large surface cracks inside the indent imprint area. As the current investigation is focused on large surface cracks, the presence of smaller cross-sectional coating cracks, resulting from column pressing inside the indent area, is not ruled out. The coating deformation and crack propagation mechanisms along with the temperature dependent deformation mechanics of compounds under monotonic indentation loading are investigated in the next chapter of this dissertation.

5.8 Deformation and fracture behavior under sliding indentation load

Figure 5.11 summarizes the results from microscratch tests on uncoated cemented carbide substrate and coated compounds at normal forces F = 300 mN, F = 500 mN and F = 1,000 mN. The deformation behavior is characterized by measurement of permanent scratch depth $h_{p.s}$ with CLSM and surface crack analysis of the scratch tracks with SEM.

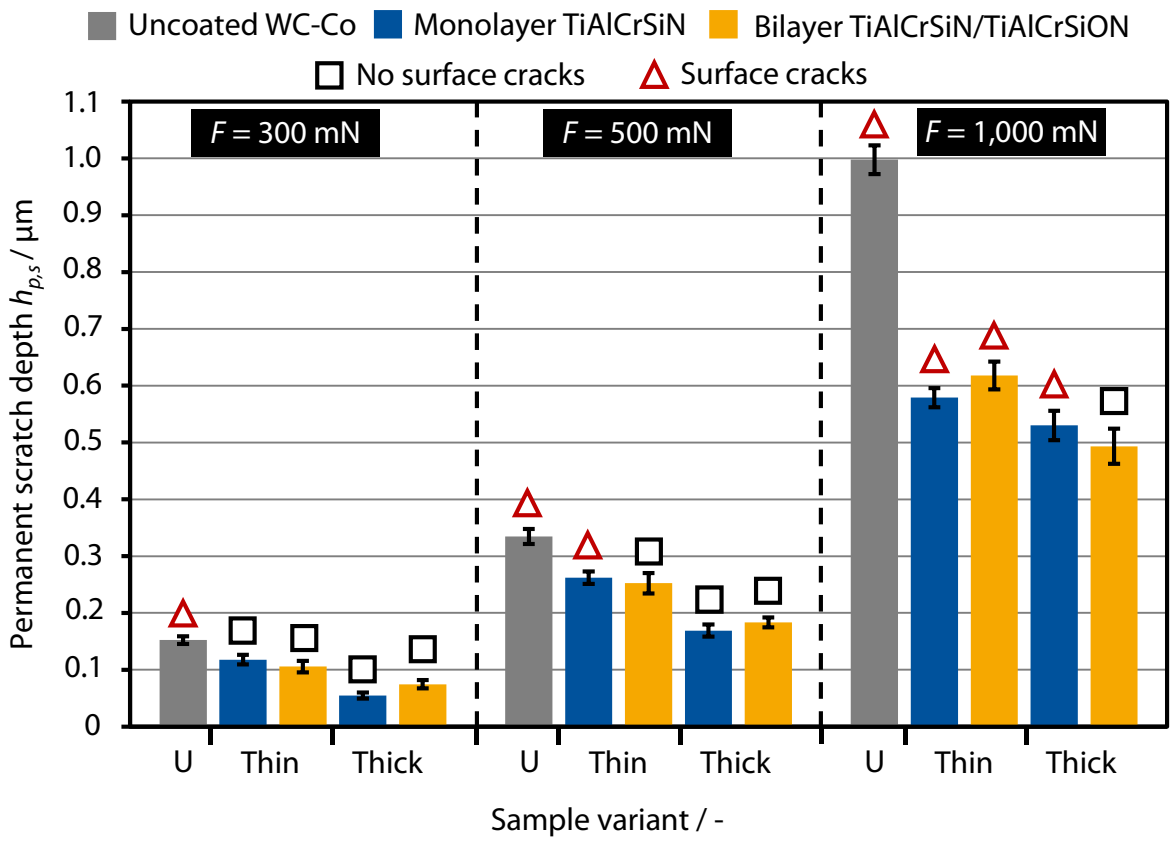

Figure 5.11: Permanent scratch depth $h_{p,s}$ and surface crack analysis of uncoated cemented carbide and coated compounds from microscratch tests, [BKT25b]

As compared to the uncoated substrate, the coated variants exhibit lower average permanent scratch depth $h_{p,s}$ and higher resistance against surface cracks. Among the coated variants, the higher coating thickness positively influences the plastic deformation resistance and load bearing capacity of the compound, as observed for monotonic indentation loading. Hence, compounds with thick coatings show lower permanent scratch depth $\Delta h_{p,s}$ = (100 ± 20) nm as well as higher surface crack resistance compared to the corresponding thin coating variants. In contrast to monotonic indentation loading, the bilayer architecture contributes to higher surface crack resistance of the compound under sliding indentation load. The thin and thick bilayer variants exhibit higher resistance against surface cracks compared to the corresponding monolayer variants at F = 500 mN and F = 1,000 mN, respectively.

To understand the deformation behavior of coating-substrate combination under sliding indentation load, Figure 5.12 exemplarily shows the fracture cross-sections and representative residual depth profiles of microscratches at F = 1,000 mN.

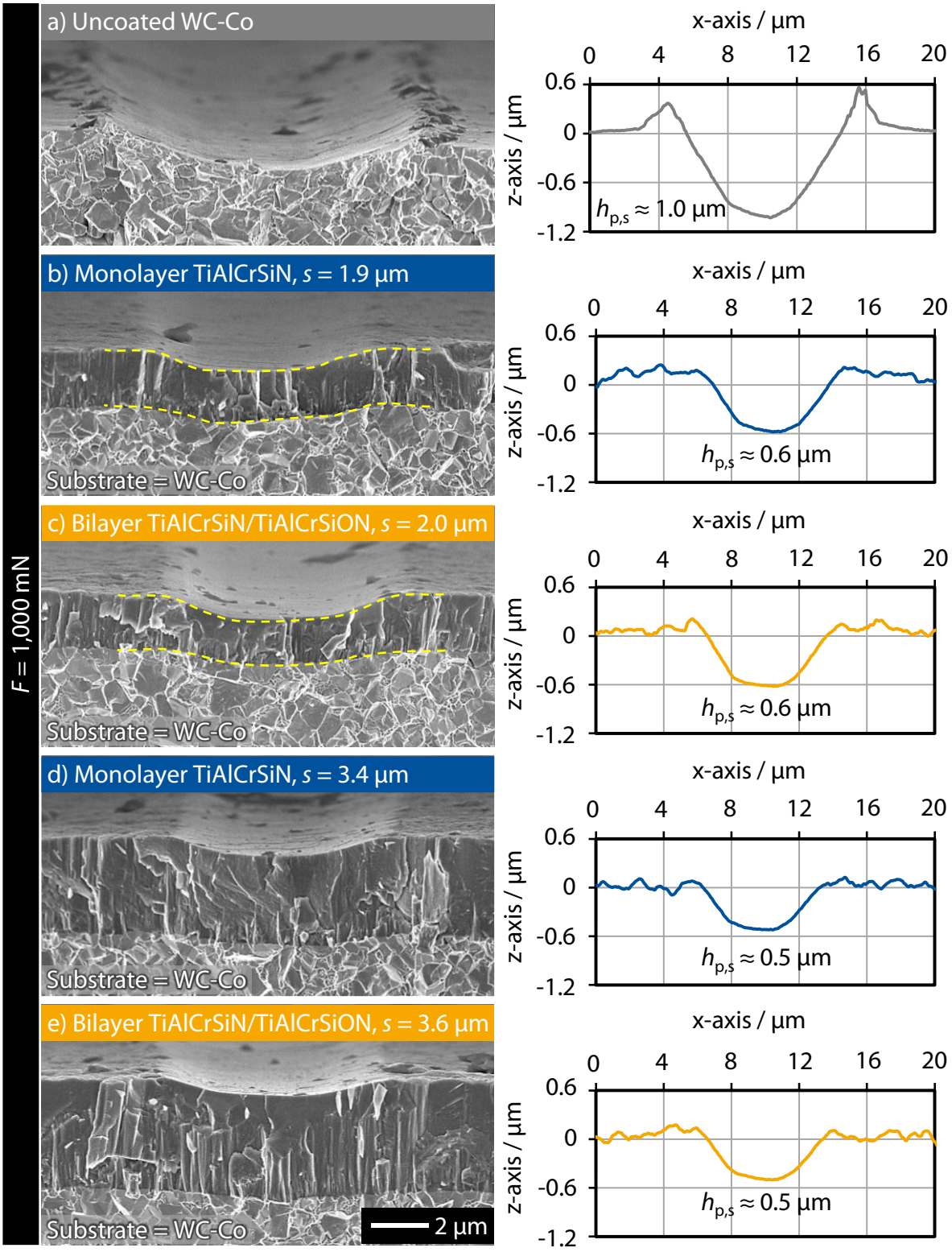

Figure 5.12: SEM images of the fracture cross-sections along with representative residual depth profiles of microscratches at F = 1,000 mN for (a) uncoated cemented carbide and (b–e) coated compounds, [BKT25b]

As compared to coated compounds, the uncoated substrate undergoes higher permanent deformation characterized by $h_{p,s}$, leading to extensive material pile-up around the shoulders of scratch track, see Figure 5.12(a). Due to the higher plastic deformation resistance, the outward protrusion of the material around scratch shoulders reduces significantly for coated variants, see Figure 5.12(b-e). The $h_{p,s}$ and material pile-up around scratch shoulders further decrease for thick coating compounds compared to the corresponding thin variants. For compounds with thin coatings, significant permanent deformation of the cemented carbide substrate is noticeable at F = 1,000 mN, see Figure 5.12(b) and (c). For the thick coating variants, the permanent deformation of the compound is largely limited to the coating, see Figure 5.12(d) and (e). These observations confirm the coating thickness role in effective distribution of the applied load to reduce the stress concentration in the substrate and decrease the overall compound deformation. For F = 500 mN, the permanent compound deformation is largely concentrated in the coating for all coated variants. Other than that, a similar trend in terms of the coating thickness effect, as discussed for F = 1,000 mN, was observed at F = 500 mN.

Figure 5.13 illustrates the representative SEM images of the scratch tracks along with surface crack areas for uncoated cemented carbide as well as thin coating compounds at F = 1,000 mN and additionally at F = 500 mN for thin bilayer variant. A comparable trend in terms of surface crack locations, when present, is observed for other combinations of normal forces and sample variants. The cracks for uncoated cemented carbide as well as coated variants are mainly limited inside the scratch track. As known from scratch tests, the surface cracks originate from the central zone of the scratch track. In this zone, the highest contact pressure occurs due to the deeper indenter tip engagement leading to maximum equivalent plastic strain [LS75]. This combined with the induced tensile stresses on the surface as well as the material ploughing by the lateral movement of the indenter tip lead to surface crack growth from the center to the edges of the scratch [Swa79]. The material pile-up around scratch shoulders, in case of uncoated cemented carbide, is visible in Figure 5.13(a). For coated compounds, no adhesive or cohesive coating failure is noticed for the considered normal forces. However, surface cracks in coatings are lengthier than the ones in uncoated cemented carbide. The same is true for monotonic indentation loading condition, see Figure 5.10. For uncoated cemented carbide, the surface crack lengths are limited by the surrounding tungsten carbide grains. Although, the coating improves the surface crack resistance of the compound, once the cracks initiate and reach critical lengths, they travel rapidly along the column boundaries of coating.

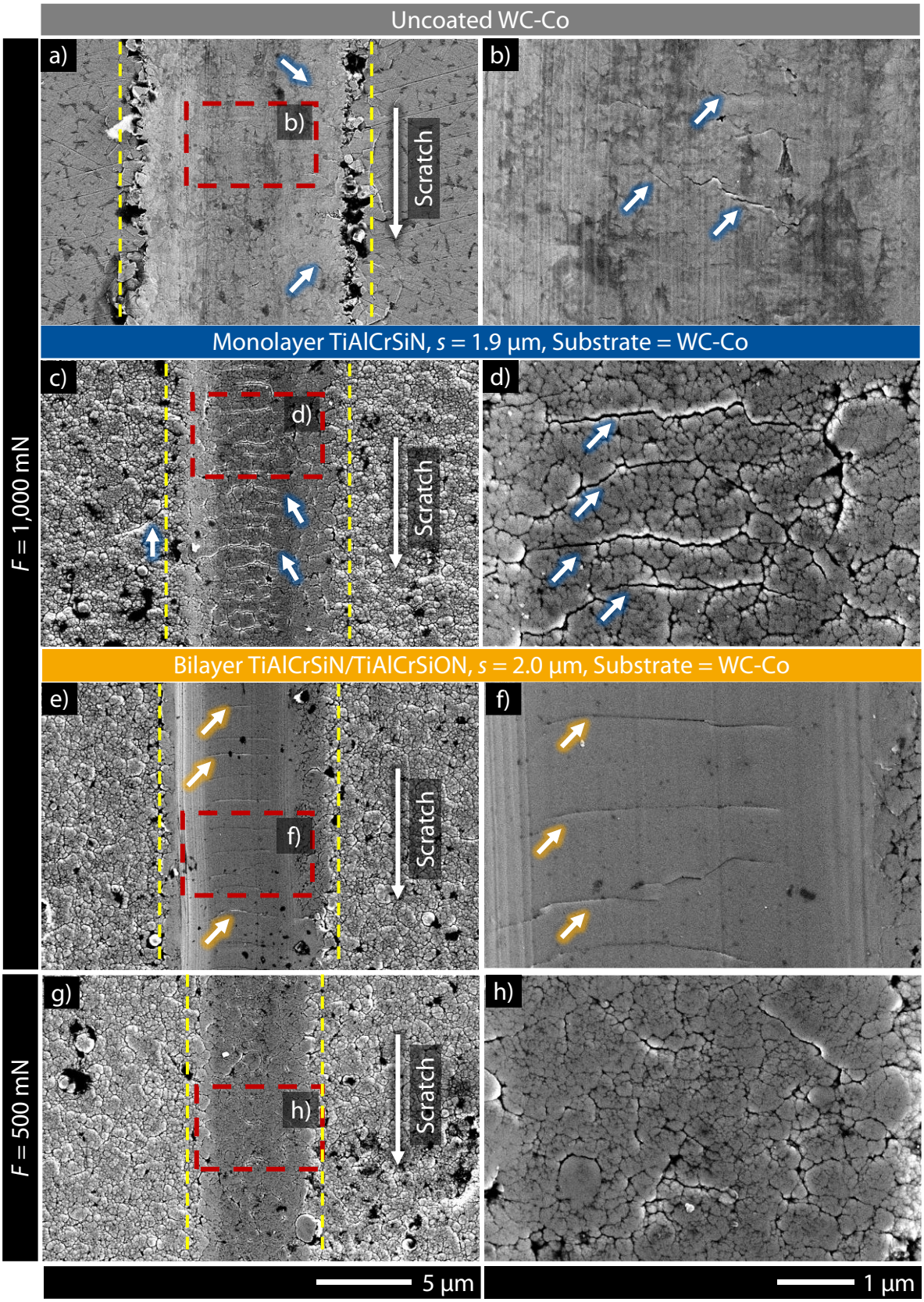

Figure 5.13: Scratch tracks and surface crack areas for (a,b) uncoated cemented carbide and coated variants with (c,d) thin monolayer and (e-h) bilayer, [BKT25b]

For thin bilayer TiAlCrSiN/TiAlCrSiON at F = 1,000 mN, the columnar structure and column boundaries are not distinguishable, see Figure 5.13(e) and (f). This was also observed for the thick bilayer variant. A further iteration of microscratch tests with the same conditions showed similar results. The non-visibility of columnar structure is not the case for the same coating at F = 500 mN, see Figure 5.13(g) and (h). This can be attributed to the hypothesis based on the presence of low melting phases in the passive layer of an oxynitride coating as per [Arg19]. When subjected to severe pressing from the moving indenter, these phases may undergo a short time liquification and cover the boundaries of coating columns before solidification. However, further investigations are recommended to validate this hypothesis.

5.9 Coating deformation and crack growth mechanisms

To understand the mesoscale coating deformation and crack growth mechanisms, selected scratches on coated variants are analyzed through a combination of FIB and TEM. The lamellae were prepared with adequate width and height to include the deformation and damage region of the coating and substrate, as exemplarily shown in Figure 5.14. This highlights the benefit of multiscale testing methods such as the instrumented indentation tests and microscratches for in-depth investigations on deformation and damage propagation in coated compounds.

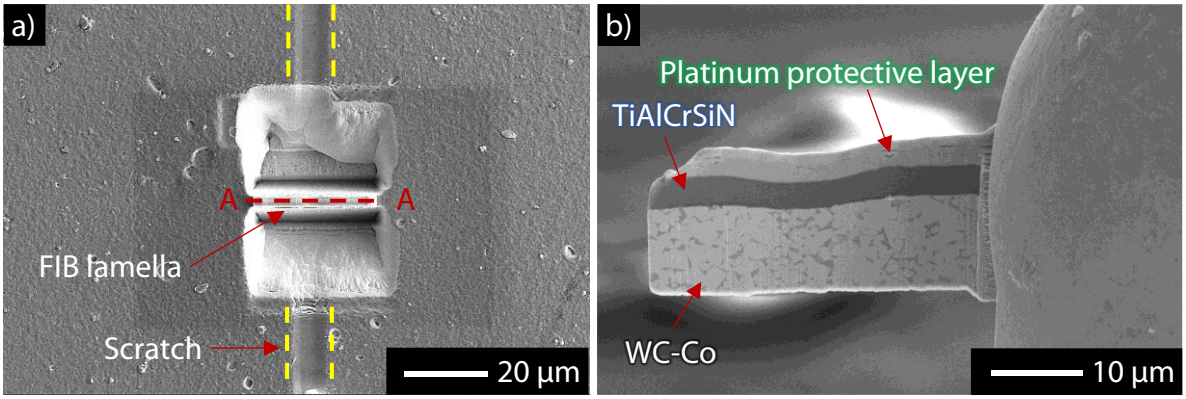

Figure 5.14: (a) Location and orientation of FIB lamella along with (b) SEM image of the prepared lamella from cross-section A-A, [BKT25b]

Figure 5.15 exhibits the STEM dark field (DF) images of the FIB lamella from the scratch cross-section on compound with thin monolayer at F = 1,000 mN. As apparent in Figure 5.15(a), the coating as well as substrate undergoes permanent deformation. The uneven platinum protective layer on top of TiAlCrSiN comes from the FIB lamella preparation. The Pt layers are used to protect the sample surface from ion beam and reduce image artifacts during TEM analysis.

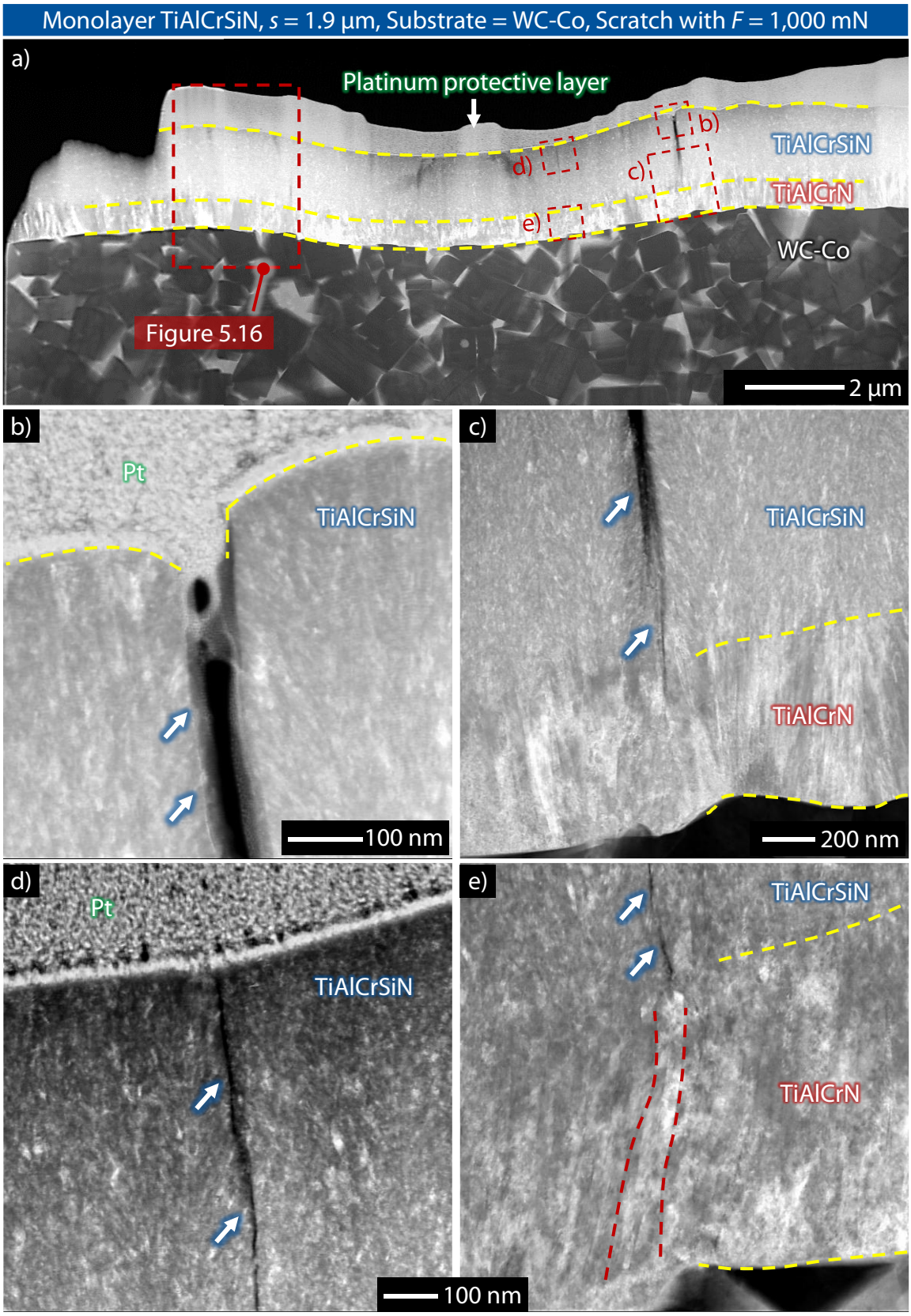

Figure 5.15: STEM DF images of (a) FIB lamella and (b–e) crack areas from F = 1000 mN scratch at compound with thin monolayer TiAlCrSiN, [BKT25b]

In shoulder region of the scratch, a large thick crack extends through the TiAlCrSiN until the TiAlCrN bond layer, see Figure 5.15(b) and (c). The crack is a result of separation between two inclined column clusters, as marked by yellow dotted line in Figure 5.15(b). The crack width reduces from the surface towards the substrate. The interface between TiAlCrSiN and TiAlCrN provides additional barrier to crack propagation, as evident by the crack width reduction in the interface region, see Figure 5.15(c). Another example of crack width reduction in the interface between TiAlCrSiN and TiAlCrN is shown in Figure 5.15(d) and (e). This crack is present in the central region of the scratch track and shows relatively lower width as compared to the one in boundary region. In both cases, the crack path is limited to the start of TiAlCrN bond layer. This confirms the role of interface between individual layers of varying chemical composition as barrier to the crack propagation. The TiAlCrN bond layer also exhibits inclination of column clusters or individual columns due to the deformation, as exemplarily marked by red dotted line in Figure 5.15(e). This column inclination can also initiate thin cracks within the TiAlCrN.

Figure 5.16 additionally shows STEM bright field (BF) images from scratch shoulder region marked in Figure 5.15(a). In BF mode, the cracks are noticeable in white color. Several thick and thin cracks in the region with material pile-up around the scratch shoulder are shown in Figure 5.16(a) and (b). Thin cracks are limited to individual TiAlCrSiN or TiAlCrN layers while relatively thicker cracks extend over the two layers. The crack paths are largely limited along the boundaries of inclined column clusters or individual columns of TiAlCrSiN and TiAlCrN. These observations indicate that the thin cracks in central region of the scratch track initiate due to the shear sliding between coating columns, whereas in shoulder region due to the combination of column inclination and shear sliding. Thick cracks in shoulder region include column separation in addition to column inclination and shear sliding. In addition to thin and thick cross-sectional cracks, small areas with adhesive coating damage are present in scratch shoulder region, see Figure 5.16(c) and (d). The outward material push from the central region of the scratch track along with ploughing effect from sliding indenter tip lead to material pile-up and an overall bending-shaped deformation profile on scratch shoulders. Accordingly, the coating-substrate interface at scratch shoulders is subjected to higher tensile stresses, resulting in initiation of adhesive failure i.e. debonding of the coating from the substrate. To study the effect of coating thickness on crack growth in the coating, Figure 5.17 displays the STEM DF images of the FIB lamella from the scratch cross-section of compound with thick monolayer TiAlCrSiN at F = 1,000 mN.

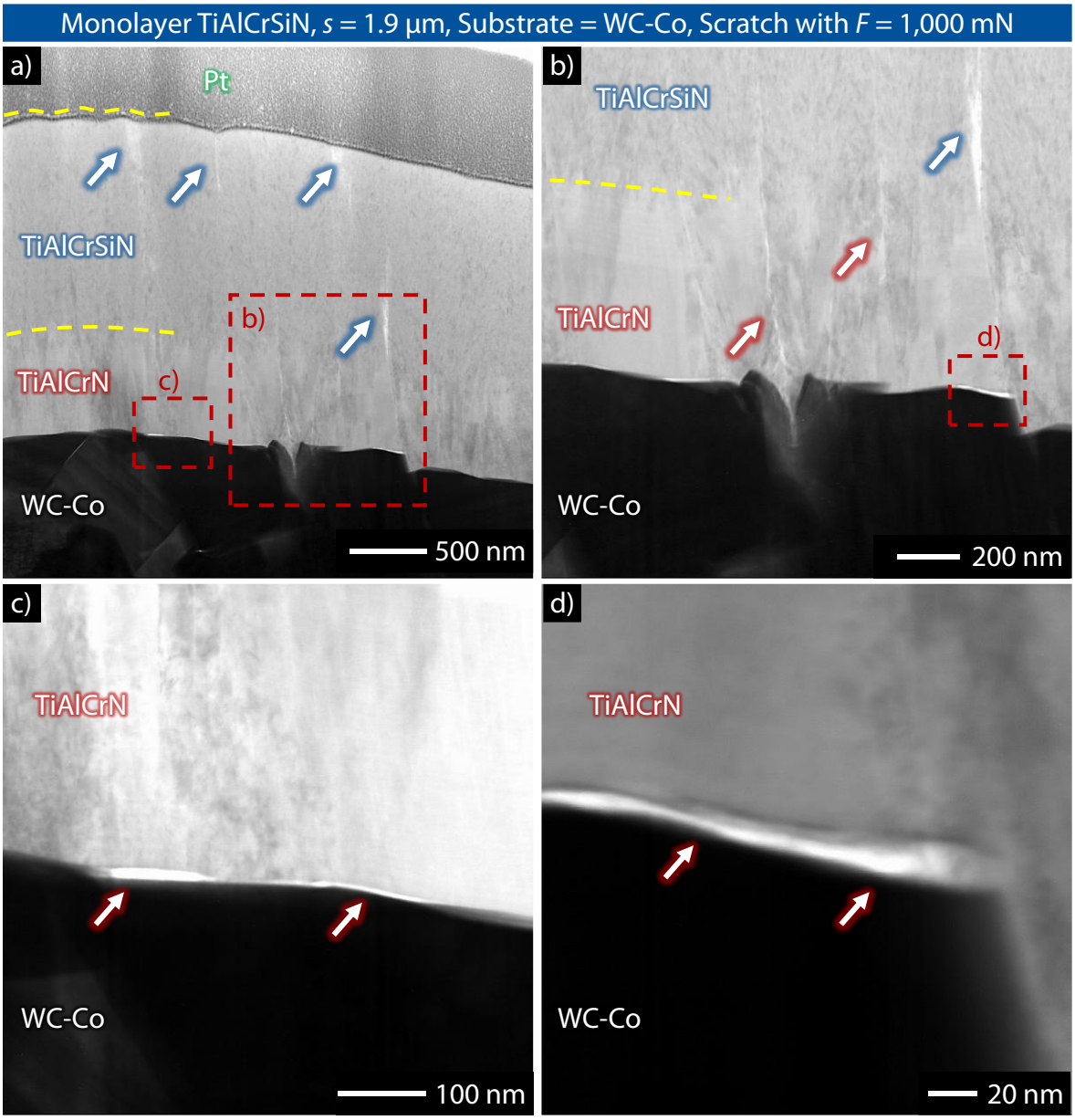

Figure 5.16: STEM BF cross-section images from the shoulder region of the F = 1000 mN scratch, marked in Figure 5.15(a), for compound with thin monolayer TiAlCrSiN, [BKT25b]

The FIB lamella with thick monolayer shows lower permanent deformation of compound as well as reduced crack formation as compared to the one with thin monolayer TiAlCrSiN see Figure 5.15(a) and Figure 5.17(a). Moreover, no areas with adhesive damage of the coating are present. This confirms higher plastic deformation resistance and load bearing capacity of the coated compounds with an increase in coating thickness. In shoulder and central region of the scratch track, thin cracks are largely limited to TiAlCrSiN, see Figure 5.17(b-d).

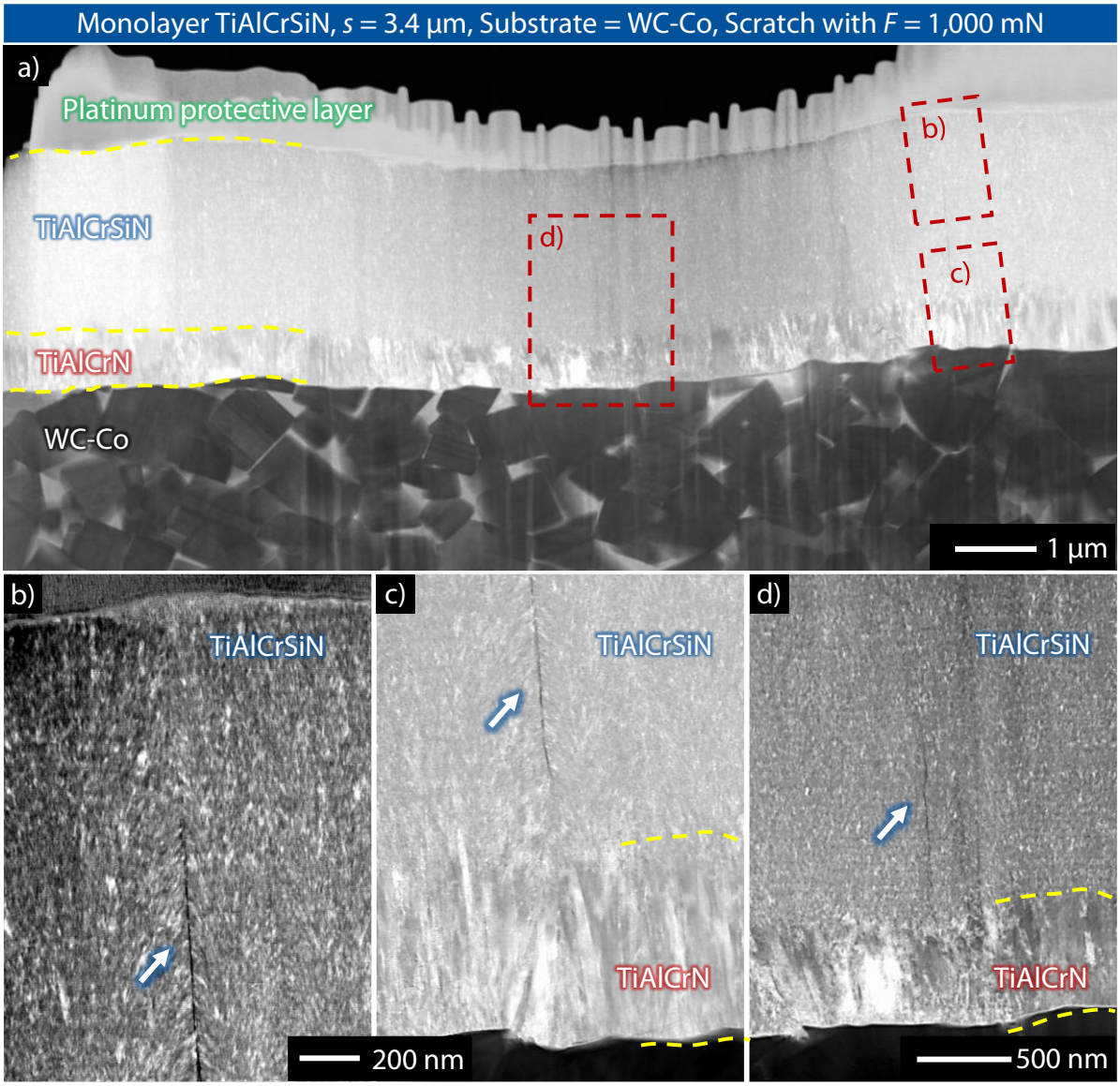

Figure 5.17: STEM DF images of (a) FIB lamella and (b–d) crack areas from F = 1000 mN scratch at compound with thick monolayer TiAlCrSiN, [BKT25b]

To study the effect of coating architecture on crack growth, Figure 5.18 shows the STEM DF images of the FIB lamella from the scratch cross-section of coated compound with thick bilayer TiAlCrSiN/TiAlCrSiON at F = 1,000 mN. Figure 5.18(a) and (b) show thin and thick cracks present in oxynitride top layer from the scratch shoulder region. As marked by yellow dotted lines, the cracks propagate along the boundaries of the inclined column clusters. Moreover, most of the thin cracks are limited to either oxynitride top layer, TiAlCrSiN interlayer or TiAlCrN bond layer. Thin cracks in TiAlCrSiON top layer, TiAlCrSiN interlayer or TiAlCrN bond layer are also present in the central region of the scratch track, see Figure 5.18(c) and (d).

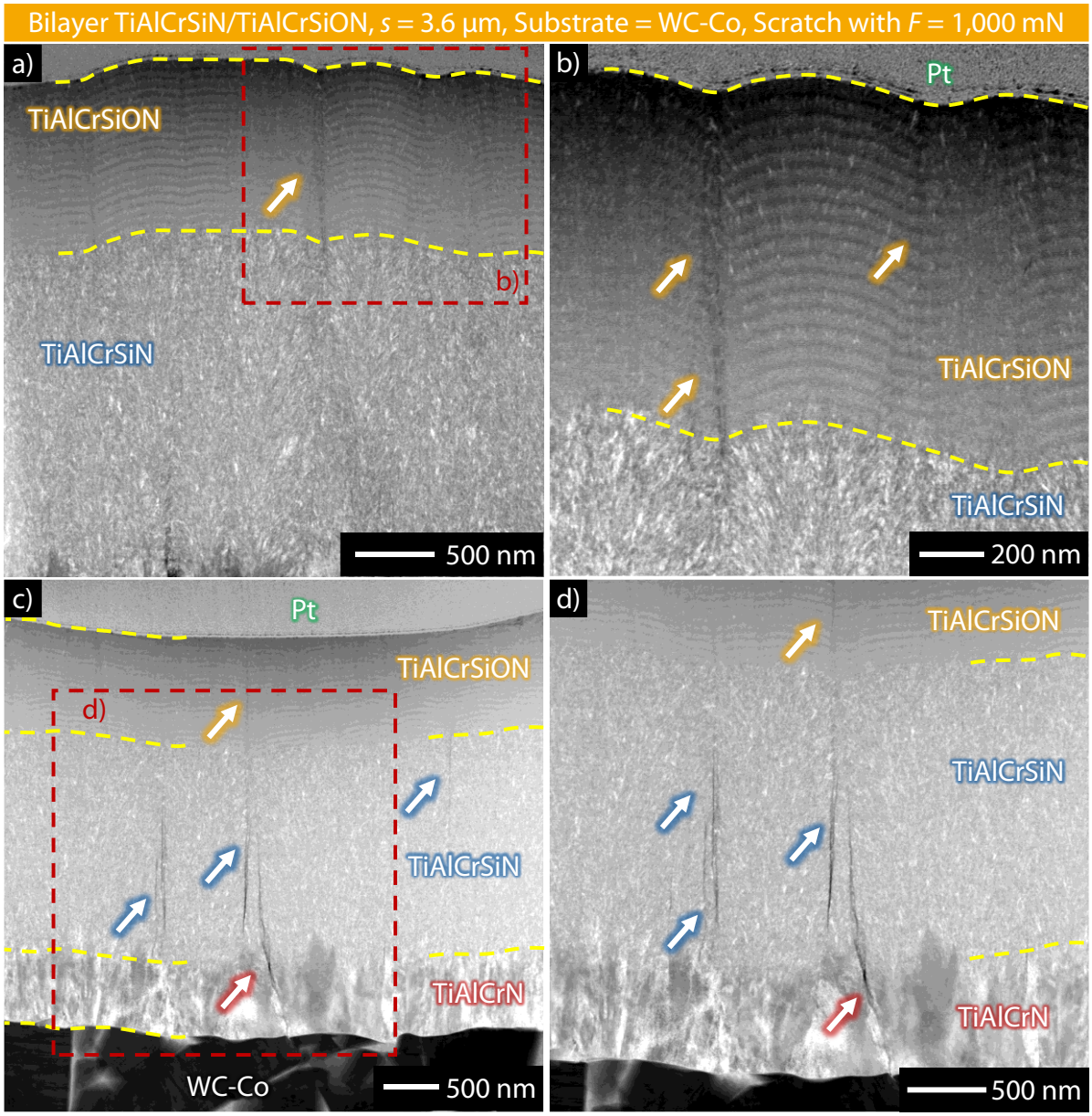

Figure 5.18: STEM DF cross-section images of the scratch track with F = 1000 mN (a,b) from shoulder and (b,d) central regions on compound with thick bilayer TiAlCrSiN/TiAlCrSiON, [BKT25b]

However, the crack width reduces at interface regions of individual layers. This explains slightly higher load bearing capacity of bilayer architecture as compared to monolayer architecture under sliding indentation load. An additional interface in the bilayer coating limits the cross-sectional cracks to individual layers by energy dissipation through crack deflection and splitting. Moreover, the interfaces can suppress the column sliding to increase the resistance

against initiation of cracks [XHM+08]. In present investigations, no evidence of the crack propagation from coating into the substrate is found.

5.10 Discussion and conclusions

Based on observations from present study on deformation and cracking behavior of compounds under sliding indentation load, the mesoscale mechanisms of coating deformation and cross-sectional crack growth are shown schematically in Figure 5.19. In central region of the scratch track, the maximum contact pressure and sample deformation, in terms of scratch depth, takes place. Here, the coating columns are pressed into the substrate and thin cross-sectional coating cracks initiate due to the shear sliding between the coating columns. These cracks grow along the boundaries of coating column clusters or individual fine columns. The compressive stresses due to the sample deformation under indentation load prevent column inclination and initiation of thick cracks in coating cross-section inside central region of the scratch track.

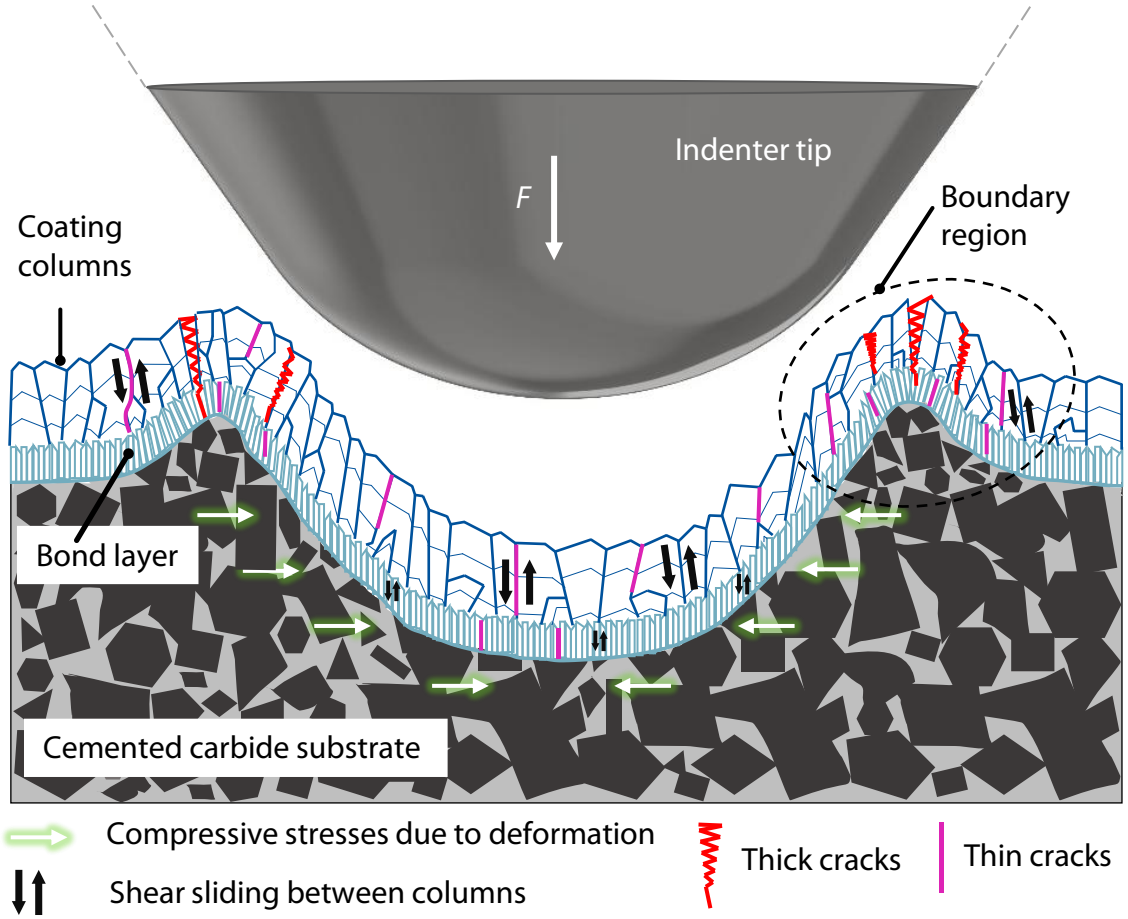

Figure 5.19: Schematic illustration of coating deformation and cross-sectional crack growth mechanisms of the compound

The high contact pressure from indenter tip in the central region of the scratch track combined with the sliding movement of the indentation load results in material flow and pile-up in boundary region of the track. The lateral movement of the indenter tip subjects the surface in central region of the scratch track to high tensile stresses. This results in initiation and propagation of large surface cracks. In boundary region of the scratch track, the coating deforms through a combination of column inclination and intercolumn shear sliding. This leads to column separation at material pile-up locations. Hence, a combination of thin and thick cross-sectional cracks in the coating are observed in the boundary region. The cross-sectional cracks in the coating require higher energy to travel through the coating-substrate interface. Therefore, no evidence of crack propagation from coating into the substrate is found in present study. This highlights the protective role of the investigated coatings to bear bulk of the tool loading in challenging applications and delay the damage propagation to the cemented carbide substrate.

In addition to the above discussion, the following are the main conclusions from this chapter which answer RQ2, RQ3 and partially address RQ5 of the dissertation:

- For TiAlCrSiN coatings on cemented carbide substrates, increasing the coating thickness from $s \approx 2.0$ µm to $s \approx 3.6$ µm increases the overall crack resistance of compounds under monotonic and sliding indentation loads. A higher coating thickness simultaneously reduces the plastic deformation as well as increases the load bearing capacity of compound. This is attributed to the higher macroscopic compressive residual stresses of the thicker coatings, which allow for effective distribution of the applied indentation load inside the coating to reduce the substrate and overall compound deformation.
- The measurement data from instrumented indentation tests provides promising basis to understand the correlations between deformation behavior and crack resistance of compounds. Moreover, the measurement data-based parameters η_{plast}, η_{elast}, η_{hp} and η_{he} provide reasonable criteria for comparing the surface crack resistance of compounds with nitride hard coatings.
- For sliding indentation loading, the combination of nitride interlayer and oxynitride top layer exhibits promising potential to improve the surface crack resistance of compound. This is attributed to the additional interface region in the coating limiting the crack growth to individual layers.

6 High temperature deformation mechanics

This chapter answers the RQ4 of the dissertation related to the influence of temperature on deformation mechanics of compounds. Moreover, the RQ5 is addressed by extending the utilization of indentation test data for high temperature investigations. For this purpose, the uncoated cemented carbide and compounds with thin as well as thick monolayer TiAlCrSiN and bilayer TiAlCrSiN/TiAlCrSiON from chapter 5 of this dissertation are further investigated using the high temperature instrumented indentation testing. Moreover, the mesoscale mechanisms of coating deformation and crack growth under monotonic indentation loadings at higher temperatures are understood using SEM and FIB/TEM analysis of indent imprints.

6.1 Instrumented indentation tests at higher temperatures

In order to investigate the temperature dependent deformation mechanics and the cracking behavior of the compounds with monolayer TiAlCrSiN and bilayer TiAlCrSiN/TiAlCrSiON, instrumented indentation tests at higher temperatures were carried out. For this purpose, the xSol© high temperature stage was installed in TriboIndenter TI 950, Bruker Corporation, Billerica, Massachusetts, USA. Figure 6.1 schematically shows the design of the xSol© high temperature stage.

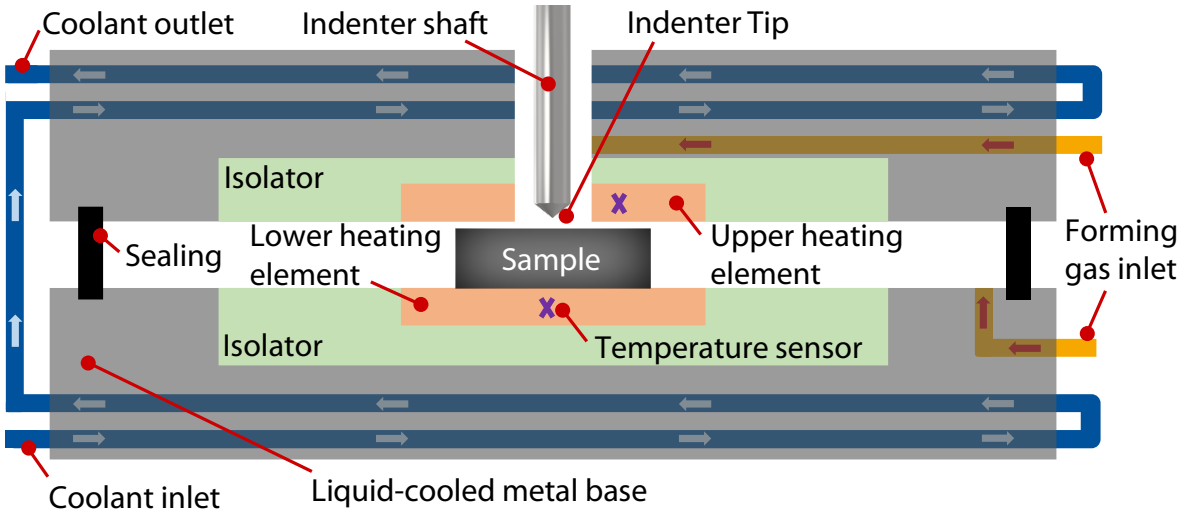

Figure 6.1: Schematic of xSol© high temperature stage

The high temperature stage consists of two heating plates with integrated heating elements, isolators, temperature sensors and water-cooling channels. The sample is placed between the two plates. In center of the upper heating plate, there is a round opening for indenter tip to access the sample. The measurement chamber is sealed with O-rings to achieve a controlled

atmosphere for high temperature measurements. In order to avoid any chemical reactions on the samples surface as well as the oxidation of the diamond indenter tip, the measurement chamber is continuously purged with forming gas 95/5, comprising of 95 % N_2 and 5 % H_2, during high temperature measurements. The temperature during measurements is monitored and automatically controlled using a proportional-integral-derivative (PID) controller.

In context of the current investigation, high temperature instrumented indentation tests were carried out in nano- and micro-range. The temperature dependent elastic-plastic deformation behavior of the thin and thick monolayer TiAlCrSiN and bilayer TiAlCrSiN/TiAlCrSiON variants was studied with nanoindentation measurements at room temperature T = 23 °C as well as at T = 200 °C, T = 400 °C and T = 600 °C. Room temperature during the measurements was maintained at T = 23 °C using an air conditioning unit. The results from room temperature measurements have been discussed in the previous chapter, see section 5.6. In this chapter, the room temperature measurements are added as reference to study the change in deformation response with the measurement temperature. Moreover, to analyze the change in deformation response of coatings after heating, additional room temperature measurements T = 23 °C-A were carried out after (A) cooling down the sample. For each sample variant and measurement temperature, 15 measurements at higher temperatures were carried out with indentation force F = 8 mN. A diamond indenter tip with Berkovich geometry and nominal radius $r \approx 150$ nm was used for this purpose. The indenter tip was air-cooled during the measurements. In order to exclude any effect of variation in tip shape, all measurements were carried out with the same indenter tip. The tip wear during the measurements was monitored by analyzing the shape of indent imprint through additional indentations on polycarbonate sample before and after high temperature measurements of each sample. The indentation hardness H_{IT} and indentation modulus E_{IT} of coatings were calculated from measurement data as per [OP92]. As commonly known for ceramic coatings, Poisson's ratio ν = 0.25 was used for calculations.

For investigation of temperature influence on compound deformation and cracking behavior, instrumented indentation tests in micro-range with F = 500 mN, F = 750 mN, F = 1,000 mN, F = 1,250 mN and F = 1,500 mN were carried out at the same measurement temperatures as nanoindentations. The room temperature results for 750 mN ≤ F ≤ 1,500 mN have been discussed in section 5.7 and are included in the current chapter as reference. In addition to coated samples, the indentations tests on uncoated substrate were carried out to exclusively

study the temperature dependent deformation response of the uncoated cemented carbide. The indentation force range for high temperature measurements was chosen on two criteria. Firstly, to characterize the temperature dependent deformation behavior of all investigated samples from relatively low to high thermomechanical loading conditions. Secondly, to have a wide range of F and T combinations for analysis and characterization of the temperature effect on cracking behavior of different sample variants. For each indentation force, temperature and sample variant combination, 5 measurements with diamond indenter tip of conical geometry, nominal cone angle $\alpha = 60°$ and nominal radius $r = 10$ µm were performed. The force function consisted of loading segment with $t_{loading} = 10$ s, hold period with $t_{hold} = 3$ s and unloading segment with $t_{unloading} = 10$ s. All measurements were carried out with the same indenter tip. In order to exclude any effect of tip wear test results, the shape of indent imprint was monitored through additional indentations on polycarbonate sample before and after high temperature measurements of each sample. The measurement data in form of force-indentation depth curves at varying F and T combinations was analyzed to characterize the elastic-plastic deformation behavior of the samples, see section 2.5.3 for further details. The indent imprints were examined for surface cracks with SEM, Zeiss DSM 982 Gemini, Carl Zeiss AG, Oberkochen, Germany. For studying coating deformation mechanism in correlation with crack growth in compounds, selected indent imprints were analyzed in cross-section using a combination of FIB and TEM. PFIB Helios 5, Thermo Fischer Scientific, Eindhoven, Netherlands, was used for FIB lamellae preparation whereas FEI Tecnai G² F20 S-TWIN, Thermo Fischer Scientific, Eindhoven, Netherlands, was used for the TEM analysis. The FIB preparations, SEM and TEM investigations were carried out at GFE, RWTH Aachen University.

6.2 High temperature nanoindentation of coatings

The indentation hardness H_{IT} and indentation modulus E_{IT} of the coatings at varying measurement temperatures are shown in Figure 6.2. Temperature $T = 23$-A represents the measurements carried out after sample cooling from $T = 600$ °C to room temperature. For the considered temperature range, monolayer variants maintain higher average temperature dependent H_{IT} compared to the bilayer variants, see Figure 6.2(a). This is attributed to the higher amorphous content of oxynitride coating, which reduces the H_{IT} of bilayer variant. As the measurement temperature increases, the H_{IT} gradually decreases for all coatings. Moreover, the difference in H_{IT} between the monolayer and bilayer variants reduces from $\Delta H_{IT} = \sim 7$ GPa at $T = 23$ °C to $\Delta H_{IT} = \sim 4$ GPa at $T = 600$ °C. This means that the bilayer architecture exhibits

the potential to reduce the H_{IT} drop at higher temperatures through additional interface in the coating. The monolayer variants do not show any significant effect of the coating thickness on the temperature dependent H_{IT}. Both thin and thick monolayer variants exhibit comparable overall percentual reduction ΔH_{IT} = -26 % at T = 600 °C compared to T = 23 °C. In case of bilayer architecture, the H_{IT} for thin coating at T = 600 °C reduces by ΔH_{IT} = -17 %, whereas for thick coating by ΔH_{IT} = -25 %. This difference is attributed to the effect of TiAlCrSiN interlayer on temperature dependent H_{IT} measurements of TiAlCrSiON top layer.

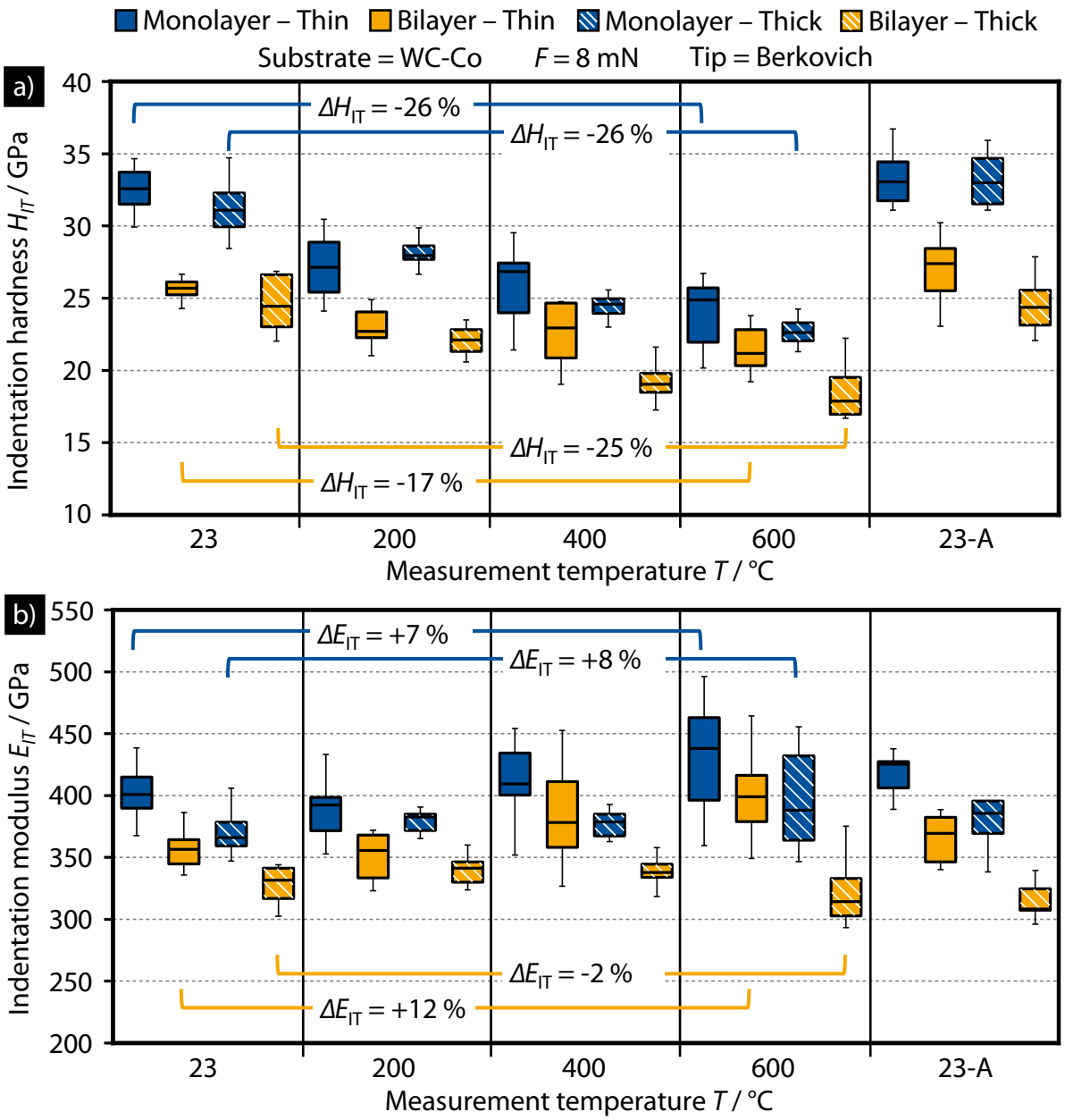

Figure 6.2: Temperature dependent (a) indentation hardness H_{IT} and (b) indentation modulus E_{IT} of monolayer and bilayer coatings with varying thickness

With the increase in measurement temperature, the maximum indentation depth h_{max} and resultantly the influence of nitride interlayer on deformation response of oxynitride top layer increases. As the chemical composition and deposition parameters of TiAlCrSiN interlayer for bilayer variants are same as monolayer TiAlCrSiN, this means that the nitride interlayer has higher temperature dependent H_{IT} compared to oxynitride top layer. For thin bilayer with lower oxynitride top layer thickness, the nitride interlayer effect on measurements increases with temperature compared to the thick bilayer variant. Hence, the thin bilayer exhibits slightly higher H_{IT} compared to the thick variant for the considered temperatures, see Figure 6.2(a).

As observed for the H_{IT}, the monolayer variants maintain higher indentation modulus E_{IT} compared to bilayer variants until T = 600 °C. In terms of coating thickness, thin coatings exhibit slightly higher E_{IT} compared to their corresponding thick variants, see Figure 6.2(b). The reason for this difference has been explained in section 5.6. In contrast to H_{IT}, the indentation modulus E_{IT} of coatings does not change significantly with the measurement temperature. The percentual differences between E_{IT} values at T = 23 °C and T = 600 °C are $\Delta E_{IT} \leq \pm$ 8 % for both monolayer and thick bilayer variants. For thin bilayer variant, an increase of ΔE_{IT} = 12 % is attributed to the nitride interlayer effect, as explained for the H_{IT}.

Figure 6.3 shows the deformation behavior of the coatings characterized in terms of plastic work percentage η_{plast}. The coating deformation, measured as maximum indentation depth h_{max}, increases with temperature and accordingly the H_{IT} reduces. However, the E_{IT} does not change significantly with the measurement temperature. This means that the permanent indentation depth h_p increases while the recovered indentation depth h_e does not change significantly. The temperature dependent h_p and h_e values are shown in Appendix III. Hence, the plastic work percentage η_{plast} increases with the measurement temperature, resulting in an overall percentual increment of $\Delta\eta_{plast}$ = (29 – 39) % at T = 600 °C compared to T = 23 °C for the coatings, see Figure 6.3. In terms of coating architecture, the bilayer variants show higher η_{plast}, which correlates to their lower temperature dependent H_{IT} and E_{IT} compared to the monolayer variants. However, the η_{plast} difference between monolayer and bilayer variants slightly reduces with higher measurement temperatures. This means that the temperature dependent increase in h_{max}, h_p of the coatings is relatively lower for bilayer variants as compared to the monolayer variants due to the additional interface and interlayer effects. Any significant differences in η_{plast}

due to the coating thickness are not noticeable at the considered measurement temperatures and indentation force for the measurements in nano-range.

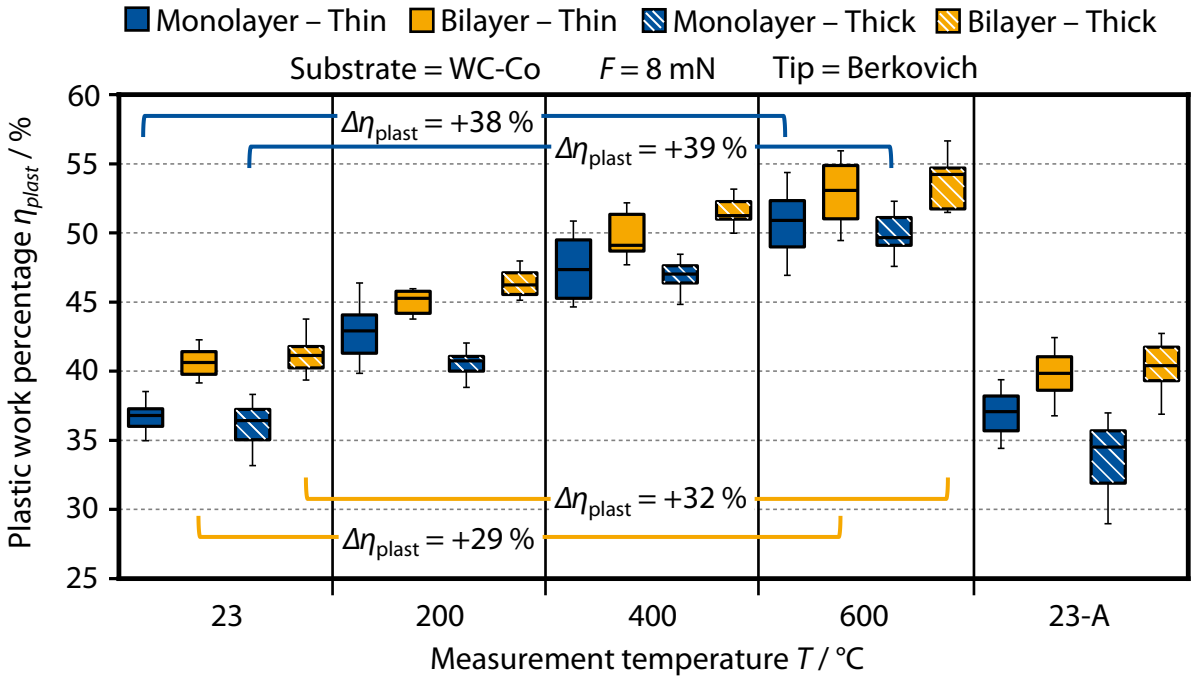

Figure 6.3: Temperature dependent plastic work percentage η_{plast} of monolayer and bilayer coatings with varying thickness at indentation force $F = 8$ mN

After cooling down, the H_{IT}, E_{IT} and η_{plast} at $T = 23$ °C-A for all four coatings are similar to their initial values at $T = 23$ °C before heating, see Figure 6.2 and Figure 6.3. Previously, TiAlCrSiN and TiAlCrSiON coatings with rather lower Al content have exhibited phase stability until $T = 1{,}200$ °C and oxidation resistance until $T = 900$ °C [BBK+21]. In the present case, no significant differences in phase composition with XRD measurements before and after high temperature nanoindentations are observed, see Appendix III. Hence, any phase change or oxidation effects on the temperature dependent deformation behavior of investigated coatings until $T = 600$ °C are ruled out. Moreover, thermally induced stresses in the compound remain within the elastic region of the coating till $T = 600$ °C. This is inferred from similar H_{IT}, E_{IT} and force-indentation depth curves of coatings before and after high temperature measurements. The average force-indentation depth curves for the thick coatings are shown in Figure 6.4. A comparable tendency of temperature effect is observed for the thin variants. The discussed trends on temperature dependent elastic-plastic deformation behavior of the variants can be attributed mainly to the changes in grain boundary strength of the coatings.

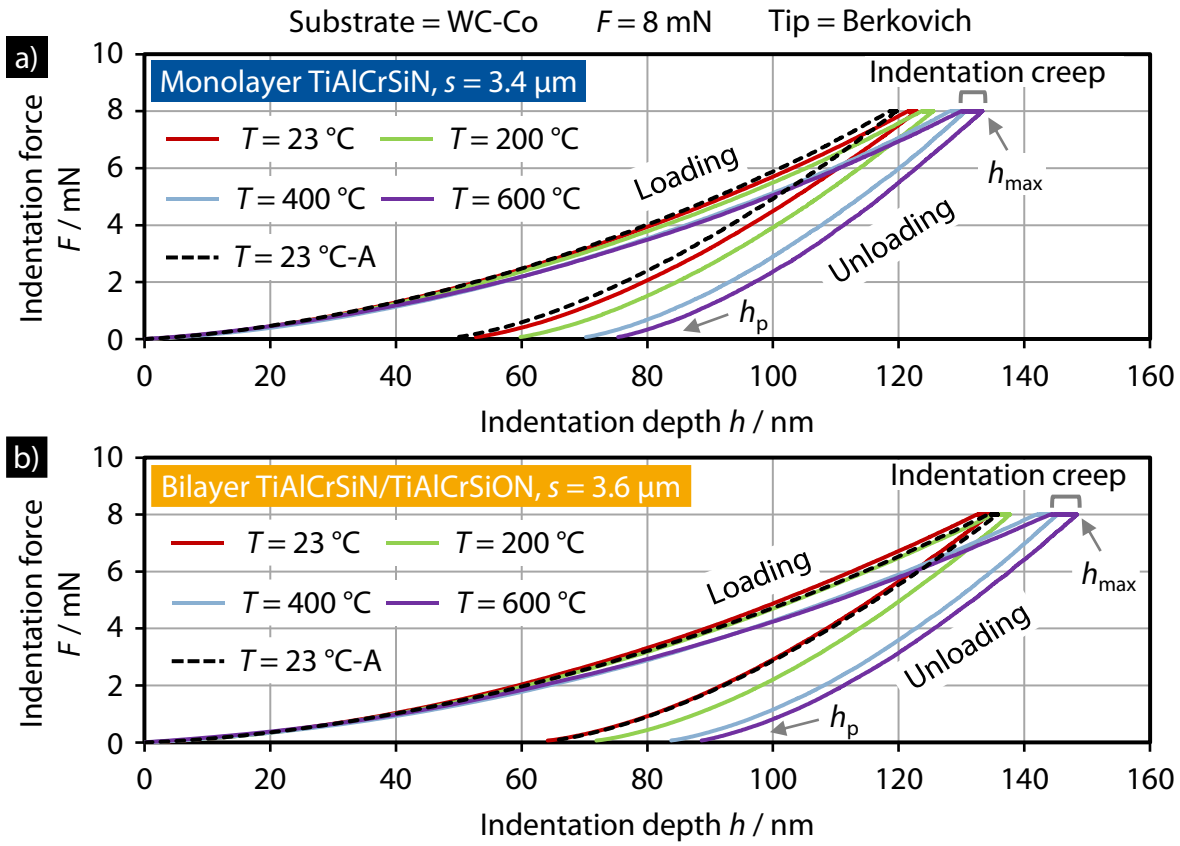

Figure 6.4: Average force-indentation depth curves of thick (a) monolayer and (b) bilayer from high temperature nanoindentations at $F = 8$ mN

As known for polycrystalline and composite materials, the atomic mobility at grain boundaries increases with the temperature. This leads to reduction in the grain boundary strength and increases the grain boundary sliding. For coatings with nanocrystals and fine columns in the present case, the increase in grain and column boundary sliding at higher temperatures reduces the coating resistance against plastic deformation. Another aspect of the coating deformation behavior, which accelerates at higher measurement temperatures is the indentation creep. Indentation creep is the time dependent deformation of materials under constant indentation load [SA92]. In present study, all nanoindentation measurements were carried out with a hold period of $t_{hold} = 3$ s. This means that after reaching the indentation force of $F = 8$ mN, the F was kept constant for $t_{hold} = 3$ s before unloading. As apparent in Figure 6.4, the indentation depth h during the hold period increases with measurement temperature. This is again attributed to the coating microstructure containing high fractions of grain and column boundaries. The grain boundary activities increase at higher temperatures and accelerate the indentation creep of the coating. Hence, the h_{max}, h_p and η_{plast} increase and consequentially the H_{IT} decreases with the

measurement temperature for the same indentation force. The slope of unloading curves exhibits only slight variations until T = 600 °C, see Figure 6.4. Accordingly, the indentation modulus E_{IT} of the coatings does not change significantly with the temperature.

These results show that the temperature dependent deformation of the nitride hard coatings is influenced by the coating chemical composition and architecture. To sum up, the monolayer variants consistently exhibit higher H_{IT} and E_{IT} as well as lower η_{plast} compared to the bilayer coatings until T = 600 °C. However, the bilayer architecture exhibits lower temperature dependent drop in plastic deformation resistance and H_{IT} due to the additional interface in the coating. For monolayer variants, coating thickness does not significantly affect the temperature dependent H_{IT}, E_{IT} and η_{plast} at F = 8 mN. For bilayer variants, slight coating thickness related differences in H_{IT} and E_{IT} are observed due to the TiAlCrSiN interlayer effect on measurements.

6.3 Temperature dependent deformation and cracking behavior of compounds

In order to investigate the temperature dependent deformation and surface cracking behavior of uncoated cemented carbide and coated compounds, instrumented indentation tests were carried out at T = 23 °C, T = 200 °C, T = 400 °C, T = 600 °C and after cooling down again at T = 23 °C-A. The tests were carried out with varying indentation forces from F = 500 mN to F = 1,500 mN with ΔF = 250 mN. The indents were analyzed afterwards for surface cracks using SEM. Figure 6.5 summarizes the temperature dependent surface cracking behavior of the sample variants. The red brackets highlight the results, where the higher measurement temperatures lead to an earlier initiation of surface cracks compared to the corresponding room temperature measurements. The uncoated cemented carbide exhibits surface cracks for all considered measurement force and temperature combinations. As measurement temperatures increased, black oxide particles formed on the surface of uncoated cemented carbide despite the forming gas atmosphere during the measurements. Hence, at T = 600 °C the surface was deemed unsuitable for surface crack analysis using SEM. Considering the results at T = 200 °C and T = 400 °C, the indent imprints at T = 600 °C are expected to show surface cracks at the considered indentation forces. At T = 23 °C-A, the results for indentations on uncoated cemented carbide carried out at room temperature after cooling down from T = 400 °C are shown. In case of coated variants, no formation of black oxide particles on the surface was observed. The thin coating compounds show an influence of measurement temperature on surface cracks resistance at F = 1,000 mN. Moreover, the surface crack resistance of the thin

coating compounds at higher temperatures exhibits slight differences in terms of coating architecture. At F = 1,000 mN, the thin bilayer variant displays surface cracks at T = 400 °C as compared to T = 600 °C for thin monolayer variant. The increase in surface crack resistance with higher coating thickness, as previously observed for room temperature measurements, remains valid for higher temperatures. Moreover, the thick coating compounds show no effect of coating architecture on the temperature dependent surface crack resistance for the considered F and T combinations.

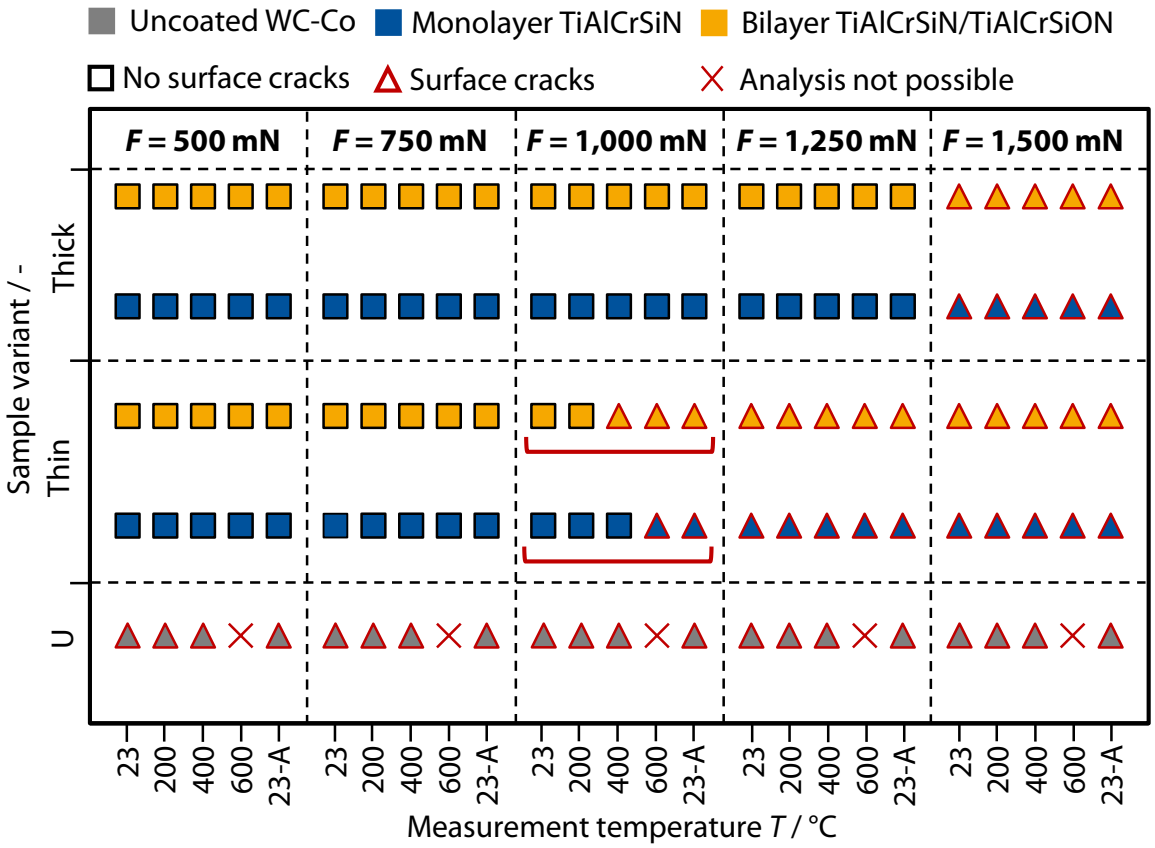

Figure 6.5: Summary of surface crack analysis of uncoated cemented carbide and coated compounds at varying measurement temperatures and indentation forces

In order to understand the effect of temperature on deformation mechanics and the surface crack resistance, the temperature dependent elastic-plastic deformation behavior of the samples is characterized using measurement data from the indentation tests. The maximum indentation depth h_{max}, as sum of h_p and h_e for F = 500 mN, F = 750 mN and F = 1,000 mN at varying measurement temperatures is shown in Figure 6.6. The Figure 6.7 displays the same for F = 1,250 mN and F = 1,500 mN.

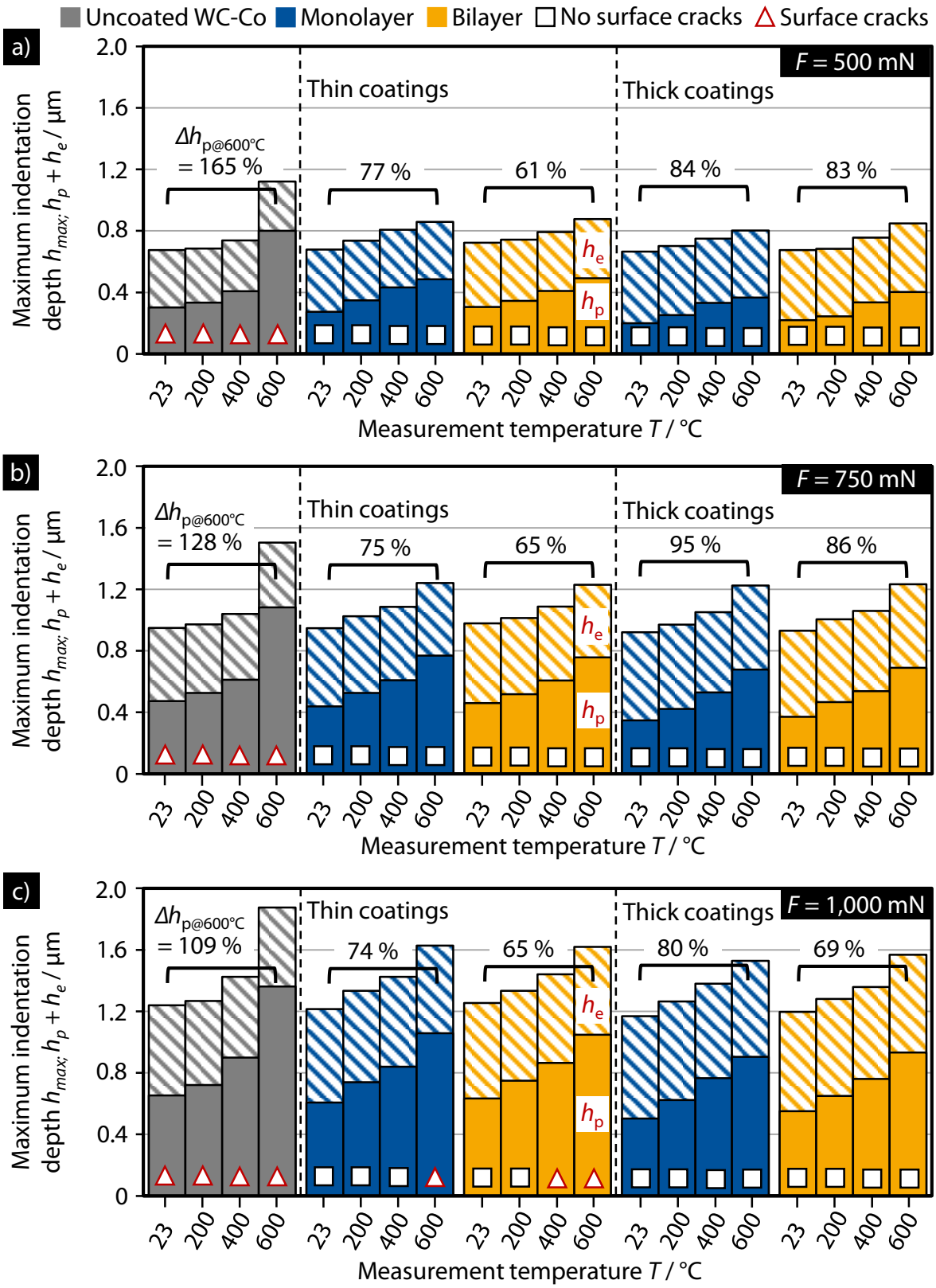

Figure 6.6: Temperature dependent maximum indentation depth h_{max} of the uncoated cemented carbide and coated compounds at (a) F = 500 mN, (b) F = 750 mN and (c) F = 1,000 mN

The $\Delta h_{p@600°C}$ in Figure 6.6 and Figure 6.7 represents percentual increase in the permanent indentation depth from T = 23 °C to T = 600 °C, see Equation 6.1. Moreover, all average values in Figure 6.6 and Figure 6.7 have a standard deviation $SD \leq 10$ %.

$$\Delta h_p = \frac{h_{p@600°C} - h_{p@23°C}}{h_{p@23°C}} \text{ x } 100\ \% \quad , \quad \Delta h_e = \frac{h_{e@600°C} - h_{e@23°C}}{h_{e@23°C}} \text{ x } 100\% \qquad \text{Equation 6.1}$$

The maximum indentation depth h_{max} and permanent indentation depth h_p increase with measurement temperatures for all sample variants. For uncoated cemented carbide, the h_p increases by $\Delta h_{p@600°C} > 100$ % from room temperature till T = 600 °C at all indentation forces.

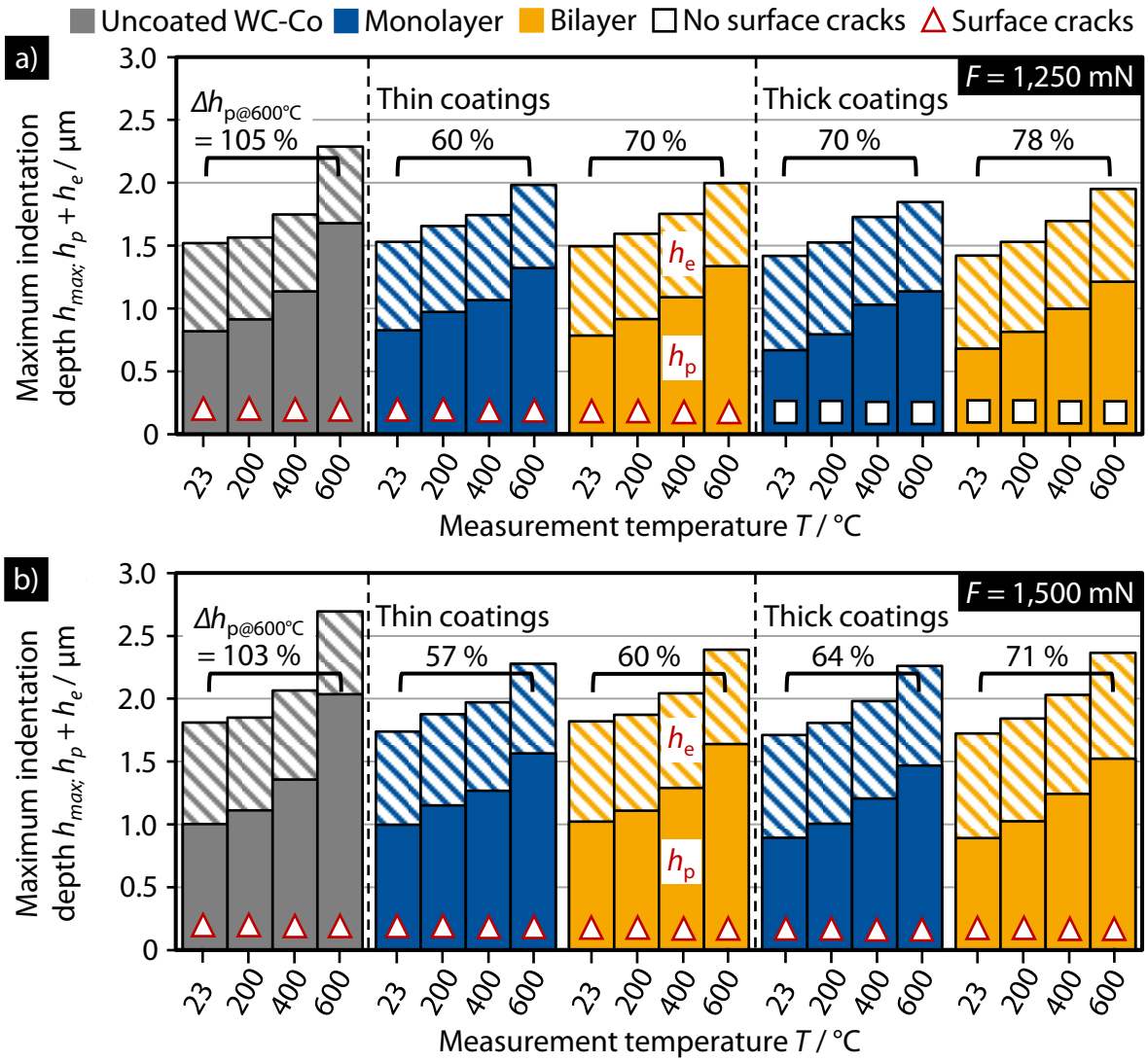

Figure 6.7: Temperature dependent maximum indentation depth h_{max} of uncoated cemented carbide and coated compounds at (a) F = 1,250 mN and (b) F = 1,500 mN

The temperature dependent increments in h_p reduce with higher indentation force, but still more than double for uncoated cemented carbide at F = 1,500 mN. Moreover, the h_{max} and h_p for uncoated substrate increase almost linearly with measurement temperatures $T \leq 400$ °C for all indentation forces. However, a non-linear jump in h_{max} and h_p of uncoated substrate is observed from T = 400 °C to T = 600 °C, see Figure 6.6 and Figure 6.7. This points towards significant reduction in thermal stability and resistance against plastic deformation of the uncoated cemented carbide at T = 600 °C. Depending on Co content and WC grain size, a steep increase in near surface deformation under indentation load and alternatively sharp drop in hardness of cemented carbides around $T \approx 600$ °C has been reported over the years [Lee83, VPG+20]. The underlaying reasons are intrinsic softening of constitutive Co-matrix [DAK63] as well as the reduction in the grain boundary strength [MLN99].

The coated compounds display almost linear temperature dependent increment in h_{max} and h_p for all indentation forces and measurement temperatures until T = 400 °C, see Figure 6.6 and Figure 6.7. The non-linear jump in h_{max} and h_p between T = 400 °C and T = 600 °C reduces significantly for the coated compounds as compared to the uncoated substrate. Hence, at T = 600 °C, the coated variants exhibit lower temperature dependent increment in h_{max}, h_p, and $\Delta h_{p@600°C}$ as well as higher surface crack resistance compared to the uncoated substrate. This confirms superior thermal stability and load bearing capacity of compounds under indentation loading at higher temperatures due to the nitride hard coatings. Interestingly, the absolute values for recovered indentation depth h_e are almost consistent for the same indentation force at varying temperatures, see Figure 6.6 and Figure 6.7. Therefore, the percentual increase in h_e from T = 23 °C to T = 600 °C remains $\Delta h_{e@600°C} < 10$ % at each indentation force for the uncoated substrate as well as the compounds. Hence, at the same indentation force, the temperature dependent increase in h_{max} and h_p along with consistent h_e confirms the reduction in plastic deformation resistance of the sample variants at higher temperatures.

In terms of coating thickness, the increase in load bearing capacity with coating thickness, previously observed at room temperature in section 5.7, translates to higher temperatures as well. For all F and T combinations, the thick coating compounds consistently show lower h_p and h_{max} compared to the corresponding thin coating variants, see Figure 6.6 and Figure 6.7. However, for the same indentation force, the h_p and h_{max} differences between the thin and thick coating compounds reduce as measurement temperature increases till T = 600 °C. Moreover,

despite the lower h_p and h_{max}, the compounds with thick coatings exhibit higher temperature influence on percentual h_p increment, as evident from the $\Delta h_{p@600°C}$ values. The thick coating compounds consistently show higher $\Delta h_{p@600°C}$ values as compared to the corresponding thin coating compounds. This means that the percentual increase in h_p with measurement temperature is higher for the thick coating variants than the thin coating compounds. However, the surface crack resistance of the thick coating compounds remains unaffected until $T = 600$ °C. Moreover, the thick coating compounds maintain lower h_p and h_{max} for the considered indentation force range until $T = 600$ °C as compared to the thin coating variants.

In terms of coating architecture effect, the bilayer variants exhibit lower $\Delta h_{p@600°C}$ compared to the corresponding monolayer variants for $F \leq 1{,}000$ mN, see Figure 6.6. The trend reverses for $F > 1{,}000$ mN, see Figure 6.7. The differences in h_{max} and h_p between the monolayer and corresponding bilayer variants remain $|\Delta| \leq 10$ % for all F and T combinations. Hence, no significant effect of the bilayer architecture on temperature dependent deformation response of coated compounds could be established. A comparison of h_{max} between $T = 23$ °C and $T = 23$ °C-A after cooling down from $T = 600$ °C is presented in Appendix III. For all coated variants, no significant change in deformation behavior is observed, as h_{max} and h_p differences are $|\Delta| \leq 10$ %. For uncoated cemented carbide, significant differences at $T = 23$ °C before and after heating are observed due to the formation of the thick oxide layer at $T = 600$ °C.

In order to clarify the temperature influence on deformation mechanics of compounds, the average force-indentation depth curves for thin monolayer variant at $F = 1{,}500$ mN are shown in Figure 6.8. The discussed trends are applicable for other F and T combinations as well as other coated variants. No pop-in events were observed in the individual curves. The slope of loading segment decreases with the measurement temperature, which denotes the decrease in plastic deformation resistance of the compound. Moreover, as observed for nanoindentations, the indentation creep at maximum indentation force increases with temperature. The indentation tests in micro-range were also carried out with a hold period of $t_{hold} = 3$ s. This temperature dependent change in deformation behavior of the compounds is associated mainly with the increase in grain boundary activities in coating and substrate, as discussed for nanoindentation measurements in section 6.2. The induced thermal stresses by the higher temperatures until $T = 600$ °C remain in the elastic region. This is inferred from the similar force-indentation depth curves at $T = 23$ °C and $T = 23$ °C-A.

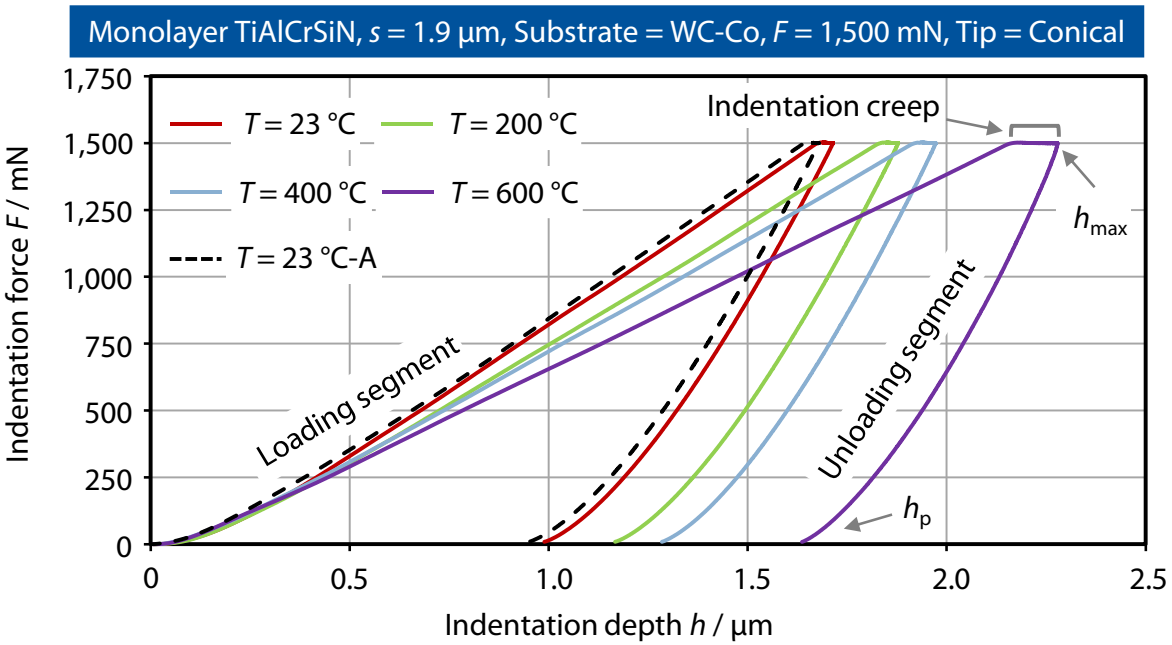

Figure 6.8: Average force-indentation depth curves of the compound with thin monolayer at F = 1,500 mN and varying measurement temperatures

The temperature dependent increase in the grain boundary activities allows the compounds to undergo higher plastic deformation before the initiation of surface cracks. Figure 6.9 shows the plastic work percentage η_{plast} and the elastic work percentage η_{elast} at varying measurement temperatures until $F \leq 1{,}000$ mN. The temperature dependent η_{plast} and η_{elast} for $F \geq 1{,}250$ mN are shown in Figure 6.10. The η_{plast} increases and η_{elast} decreases linearly for all samples and indentation forces until T = 400 °C. For temperature T = 600 °C, non-linear increment in η_{plast} and decrement in η_{elast}, respectively, is apparent. This correlates well with the elastic-plastic deformation behavior characterized in terms of h_{max}, h_p and h_e. For each indentation force, the temperature dependent increments in h_{max} and h_p along with almost constant h_e result in higher η_{plast} and alternatively lower η_{elast} at elevated measurement temperatures.

The deformation response of the coated compounds in comparison to the uncoated cemented carbide, in terms of η_{plast} and η_{elast}, varies depending on the indentation force, measurement temperature, coating thickness and resulting indentation depth. Barring the few exceptions, the thin coating variants show η_{plast} and η_{elast} absolute differences of $|\Delta\eta| = (2 - 7)$ % as compared to uncoated substrate for all F and T combinations until $F \leq 750$ mN, see Figure 6.9(a) and (b). For all measurements with $F \geq 1{,}000$ mN, the η_{plast} and η_{elast} differences between the thin coating compounds and the uncoated substrate reduce to $|\Delta\eta| \leq 3$ %, see Figure 6.9(c) and Figure 6.10.

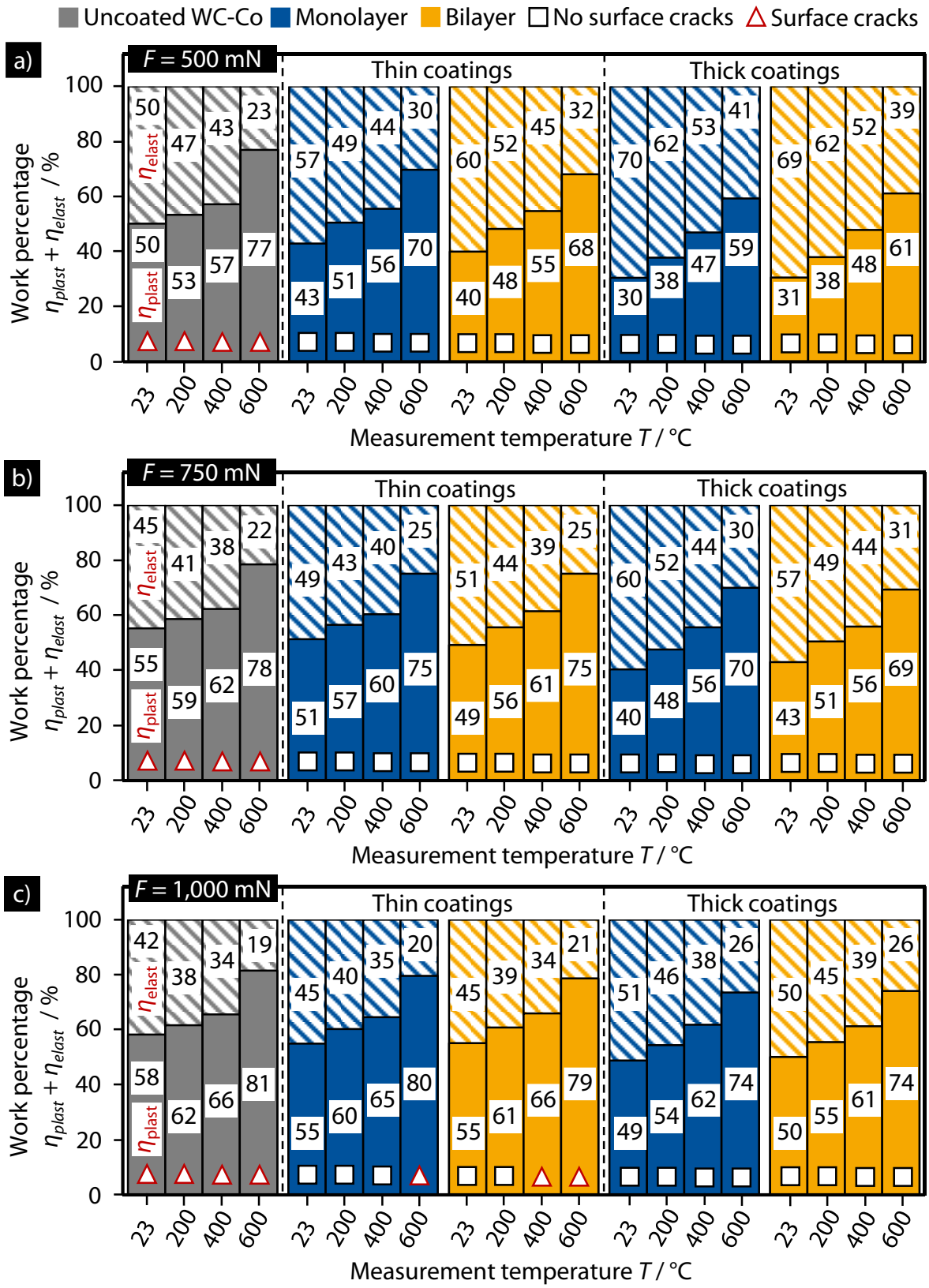

Figure 6.9: Temperature dependent work percentages η_{plast} and η_{elast} of uncoated cemented carbide and coated compounds at (a) F = 500 mN, (b) F = 750 mN and (c) F = 1,000 mN

For thick coating compounds, the η_{plast} and η_{elast} differences with the uncoated substrate remain $|\Delta\eta| \geq 4$ % for all F and T combinations until $F \leq 1{,}250$ mN, see Figure 6.9 and Figure 6.10(a). One exception is observed at $F = 1{,}250$ mN and $T = 400$ °C. For relatively higher indentation depths at $F = 1{,}500$ mN, the η_{plast} and η_{elast} differences between the uncoated cemented carbide and the thick coating compounds reduce to $|\Delta\eta| \leq 3$ %, indicating a dominant influence of the substrate on the deformation response of compounds, see Figure 6.10(b).

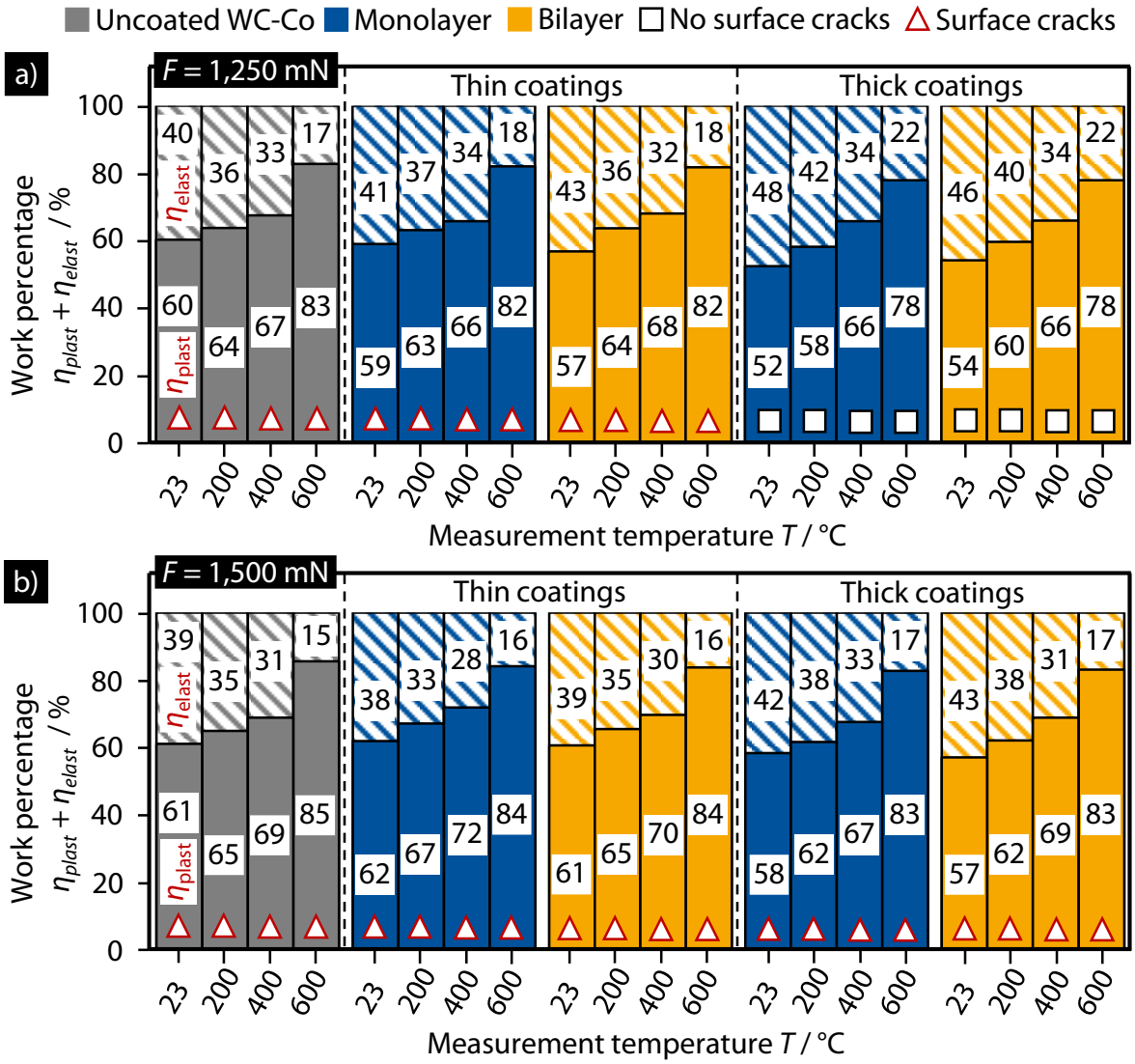

Figure 6.10: Temperature dependent work percentages η_{plast} and η_{elast} of uncoated cemented carbide and coated compounds at (a) $F = 1{,}250$ mN and (b) $F = 1{,}500$ mN

Among the coated variants, thick coating compounds consistently exhibit lower η_{plast} and higher η_{elast} as compared to thin coating compounds for all and F and T combinations, see Figure 6.9

and Figure 6.10. However, as observed for h_{max} and h_{plast}, the η_{plast} and η_{elast} differences between the thin and thick coating compounds reduce with the increase in indentation force or measurement temperature. Nonetheless, the thick coating compounds maintain a difference of $|\Delta\eta| \geq 4$ % with thin coating variants for most of the measurements until $F \leq 1{,}250$ mN. This combined with the lower h_{max}, h_{plast}, higher h_e and higher surface crack resistance confirm the superior resistance against plastic deformation and load bearing capacity of the thick coating compounds at higher temperatures. In terms of the coating architecture, the monolayer and the corresponding bilayer variants exhibit comparable temperature dependent deformation mechanics as coating architecture related η_{plast} and η_{elast} differences remain $|\Delta\eta| \leq 3$ %.

The η_{plast} limits for initiation of surface cracks in coated compounds increase with measurement temperature, see Figure 6.9 and Figure 6.10. Irrespective of the coating thickness and the indentation force, the coated variants with $\eta_{plast} \leq$ ~55 % at $T = 23$ °C show no surface cracks. This limit increases to $\eta_{plast} \leq$ ~61 % at $T = 200$ °C for all coated variants. At $T = 400$ °C, slight coating thickness related difference in η_{plast} limit for surface cracks is observed. The thin coating variants exhibit no surface cracks for $\eta_{plast} \leq$ ~65 %, while the η_{plast} limit increases to $\eta_{plast} \leq$ ~66 % for thick coating variants. This minor difference of $\Delta\eta \approx 1$ % is attributed to the decimal place rounding off error. At $T = 600$ °C, the η_{plast} limit of surface crack resistance significantly increases to $\eta_{plast} \leq$ ~78 % for all coated compounds. Depending on the coating thickness, these temperature dependent η_{plast} limits for the surface crack resistance are reached at different indentation forces. For instance, at $T = 600$ °C, the corresponding η_{plast} limits for the surface crack resistance are reached by thin coating compounds at $F = 1{,}000$ mN and by the thick coating variants at $F = 1{,}500$ mN. The percentual contributions η_{hp} and η_{he} of h_p and h_e to h_{max}, respectively, are shown in Appendix III. There again, the η_{hp} limit of surface crack resistance increases from $\eta_{hp} \leq$ ~51% at $T = 23$ °C to $\eta_{hp} \leq$ ~63 % at $T = 600$ °C.

The effect of measurement temperature on energy consumption by elastic-plastic deformation of the sample, characterized as total mechanical work W_t, is shown in Figure 6.11 for compounds with thin and thick monolayer TiAlCrSiN. A similar trend for bilayer variants is observed. For each indentation force, the compounds exhibit almost linear temperature dependent increase in W_t until the temperature $T = 400$ °C. However, a non-linear increase in W_t from $T = 400$ °C to $T = 600$ °C is apparent, as previously observed for h_{max}, h_p, η_{plast} and η_{elast}. The W_t non-linearity at $T = 600$ °C is more noticeable for higher indentation forces. The thick

coating compounds exhibit higher energy consumption in terms of W_t before surface cracks initiation compared to thin coating for all measurement temperatures.

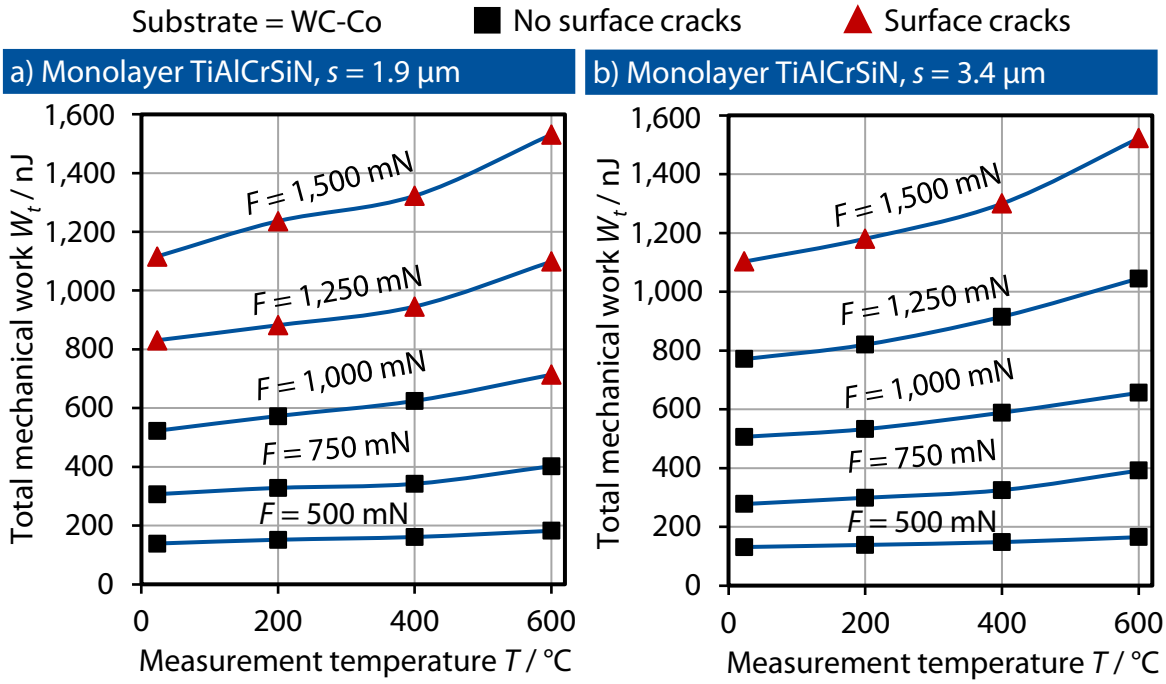

Figure 6.11: Total mechanical work W_t for compounds with (a) thin and (b) thick monolayer during indentation at varying indentation forces and measurement temperatures

The discussed results help to understand the temperature dependent compound deformation mechanics under indentation loading for applications such as warm forming and cutting tools. Increasing the thickness of nitride hard coatings until $s \approx 3.6$ µm does not arrest the temperature dependent drop in plastic deformation resistance of the compounds. However, the thick coating compounds do maintain their higher plastic deformation resistance and surface crack resistance as compared to thin coating compounds until $T = 600$ °C. In terms of coating architecture influence, the additional interface in the coating can restrict the grain boundary activities at elevated temperatures and arrest the drop in plastic deformation resistance and H_{IT} of the coating. This is evident from the reduced difference in elastic-plastic deformation behavior of monolayer and bilayer variants at elevated temperatures during nanoindentation. The additional interface in the bilayer TiAlCrSiN/TiAlCrSiON also contributes to the comparable deformation behavior and surface crack resistance of compounds with bilayer and monolayer coatings under monotonic indentation loadings until $T = 600$ °C. This is confirmed in following investigations on crack growth and damage propagation in compounds.

6.4 Crack growth and damage propagation

The exemplary indent imprints along with the surface crack areas for compounds with thin and thick monolayer TiAlCrSiN at F = 1,500 mN and T = 600 °C are shown in Figure 6.12. The yellow circles mark the indent imprint area, whereas red arrows point out the surface crack locations. The indent imprints at F = 1,500 mN and T = 23 °C for these coated variants have been discussed in section 5.7 of the previous chapter.

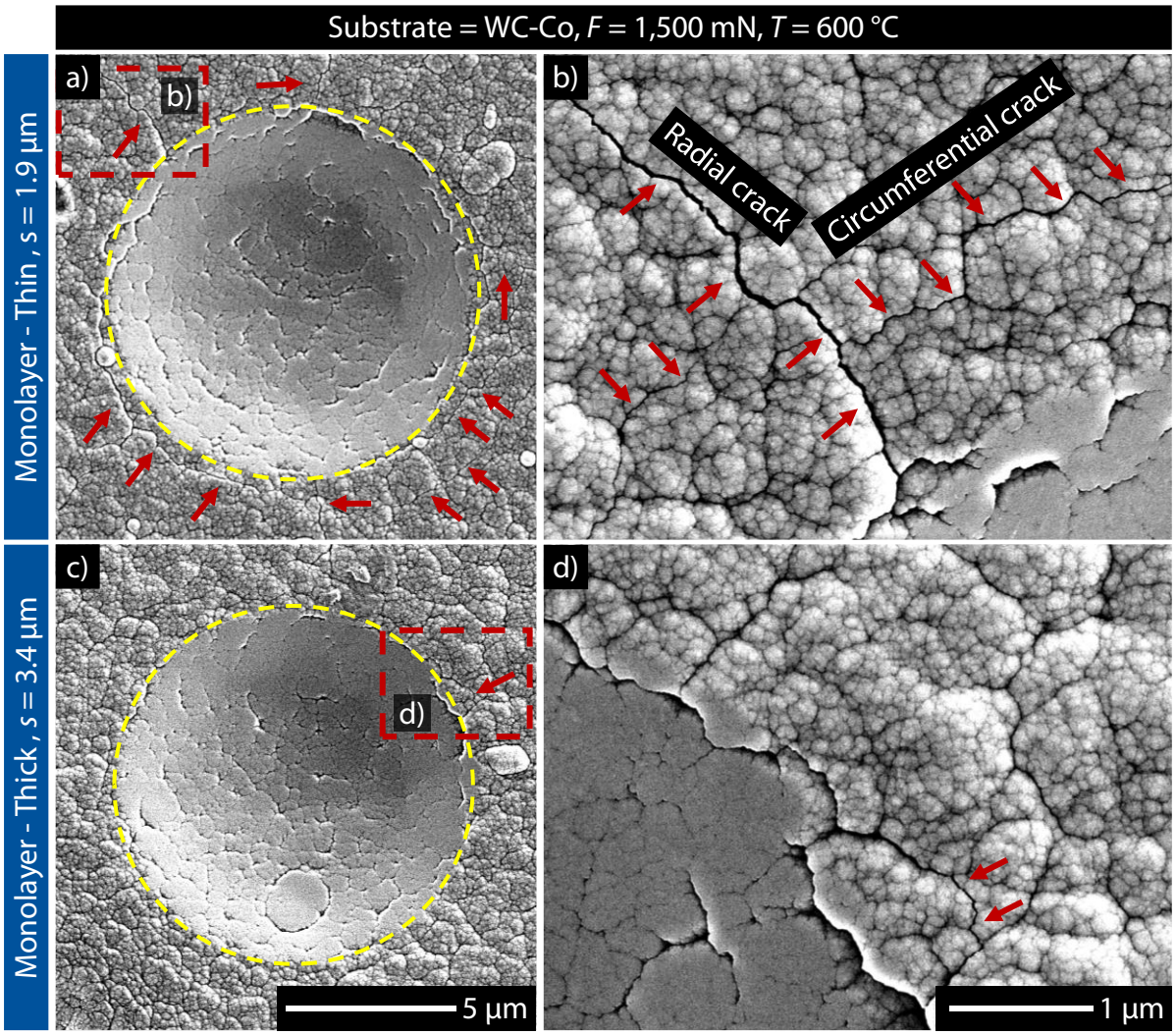

Figure 6.12: Indent imprints with enlarged surface crack areas for compounds with (a,b) thin and (c,d) thick monolayer TiAlCrSiN at F = 1,500 mN and T = 600 °C

A comparable trend in terms of surface crack locations was observed for bilayer variants. For the coated compounds, radial surface cracks are observed until T = 400 °C. At T = 600 °C, differences in crack growth directions appear between thin and thick variants. In addition to

radial cracks, thin coating compounds show circumferential cracks around the indent boundary region at $F \geq 1{,}250$ mN and $T = 600$ °C, see Figure 6.12(a). These circumferential surface cracks are not observed for the indent imprints on thin coating compounds with $F \geq 1{,}250$ mN and $T \leq 400$ °C. Moreover, for the thick coating compounds, no circumferential surface cracks are present even for the extreme values of $F = 1{,}500$ mN and $T = 600$ °C, see Figure 6.12(b). This difference related to the initiation of circumferential surface cracks can be understood by correlating the coating deformation, characterized by permanent indentation depth h_p, to the coating thickness s of the compound. For thin coating compounds, the h_p at $F \geq 1{,}250$ mN and $T = 600$ °C is $h_p \geq \sim 70$ % of the coating thickness. However, for thick coating compounds the permanent indentation depth is $h_p \leq \sim 35$ % of the coating thickness. Hence, for present case, the circumferential cracks around indent imprints in coated compounds originate at higher thermomechanical loading conditions resulting in permanent indentation depths $h_p \geq \sim 70$ % of the coating thickness. A comparison of surface cracks at room temperature and at $T = 600$ °C for the thin and thick monolayer compounds is shown in Appendix III. For thin coating compounds, the surface cracks at $F = 1{,}500$ mN increase with the measurement temperature. However, for the thick coating compounds no increase in number of surface cracks with measurement temperature is observed at $F = 1{,}500$ mN. As previously observed for room temperature measurements, the crack paths are largely limited along the boundaries of large column clusters or through the column clusters along the boundaries of individual fine columns, see Figure 6.12(b) and (d). However, the width of radial surface cracks in thin coatings compounds increase at $T = 600$ °C as compared to thick coating compounds at $T = 600$ °C. This points to increase in coating column separation along the crack paths because of higher deformation of thin coating at $T = 600$ °C.

No significant differences between monolayer and bilayer architectures in terms of surface crack locations are observed, see Figure 6.12 and Figure 6.13. However, the compounds with bilayer TiAlCrSiN/TiAlCrSiON exhibit slight change in surface morphology inside the indent imprint at $T = 600$ °C, see Figure 6.13(a,b). As mentioned in [Arg19], this could presumably be attributed to presence of low melting phases in passive layer for the oxynitride coating. When subjected to severe pressing from the indenter tip at higher temperature of $T = 600$ °C, these phases may undergo a short-time liquification, as marked by yellow arrows in Figure 6.13(a,b). This phenomenon of change in surface appearance is not observed at the lower measurement temperatures $T \leq 400$ °C, see Figure 6.13(c,d).

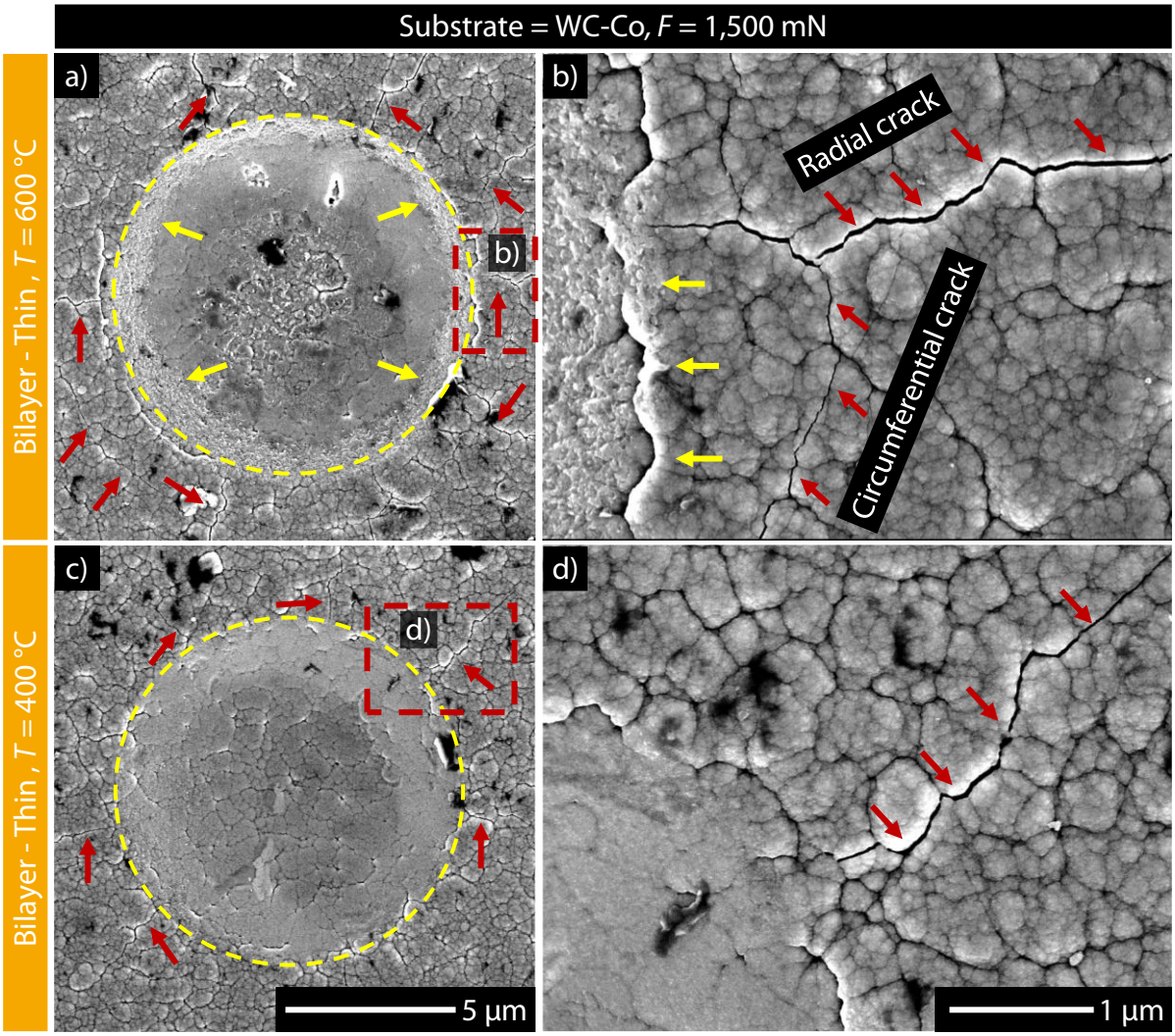

Figure 6.13: Indent imprints with surface crack areas for compound with thin bilayer TiAlCrSiN/TiAlCrSiON at F = 1,500 mN, (a,b) T = 600 °C and (c,d) T = 400 °C

The crack growth in cross-section of selected indent imprints is analyzed using a combination of FIB and TEM. Exemplary images from FIB lamella preparation are shown in Appendix III. Figure 6.14 exhibits the STEM dark field (DF) images of the FIB lamella and the crack areas from the indent cross-section on coated compound with thin monolayer TiAlCrSiN subjected to F = 1,500 mN at T = 600 °C. As evident from Figure 6.14(a), the coating as well as substrate undergo permanent deformation. In boundary region of the indent imprint, thin and thick cross-sectional cracks propagating from TiAlCrSiN towards the substrate are present. The cracks initiate near the surface along the boundary of inclined coating column clusters or individual columns, as marked by dotted lines in Figure 6.14(b), (d) and (e).

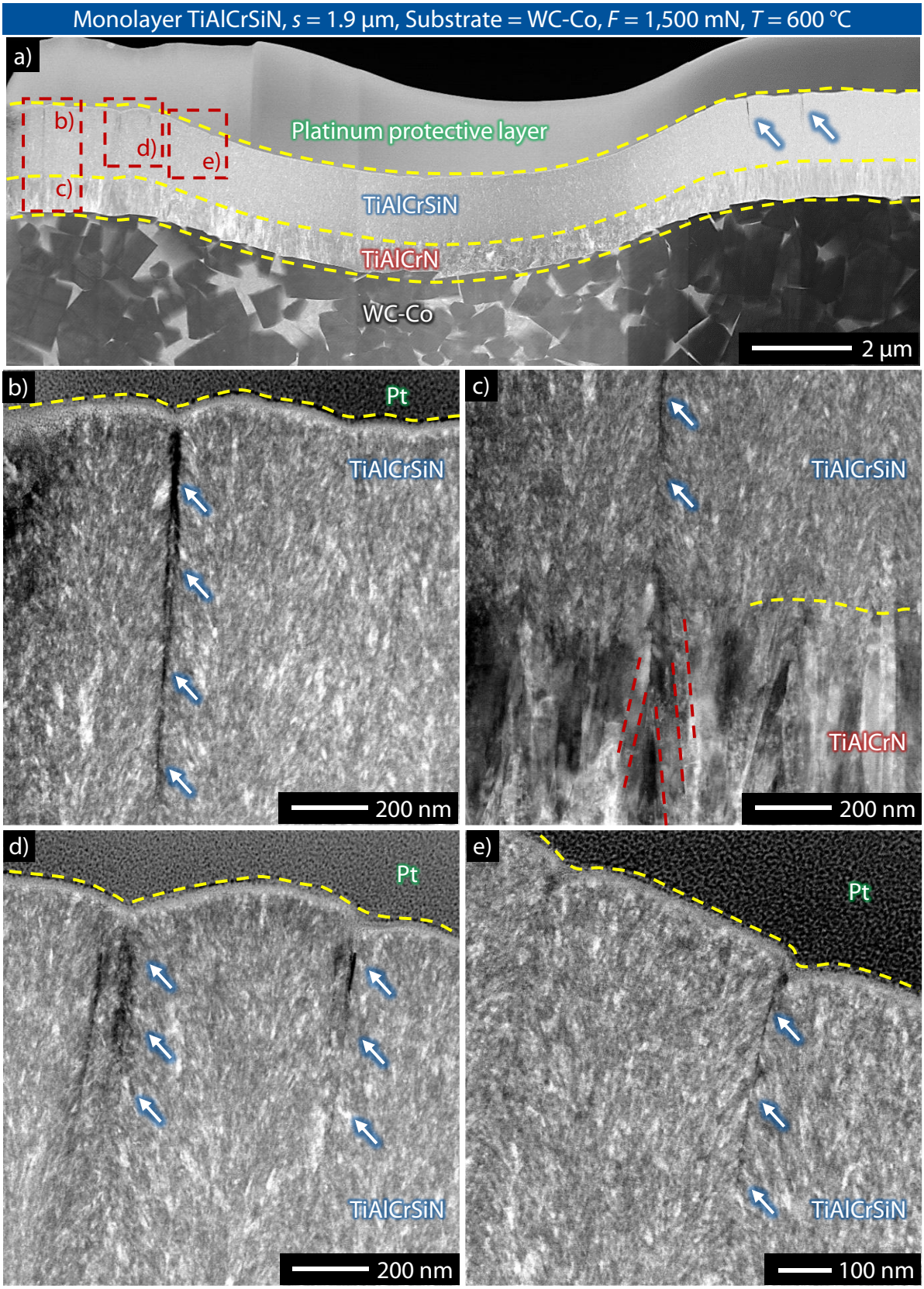

Figure 6.14: STEM dark field (DF) images of (a) cross sectionally cut FIB lamella and (b–e) crack areas from indent on compound with thin monolayer TiAlCrSiN

The crack width reduces along the crack path from the coating surface towards the substrate, see Figure 6.14(b-d). In central region of the indent imprint, only thin cross-sectional cracks, similar to the one shown in Figure 6.14(e), are observed. This indicates that the crack initiation in central region is mainly due to shear sliding between coating columns, whereas in boundary region due to the combination of column separation with column inclination and shear sliding. Moreover, the interface region between the TiAlCrSiN top layer and the TiAlCrN bond layer acts as barrier to crack propagation, see Figure 6.14(c). The TiAlCrN bond layer also shows inclination of columns as exemplarily marked by red dotted line in Figure 6.14(c). This column inclination can initiate smaller thin cracks in TiAlCrN bond layer.

Figure 6.15 displays STEM DF images of cross-sectionally cut FIB lamella and crack areas from the indent imprint on thin bilayer TiAlCrSiN/TiAlCrSiON variant subjected to F = 1,500 mN at T = 600 °C. The nanolaminate structure, more noticeable within the TiAlCrSiON, represents nanolayers of varying chemical composition resulting from different target compositions used during the coating deposition. As observed for thin monolayer variant, thin and thick cross-sectional cracks in the boundary region of indent are present. However, the width of thick cracks in boundary region is higher in the oxynitride top layer, see Figure 6.15(b) and (c). This point towards relatively lower crack resistance of TiAlCrSiON, due to the higher amorphous content, as compared to the TiAlCrSiN at measurement temperature T = 600 °C. Nevertheless, the cross-sectional cracks in the boundary region of indent on bilayer variant are largely limited to the TiAlCrSiON top layer. The crack width reduces in the interface region between TiAlCrSiON and TiAlCrSiN, see Figure 6.15(b) and (c). Hence, despite the lower crack resistance of TiAlCrSiON, the interface between the oxynitride top layer and nitride interlayer provides the bilayer TiAlCrSiN/TiAlCrSiON an additional barrier to the crack growth as compared to the monolayer TiAlCrSiN. The additional interface increases the required energy for cracks to enter the TiAlCrSiN interlayer. This explains the comparable crack resistance of bilayer variants to the corresponding monolayer variants. The cross-sectional cracks in the bilayer variant propagate along the boundaries of coating column clusters or individual columns, see Figure 6.15(b) and (d). The crack initiation mechanism is associated with the coating column inclination as well as shear sliding for the thin cracks and additional column separation for relatively thicker cracks. An example of thin crack in central region of indent is shown in Figure 6.15(d) and (e). The crack growth is limited to the interface between TiAlCrSiN interlayer and TiAlCrN bond layer, confirming the role of interface as barrier to crack growth.

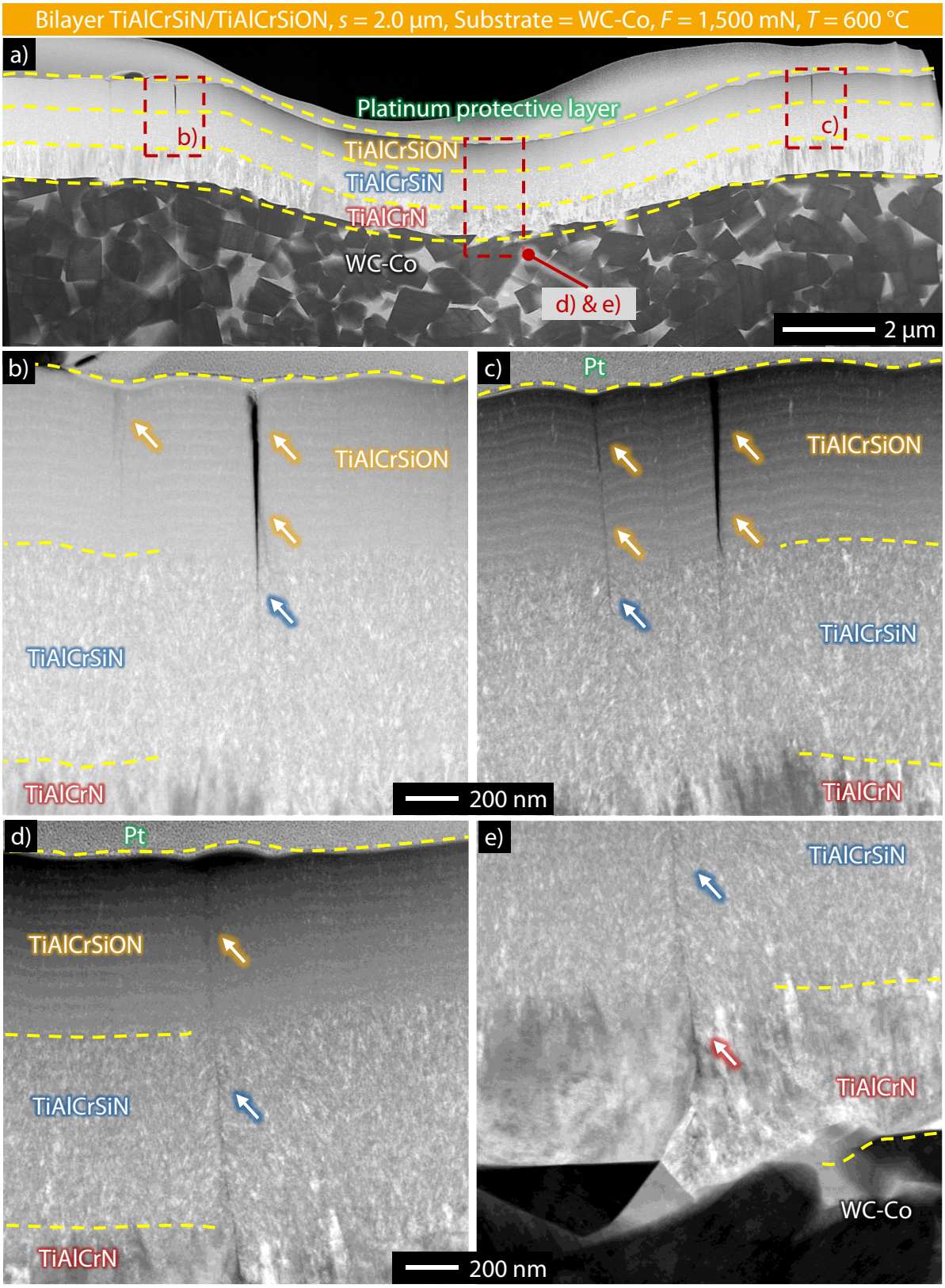

Figure 6.15: STEM DF images of (a) cross sectionally cut FIB lamella and (b–e) crack areas from indent on compound with thin bilayer TiAlCrSiN/TiAlCrSiON

The crack growth in correlation with the coating deformation mechanism can further be understood by considering the deformation profiles of the indents. Figure 6.16 displays the exemplary residual depth profiles, measured by CLSM, for the indents with F = 1.500 mN and T = 600 °C on thin coating variants. The downward material push in the central region of the indent leads to the material pile-up around the boundary region. This results in extensive inclination, shear sliding as well as separation of coating column clusters or individual columns in the boundary region. Hence, large surface cracks as well as thick cross-sectional cracks in the coatings are observed within boundary region of the indent imprint.

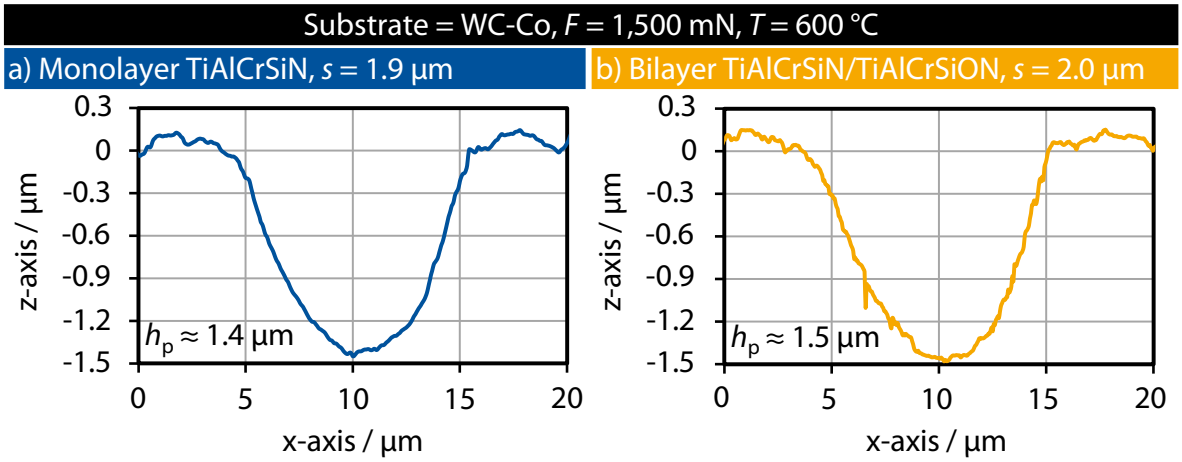

Figure 6.16: Residual depth profiles of indents imprints on the compounds with (a) thin monolayer TiAlCrSiN and (b) bilayer TiAlCrSiN/TiAlCrSiON

A similar trend in terms of crack initiation and propagation mechanisms in coating cross-section is observed during the FIB/TEM analysis of the indent on the thick monolayer variant subjected to F = 1,500 mN at T = 600 °C, see Figure 6.17. The number of cracks as well as the width of cracks in boundary region of the indent is lower with the higher coating thickness as compared to the compounds with thin coatings. Moreover, no cracks are observed in the central region of the indent, see Appendix III. This confirms the coating thickness role in effective distribution of the applied indentation load inside the coating to reduce the stress concentration in the cemented carbide substrate, reduce the overall compound deformation and increase the crack resistance of compound at room as well as at higher temperatures until T = 600 °C for the considered load range. It is also important to consider the role of substrate material. As compared to steel substrates, the cemented carbide provides better support to the nitride hard coatings for resisting plastic deformation under indentation loading. This also helps the thick

coatings with $s \approx 3.6$ µm to simultaneously increase the plastic deformation and crack resistance of the compounds. In present investigations, no evidence of crack propagation from coating into the cemented carbide substrate is found. This highlights the protective role of investigated coatings to bear bulk of the loading in application and delay the damage propagation in substrate of coated tools subjected to indentation loadings at higher temperatures.

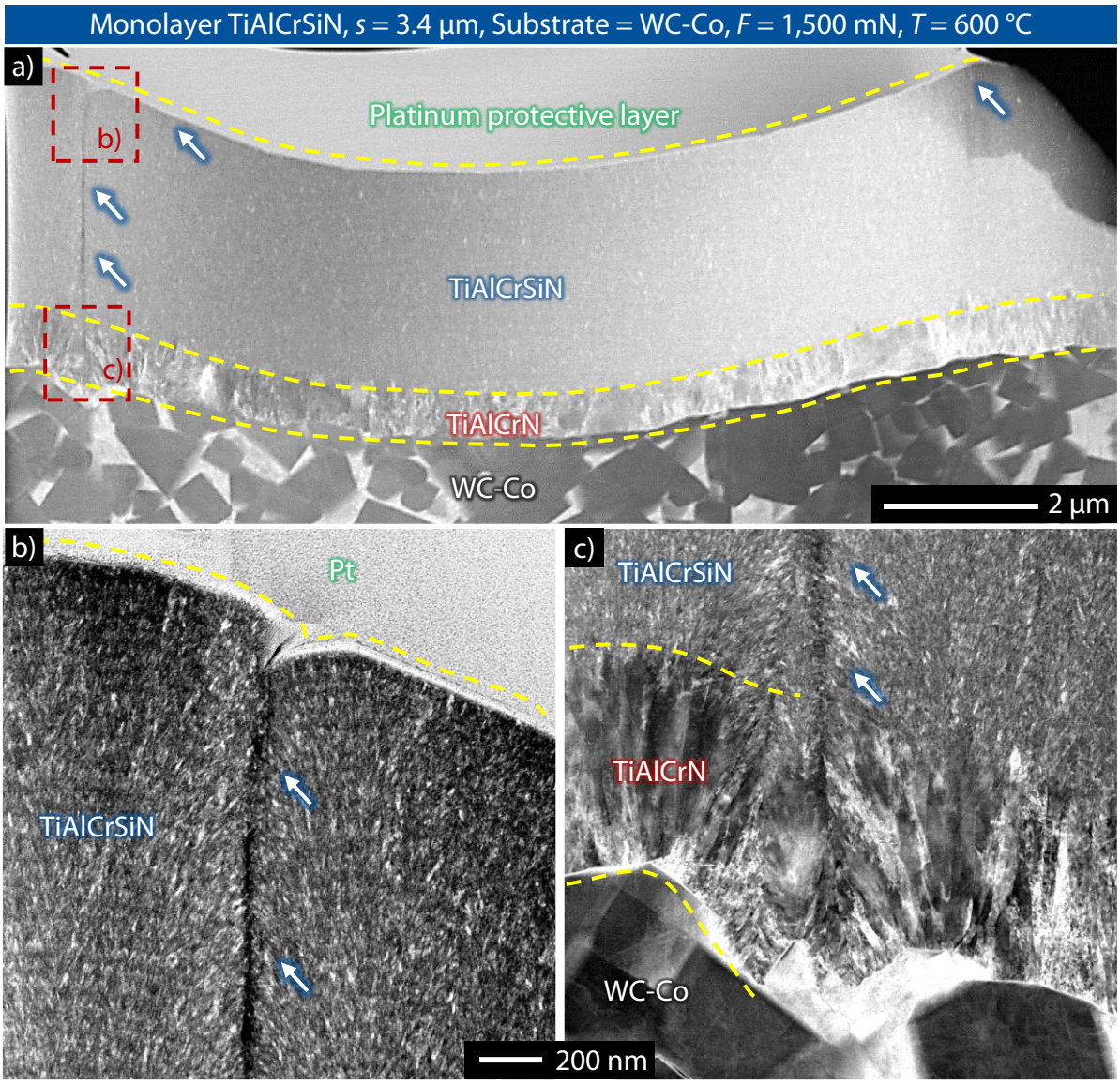

Figure 6.17: STEM DF images of (a) cross sectionally cut FIB lamella and (b,c) crack areas from indent on compound with thick monolayer TiAlCrSiN

The observations from chapter 5 and chapter 6 of this dissertation confirm that the mesoscale mechanisms of plastic deformation and cross-sectional crack initiation in the columnar nitride

hard coatings under monotonic and sliding indentation loadings are similar. However, the crack propagation along the coating surface is influenced by the loading condition. For monotonic indentation load, radial surface cracks grow along the column boundaries in the boundary region of indent imprint. Moreover, for higher compound deformation in terms of the permanent indentation depth $h_p > \sim 70$ % of the coating thickness, circumferential surface cracks accompany the radial cracks in the boundary region of indent imprint. In case of sliding indentation load, the additional material ploughing by the indenter tip contributes to surface crack growth along the coating columns from center to shoulder region of the scratch track.

6.5 Conclusions on temperature dependent deformation mechanics

The main findings from this chapter, which answer RQ4 and RQ5 of the dissertation, are as follows:

- The plastic deformation and indentation creep of columnar nitride hard coatings as well as the compounds with cemented carbide substrate increase at higher temperatures until $T = 600$ °C mainly due to the escalation of grain boundary activities. Hence, increasing the coating thickness from $s \approx 2.0$ µm to $s \approx 3.6$ µm does not arrest the temperature dependent drop in plastic deformation resistance of compounds. However, the thick coating compounds maintain their higher plastic deformation resistance and surface crack resistance from room temperature until $T = 600$ °C compared to the thin coating variants.
- The indentation test data-based parameters h_{max}, h_p, h_e, W_t, W_{elast}, W_{plast}, η_{plast} and η_{elast} provide promising basis to understand high temperature deformation mechanics of compounds. Moreover, the η_{plast} and η_{hp} continue to provide reasonable criteria for comparing the temperature dependent surface crack resistance of compounds with nitride hard coatings. The temperature driven increase in grain boundary activities allows the compounds to undergo higher plastic deformation before surface crack initiation. Accordingly, η_{plast} and η_{hp} limits for surface crack resistance increase with the temperature.
- The higher amorphous content reduces the high temperature crack resistance of TiAlCrSiON as compared to the TiAlCrSiN under monotonic indentation loading. However, the additional interface inside the coating allows the compounds with bilayer TiAlCrSiN/TiAlCrSiON to maintain comparable temperature dependent surface crack resistance to the ones with monolayer TiAlCrSiN.

7 Data driven models for prediction of deformation mechanics

This chapter addresses RQ6 by evaluating the potential of data driven modeling approaches based on machine learning algorithms for predicting the temperature dependent deformation mechanics of compounds. Machine learning (ML) is a subset of artificial intelligence, dealing with algorithms and statistical models to identify patterns in the data. ML models allow computers to interpret, learn and adapt from the given data to make predictions and decisions like humans. Three machine learning algorithms, each for prediction of temperature dependent compound deformation and surface cracking behavior are trained, tested and evaluated. For this purpose, the experimental data of instrumented indentation tests and coating properties of compounds with monolayer TiAlCrSiN and bilayer TiAlCrSiN/TiAlCrSiON from chapters 5 and 6 are used as exemplary dataset.

7.1 Modeling approach

In order to predict the temperature dependent deformation mechanics of compounds, the data driven modeling approach is subdivided into two primary ML tasks, namely, regression and classification, see Figure 7.1. The regression models predict continuous values based on the input data. A classical example for such tasks is polynomial regression. Classification tasks involve prediction of discrete outcomes or categorization of data into different classes. In present study, the prediction of indentation test data-based parameters, such as maximum indentation depth h_{max}, etc., to characterize the deformation behavior of compounds represents a regression task. The prediction whether the compound exhibits surface cracks at the given indentation force F and temperature T is a classification task. The coating characteristics, used as inputs, are the coating architecture, coating thickness as well as the temperature dependent H_{IT}, E_{IT}, $\eta_{plast,coating}$ and $\eta_{elast,coating}$ from high temperature nanoindentations at F = 8 mN.

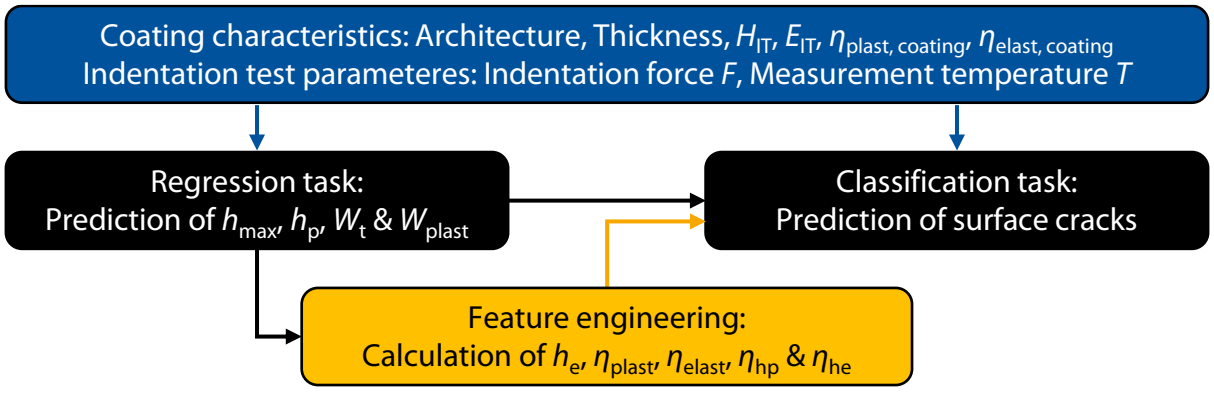

Figure 7.1: Data driven approach for prediction of compound deformation mechanics

Indentation force F and measurement temperature T, at which the compound deformation response is to be predicted, count as inputs of indentation test parameters in micro-range. The regression models are developed to predict the maximum indentation depth h_{max}, permanent indentation depth h_p, total mechanical work W_t and plastic work W_{plast}, see Figure 7.1. Using these four outputs, the remaining parameters for characterization of compound deformation, recovered indentation depth h_e, elastic reverse deformation work W_{elast}, plastic work percentage η_{plast}, elastic work percentage η_{elast}, permanent indentation depth percentage η_{hp} and recovered indentation depth percentage η_{he} can be calculated as mentioned in sections 2.5.3 and 5.7. This step represents feature engineering, where additional features from the data are generated to improve data interpretability as well as the model performance. The inputs for the classification models include the coating characteristics, indentation force F, measurement temperature T and characterized compound deformation behavior. Once trained and tested, the regression and classification models can be coupled to predict the deformation mechanics of compounds under the indentation loading and reduce the required experimental effort.

7.2 Machine learning algorithms

For the development of prediction models, three widely used machine learning algorithms in the literature were chosen. In following section, the architecture and working principle of these algorithms are briefly introduced based on the basic knowledge derived from [RM19, Mur22].

Polynomial regression

Polynomial regression (PR) is a classical technique from statistics to find relationships between independent and dependent variables. The technique is an extension of linear regression to model non-linear relationships between the input and output variables, see Figure 7.2. In present study, polynomial regression is used as an example of classical statistical models for comparison with advanced machine learning algorithms.

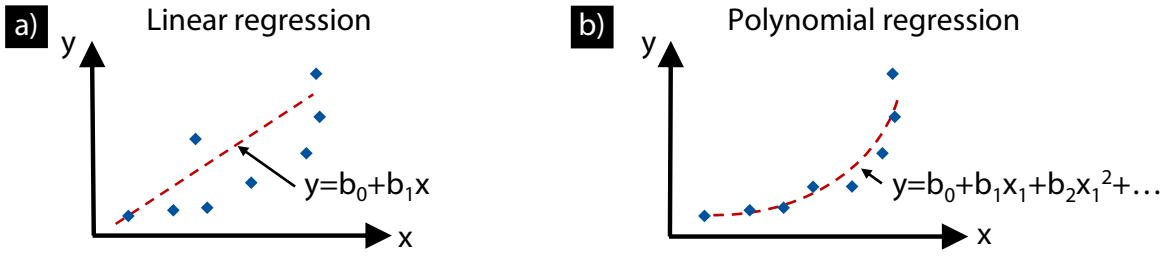

Figure 7.2: Schematic of (a) linear and (b) polynomial regression methods

Multilayer perceptron

Multilayer perceptron (MLP) is a type of feed-forward artificial neural network (ANN). ANNs are inspired by the functioning principle of human brain and consist of interconnected "neurons" organized in layers. The MLPs comprise of an input layer, output layer and one or more hidden layers in between, see Figure 7.3(a). The working principle of neurons in MLP is shown schematically in Figure 7.3(b). Each neuron generates a weighted sum of n inputs from the previous layer and adds it to the bias term. The activation or step function compares the final sum to a certain threshold value [JMM96]. Depending on the choice of activation function, the output y from each neuron can take discrete or continuous values after threshold comparison. The training of MLPs consists of iterative forward and backward passes until the model converges to a minimal error between the predicted and actual values. During the forward pass, predictions and the corresponding errors to the actual values are computed. During the backward pass, the weights and biases are adjusted to minimize the errors between the predicted and actual values. In the present study, the MLP algorithm is used for regression as well as classification task.

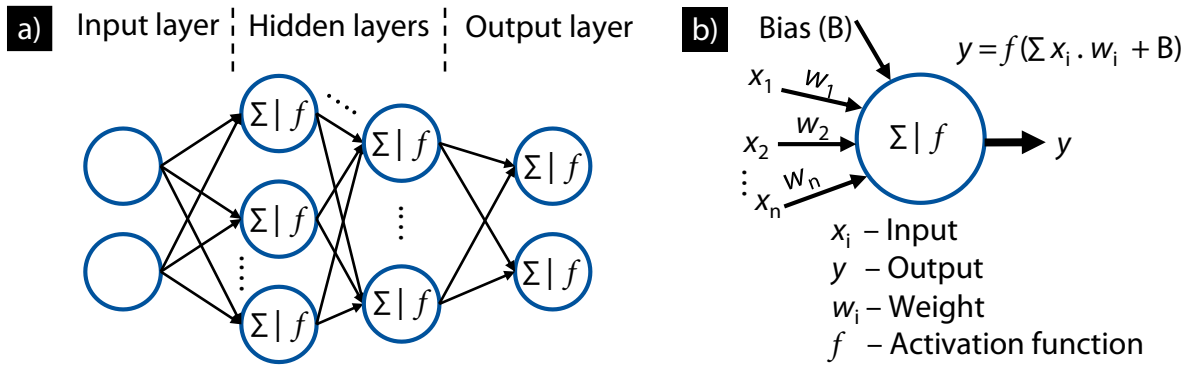

Figure 7.3: Schematic of (a) multilayer perception and (b) working principle of neurons

Random forest

Random forest (RF) belongs to the ensemble learning technique of ML, in which several small and relatively weaker sub-models are combined to achieve better predictions than the single model approach. The RF architecture consists of multiple decision trees, see Figure 7.4. Each decision tree contains random subsets of data points as well as features. The data subsets are chosen from the training data using the bagging method as per [Bre96]. During bagging, the individual data points are randomly selected, whereby some of the data points are repeated in multiple decision trees while others are excluded. To ensure low correlation among the decision

trees and diversity within the forest, the data features are also selected in a similar fashion as bagging for each decision tree [Bre01]. For regression tasks, the final estimation from random forests is the average of outputs from individual decision trees. In case of classification, the final decision is based on the majority voting. In the present study, the random forest algorithm is used for regression as well as classification task.

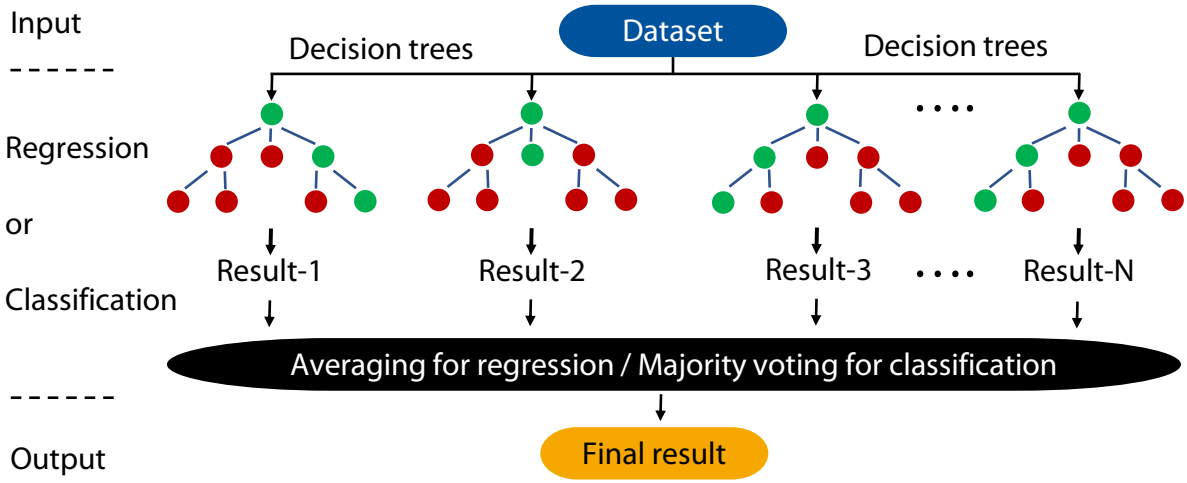

Figure 7.4: Schematic of the architecture of random forest ML algorithm

Support vector machine

Support vector machine (SVM) works by finding one or more optimal hyperplanes (HP) in a multidimensional space to separate the data points into different classes. The optimal hyperplane is the one that maximizes the margins between the different classes, see for instance HP2 in Figure 7.5(a).

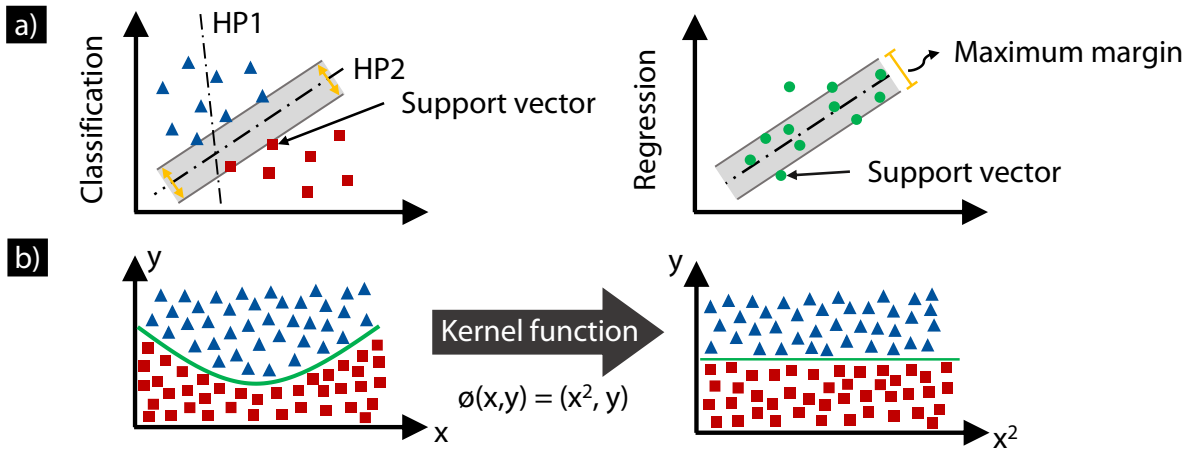

Figure 7.5: Schematic of (a) SVM working principle and (b) the kernel function

With the help of kernel functions, the deterministic algorithms of SVM can handle non-linear classifications by mapping the data in higher-dimensional space, see Figure 7.5(b). The goal for the regression task is to find an optimal hyperplane function to predict the data points within the defined deviation range or margins, see Figure 7.5(a). Support vectors are the margins of calculated deviation range. In present study, SVM algorithm is used for only classification task.

7.3 Model training and testing

The model training and testing approach for the regression and classification tasks is shown in Figure 7.6. For this purpose, the program was written in Python programming language. After cleaning, the dataset for regression task consisted of 365 data points with varying indentation force F, measurement temperature T and coated compound combinations. To account for the experimental variation in outputs with the same set of inputs, the dataset included repetitive measurements at each F, T and coated variant combination. This is not applicable for the classification task. Hence, average of 5 individual measurements for each F, T and coated variant combination was considered, resulting in a total of 80 data points. The database structure for both tasks is shown in Appendix IV. 80 % of the data was used for training and validation while the remaining 20 % was set aside for the testing. The test dataset consisted of randomly selected data points, which the model did not encounter during the training or validation. Hence, additional testing of the models is not necessarily required with the considered approach.

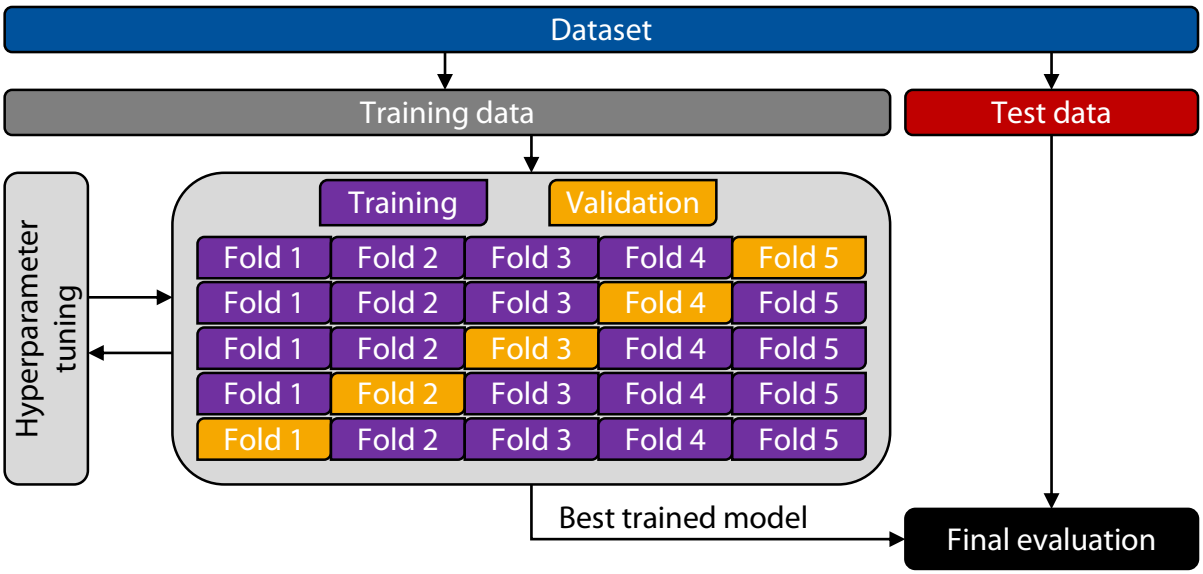

Figure 7.6: Schematic illustration of the ML model training and testing approach for the regressions and classification tasks

Python library GridSearch was used to find the optimal hyperparameters, train as well as cross-validate the ML models. Hyperparameters are configuration settings of ML algorithms that control the training process. For hyperparameter tuning, the ML model is trained and validated with varying hyperparameters. Depending on the number of folds in the training dataset, the cross-validation method involves iterative training and validation steps. In each step, the position of validation data fold is varied until the model is trained as well as validated with all the data points from the training dataset, see Figure 7.6. At the end, the results from each training step are averaged to evaluate the model training and validation performance. As compared to the single step train-test approach, the cross-validation method provides better evaluation of the model generalization ability. In the present case, the training dataset was sub-divided into five equal folds. Four folds were utilized to train the models and one fold of data was used for the validation in each training step. Hence, during the hyperparameter tuning, the ML models were trained and cross-validated five times for each set of hyperparameters. At the end, the best trained ML model with the optimal hyperparameters resulting in the least average error from the five training-validation steps was selected for performance evaluation with the test data. The described training and testing approach was repeated for each of the advanced ML algorithms namely, MLP and RF for the regression task as well as SVM, MLP and RF for the classification task. The model parameters for each considered ML algorithm are mentioned in Appendix IV.

7.4 Prediction of temperature dependent deformation behavior

The prediction models with the three ML algorithms are evaluated on test dataset using four different metrics. Table 7.1 shows the performance evaluation of the ML models for prediction of temperature dependent compound deformation behavior. R-squared (R^2) is a metric to evaluate how well the predictions from ML model match the actual data. R^2 varies between -1 and 1, where the values close to 1 indicate the model ability to explain the variance in the data. Mean absolute percentage error (*MAPE*) is a metric for model accuracy and represents the mean absolute error (*MAE*) between the predicted and actual value as percentage. Unlike averaging the error in *MAE*, the maximum absolute error (*MaxAE*) is the single largest error between predicated and actual values. *MaxAE* is a metric to evaluate the worst-case prediction of the ML regression model. Among the three ML models, the top performing metric values are represented in blue color while the least suitable values are shown in red, see Table 7.1. For all four outputs and evaluation metrices, the RF algorithm exhibits an overall best performance

among the considered models. The PR also displays a promising potential to predict h_{max}, W_t and W_{plast} with high accuracy. However, the PR based ML model exhibit a difference of $MaxAE$ = 299.7 nm from the actual h_p value in worst case. The MLP based ML model performs reasonably well for h_{max} and h_p prediction. However, the model performance significantly decreases for W_t and W_{plast}. Moreover, the MLP exhibits high $MaxAE$ values for all four outputs.

Table 7.1: Evaluation of the ML models for regression task on test dataset

Output	Metric	Polynomial regression (PR)	Multilayer perceptron (MLP)	Random forest (RF)
Maximum indentation depth h_{max}	R^2 / -	0.995	**0.981**	**0.996**
	$MAPE$ / %	**1.6**	2.9	2.0
	MAE / nm	**22.7**	42.3	23.9
	$MaxAE$ / nm	120.0	**241.7**	**92.0**
Permanent indentation depth h_p	R^2 / -	**0.976**	0.982	**0.993**
	$MAPE$ / %	4.6	**5.1**	**4.4**
	MAE / nm	29.8	**33.0**	**24.2**
	$MaxAE$ / nm	**299.7**	223.0	**88.4**
Total mechanical work W_t	R^2 / -	0.997	**0.592**	**0.999**
	$MAPE$ / %	3.5	**49.9**	**1.9**
	MAE / nJ	15.5	**221**	**10.4**
	$MaxAE$ / nJ	80.9	**645.6**	**44.6**
Plastic work W_{plast}	R^2 / -	0.993	**0.737**	**0.999**
	$MAPE$ / %	10.2	**79.8**	**3.8**
	MAE / nJ	20.9	**136**	**11.5**
	$MaxAE$ / nJ	74.9	**512.0**	**46.7**

Most suitable value | **Least suitable value**

The performance evaluation of the random forest-based ML model is shown graphically in Figure 7.7. Although the test data is randomly selected, the data for each output is arranged in ascending order for better interpretation. Some small differences are visible in h_{max} and h_p predictions for relatively lower values. However, the ML model performance is consistent over the entire data range. This means that the RF based ML model is able to learn and predict the non-linearities in the temperature dependent deformation behavior of the compounds over the entire range of considered indentation force F and measurement temperature T combinations.

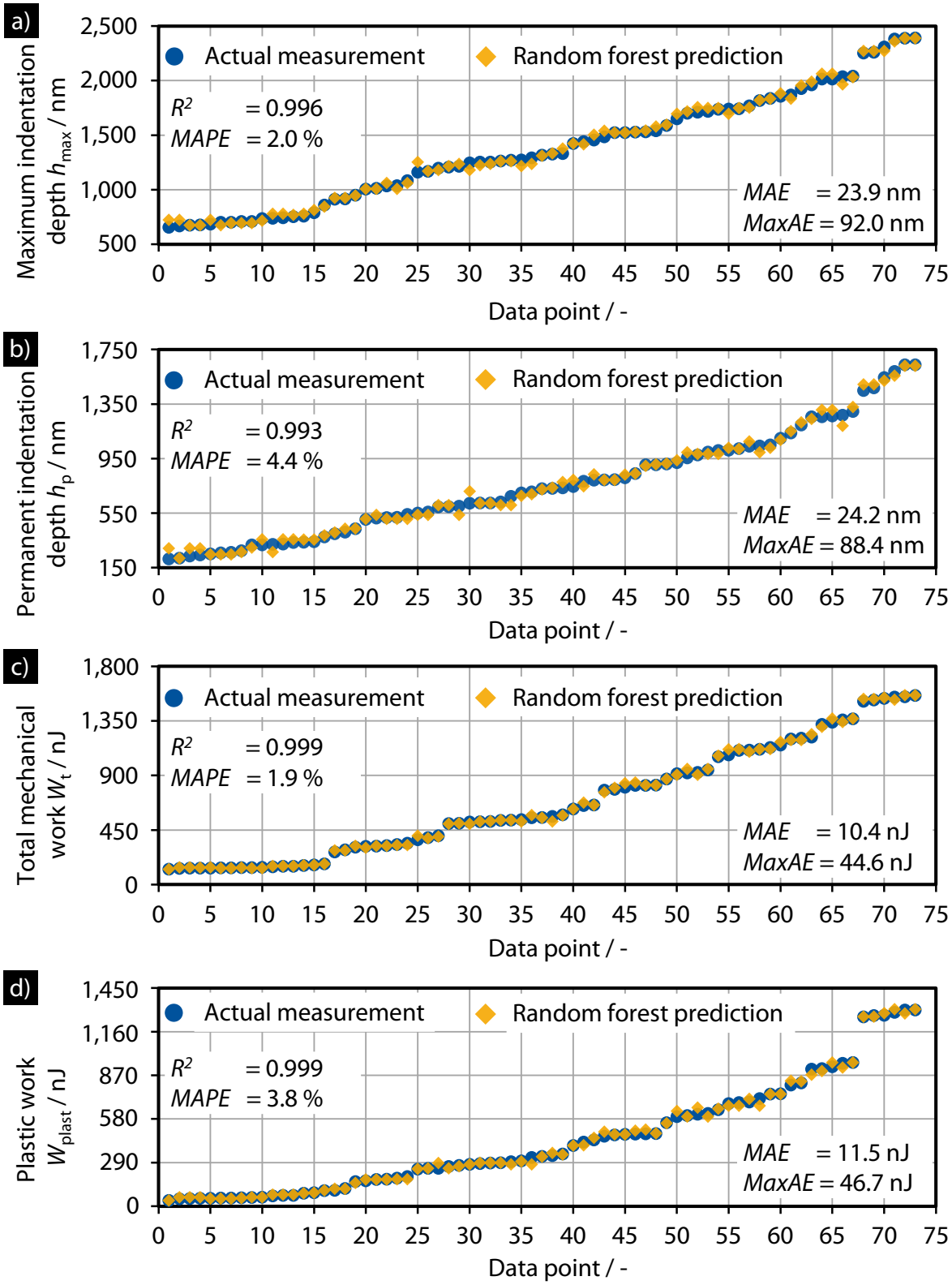

Figure 7.7: Comparison of actual and predicted values of the random forest based ML model for (a) h_{max}, (b) h_p, (c) W_t and (d) W_{plast} on the test dataset which the model did not encounter during the training

7.5 Prediction of temperature dependent surface cracking behavior

The performance evaluation of different ML models for prediction of temperature dependent surface cracking behavior of compounds is shown in Figure 7.8. For classification task, the model accuracy (*ACC*) from the cross-validation during the training and testing is considered as comparison metric. The *ACC* represents the percentual contribution of correct predictions to the total predictions by the model. SVM, MLP as well as RF perform reasonably well. The model accuracy for the RF slightly reduces for the test data but remains *ACC* > 85 %. Overall, the SVM and MLP exhibit comparable model generalization ability to maintain the *ACC* from the training and validation data to the new, unseen test data.

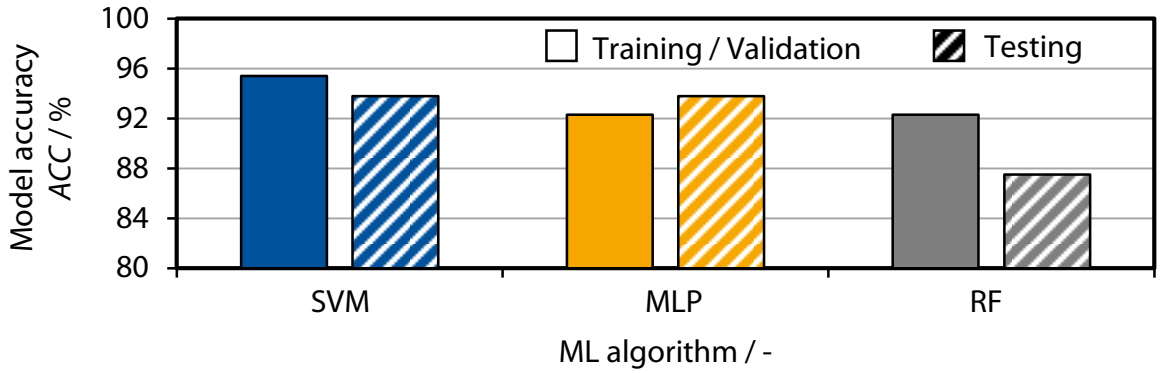

Figure 7.8: Accuracy of the developed machine learning models for the classification task

In addition to the model accuracy, the performance of ML models is evaluated with confusion matrix and corresponding calculated model precision for the test dataset, see Figure 7.9. The confusion matrix evaluates model predictions, while highlighting the different cases of correct and incorrect classifications. The model precision (*PPV*) is defined as the percentual contribution of true positives to the sum of true and false positive predictions by the model. In the present case, the positive prediction is when the model suggests that the compound exhibits surface cracks. The trained ML models show better fit for the negative outcomes as compared to the positive outcomes. This is attributed to the higher number of data points for negative outcomes as compared to the positive outcomes in the training and validation data. Moreover, the SVM and MLP exhibit model precision *PPV* > 80 %, whereas for the RF the precision reduces to *PPV* ≈ 67 %. Due to the limited data availability, the model *ACC* and *PPV* values change significantly for the small differences in the prediction results. Nonetheless, the employed ML models exhibit promising potential to accurately predict the temperature dependent surface cracking behavior of the compounds.

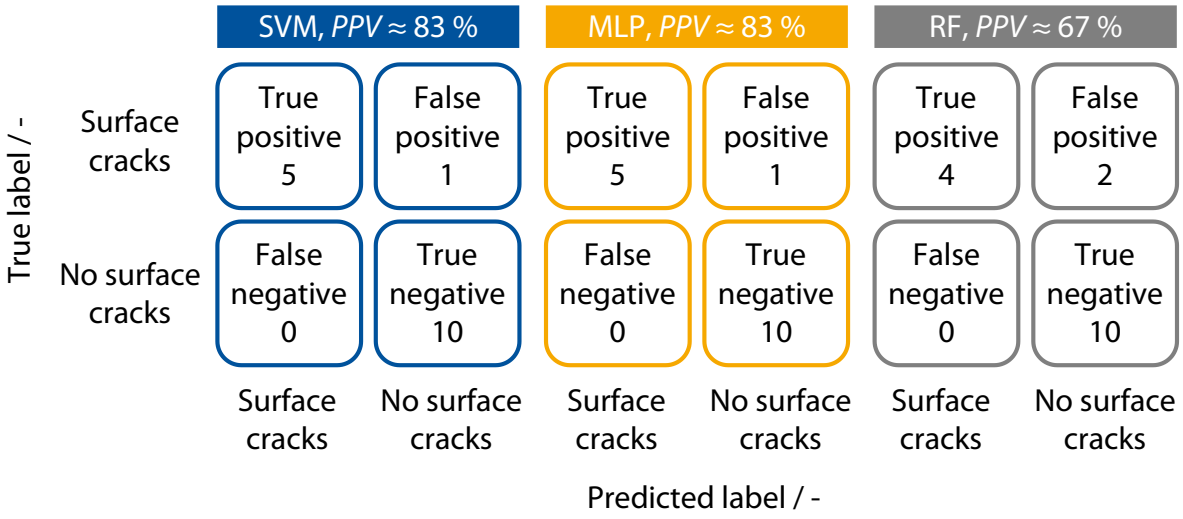

Figure 7.9: Confusion matrices of the developed machine learning models for prediction of temperature dependent surface cracking behavior

Figure 7.10 shows a comparison matrix of actual temperature dependent surface cracking behavior of compounds with predictions by SVM based ML model on the test data. Out of the 16 randomly selected data points, the ML model correctly predicts 15 test data points. The ML model falsely classifies the surface crack initiation at $F = 1{,}000$ mN and $T = 400$ °C for the compound with thin bilayer variant. This data point represents the false positive in Figure 7.9.

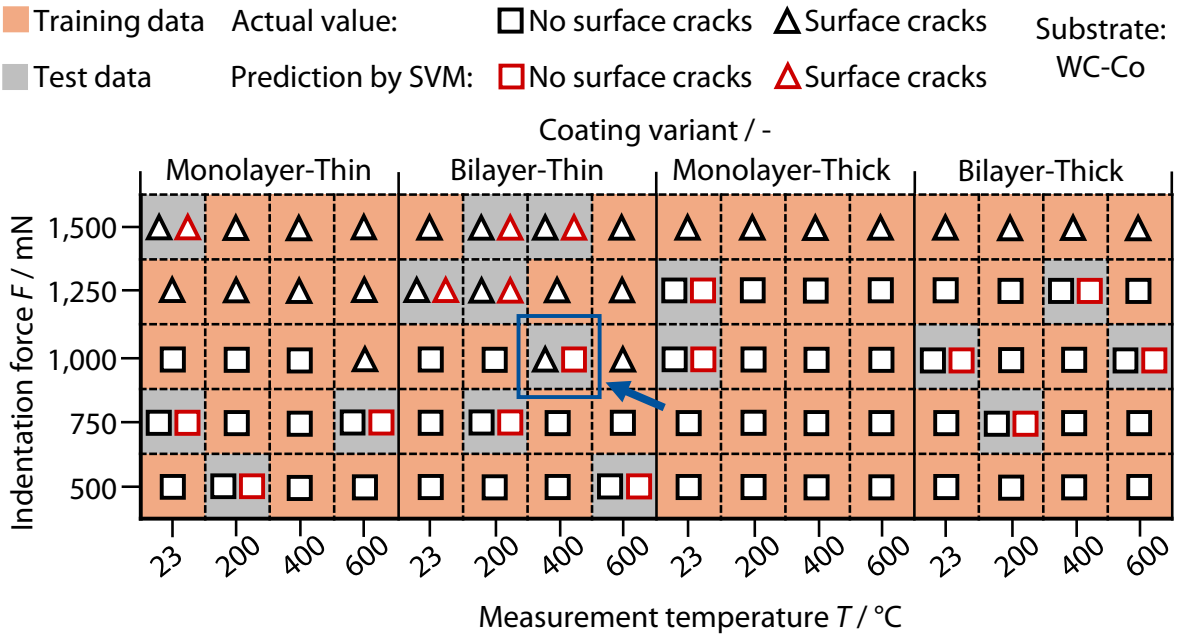

Figure 7.10: Comparison of actual and prediction by the support vector machine based ML model regarding surface cracking behavior of compounds

The comparison matrix for MLP was similar to SVM, whereas for the RF an additional data point corresponding to $F = 1{,}250$ mN and $T = 23$ °C for the thin bilayer variant was falsely predicted. The performance evaluation results show that the SVM and MLP based ML models are able to learn and predict most of the non-linearities in the temperature dependent surface cracking behavior of compounds over the considered combinations of indentation force F and measurement temperature T.

7.6 Conclusions on data driven predictive models

To answer RQ6 related to evaluation of data driven modeling approach for the prediction of temperature dependent deformation mechanics of compounds under monotonic indentation loading, three machine learning algorithms were compared in this chapter. In the presented study, the ML model with random forest algorithm shows the most promising results to learn and predict the non-linearities in compound deformation behavior arising from different combinations of coating characteristics, indentation forces and measurement temperatures in exemplary dataset. Moreover, the support vector machine and multilayer perceptron are the ML algorithms of choice for prediction of temperature dependent surface cracking behavior of the compounds. It is pertinent to mention that the modeling approach and the corresponding ML algorithms are evaluated on exemplary dataset having limited variation of coating properties and characteristics. Nonetheless, the presented approach exhibits a promising potential to understand the influence of coating dependent variables on deformation mechanics of compounds. The dataset should be increased to incorporate the variations of other coating properties, coating systems, substrate materials and indenter tip geometries of interest. The extended ML models can help to identify unknown correlations between the coating as well as substrate characteristics and the temperature dependent deformation mechanics of compounds. Moreover, the temperature dependent deformation and surface crack resistance of compounds can be characterized with minimal experimental effort during coating development phase using the ML models developed with the presented approach.

8 Summary

The dissertation focused on the investigation of compound deformation behavior and fracture mechanics in correlation with the coating properties under indentation loading conditions. The research motivation was to enable knowledge-based designs of nitride hard coatings for higher functional capability and higher service life of tools during challenging forming or cutting operations. For this purpose, utilization of measurement data from instrumented indentation testing was particularly extended to understand compound deformation behavior in correlation with the crack growth in the coatings on high-speed steel and cemented carbide substrates.

In chapter 4 the effect of coating chemical composition, thickness and resulting compressive residual stresses σ_r on deformation mechanics and impact fatigue behavior of CrAlN coated high-speed steel HS6-5-2C was studied. It is shown that compressive residual stresses σ_r increase with the Al content or thickness of coating. The coupling of higher coating thickness up to $s \approx 3.5$ µm and higher compressive residual stress increases the plastic deformation resistance of the compound under indentation loading. Moreover, for comparable coating thickness, increasing the coating Al content up to $x(Al) \approx 34$ at. % improves the elastic recovery of compound. However, simultaneous increase in the thickness and the compressive residual stresses $|\sigma_r| > 3$ GPa amplifies the brittle fracture of coating under sliding indentation load. These findings contributed to understanding the fatigue behavior of compound under cyclic impact loading. A combination of the coating thickness $s \approx 1.7$ µm and the Al content $x(Al) \approx 34$ at. % leads to moderate compressive residual stresses $|\sigma_r| = (2 - 3)$ GPa and increases the fatigue resistance of compound under cyclic impact loading. Increasing the CrAlN thickness from $s \approx 1.7$ µm to $s \approx 3.5$ µm reduces the compound plastic deformation in terms of impact imprint depth but negatively affects the resistance against crack growth. Furthermore, the coating deformation and crack initiation mechanisms under cyclic impact loading were studied. The increase in coating column inclination and shear sliding over the impact cycles leads to crack initiation and growth along the column boundaries in the boundary region of impact imprint. Despite the lower indentation depth of impact imprints, the augmented brittle fracture behavior of thick coatings combined with extensive inclination and shear sliding of the lengthier coating columns inhibit any improvement in compound resistance against impact fatigue. These findings answer RQ1 of the dissertation.

In chapters 5 and 6 the influence of the coating thickness and the coating architecture on temperature dependent deformation behavior and fracture mechanics of cemented carbide coated with the monolayer TiAlCrSiN and bilayer TiAlCrSiN/TiAlCrSiON was investigated. Increasing the coating thickness from $s \approx 2.0$ µm to $s \approx 3.6$ µm increases the plastic deformation resistance and load carrying capacity of the compounds under monotonic indentation load until measurement temperatures of $T = 600$ °C and under sliding indentation load at room temperature. The expected higher compressive residual stresses of the thicker coatings allow for effective distribution of the applied indentation load inside the coating to reduce the stress concentration in the substrate and decrease the compound deformation. The plastic deformation and indentation creep of columnar nitride hard coatings as well as the compounds increase at higher temperatures until $T = 600$ °C mainly due to the escalation of grain boundary activities. Therefore, increasing the coating thickness to $s \approx 3.6$ µm does not arrest the temperature dependent drop in the plastic deformation resistance of compounds. However, the compounds with thick coatings maintain higher resistance against plastic deformation and surface cracks from room temperature till $T = 600$ °C as compared to the thin coating variants. Despite the lower crack resistance of oxynitride top layer, because of the higher amorphous content, the compounds with bilayer TiAlCrSiN/TiAlCrSiON show comparable temperature dependent crack resistance to the ones with monolayer TiAlCrSiN. This is attributed to the additional interface in the bilayer coating, which can reduce the grain boundary activities as well as arrest the drop in plastic deformation resistance and H_{IT} of the coating at elevated temperatures. Moreover, the additional interface acts as barrier to cross-sectional crack propagation in the bilayer coating. The coating deformation and crack growth mechanisms are understood under monotonic and sliding indentation loading for deformation zones extending beyond the coating. In the central region of the indent imprint and scratch track, shear sliding between the coating columns during the compound deformation results in growth of thin cracks along the column boundaries. The thin cracks in the boundary region of deformation zones involve column inclination and shear sliding. The thick cross-sectional cracks in the boundary region of indent imprint and scratch tracks originate by coating column separation in addition to the column inclination and shear sliding due to the material pile-up. Moreover, the correlations between the temperature dependent compound deformation behavior and crack resistance were understood and explained using measurement data-based parameters h_{max}, h_p, h_e, W_t, W_{elast}, W_{plast}, η_{plast}, η_{elast}, η_{hp} and η_{he} from the instrumented indentation tests. The η_{plast}, η_{elast}, η_{hp} and η_{he} provide reasonable criteria for comparing the temperature dependent

crack resistance of compounds. With these findings, hypothesis H1 of the dissertation is validated and RQ2 – RQ5 are answered.

In the end, a data driven modeling approach was presented to combine the measurement data from instrumented indentation tests with the coating characteristics for the prediction of temperature dependent compound deformation mechanics. To complete the validation of hypothesis H2 as well as answer RQ6, three machine learning algorithms for prediction of h_{max}, h_p, h_e, W_t, W_{elast} and surface cracking behavior, were trained tested and evaluated. Machine learning model with random forest algorithm exhibits the most promising potential to learn and predict the indentation force, measurement temperature or coating related non-linearities in the compound deformation behavior. The support vector machine and multilayer perceptron are the machine learning algorithms of choice for prediction regarding initiation of surface cracks in compounds at given indentation force and measurement temperature.

The dissertation extends the fundamental understanding on the influences of chemical composition, thickness and architecture of PVD nitride hard coatings on the temperature dependent deformation behavior and the fracture mechanics of compounds. The presented findings serve as coating design guidelines to increase the resistance of PVD coated tool materials against plastic deformation and crack growth under indentation loadings. Moreover, the promising potential of the measurement data from instrumented indentation testing and data driven modeling approach to enable such knowledge-based coating designs is confirmed.

9 Outlook

As future work for CrAlN coated high-speed steels, the scope of fundamental investigations should be extended to the high temperature deformation and thermomechanical fatigue behavior of compounds for warm and hot forming tools. Accordingly, suitable ranges for the advantageous couplings of coating chemical composition, thickness, architecture and resulting compressive residual stresses can be identified for different high-speed steel substrates. For compounds with cemented carbide substrates coated with monolayer TiAlCrSiN and bilayer TiAlCrSiN/TiAlCrSiON, the temperature dependent compound deformation and fracture mechanics under cyclic indentation loadings could be of interest. Moreover, the effect of interface volume and oxygen content on temperature dependent deformation mechanics of the compounds with multilayer TiAlCrSiN/TiAlCrSiON should be investigated.

In general, fundamental understanding of correlations between the temperature dependent deformation behavior and the fracture mechanics of compounds under indentation loadings should be extended. Here, the underlying reasons for pop-in events in individual force-indentation depth curves during monotonic loading, when present, should be investigated in detail. A possible strategy for characterization of pop-in events could be the first derivative of indentation depth over time. This combined with in situ- and ex situ-electron microscopy analysis can help to correlate the pop-in events with deformation and fracture mechanics of coatings as well as compounds. A particular focus in high temperature investigations should be placed on finding out which coating and substrate dependent factors can reduce the indentation creep of compounds.

For the development of data driven predictive models, instrumented indentation tests with different combinations of substrate materials, coating systems and coating properties can be carried out. The simulation models can be used to extend the dataset and include additional information on stress-strain distribution within the compound. However, the volume effect should be considered during development of such simulation models. Unlike the conventional tensile or compression tests, in instrumented indentation tests the effective volume of material subjected to loading increases with the indentation force due to the growing contact area and indentation depth. Simultaneously, machine learning algorithms can be employed to combine experimental and simulative data with the coating, substrate and compound properties or characteristics for prediction of the compound deformation and cracking behavior. Once the

predictive machine learning models with extended database are developed, input parameters of the models can be varied to identify and understand unknown correlations between the coating as well as substrate dependent variables and the compound deformation mechanics with minimal experimental effort.

More importantly, the findings from fundamental investigations and data driven machine learning models should be transferred and validated with the field testing of coated tools for challenging forming and cutting operations. Accordingly, the field validated knowledge-based guidelines for coating designs can reduce the coating development efforts through targeted adjustment of coating chemical composition, thickness, architecture and deposition process parameters for different coating systems and substrate material combinations.

10 References

[ABS09] J. Alami, S. Bolz, K. Sarakinos, High power pulsed magnetron sputtering: Fundamentals and applications, Journal of Alloys and Compounds, 483 (2009), 530–534, DOI: 10.1016/j.jallcom.2008.08.104

[ACL+81] G. R. Anstis, P. Chantikul, B. R. Lawn, D. B. Marshall, A Critical Evaluation of Indentation Techniques for Measuring Fracture Toughness: I, Direct Crack Measurements, Journal of the American Ceramic Society, 64 (1981), 533–538, DOI: 10.1111/j.1151-2916.1981.tb10320.x

[And07] R. A. Andrievski, Nanostructured superhard films as typical nanomaterials, Surface and Coatings Technology, 201 (2007), 6112–6116, DOI: 10.1016/j.surfcoat.2006.08.119

[Arg19] M. Arghavani, Elastic-Plastic deformation and cracking behavior of thin hard chromium-based coatings, RWTH Aachen University, Dissertation, in: K. Bobzin (Hrsg.), Schriftenreihe Oberflächentechnik, Volume 55, 2019, Düren: Shaker Verlag, ISBN: 978-3-8440-6625-8

[BAC+05] J. Bohlmark, J. Alami, C. Christou, A. P. Ehiasarian, U. Helmersson, Ionization of sputtered metals in high power pulsed magnetron sputtering, Journal of Vacuum Science & Technology A, 23 (2005), 18–22, DOI: 10.1116/1.1818135

[BBB+15] K. Bobzin, T. Brögelmann, R. H. Brugnara, M. Arghavani, T.-S. Yang, Y.-Y. Chang, S.-Y. Chang, Investigation on plastic behavior of HPPMS CrN, AlN and CrN/AlN-multilayer coatings using finite element simulation and nanoindentation, Surface and Coatings Technology, 284 (2015), 310–317, DOI: 10.1016/j.surfcoat.2015.07.081

[BBI+09] K. Bobzin, N. Bagcivan, P. Immich, S. Bolz, J. Alami, R. Cremer, Advantages of nanocomposite coatings deposited by high power pulse magnetron sputtering technology, Journal of Materials Processing Technology, 209 (2009), 165–170, DOI: 10.1016/j.jmatprotec.2008.01.035

[BBI+19] B. D. Beake, A. Bird, L. Isern, J. L. Endrino, F. Jiang, Elevated temperature micro-impact testing of TiAlSiN coatings produced by physical vapour deposition, Thin Solid Films, 688 (2019), 137358, DOI: 10.1016/j.tsf.2019.06.008

[BBK+16] K. Bobzin, T. Brögelmann, N. C. Kruppe, M. Arghavani, J. Mayer, T. E. Weirich, On the plastic deformation of chromium-based nitride hard coatings deposited by hybrid dcMS/HPPMS: A fundamental study using nanoscratch test, Surface and Coatings Technology, 308 (2016), 298–306, DOI: 10.1016/j.surfcoat.2016.05.093

[BBK+17a] K. Bobzin, T. Brögelmann, N. C. Kruppe, M. Arghavani, J. Mayer, T. E. Weirich, Plastic deformation behavior of nanostructured CrN/AlN multilayer coatings deposited by hybrid dcMS/HPPMS, Surface and Coatings Technology, 332 (2017), 253–261, DOI: 10.1016/j.surfcoat.2017.06.092

[BBK+17b] K. Bobzin, T. Brögelmann, N. C. Kruppe, M. Arghavani, Investigations on Mechanical and Tribological Behavior of dcMS/HPPMS CrN and (Cr,Al)N Hard Coatings Using Nanoscratch Technique, Advanced Engineering Materials, 19 (2017), DOI: 10.1002/adem.201600632

[BBK+20] K. Bobzin, T. Brögelmann, N. C. Kruppe, M. Carlet, Wear behavior and thermal stability of HPPMS (Al,Ti,Cr,Si)ON, (Al,Ti,Cr,Si)N and (Ti,Al,Cr,Si)N coatings for cutting tools, Surface and Coatings Technology, 385 (2020), 125370, DOI: 10.1016/j.surfcoat.2020.125370

[BBK+21] K. Bobzin, T. Brögelmann, N. C. Kruppe, M. Carlet, Investigation on the incorporation of oxygen and thermal stability of HPPMS TiAlCrSiON nanolayer coatings, Surface and Coatings Technology, 418 (2021), 127231, DOI: 10.1016/j.surfcoat.2021.127231

[BBK+22] K. Bobzin, T. Brögelmann, N. C. Kruppe, H. J. Maier, T. Heidenblut, H.-B. Besserer, C. Kahra, J. Janowitz, CrN/AlN nanolaminates: Architecture, residual stresses, and cracking behavior, Journal of Vacuum Science & Technology A, 40 (2022), DOI: 10.1116/6.0001462

[BBM+21] K. Bobzin, T. Brögelmann, H. J. Maier, T. Heidenblut, C. Kahra, M. Carlet, Influence of residual stresses in hard tool coatings on the cutting performance, Journal of Manufacturing Processes, 69 (2021), 340–350, DOI: 10.1016/j.jmapro.2021.08.011

[BD13] B. Breidenstein, B. Denkena, Significance of residual stress in PVD-coated carbide cutting tools, CIRP Annals, 62 (2013), 67–70, DOI: 10.1016/j.cirp.2013.03.101

[Bea21] B. D. Beake, Elevated temperature nanomechanics of coatings for high-temperature applications: a review, Emergent Materials, 4 (2021), 1531–1545, DOI: 10.1007/s42247-021-00255-w

[BGG+21] Y. Bai, J. Gao, T. Guo, K. Gao, A. A. Volinsky, X. Pang, Review of the fatigue behavior of hard coating-ductile substrate systems, International Journal of Minerals, Metallurgy and Materials, 28 (2021), 46–55, DOI: 10.1007/s12613-020-2203-0

[BJB05] S. Bhowmick, V. Jayaram, S. BISWAS, Deconvolution of fracture properties of TiN films on steels from nanoindentation load-displacement curves, Acta Materialia, 53 (2005), 2459–2467, DOI: 10.1016/j.actamat.2005.02.008

[BKC+21] K. Bobzin, C. Kalscheuer, M. Carlet, M. Tayyab, Influence of Aluminum Content on the Impact Fatigue of HPPMS CrAlN Coatings on Tool Steel, Physical Mesomechanics, 24 (2021), 625–632, DOI: 10.1134/S1029959921050143

[BKC+22] K. Bobzin, C. Kalscheuer, M. Carlet, C. Schulze, Hybrid reactive sputtering of transition metal aluminum oxynitrides, Thin Solid Films, 742 (2022), 139028, DOI: 10.1016/j.tsf.2021.139028

[BKC+23] K. Bobzin, C. Kalscheuer, M. Carlet, S. Schmauder, V. Guski, W. Verestek, M. Tayyab, 3D deformation modeling of CrAlN coated tool steel compound during nanoindentation, Surface and Coatings Technology, 453 (2023), 129148, DOI: 10.1016/j.surfcoat.2022.129148

[BKG+21] K. Bobzin, C. Kalscheuer, G. Grundmeier, T. de los Arcos, S. Schwiderek, M. Carlet, Design of a TiAlON multilayer coating: Oxidation stability and deformation behavior, Surface and Coatings Technology, 421 (2021), 127417, DOI: 10.1016/j.surfcoat.2021.127417

[BKM+25] K. Bobzin, C. Kalscheuer, M. P. Möbius, P. Hassanzadegan Aghdam, Deformation behavior of high Al content CrAlON coatings with varying oxygen content, Surface and Coatings Technology, 496 (2025), 131639, DOI: 10.1016/j.surfcoat.2024.131639

[BKT23] K. Bobzin, C. Kalscheuer, M. Tayyab, Effect of CrAlN coating properties on impact fatigue of tool steel, Surface and Coatings Technology, 471 (2023), 129869, DOI: 10.1016/j.surfcoat.2023.129869

[BKT24a] K. Bobzin, C. Kalscheuer, M. Tayyab, A case study on fatigue damage in PVD coated tool steel under cyclic bending load, Surface and Coatings Technology, 478 (2024), 130505, DOI: 10.1016/j.surfcoat.2024.130505

[BKT24b] K. Bobzin, C. Kalscheuer, M. Tayyab, Tribological behavior of TiAlCrSiN coated cutting tools, Vakuum in Forschung und Praxis, 36 (2024), 18–22, DOI: 10.1002/vipr.202400817

[BKT+25a] K. Bobzin, C. Kalscheuer, M. Tayyab, T. Bergs, M. Meurer, M. Abouridouane, A case study on extended approach for wear analysis of TiAlCrSiN coated cutting inserts, Wear, 572-573 (2025), 206040, DOI: 10.1016/j.wear.2025.206040

[BKT25b] K. Bobzin, C. Kalscheuer, M. Tayyab, Cracking behavior of wear resistant TiAlCrSiN coated cemented carbide compounds, Wear (2025), 205810, DOI: 10.1016/j.wear.2025.205810

[BME+14] Z. Baccouch, R. Mnif, R. Elleuch, C. Richard, Analysis of friction, wear and oxidation behaviour of X40CrMoV5/Fe360B steel couple in an open-sliding contact, Proceedings of the Institution of Mechanical Engineers, Part J: Journal of Engineering Tribology, 228 (2014), 276–287, DOI: 10.1177/1350650113504564

[Bob13] K. Bobzin, Oberflächentechnik für den Maschinenbau, Weinheim: Wiley-VCH, 1. Aufl., 2013, ISBN: 978-3-527-33018-8

[Bob17] K. Bobzin, High-performance coatings for cutting tools, CIRP Journal of Manufacturing Science and Technology, 18 (2017), 1–9, DOI: 10.1016/j.cirpj.2016.11.004

[Bre01] L. Breiman, Random Forests, Machine Learning, 45 (2001), 5–32, DOI: 10.1023/A:1010933404324

[Bre96] L. Breiman, Bagging predictors, Machine Learning, 24 (1996), 123–140, DOI: 10.1007/BF00058655

[BSG+07] B. D. Beake, J. F. Smith, A. Gray, G. S. Fox-Rabinovich, S. C. Veldhuis, J. L. Endrino, Investigating the correlation between nano-impact fracture resistance and hardness/modulus ratio from nanoindentation at 25–500 °C and the fracture resistance and lifetime of cutting tools with Ti1−xAlxN (x=0.5 and 0.67) PVD coatings in milling operations, Surface and Coatings Technology, 201 (2007), 4585–4593, DOI: 10.1016/j.surfcoat.2006.09.118

[BV14] S. Baragetti, F. Villa, An Updated Review of the Fatigue Behavior of Components Coated with Thin Hard Corrosion-Resistant Coatings, The Open Materials Science Journal, 8 (2014), 87–98, DOI: 10.2174/1874088X01408010087

[BXH+04] S. Bhowmick, Z.-H. Xie, M. Hoffman, V. Jayaram, S. K. Biswas, Nature of contact deformation of TiN films on steel, Journal of Materials Research, 19 (2004), 2616–2624, DOI: 10.1557/JMR.2004.0339

[Car23] M. Carlet, Potentiale oxinitridischer PVD-Hartstoffschichten für Zerspanwerkzeuge, RWTH Aachen University, Dissertation, in: K. Bobzin (Hrsg.), Schriftenreihe Oberflächentechnik, Volume 75, 2023, Düren: Shaker Verlag, ISBN: 978-3-8440-9276-9

[Chr05] D. J. Christie, Target material pathways model for high power pulsed magnetron sputtering, Journal of Vacuum Science & Technology A, 23 (2005), 330–335, DOI: 10.1116/1.1865133

[CTD+13] P.-A. Cormier, A.-L. Thomann, V. Dolique, A. Balhamri, R. Dussart, N. Semmar, T. Lecas, P. Brault, R. Snyders, S. Konstantinidis, IR emission from the target during plasma magnetron sputter deposition, Thin Solid Films, 545 (2013), 44–49, DOI: 10.1016/j.tsf.2013.07.025

[CTS+04] D. J. Christie, F. Tomasel, W. D. Sproul, D. C. Carter, Power supply with arc handling for high peak power magnetron sputtering, Journal of Vacuum Science & Technology A, 22 (2004), 1415–1419, DOI: 10.1116/1.1688365

[CYH02] W.-J. Chou, G.-P. Yu, J.-H. Huang, Mechanical properties of TiN thin film coatings on 304 stainless steel substrates, Surface and Coatings Technology, 149 (2002), 7–13, DOI: 10.1016/S0257-8972(01)01382-2

[DAK63] W. Dawihl, G. Altmeyer, M. Kumar Mal, Das Verformungsverhalten von Wolframkarbid- Kobalt-Legierungen bei Temperaturen bis zu 1000°C, International Journal of Materials Research, 54 (1963), 66–72, DOI: 10.1515/ijmr-1963-540202

[FEB+08] G. S. Fox-Rabinovich, J. L. Endrino, B. D. Beake, M. H. Aguirre, S. C. Veldhuis, D. T. Quinto, C. E. Bauer, A. I. Kovalev, A. Gray, Effect of temperature of annealing below 900 °C on structure, properties and tool life of an AlTiN coating under various cutting conditions, Surface and Coatings Technology, 202 (2008), 2985–2992, DOI: 10.1016/j.surfcoat.2007.10.034

[FSO+14] F. Ferreira, R. Serra, J. C. Oliveira, A. Cavaleiro, Effect of peak target power on the properties of Cr thin films sputtered by HiPIMS in deep oscillation magnetron sputtering (DOMS) mode, Surface and Coatings Technology, 258 (2014), 249–256, DOI: 10.1016/j.surfcoat.2014.09.020

[GCB+19] F. Giuliani, C. Ciurea, V. Bhakhri, M. Werchota, L. J. Vandeperre, P. H. Mayrhofer, Deformation behaviour of TiN and Ti–Al–N coatings at 295 to 573 K, Thin Solid Films, 688 (2019), 137363, DOI: 10.1016/j.tsf.2019.06.013

[Ges02] Gesellschaft für Tribologie e.V. (GfT), Arbeitsblatt 7 - Tribologie. Verschleiß,Reibung, Definitionen, Begriffe, Prüfung, Arbeitsblätter GfT (2002)

[GKH+14] Z. Gronostajski, M. Kaszuba, M. Hawryluk, M. Zwierzchowski, A review of the degradation mechanisms of the hot forging tools, Archives of Civil and Mechanical Engineering, 14 (2014), 528–539, DOI: 10.1016/j.acme.2014.07.002

[GSM+20] Y. Guo, T. Staedler, J. Müller, S. Heuser, B. Butz, X. Jiang, A detailed analysis of the determination of fracture toughness by nanoindentation induced radial cracks, Journal of the European Ceramic Society, 40 (2020), 276–289, DOI: 10.1016/j.jeurceramsoc.2019.10.013

[GvS01] A. Gouldstone, K. J. van Vliet, S. Suresh, Nanoindentation. Simulation of defect nucleation in a crystal, Nature, 411 (2001), 656, DOI: 10.1038/35079687

[GW66] J. A. Greenwood, J. Willamson, Contact of nominally flat surfaces, Proceedings of the Royal Society of London. Series A. Mathematical and Physical Sciences, 295 (1966), 300–319, DOI: 10.1098/rspa.1966.0242

[Hal86] J. Halling, The Tribology of Surface Coatings, Particularly Ceramics, Proceedings of the Institution of Mechanical Engineers, Part C: Journal of Mechanical Engineering Science, 200 (1986), 31–40, DOI: 10.1243/PIME_PROC_1986_200_091_02

[HE19] P. E. Hovsepian, A. P. Ehiasarian, Six strategies to produce application tailored nanoscale multilayer structured PVD coatings by conventional and High Power Impulse Magnetron Sputtering (HIPIMS), Thin Solid Films, 688 (2019), 137409, DOI: 10.1016/j.tsf.2019.137409

[Her13] R. Herbertz, Massivumformung kurz und bündig, Hagen: Industrieverband Massivumformung, 1 Aufl., 2013, ISBN: 978-3-928726-32-0

[HJ90] S. Hofmann, H. A. Jehn, Oxidation behavior of CrN_x and $(Cr,Al)N_x$ hard coatings, Materials and Corrosion, 41 (1990), 756–760, DOI: 10.1002/maco.19900411222

[Hol84] H. Holleck, Binäre und ternäre Carbid- und Nitridsysteme der Übergangsmetalle. Mit 29 Tabellen. Zugl.: Karlsruhe, Univ., Diss., 1981, Berlin: Borntraeger, 1984, ISBN: 978-3-443-23007-4

[Hol90] H. W. Holleck, Advanced concepts of PVD hard coatings, Vacuum, 41 (1990), 2220–2222, DOI: 10.1016/0042-207X(90)94229-J

[HS95] H. Holleck, V. Schier, Multilayer PVD coatings for wear protection, Surface and Coatings Technology, 76-77 (1995), 328–336, DOI: 10.1016/0257-8972(95)02555-3

[HT77] D. W. Hoffman, J. A. Thornton, Internal stresses in sputtered chromium, Thin Solid Films, 40 (1977), 355–363, DOI: 10.1016/0040-6090(77)90137-7

[IS14] A. Inspektor, P. A. Salvador, Architecture of PVD coatings for metalcutting applications: A review, Surface and Coatings Technology, 257 (2014), 138–153, DOI: 10.1016/j.surfcoat.2014.08.068

[JLL+16] J. Jian, J. H. Lee, Y. Liu, F. Khatkhatay, K. Yu, Q. Su, X. Zhang, L. Jiao, H. Wang, Plastic deformation in nanocrystalline TiN at ultra-low stress: An in situ nanoindentation study, Materials Science and Engineering: A, 650 (2016), 445–453, DOI: 10.1016/j.msea.2015.10.002

[JMM96] A. K. Jain, J. Mao, K. M. Mohiuddin, Artificial neural networks: a tutorial, Computer, 29 (1996), 31–44, DOI: 10.1109/2.485891

[Joh85] K. L. Johnson, Contact mechanics, Cambridge Cambridgeshire, New York, Port Melbourne, Madrid, Cape Town: Cambridge University Press, 1985, ISBN: 0-521-34796-3

[JSM+04] N. Jiang, Y. Shen, Y.-W. Mai, T. Chan, S. C. Tung, Nanocomposite Ti–Si–N films deposited by reactive unbalanced magnetron sputtering at room temperature, Materials Science and Engineering: B, 106 (2004), 163–171, DOI: 10.1016/j.mseb.2003.09.033

[KAB+90] O. Knotek, M. Atzor, A. Barimani, F. Jungblut, Development of low temperature ternary coatings for high wear resistance, Surface and Coatings Technology, 42 (1990), 21–28, DOI: 10.1016/0257-8972(90)90111-O

[KD95] G. Kienel; H. F. Döbele, Vakuumbeschichtung 1. Plasmaphysik - Plasmadiagnostik - Analytik., Düsseldorf: VDI-Verl., 1995, ISBN: 3184013111

[KGS+10] F. Klocke, C. Gorgels, A. Stuckenberg, E. Bouzakis, Qualification of Coatings to Predict Wear Behavior of Micro Blasted Cutting Tools, Key Engineering Materials, 438 (2010), 23–29, DOI: 10.4028/www.scientific.net/KEM.438.23

[KK08] F. Klocke, W. König, Drehen, Fräsen, Bohren, Berlin: Springer, 8., [neu bearb.] Aufl., 2008, ISBN: 978-3-540-23458-6

[Klo17] F. Klocke, Fertigungsverfahren 1. Zerspanung mit geometrisch bestimmter Schneide, Berlin: Springer Vieweg, 2017, ISBN: 978-3-662-54206-4

[Kre10] A. Krella, Cavitation degradation model of hard thin pvd coatings, Advances in Materials Sciences, 10 (2010), DOI: 10.2478/v10077-010-0010-4

[KSB09] A. M. Korsunsky, M. Sebastiani, E. Bemporad, Focused ion beam ring drilling for residual stress evaluation, Materials Letters, 63 (2009), 1961–1963, DOI: 10.1016/j.matlet.2009.06.020

[KSB10] A. M. Korsunsky, M. Sebastiani, E. Bemporad, Residual stress evaluation at the micrometer scale: Analysis of thin coatings by FIB milling and digital image correlation, Surface and Coatings Technology, 205 (2010), 2393–2403, DOI: 10.1016/j.surfcoat.2010.09.033

[Kul92] E. Kuljanic, Macro Plastic Deformation of Cutting Edge — A Method for Maximum Utilization of Cutting Tool, CIRP Annals, 41 (1992), 151–154, DOI: 10.1016/S0007-8506(07)61173-1

[KWC+02] A. Karimi, Y. Wang, T. Cselle, M. Morstein, Fracture mechanisms in nanoscale layered hard thin films, Thin Solid Films, 420-421 (2002), 275–280, DOI: 10.1016/S0040-6090(02)00944-6

[Läp16] V. Läpple, Einführung in die Festigkeitslehre. Lehr- und Übungsbuch, Wiesbaden: Springer Vieweg, 4., aktualisierte Auflage, 2016, ISBN: 978-3-658-10610-2

[Lau87] M. T. Laugier, New formula for indentation toughness in ceramics, Journal of Materials Science Letters, 6 (1987), 355–356, DOI: 10.1007/BF01729352

[LCG+92] K. Lange, L. Cser, M. Geiger, J. Kals, Tool Life and Tool Quality in Bulk Metal Forming, CIRP Annals, 41 (1992), 667–675, DOI: 10.1016/S0007-8506(07)63253-3

[Lee83] M. Lee, High temperature hardness of tungsten carbide, Metallurgical Transactions A, 14 (1983), 1625–1629, DOI: 10.1007/BF02654390

[LEM80] B. R. Lawn, A. G. Evans, D. B. Marshall, Elastic/Plastic Indentation Damage in Ceramics: The Median/Radial Crack System, Journal of the American Ceramic Society, 63 (1980), 574–581, DOI: 10.1111/j.1151-2916.1980.tb10768.x

[LM00] A. Leyland, A. Matthews, On the significance of the H/E ratio in wear control: a nanocomposite coating approach to optimised tribological behaviour, Wear, 246 (2000), 1–11, DOI: 10.1016/S0043-1648(00)00488-9

[LPS15] L. Lind, P. Peetsalu, F. Sergejev, Wear of different PVD coatings at industrial fine-blanking field tests, Materials Science, 21 (2015), DOI: 10.5755/j01.ms.21.3.7249

[LS75] B. R. Lawn, M. V. Swain, Microfracture beneath point indentations in brittle solids, Journal of Materials Science, 10 (1975), 113–122, DOI: 10.1007/BF00541038

[LWM+16] S. Liu, J. M. Wheeler, J. Michler, X. T. Zeng, W. J. Clegg, Plastic flow at the theoretical yield stress in ceramic films, Scripta Materialia, 117 (2016), 24–27, DOI: 10.1016/j.scriptamat.2016.02.008

[Mat10] D. M. Mattox, Handbook of physical vapor deposition (PVD) processing, Oxford, Amsterdam, Heidelberg: William Andrew; Elsevier William Andrew, 2. ed., 2010, ISBN: 978-0-81-552037-5

[MCH+05] L. W. Ma, J. M. Cairney, M. Hoffman, P. R. Munroe, Deformation mechanisms operating during nanoindentation of TiN coatings on steel substrates, Surface and Coatings Technology, 192 (2005), 11–18, DOI: 10.1016/j.surfcoat.2004.04.002

[MCH+06] L. W. Ma, J. M. Cairney, M. J. Hoffman, P. R. Munroe, Deformation and fracture of TiN and TiAlN coatings on a steel substrate during nanoindentation, Surface and Coatings Technology, 200 (2006), 3518–3526, DOI: 10.1016/j.surfcoat.2004.09.034

[MKŞ+20] A. Mussa, P. Krakhmalev, A. Şelte, J. Bergström, Development of a New PM Tool Steel for Optimization of Cold Working of Advanced High-Strength Steels, Metals, 10 (2020), 1326, DOI: 10.3390/met10101326

[MLN99] Y. Milman, S. Luyckx, I. T. Northrop, Influence of temperature, grain size and cobalt content on the hardness of WC–Co alloys, International Journal of Refractory Metals and Hard Materials, 17 (1999), 39–44, DOI: 10.1016/S0263-4368(98)00038-9

[MPM+01] H.-D. Männling, D. Patil, K. Moto, M. Jilek, S. Veprek, Thermal stability of superhard nanocomposite coatings consisting of immiscible nitrides, Surface and Coatings Technology, 146-147 (2001), 263–267, DOI: 10.1016/S0257-8972(01)01474-8

[Mur22] K. P. Murphy, Probabilistic machine learning. An introduction, Cambridge, Massachusetts, London, England: The MIT Press, 2022, ISBN: 978-0262046824

[OP92] W. C. Oliver, G. M. Pharr, An improved technique for determining hardness and elastic modulus using load and displacement sensing indentation experiments, Journal of Materials Research, 7 (1992), 1564–1583, DOI: 10.1557/JMR.1992.1564

[OW95] H. Oettel, R. Wiedemann, Residual stresses in PVD hard coatings, Surface and Coatings Technology, 76-77 (1995), 265–273, DOI: 10.1016/0257-8972(95)02581-2

[PH93] T. F. Page, S. V. Hainsworth, Using nanoindentation techniques for the characterization of coated systems: a critique, Surface and Coatings Technology, 61 (1993), 201–208, DOI: 10.1016/0257-8972(93)90226-E

[PL15] B. Podgornik, V. Leskovšek, Wear mechanisms and surface engineering of forming tools, Materiali in tehnologije, 49 (2015), 313–324, DOI: 10.17222/mit.2015.005

[PMD+24] P. Panjan, A. Miletić, A. Drnovšek, P. Terek, M. Čekada, L. Kovačević, M. Panjan, Cracking Resistance of Selected PVD Hard Coatings, Coatings, 14 (2024), 1452, DOI: 10.3390/coatings14111452

[POM92] T. F. Page, W. C. Oliver, C. J. McHargue, The deformation behavior of ceramic crystals subjected to very low load (nano)indentations, Journal of Materials Research, 7 (1992), 450–473, DOI: 10.1557/JMR.1992.0450

[PRB+22] U. Patel, S. Rawal, B. Bose, A. Arif, S. Veldhuis, Performance evaluations of Ti-based PVD coatings deposited on cermet tools for high-speed dry finish turning of AISI 304 stainless steel, Wear, 492-493 (2022), 204214, DOI: 10.1016/j.wear.2021.204214

[RDS+12] A. Riedl, R. Daniel, M. Stefenelli, T. Schöberl, O. Kolednik, C. Mitterer, J. Keckes, A novel approach for determining fracture toughness of hard coatings on the micrometer scale, Scripta Materialia, 67 (2012), 708–711, DOI: 10.1016/j.scriptamat.2012.06.034

[RM19] S. Raschka, V. Mirjalili, Python machine learning. Machine learning and deep learning with Python, scikit-learn, and TensorFlow 2, Birmingham, Mumbai: Packt, Third edition, December 2019, ISBN: 978-1-78995-575-0

[SA92] P. M. Sargent, M. F. Ashby, Indentation creep, Materials Science and Technology, 8 (1992), 594–601, DOI: 10.1179/026708392790171107

[SBK+17] G. Skordaris, K. D. Bouzakis, T. Kotsanis, P. Charalampous, E. Bouzakis, B. Breidenstein, B. Bergmann, B. Denkena, Effect of PVD film's residual stresses on their mechanical properties, brittleness, adhesion and cutting performance of coated tools, CIRP Journal of Manufacturing Science and Technology, 18 (2017), 145–151, DOI: 10.1016/j.cirpj.2016.11.003

[Sch94] E. Schedin, Galling mechanisms in sheet forming operations, Wear, 179 (1994), 123–128, DOI: 10.1016/0043-1648(94)90229-1

[SFA+09] N. A. Sakharova, J. V. Fernandes, J. M. Antunes, M. C. Oliveira, Comparison between Berkovich, Vickers and conical indentation tests: A three-dimensional numerical simulation study, International Journal of Solids and Structures, 46 (2009), 1095–1104, DOI: 10.1016/j.ijsolstr.2008.10.032

[SJH+15a] M. Sebastiani, K. E. Johanns, E. G. Herbert, G. M. Pharr, Measurement of fracture toughness by nanoindentation methods: Recent advances and future challenges, Current Opinion in Solid State and Materials Science, 19 (2015), 324–333, DOI: 10.1016/j.cossms.2015.04.003

[SJH+15b] M. Sebastiani, K. E. Johanns, E. G. Herbert, F. Carassiti, G. M. Pharr, A novel pillar indentation splitting test for measuring fracture toughness of thin ceramic coatings, Philosophical Magazine, 95 (2015), 1928–1944, DOI: 10.1080/14786435.2014.913110

[SKM97] A. Sugishima, H. Kajioka, Y. Makino, Phase transition of pseudobinary Cr–Al–N films deposited by magnetron sputtering method, Surface and Coatings Technology, 97 (1997), 590–594, DOI: 10.1016/S0257-8972(97)00402-7

[SSB08] B. Shi, J. L. Sullivan, B. D. Beake, An investigation into which factors control the nanotribological behaviour of thin sputtered carbon films, Journal of Physics D: Applied Physics, 41 (2008), 45303, DOI: 10.1088/0022-3727/41/4/045303

[SSK+22] J. Smolik, S. Sowa, J. Kacprzyńska-Gołacka, A. Piasek, Evaluation of the Fracture Toughness KIc for Selected Magnetron Sputtering Coatings by Using the Laugier Model, Materials (Basel, Switzerland), 15 (2022), DOI: 10.3390/ma15249061

[STG+14] T. Sprute, W. Tillmann, D. Grisales, U. Selvadurai, G. Fischer, Influence of substrate pre-treatments on residual stresses and tribo-mechanical properties of TiAlN-based PVD coatings, Surface and Coatings Technology, 260 (2014), 369–379, DOI: 10.1016/j.surfcoat.2014.08.075

[Swa79] M. V. Swain, Microfracture about scratches in brittle solids, Proceedings of the Royal Society of London. Series A. Mathematical and Physical Sciences, 366 (1979), 575–597, DOI: 10.1098/rspa.1979.0070

[Tab51] D. Tabor, The hardness of metals, New York, Oxford: Oxford University Press, 1951, ISBN: 978-0198507765

[TPO+95] T. Y. Tsui, G. M. Pharr, W. C. Oliver, C. S. Bhatia, R. L. White, S. Anders, A. Anders, I. G. Brown, Nanoindentation and Nanoscratching of Hard Carbon Coatings for Magnetic Disks, MRS Proceedings, 383 (1995), DOI: 10.1557/PROC-383-447

[TTW00] E. M. Trent, E. M. Trent, P. K. Wright, Metal cutting, Boston, Mass.: Butterworth-Heinemann, 4. ed., 2000, ISBN: 0-7506-7069-X

[US17] R. Useldinger, U. Schleinkofer, Creep behaviour of cemented carbides — Influence of binder content, binder composition and WC grain size, International Journal of Refractory Metals and Hard Materials, 62 (2017), 170–175, DOI: 10.1016/j.ijrmhm.2016.06.013

[Vep97] S. Vepřek, Conventional and new approaches towards the design of novel superhard materials, Surface and Coatings Technology, 97 (1997), 15–22, DOI: 10.1016/S0257-8972(97)00279-X

[VNM+00] S. Veprek, A. Niederhofer, K. Moto, T. Bolom, H.-D. Männling, P. Nesladek, G. Dollinger, A. Bergmaier, Composition, nanostructure and origin of the ultrahardness in nc-TiN/a-Si3N4/a- and nc-TiSi2 nanocomposites with HV=80 to ≥105 GPa, Surface and Coatings Technology, 133-134 (2000), 152–159, DOI: 10.1016/S0257-8972(00)00957-9

[VPG+20] A. Vornberger, J. Pötschke, T. Gestrich, M. Herrmann, A. Michaelis, Influence of microstructure on hardness and thermal conductivity of hardmetals, International Journal of Refractory Metals and Hard Materials, 88 (2020), 105170, DOI: 10.1016/j.ijrmhm.2019.105170

[VRS95] S. Vepřek, S. Reiprich, L. Shizhi, Superhard nanocrystalline composite materials: The TiN/Si3N4 system, Applied Physics Letters, 66 (1995), 2640–2642, DOI: 10.1063/1.113110

[WAH+15] J. M. Wheeler, D. Armstrong, W. Heinz, R. Schwaiger, High temperature nanoindentation: The state of the art and future challenges, Current Opinion in Solid State and Materials Science, 19 (2015), 354–366, DOI: 10.1016/j.cossms.2015.02.002

[WRC+14] J. M. Wheeler, R. Raghavan, V. Chawla, M. Morstein, J. Michler, Deformation of Hard Coatings at Elevated Temperatures, Surface and Coatings Technology, 254 (2014), 382–387, DOI: 10.1016/j.surfcoat.2014.06.048

[WSG+14] P. Wieciński, J. Smolik, H. Garbacz, K. J. Kurzydłowski, Failure and deformation mechanisms during indentation in nanostructured Cr/CrN multilayer coatings, Surface and Coatings Technology, 240 (2014), 23–31, DOI: 10.1016/j.surfcoat.2013.12.006

[WZY16] Q. Wang, F. Zhou, J. Yan, Evaluating mechanical properties and crack resistance of CrN, CrTiN, CrAlN and CrTiAlN coatings by nanoindentation and scratch tests, Surface and Coatings Technology, 285 (2016), 203–213, DOI: 10.1016/j.surfcoat.2015.11.040

[XHM+08] Z. H. Xie, M. Hoffman, P. Munroe, A. Bendavid, P. J. Martin, Deformation mechanisms of TiN multilayer coatings alternated by ductile or stiff interlayers, Acta Materialia, 56 (2008), 852–861, DOI: 10.1016/j.actamat.2007.10.047

11 Appendix I

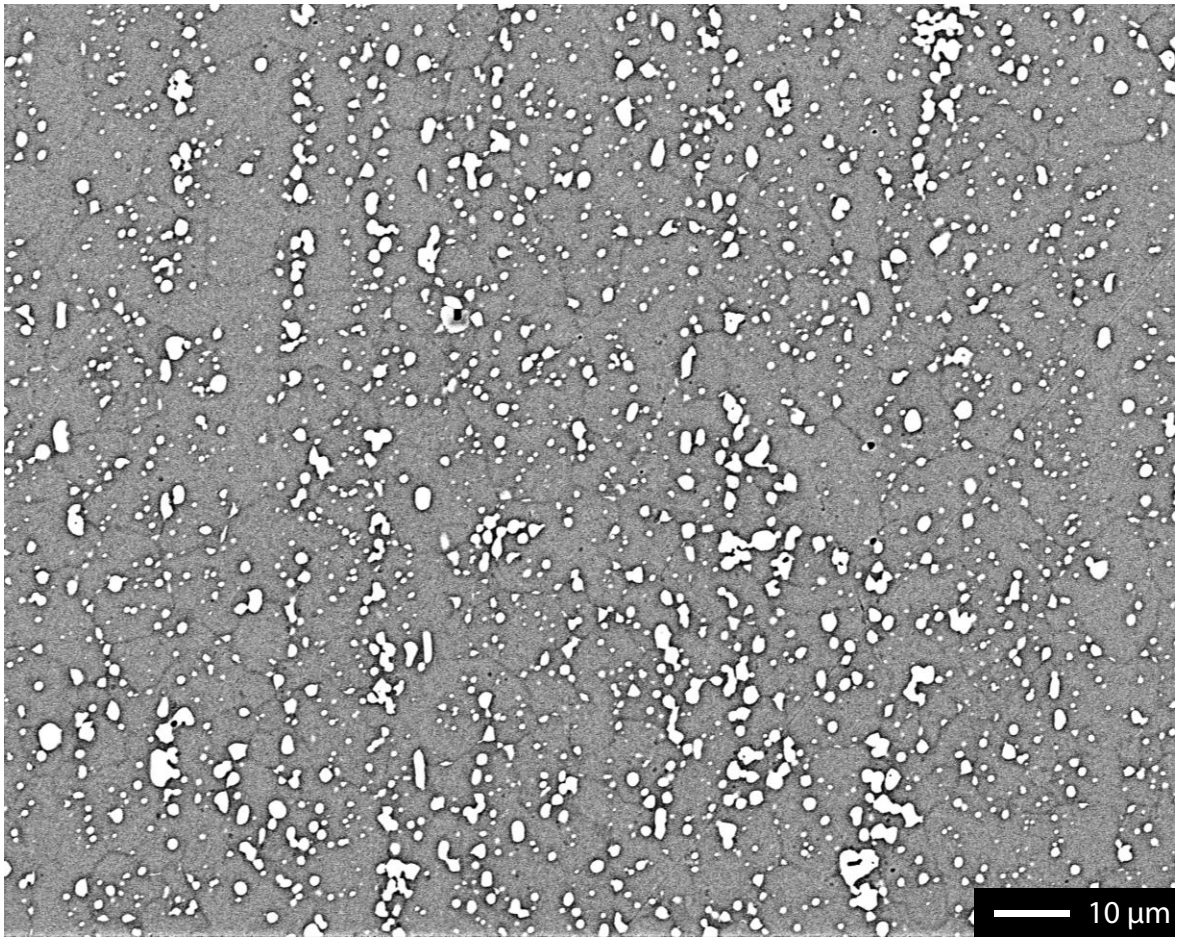

Figure 11.1: SEM image, with backscattered electron detector mode, of the substrate high-speed steel HS6-5-2C grain structure from sample cross-section after quenching and tempering

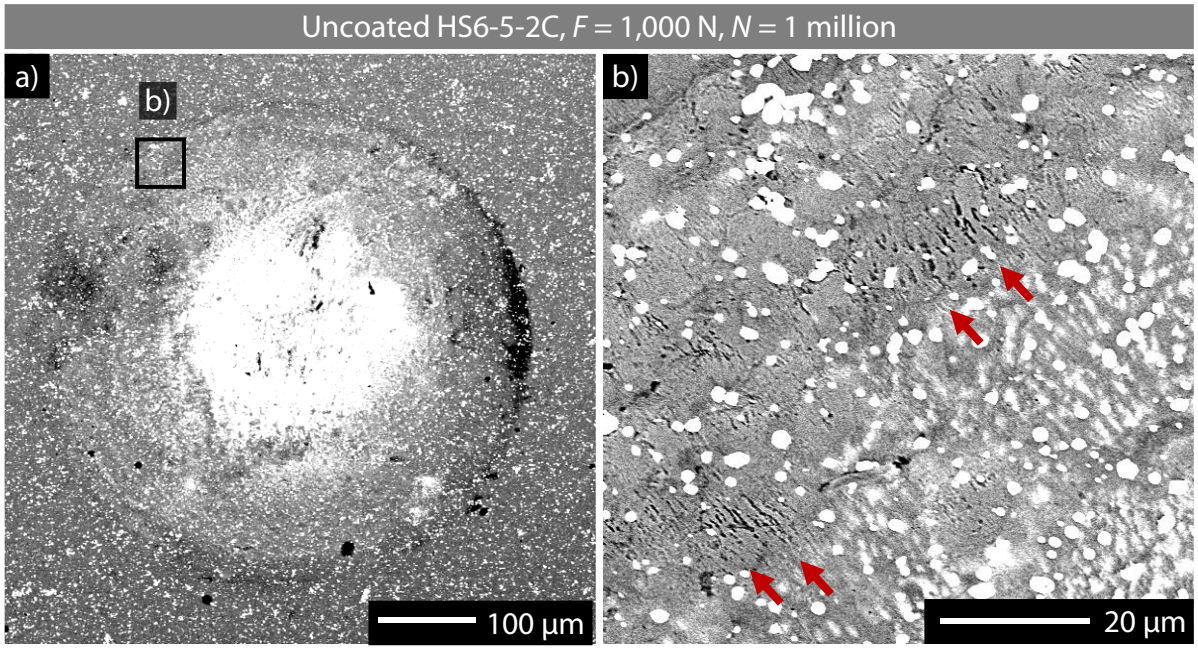

Figure 11.2: (a) Impact imprint with (b) enlarged crack areas for uncoated HS6-5-2C substrate after N = 1 million impacts with F = 1,000 N

12 Appendix II

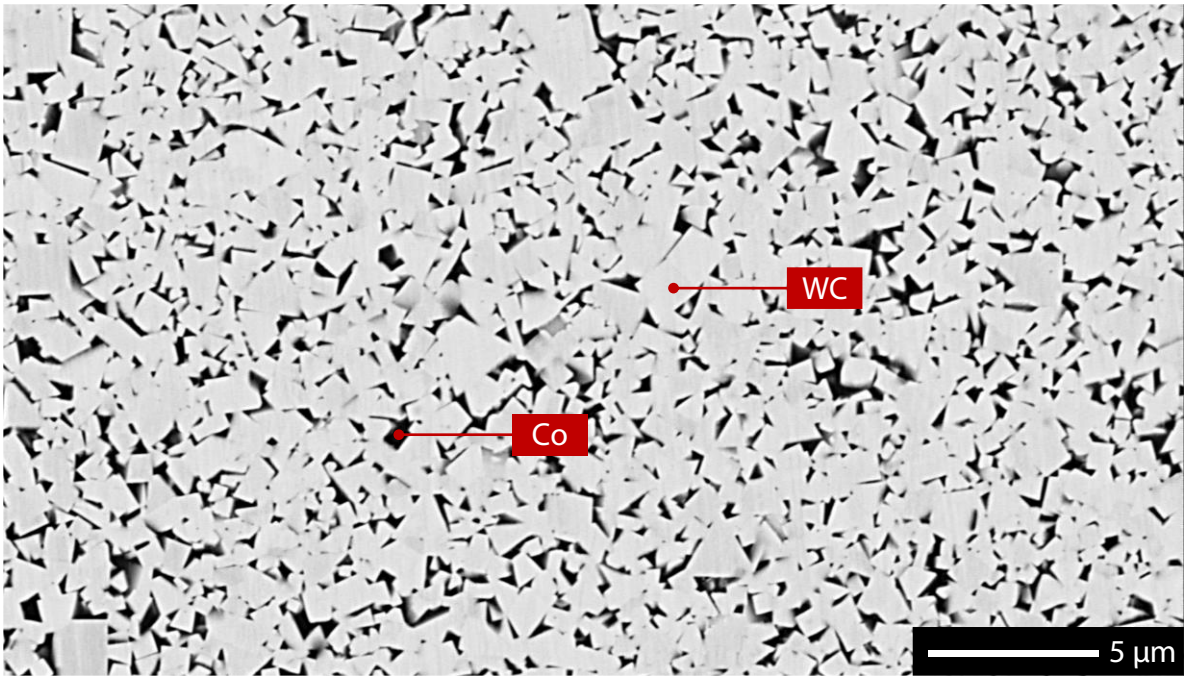

Figure 12.1: SEM image, with backscattered electron detector mode, of the grain structure of cemented carbide substrate

13 Appendix III

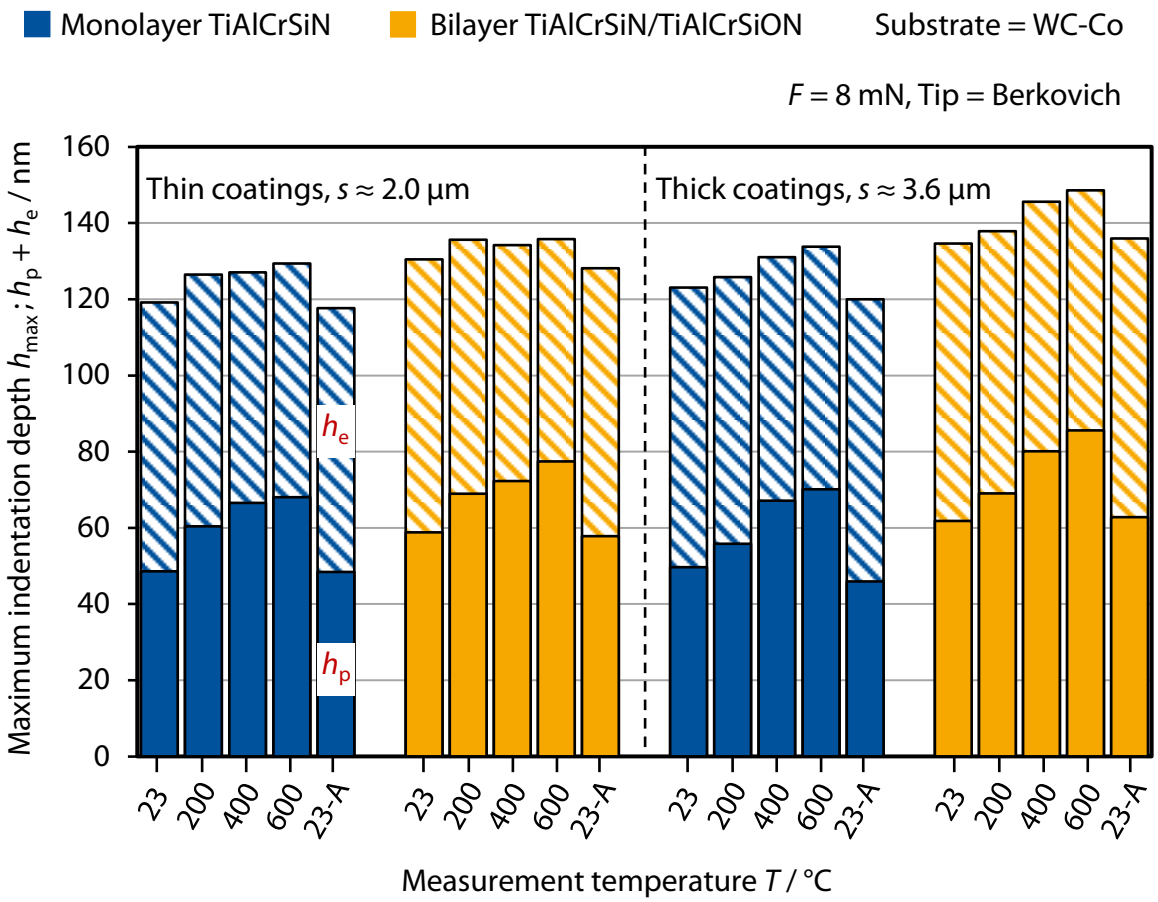

Figure 13.1: Temperature dependent maximum indentation depth h_{max} of monolayer and bilayer coatings with varying thickness at indentation force $F = 8$ mN

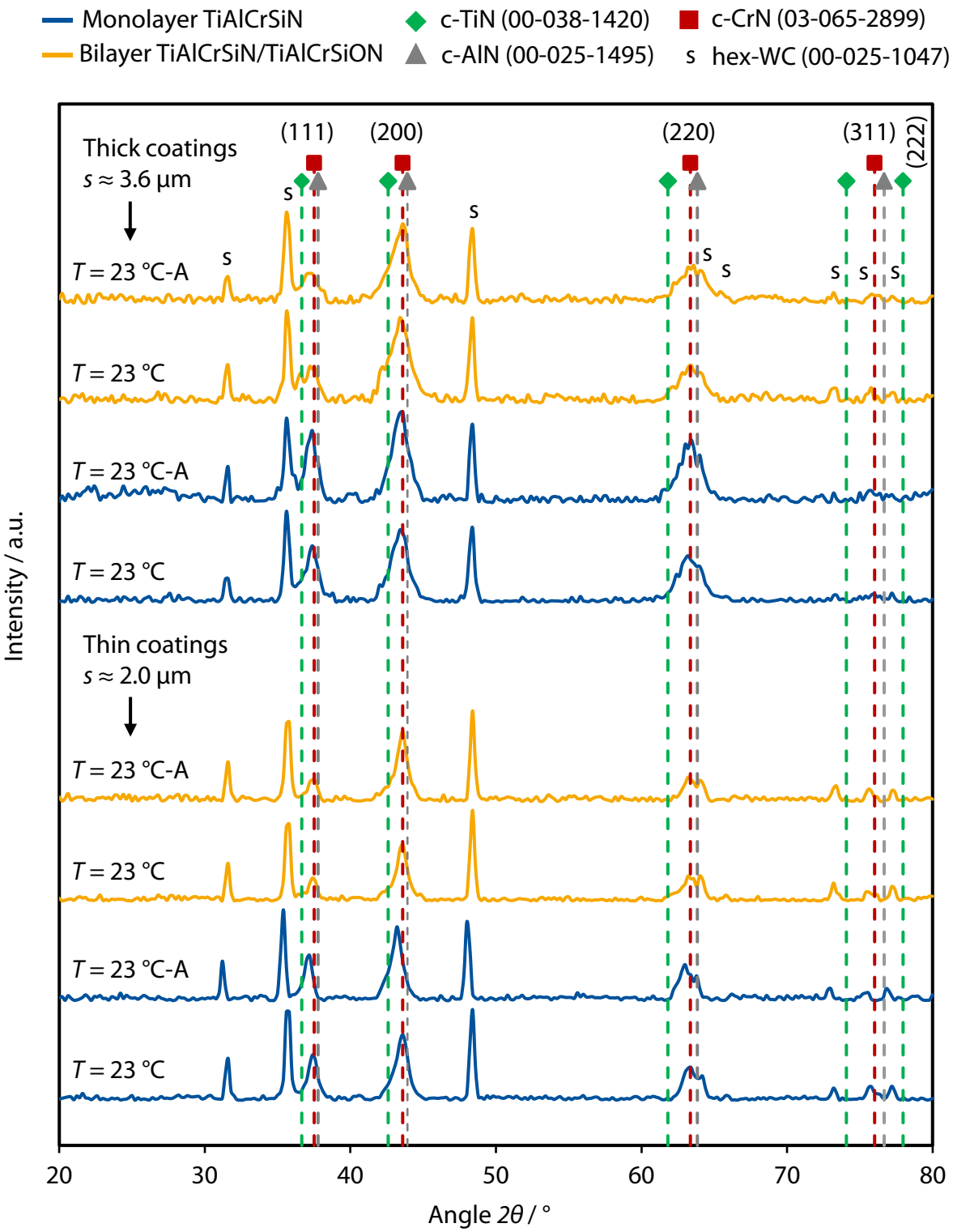

Figure 13.2: XRD diffractograms of monolayer and bilayer coatings at $T = 23$ °C before sample heating and at $T = 23$ °C-A after sample cooling from $T = 600$ °C during high temperature nanoindenation experiments

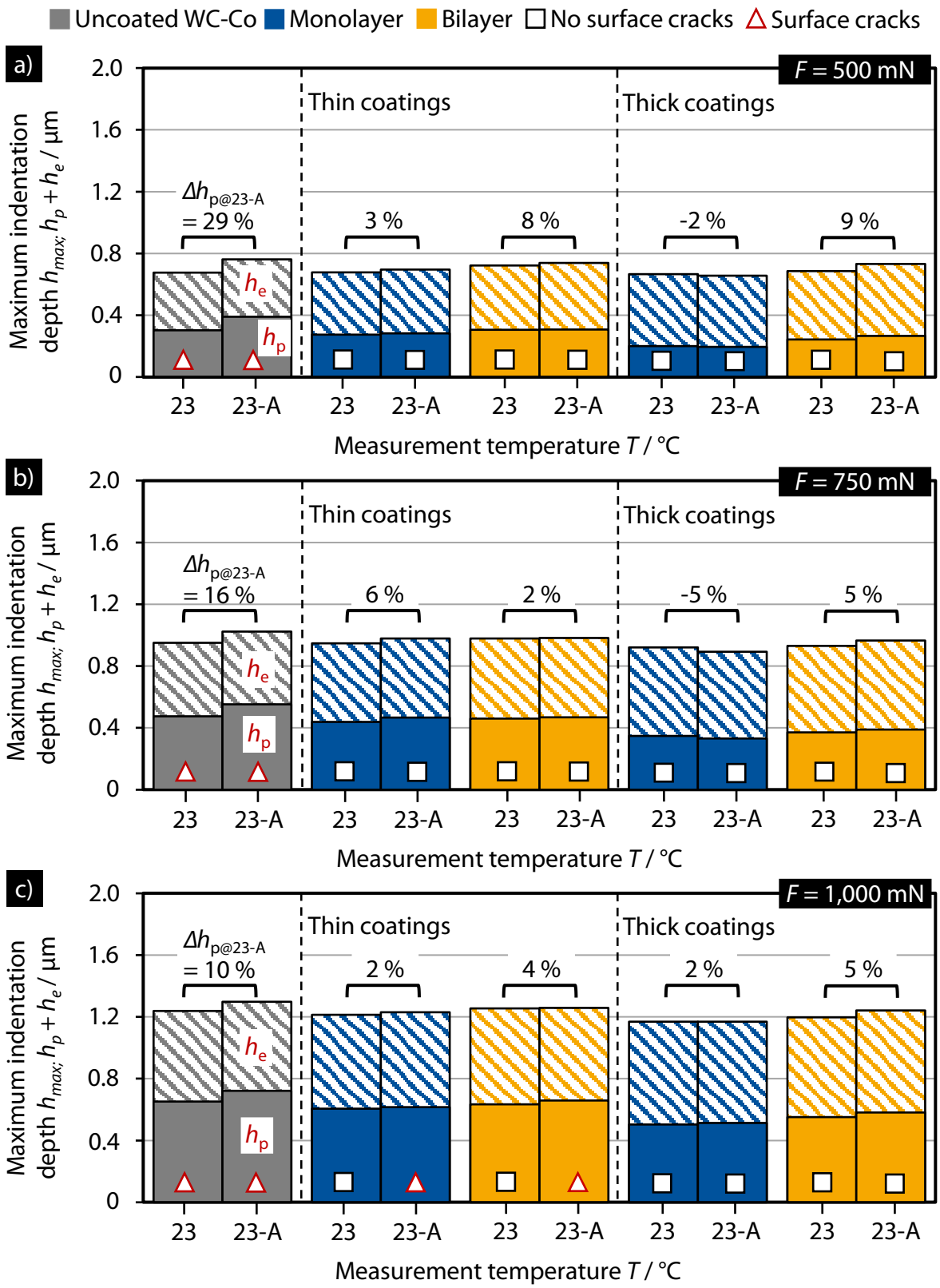

Figure 13.3: Maximum indentation depth h_{max} of the uncoated cemented carbide and compounds at (a) F = 500 mN, (b) F = 750 mN and (c) F = 1,000 mN before sample heating and after sample cooling from T = 600 °C

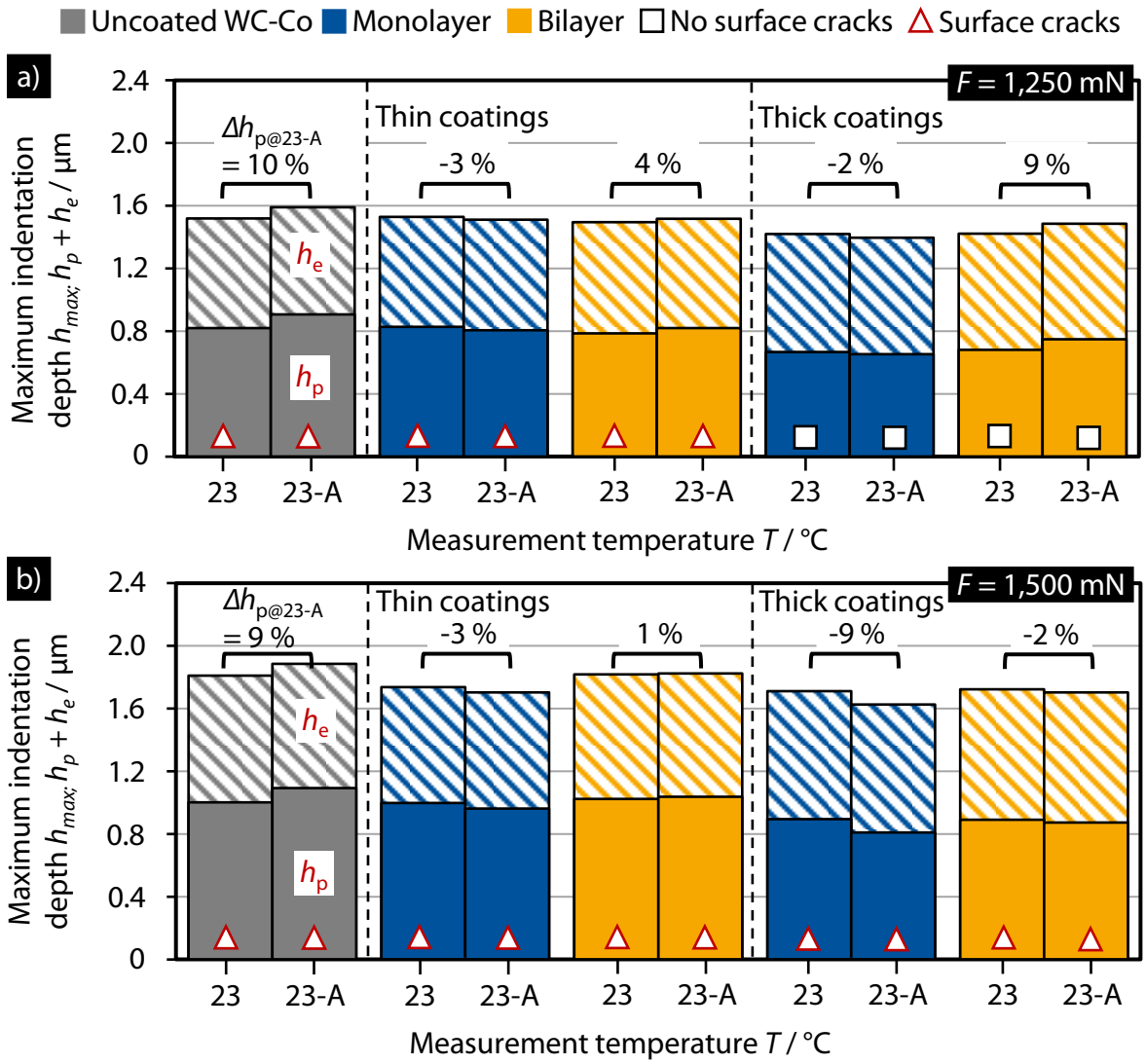

Figure 13.4: Maximum indentation depth h_{max} of the uncoated cemented carbide and coated compounds at (a) F = 1,250 mN and (b) F = 1,500 mN before sample heating and after sample cooling from T = 600 °C

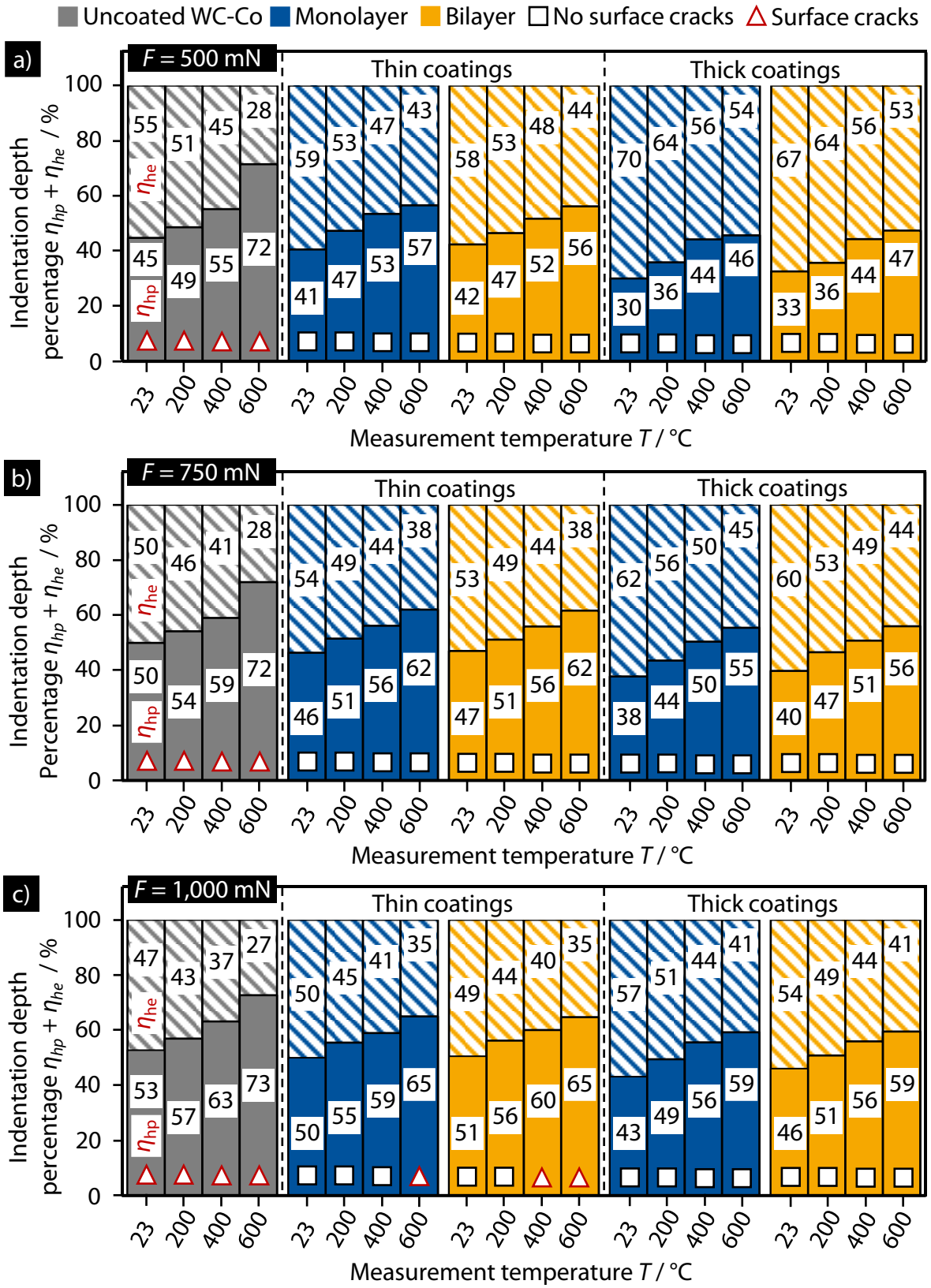

Figure 13.5: Temperature dependent indentation depth percentages η_{hp} and η_{he} of uncoated cemented carbide and coated compounds at (a) F = 500 mN, (b) F = 750 mN and (c) F = 1,000 mN

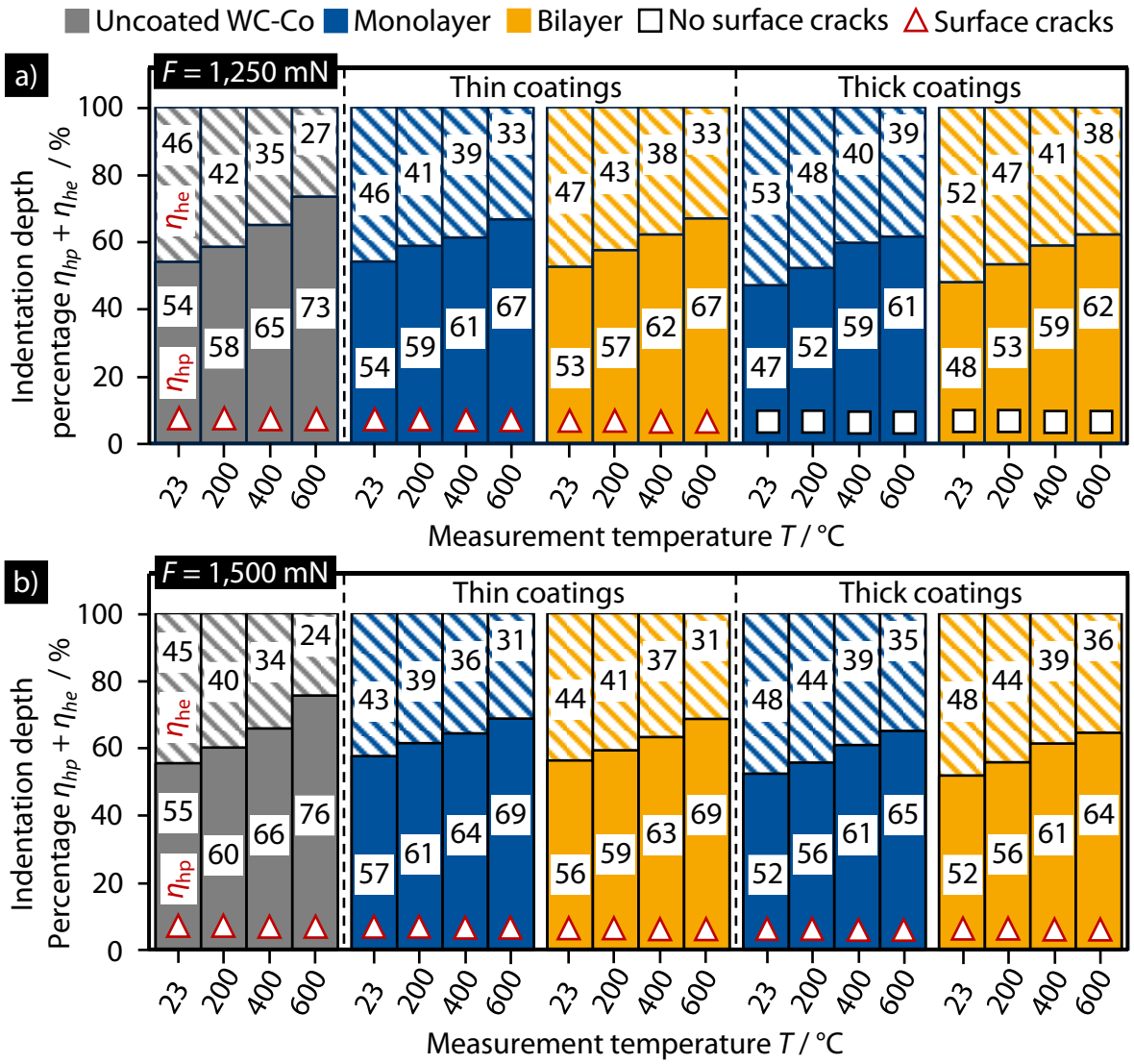

Figure 13.6: Temperature dependent indentation depth percentages η_{hp} and η_{he} of the uncoated cemented carbide and coated compounds at (a) F = 1,250 mN and (b) F = 1,500 mN

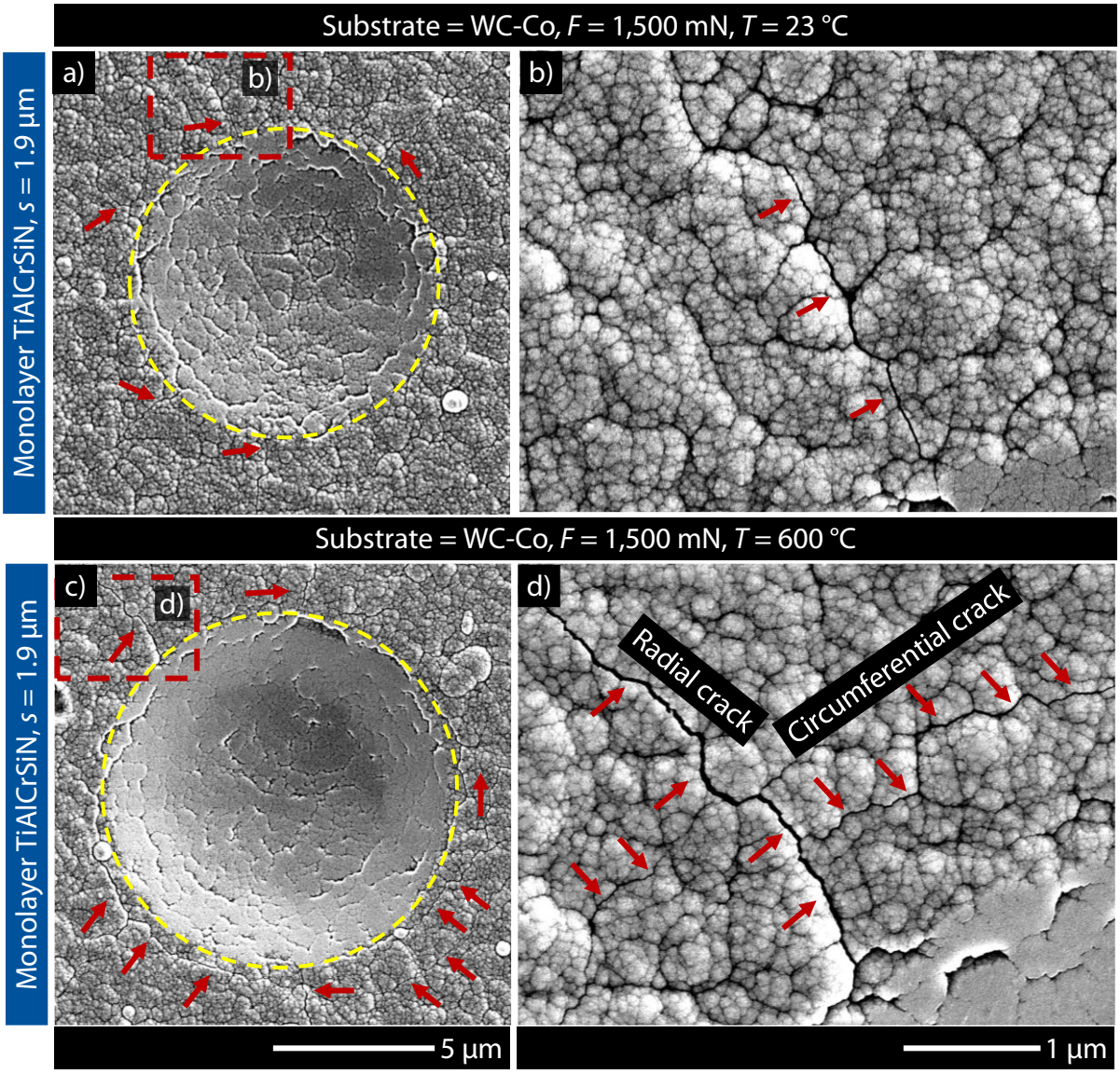

Figure 13.7: Indent imprints with enlarged surface crack areas for compounds with thin monolayer TiAlCrSiN carried out at F = 1,500 mN with measurement temperatures (a,b) T = 23 °C and (c,d) T = 600 °C

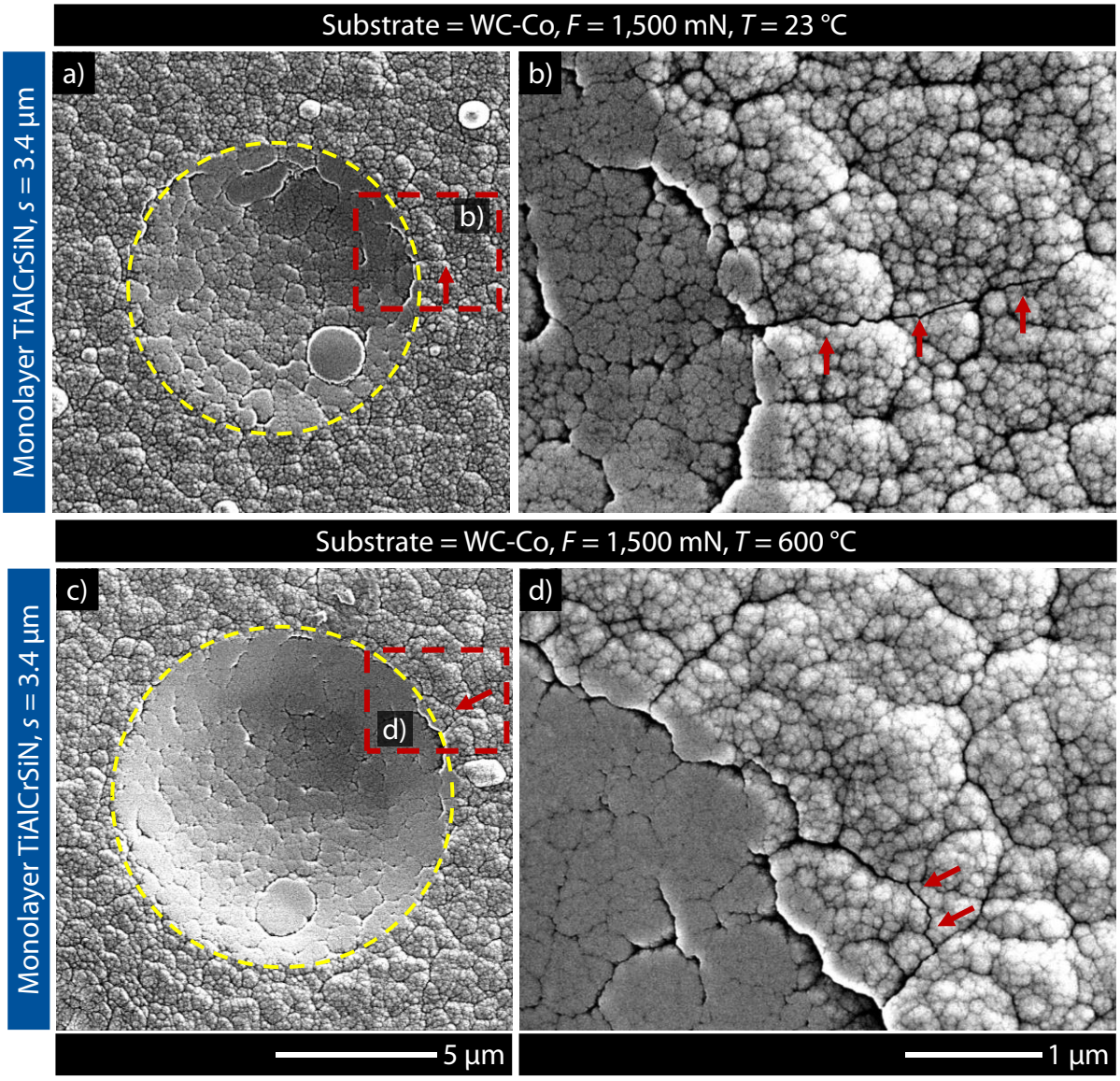

Figure 13.8: Indent imprints with enlarged surface crack areas for compounds with thick monolayer TiAlCrSiN carried out at F = 1,500 mN with measurement temperatures (a,b) T = 23 °C and (c,d) T = 600 °C

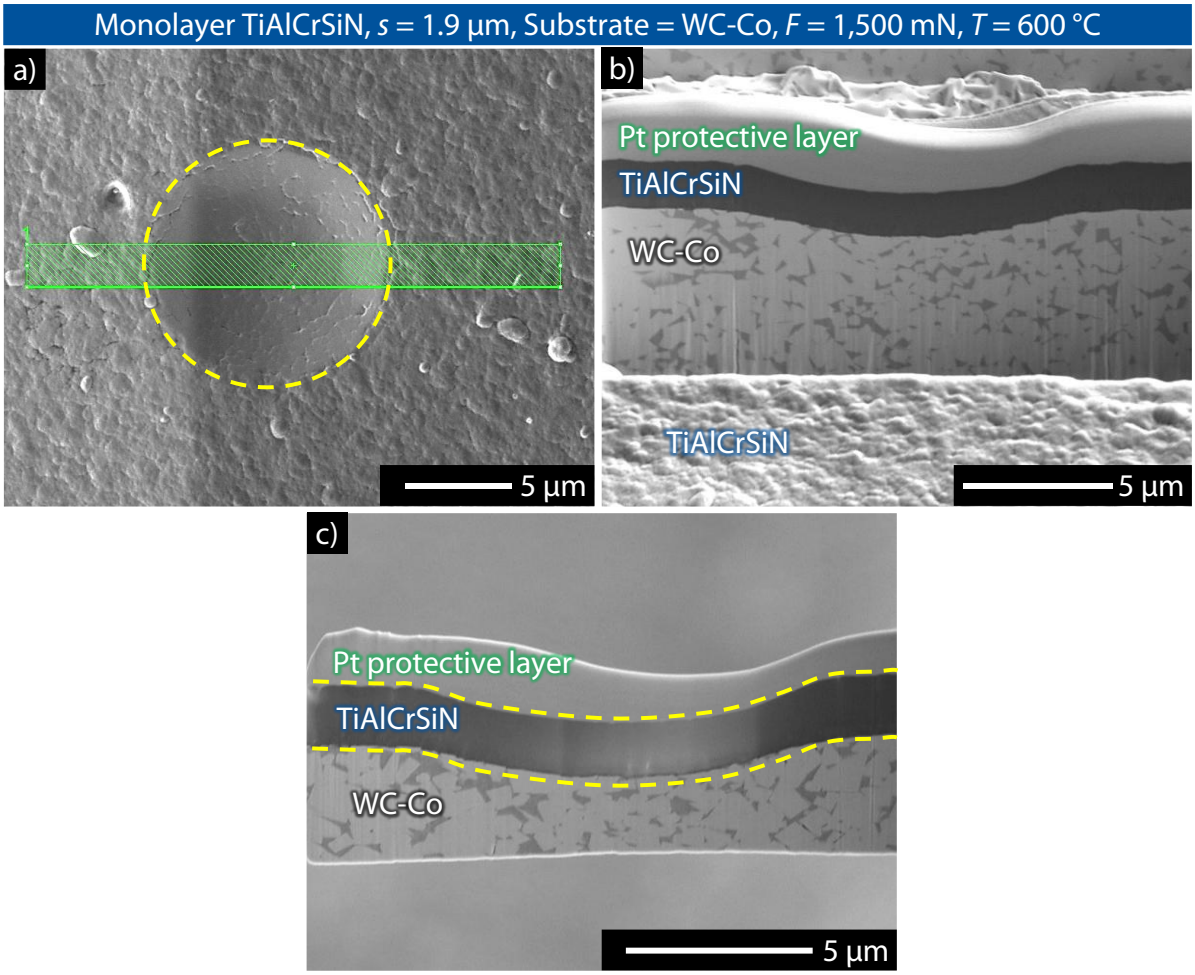

Figure 13.9: Exemplary SEM images from cross-sectional lamella preparation of indent on compound with thin TiAlCrSiN, (a) selection of lamella width, (b) FIB cutting of lamella and (c) prepared lamella

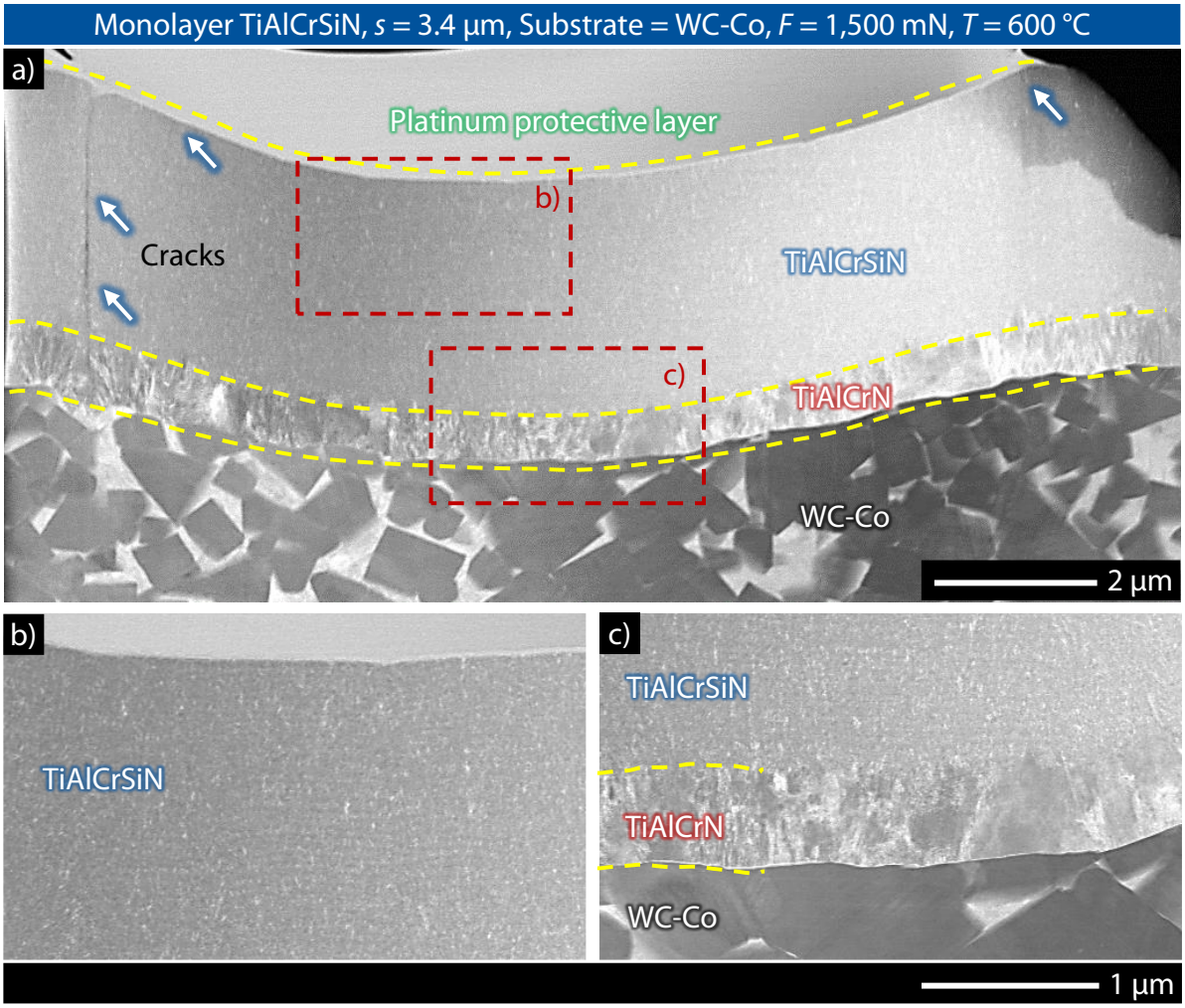

Figure 13.10: STEM DF images of (a) FIB lamella and (b,c) enlarged central region from indent on compound with thick monolayer TiAlCrSiN

14 Appendix IV

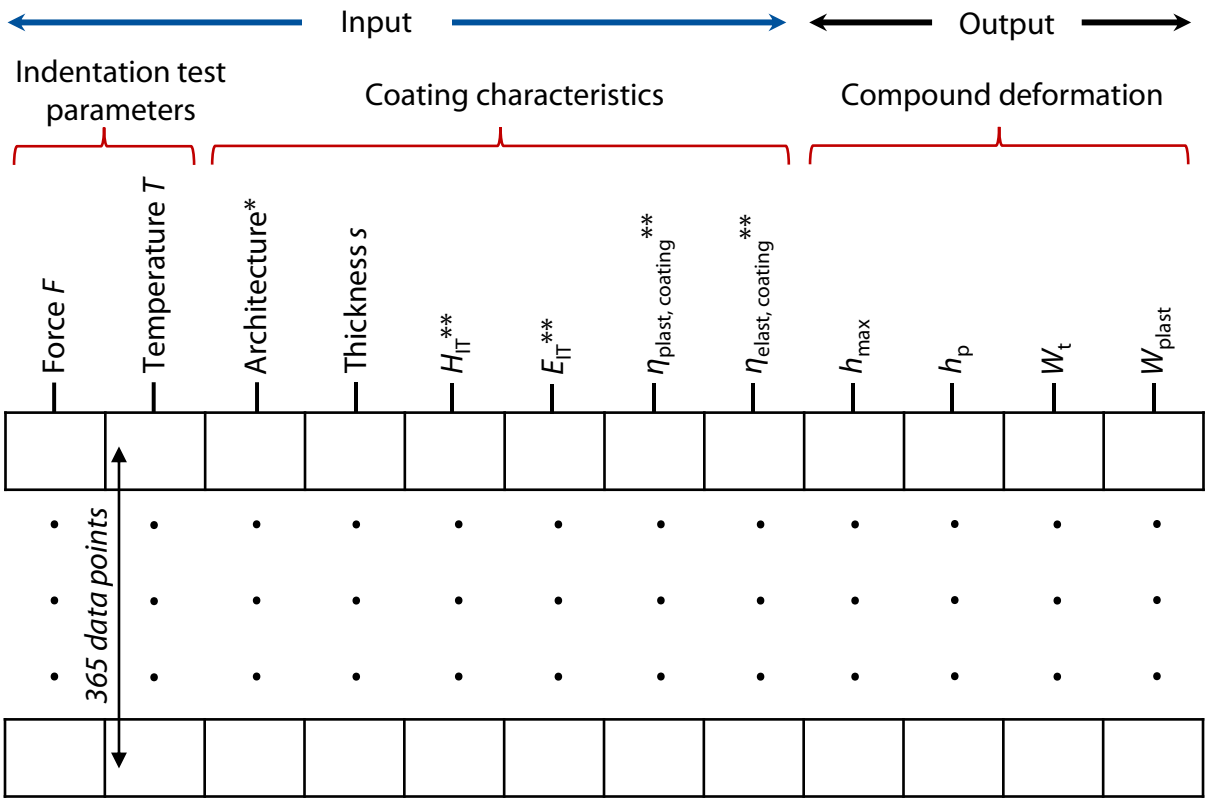

* Monolayer = 0, Bilayer = 1

** Average value from nanoindentation measurements at corresponding temperature

Figure 14.1: Database structure for training and testing machine learning models for the regression task

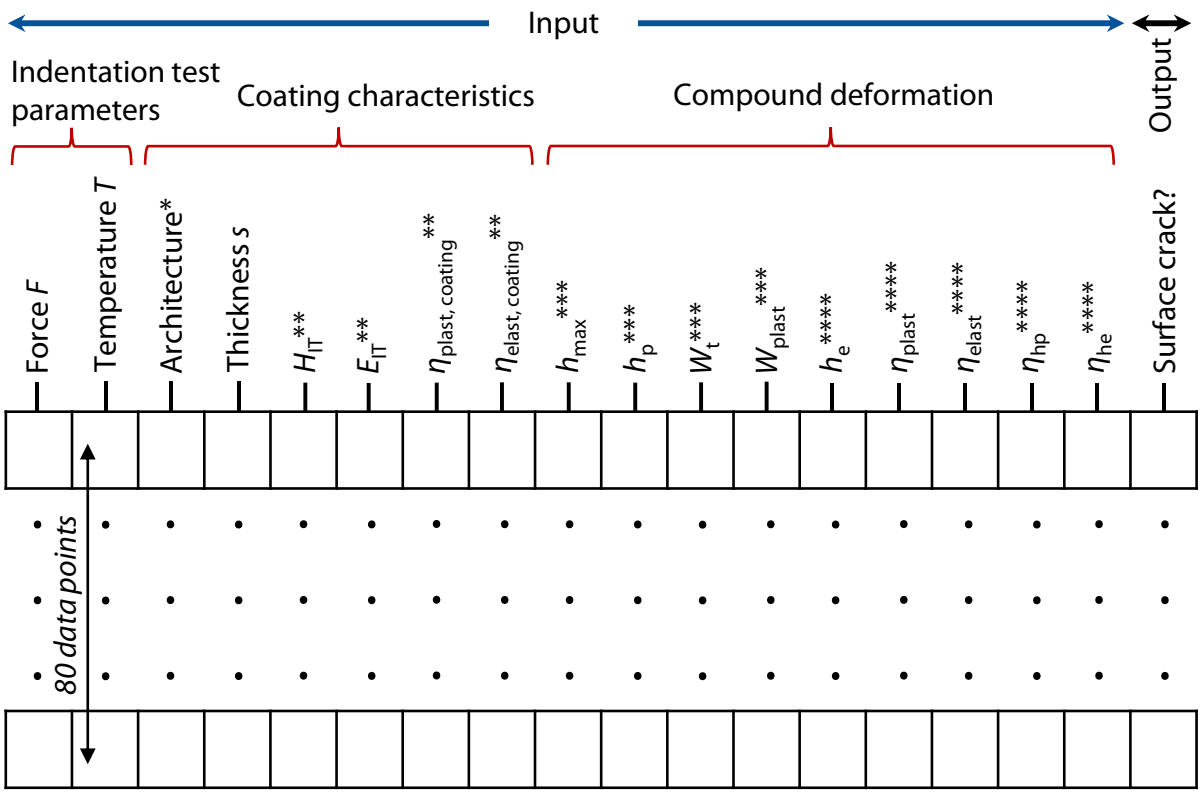

* Monolayer = 0, Bilayer = 1

** Average value from nanoindentation measurements at corresponding temperature

*** Average value from 5 repetitive measurements of indentation tests in micro-range

**** Feature engineering

Figure 14.2: Database structure for training and testing machine learning models for the classification task

Table 14.1: Parameters of the developed prediction models with the corresponding machine learning algorithms

Algorithm	Task	Parameter
Polynomial regression	Regression	Degree = 2
Multilayer perceptron	Regression	Number of hidden layers = 1 Number of neurons in each hidden layer = 100 Solver = Stochastic gradient descent Activation function = tanh Alpha = 0.01 Max_iter = 1000
Random forest	Regression	n_estimators = 50 bootstrap = True max_depth = 10 min_sample_leaf = 1 min_sample_split = 2
Support vector machine	Classification	Kernel = Radial basis function Gamma = scale C = 10
Multilayer perception	Classification	Number of hidden layers = 2 Number of neurons in each hidden layer = 50 Solver = adam Activation function = tanh Alpha = 0.01 Max_iter = 200
Random forest	Classification	n_estimators = 50 bootstrap = True max_depth = none min_sample_leaf = 1 min_sample_split = 2

In der Schriftenreihe Oberflächentechnik des Instituts für Oberflächentechnik der RWTH Aachen sind bisher erschienen:

Band 1: Seemann, Klaus: Vorhersage von Prozess- und Schichtcharakteristiken beim atmosphärischen Plasmaspritzen mittels statistischer Modelle und neuronaler Netze

Band 2: Parco, Maria: Thermische Beschichtung von Leichtbaulegierungen aus Magnesium zum Verschleiß- und Korrosionsschutz

Band 3: Bobzin, K. (Hrsg.): Oberflächentechnik Jahrbuch 2004/2005

Band 4: Bobzin, K. (Hrsg.): 1. Aachener Oberflächentechnik Kolloquium 2006

Band 5: Nickel, Reimo: Die beschichtungsprozessabhängige Materialmodellierung von EB-PVD- und APS-Wärmedämmschichten

Band 6: Ernst, Felix: Qualitätskontrolle auf Basis optischer Prozessdiagnostik und neuronaler Netze beim Thermischen Spritzen

Band 7: Maes, Michel: Gepulste Abscheidung von (Cr,Al)N PVD-Niedertemperaturschichtsystemen für Hochleistungsbauteile

Band 8: Bobzin, K. (Hrsg.): 2. Aachener Oberflächentechnik Kolloquium 2007

Band 9: Hurevich, Vitalii: Einfluss einer Verschleißschutzschicht bei Skalierung des Bohrprozesses in den Mikrobereich

Band 10: Zwick, Jochen: Herstellung und Charakterisierung oxiddispersionsverstärkter Pulver für das Thermische Spritzen

Band 11: Comenares de Piñero, Carmen Leonor: Entwicklung nanostrukturierter PVD-Schichtsysteme für Zerspanung und Kaltumformung durch Einsatz der Pulstechnologie

Band 12: Bobzin, K. (Hrsg.): 3. Aachener Oberflächentechnik Kolloquium 2008

Band 13: Bagcivan, Nazlim: Entwicklung von EB-PVD-Wärmedämmschichten auf Lanthanzirkonatbasis und gesputterten Oxidationsschutzschichten für den Einsatz auf intermetallischen Ni-Basislegierungen

Band 14: Richardt, Katharina: Eigenschaften und Potentiale Atmosphärischer Plasmaspritzsysteme

Band 15: Bobzin, K. (Hrsg.): 4. Aachener Oberflächentechnik Kolloquium 2009

Band 16: Meeß, Rudolf: Entwicklung von Mikrowälzführungen

Band 17: Bobzin, K. (Hrsg.): 5. Aachener Oberflächentechnik Kolloquium 2010

Band 18: Immich, Heinrich Philipp: Maßgeschneiderte oxidische und nitridische PVD-Werkstoffverbunde für metallische Werkzeuge in der Stahlformgebung

Band 19: Rojas Yoris,Yelena: Entwicklung von Lotwerkstoffen zum Vakuumlöten von Nickel- und Titanaluminiden

Band 20: Stephan Bolz: Abscheidung nanostrukturierter Verschleißschutzschichten für Zerspanwerkzeuge mittels Kathodenzerstäubung

Band 21: Daniel Parkot: Simulative und plasmadiagnostische Untersuchungen des Magnetron Sputterns

Band 22: Stefania Ferrara: Entwicklung von Weichaktivloten und Transient-Liquid-Phase-Lotsystemen für Mikrolötverbindungen im Bereich der Medizin und Luft- und Raumfahrt

Band 23: Bobzin, K. (Hrsg.): 6. Aachener Oberflächentechnik Kolloquium 2011

Band 24: Nils Kopp: Reactive Air Brazing

Band 25: Mara Ewering: Synthese, thermische Stabilität und tribologisches Verhalten nanokristalliner gamma-Al2O3-Schichten für die Zerspanung

Band 26: Kirsten Bobzin (Hrsg.): 7. Aachener Oberflächentechnik Kolloquium 2012

Band 27: Konstantinos-Dionysios Bouzakis, Kirsten Bobzin, Berend Denkena, Marion Merklein (Eds.): Proceedings of the 10th International Conference The "A" Coatings 2013

Band 28: Thomas Warda: Thermisch gespritzte eisenbasierte Feinstpulverschicht-systeme für Verschleiß- und Korrosionsschutzanwendungen

Band 29: Sebastian Theiß: Analyse gepulster Hochleistungsplasmen zur Entwicklung neuartiger PVD-Beschichtungen für die Kunststoffverarbeitung

Band 30: Marcel Pascal Schäfer: Modellierung, Simulation und Optimierung von kerosinbetriebenen HVOF-Beschichtungssystemen

Band 31: Sabrina Michelle Puidokas: Design of Highly Stressed Brazed Joints

Band 32: Kirsten Bobzin (Hrsg.): 8. Aachener Oberflächentechnik Kolloquium 2013

Band 33: Hasan Koray Yilmaz: Untersuchung der Einflussgrößen auf das Reibverhalten von Kohlenstoffschichten in geschmierten Tribosystemen

Band 34: Raphael Weiß: Entwicklung und Untersuchung mehrlagiger PVD-Kohlenstoff-schichten als Schutz vor tribologischer und korrosiver Beanspruchung

Band 35: Ivica Petković: Modellierung und Simulation als Werkzeug zur Verbesserung des APS-Prozesses mittels Mehrlichtbogen-Plasmagenerator

Band 36: Markus Brühl: Elektromagnetische Eigenschaften von thermisch gespritzten ferromagnetischen Schichten

Band 37: Kirsten Bobzin (Hrsg.): 9. Aachener Oberflächentechnik Kolloquium 2014

Band 38: Tobias Münstermann: Synthese, Charakterisierung und Qualifizierung von MSIP-Edelmetallbeschichtungen für das Präzisionsblankpressen von Glas

Band 39: Marc-Manuel Matz: Lichtbogendrahtspritzen zur Armierung der ersten Kolbennut für moderne Verbrennungsmotoren

Band 40: Thomas Schläfer: Entwicklung von Verfahren zur Bestimmung der Haftzugfestigkeit von thermisch gespritzten Zylinderlaufbahnen

Band 41: Baycan Yildirim: Mehrlagige EB-PVD-Wärmedämmschichten auf Basis von Seltenerdoxiden

Band 42: Kirsten Bobzin (Hrsg.): 10. Aachener Oberflächentechnik Kolloquium 2015

Band 43: Ricardo Henrique Brugnara: Hochtemperaturaktive HPPMS-Verschleißschutzschichten durch Bildung reibmindernder Magnéli-Phasen im System (Cr,Al,X)N

Band 44: Mehmet Öte: Understanding Multi-Arc Plasma Spraying

Band 45: Martin Hilaire Djoufack: Tribological Evaluation of Hydrogenated a-C:H and Hydrogen-free ta-C Diamond-like Carbon Coatings in Diesel Lubricated Model Tests

Band 46: Leander Schramm: Development of a Robust Cylinder Bore Coating Process and Investigation of Different Feedstock Materials

Band 47: Kirsten Bobzin (Hrsg.): 11. Aachener Oberflächentechnik Kolloquium 2016

Band 48: Tobias Brögelmann: Reibungsreduzierung durch gradierte diamantähnliche Kohlenstoffschichten a-C:H:Zr und a-C:H:Ti in EHD-Kontakten des Automobilantriebsstrangs

Band 49: Christiane Schulz: Thermisch gespritzte ZnMgAl-Schichten als Korrosionsschutz in chloridhaltiger Atmosphäre

Band 50: Thomas Frederik Linke: Entwicklung eines thermisch gespritzten Oxidationsschutzsystems zur Erhöhung der Lebensdauer von γ-Titanaluminiden

Band 51: Kirsten Bobzin (Hrsg.): 12. Aachener Oberflächentechnik Kolloquium 2017

Band 52: Serhan Bastürk: Oxidische und sulfidische HPPMS-Beschichtungen für den Einsatz in der Zerspan- und Umformtechnik

Band 53: Stefanie Wiesner: Einfluss der Ag-Basislote auf das Alterungsverhalten reaktiv gelöteter Verbunde aus Keramik und Metall

Band 54: Kirsten Bobzin (Hrsg.): 13. Aachener Oberflächentechnik Kolloquium 2018

Band 55: Mostafa Arghavani: Elastic-Plastic Deformation and Cracking Behavior of Thin Hard Chromium-Based Coatings

Band 56: Martin Gottfried Engels: Korrelation von Plasma- und Schichteigenschaften bei der reaktiven Plasmasynthese von Hartstoffschichten

Band 57: Xifang Liao: Metallisierung von Kunststoffbauteilen mittels In-Mold-Metal-Spraying

Band 58: Martin Andreas Knoch: Korrosionsverhalten thermisch gespritzter ZnAl15-Korrosionsschutzschichten

Band 59: Kirsten Bobzin (Hrsg.): 14. Aachener Oberflächentechnik Kolloquium 2019

Band 60: Nathan C. Kruppe: Entwicklung hybrider PVD-Prozesse zur Abscheidung nanostrukturierter, oxinitridischer Hartstoffschichten

Band 61: Jan Sommer: HVAF-gespritzte FeCr25B5-Beschichtungen für den Verschleiß- und Korrosionsschutz

Band 62: Tiancheng Liang: Schichtentwicklung zum Oxidationsschutz von Titanaluminiden mittels HS-PVD

Band 63: Christian Kalscheuer: Entwicklung triboaktiver (Cr,Al,X)N-Beschichtungen für den Einsatz auf Maschinenelementen

Band 64: Matthias Thiex: Wechselwirkungen zwischen gradierten diamantähnlichen Kohlenstoffschichten und additivierten Schmierstoffen

Band 65: Tim Denis Stefan Königstein: Eisenbasierte, teilamorphe Hochleistungsbeschichtungen

Band 66: Mona Naderi: Nitride and Oxynitride High Performance PVD Hard Coatings with Laser-processed Surfaces

Band 67: Martin Welters: Potenzial der High-Speed Physical Vapour Deposition Technologie zur Abscheidung oxidischer Werkzeugbeschichtungen

Band 68: Leonid Gerdt: Beschichtungen für das Druckgießen von stoffschlüssigen Hybridbauteilen aus Aluminiumguss und Stahlblech

Band 69: Wolfgang Maximilian Wietheger: Maßgeschneiderte Gleitlagerbeschichtungen für hochbelastete Lagerstellen durch Thermisches Spritzen

Band 70: Ilkin Alkhasli: Multiscale Modelling of Plasma Spraying

Band 71: Kirsten Bobzin (Hrsg.): 15. Aachener Oberflächentechnik Kolloquium 2021

Band 72: Julian Hebing: Ti-Impfen von Ni-Basisloten zur Steigerung der Präzision im Lötgut

Band 73: Kirsten Bobzin (Hrsg.): 16. Aachener Oberflächentechnik Kolloquium 2022

Band 74: Seyed Ruhollah Dokhanchi: Towards Digital Shadow in Plasma Spraying

Band 75: Marco Carlet: Potentiale oxinitridischer PVD-Hartstoffschichten für Zerspanwerkzeuge

Band 76: Kirsten Bobzin (Hrsg.): 17. Aachener Oberflächentechnik Kolloquium

Band 77: Andreas Schacht: Thermisch gespritzte Heizschichten für das Kunststoffspritzgießen

Band 78: Hendrik Heinemann: Plasmaspritzen mit einem kaskadierten Einzellichtbogen

Band 79: Marvin Schulz: Metallisch dichtende Beschichtungen im Armaturenbau

Band 80: Kirsten Bobzin (Hrsg.): 18. Aachener Oberflächentechnik Kolloquium

Band 81: Elisa Olesch: Methodik zur Bewertung und Entwicklung plasmagespritzter Schichten zur elektrischen Isolation

Band 82: Nina Isabell Inge Stachowski: Triboaktive Beschichtungen aus CrAlVN und CrAlMoN für den Einsatz in der Drehbearbeitung von TiAl6V4

Band 83: Christoph Franz Robert Schulze: OES-Datenerfassung in reaktiven HPPMS-Prozessen und Datenanalyse mittels künstlicher neuronaler Netze

Band 84: Kirsten Bobzin (Hrsg.): 19. Aachener Oberflächentechnik Kolloquium

Band 85: Muhammad Tayyab: Deformation and Fracture Mechanics of Compounds with Nitride Hard Coatings for Tooling Applications